AN INVESTIGATION OF THE ALUMINUM K-EDGE BY SPATIALLY RESOLVED X-RAY ABSORPTION SPECTROSCOPY

A Dissertation

Presented to the Faculty of the Graduate School

of Cornell University

in Partial Fulfillment of the Requirements for the Degree of

Doctor of Philosophy

by

Adam Daniel Cahill

May 2016

AN INVESTIGATION OF THE ALUMINUM K-EDGE BY SPATIALLY RESOLVED X-RAY ABSORPTION SPECTROSCOPY

Adam Daniel Cahill, Ph.D.

Cornell University 2016

X-ray absorption spectroscopy is a diagnostic technique that is able to probe the state of a plasma in detail. Such a measurement usually requires that the plasma under study not radiate in the bandwidth of the probing X-ray flux. This is usually accomplished by limiting the temperature of the sample plasma. The research presented in this thesis extends the temperature range of absorption spectroscopy so that more plasmas may be explored with this diagnostic. This is realized in the design of a novel spectrometer based around the geometry of an ellipse. The design is able to discriminate between probing X-rays and those emitted by a sample plasma, relaxing the temperature restriction.

The spectrometer's unique design uses a doubly curved mica crystal for X-ray dispersion. The geometry of the spectrometer is verified by ray tracing calculations assuming Bragg reflection from mica in the second order. Control of other reflection orders is attempted by means of filtering and control of the source spectrum. This is found to be insufficient to control fifth order reflections. Potential solutions are presented to combat these fifth order reflections, but all were considered unlikely to succeed in a timely manner.

The broad X-ray spectroscopy expertise gained from the development and implementation of the elliptical design is then used to explore the physics of aluminum's K-edge. This is done using point projection absorption spectroscopy to study a single 25 µm diameter 1199 alloy aluminum wire through which a peak cur-

rent of 120 kA is passed. The current heats the aluminum from room temperature to a few electronvolts. The plasma is diagnosed using a spherical quartz crystal spectrograph that records the details of the X-ray spectrum near aluminum's K-edge at 1559 eV.

The spectroscopic features of the aluminum plasma are analyzed using a genetic algorithm to match observed spectra to theoretical opacity values. The quality of the fit is discussed by identifying the spectral features that are both present and missing from the opacity calculations. Comparisons are also made to past laser driven studies of the aluminum K-edge. A hypothesis to explain the missing features is proposed.

BIOGRAPHICAL SKETCH

Adam Daniel Cahill was born in Amsterdam, Netherlands in May of 1986. He moved to Kentucky where he grew up and attended Saint Henry District High School from 2000 to 2004. It was during this time that he discovered his love of science and engineering. In the fall of 2004 he enrolled in the University of Louisville's Speed School of Engineering. He graduated in the Spring of 2009 with a Master's degree in Electrical Engineering.

He began pursuit of his Ph.D. in the Electrical Engineering department at Cornell University in the fall of 2009. It was during his first year of graduate school that he discovered the field of plasma physics and joined the Laboratory of Plasma Physics as a student of Dr. David Hammer. In late 2011 he was awarded a Stockpile Stewardship Graduate Fellowship from the Department of Energy. He received his Master of Science degree in 2014 and completed the defense of his thesis in the fall semester of 2015.

He met his wife, Audrey, while attending Kentucky's Governor's Scholars Program during the summer of 2003. They were married in August of 2008. In September of 2014, Audrey gave birth to their daughter Alexandra.

This thesis is dedicated to my father.

ACKNOWLEDGMENTS

I would like to begin by thanking my wife, Audrey, for her continuous support through my graduate career. I do not believe that I could have completed this academic program without her help. I am forever indebted to her for the sacrifices she has made to allow me this opportunity.

To my advisor, David Hammer, and mentors, Sergei Pikuz and Tania Shelkovenko, thank you for your patience. The scientist that I am today is due to your constant encouragement. You have taught me to question every result and that there is always something new to learn and discover.

The entire LPS technical staff has been invaluable in the completion of this work. Todd Blanchard taught me to use the machine shop to fabricate experimental hardware. Without him, many of the experiments in this thesis would not have been possible. Harold Wilhelm has been a source of encouragement and advice in the laboratory. Daniel Hawkes has been a constant source of assistance when repairing pulsed power failures. He has never hesitated to address failures from the mundane to the obscene. My thanks goes out to these men.

Finally, I would like to thank the staff of the KRELL Institute for their administration of the Stockpile Stewardship Graduate Fellowship. Not only has it provided financial support, but also a wealth of contacts across many fields of scientific study. I am honored to have been a part of this program.

This work was supported by the Department of Energy National Nuclear Security Administration under contracts DE-NA0002135 and DE-NA0001836.

TABLE OF CONTENTS

LIST OF FIGURES

LIST OF TABLES

CHAPTER 1

INTRODUCTION

The value of x-ray absorption spectroscopy for the diagnosis of plasmas over a large range of temperatures and densities has long been appreciated [1–3]. Emission spectroscopy generally requires higher temperatures than absorption spectroscopy before signals sufficiently above the system noise floor can be recorded. This requirement is due to the fact that emission spectra are detectable only when adequate populations of excited ions are present. Electron temperatures are required to be high enough to excite the upper states of emission lines. High densities generate a healthy signal to noise ratio. Absorption spectroscopy, on the other hand, carries with it only the requirement that a population of ground state ions exists. This makes absorption spectra an ideal diagnostic for plasmas that are too cold or tenuous to produce a clear emission spectrum.

As sample plasma temperatures and densities rise, emission lines begin to appear in the spectra recorded by any spectrometer with a line of sight to a sample, as is the case in the point projection absorption spectroscopy illustration shown in Figure 1.1 [4]. This complicates, and in some cases makes impossible, the interpretation of absorption spectra as both emission and absorption lines transition between the same excited and ground states. With rising temperature and density, the signal-to-noise ratio of emission spectroscopy rises faster than that of absorption spectroscopy. This is because emission intensity is proportional to the product of n_e and n_i which both rise with temperature. Absorption opacity depends on n_i only. Thus, it would seem that absorption techniques have little utility in the study of high temperature plasmas.

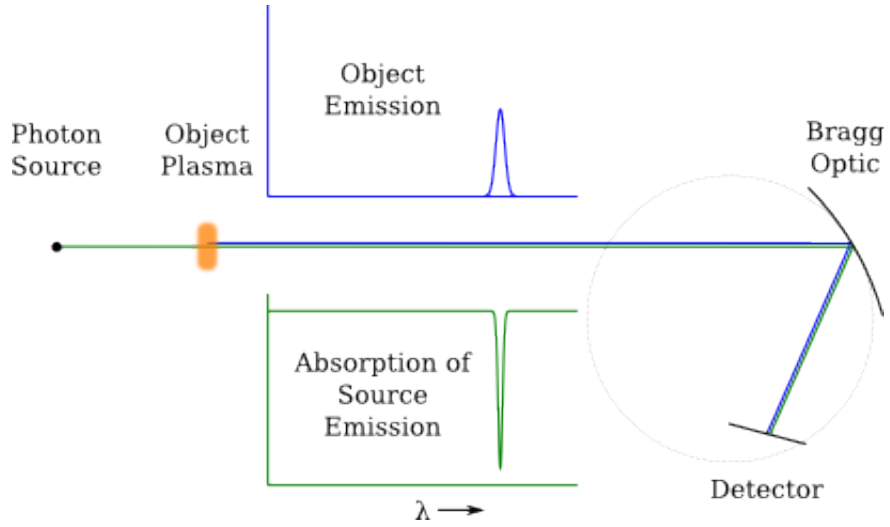

Figure 1.1: The object plasma emission (blue) is collinear with the emission from the X-ray source for the absorption spectrum (green). The overlapping of the two spectra at the detector prevents the spectrum from being interpreted. This can be avoided by requiring the object to remain relatively cool.

Furthermore, intensely radiating plasmas are often surrounded by regions of cooler and lower density material which can have a significant impact on a plasma's evolution [5]. Spectra from these cold and low density plasmas, whether they be emissive or absorptive, are often overpowered by emission spectra generated in nearby regions of high temperature and/or density. In order to investigate conditions in such a plasma, an x-ray crystal spectrometer has been developed that is intended to be able to record spatially resolved x-ray absorption spectra of a plasma under study in the presence of bright x-ray emission from that plasma.

The spectrometer is realized by using a novel combination of elliptical and cylindrical geometries in the orthogonal planes of the dispersing crystal to define the crystal's surface together with a unique arrangement of experimental components. Contrary to a point projection absorption experiment, in which source radiation first interacts with an object plasma before dispersion by an X-ray optic (Figure 1.1), this design disperses probe radiation before interaction with the object (Fig-

ure 4.4). It is this feature that generates a resolved absorption spectrum while leaving the object plasma emission spectrum unresolved.

The crystal chosen to disperse the probing radiation in the elliptical spectrometer is mica which is chosen for it's mechanical flexibility. While mica reflects the probing spectrum well, it also disperses unwanted radiation in high orders. The assumption that this property could be controlled through careful experimental design was found to be overly optimistic. The elliptical design can function as intended if an alternative crystal material such as quartz can be molded to the elliptical geometry. The details of this solution are discussed in section 4.5. The expertise gained from the implementation of the elliptical design is then leveraged to study aluminum's K-edge in a point projection absorption experiment. This is presented in Chapter 5.

An absorption spectrum can provide detailed information on the state of a plasma. The degree of absorption is determined by the opacity of a plasma (discussion in section 2.4), which is itself dependent on both the temperature and density of a plasma. Thus, given an accurate representation of opacity as a function of temperature and density, absorption spectra can be interpreted to determine plasma conditions. A series of time resolved spectra can be used to study the evolution of a plasma as well as its density and temperature as functions of time and space.

Alternatively, if temperature and density are determined by other diagnostic means, then opacity can be experimentally measured. Differences between experimental and computational opacities point to deficiencies in the understanding and/or computational modeling of the fundamental atomic physics that give rise to opacity. This information can be used to guide the refinement of theoretical

models and/or computational methods to determine opacity values.

The remainder of this thesis is laid out in ten chapters. Chapter 2 presents a review of the relevant literature and the studies [5–21] that led to the present work. Spectroscopic techniques are reviewed, and a gap in diagnostic capabilities is identified. Chapter 3 addresses the plasma diagnostics used for this work, including PCDs, Rogowski coils, radiography, and X-ray spectroscopy. Chapter 4 details the design of the new elliptical spectrometer. Goals, geometry, material selection and other details are presented. Results obtained with a mica crystal are presented and why a mica crystal could not be used with the elliptical spectrometer is explained. Chapter 5 presents a point projection absorption experiment that is used to study the details of the K-edge in an aluminum sample. This is followed by a characterization of system errors in Chapter 6. The dominant error sources are found to be the X-ray source size and the rocking curve of the crystal. Chapter 7 is dedicated to the analysis of the acquired data. The techniques used to calibrate the spectral films and extract data from the images are detailed. Chapter 8 presents the results of these analytical techniques. A discussion of the results follows in Chapter 9. Finally, Chapter 10 draws conclusions and Chapter 11 suggests a logical continuation of the work.

CHAPTER 2

BACKGROUND

The development of the X-pinch is reviewed and its use as a point source of X-rays is justified. Additionally, the formation of plasma jets along the axis of an X-pinch is presented. These jets have been studied computationally, but an experimental determination of their temperature has remained elusive. An overview of emissive and absorptive spectroscopic techniques demonstrates the experimental realities that have prevented this data from being collected. This missing data motivated the research in this thesis, although we were thwarted from filling this gap as part of this thesis by the reflection properties of mica crystals as will be discussed in section 4.5.

2.1 The X-pinch

The X-pinch serves as the source of X-rays and was also intended to be the sample plasma in this research. As a source, a hybrid X-pinch generates continuum radiation from a hotspot that is used to diagnose the sample. As a sample, a two wire X-pinch generates plasma jets which were to be probed by the source.

2.1.1 Historical Development

The earliest work concerned with the study of X-pinches was that of Zakharov *et al.* published in 1982 [6]. In that work, a novel configuration of fine wires was used as the experimental load on the Don generator at the P. N. Lebedev Institute

in Moscow. The load consisted of two fine metal wires between the machine's anode and cathode with diameters ranging from 8 µm to 50 µm that crossed each other to form a geometry resembling the letter X. The Don generator was able to drive these X-pinch experiments with approximately 100 kA of current with a 30 ns rise time. The plasma diagnostics fielded with this experiment included laser shadowgraphy, filtered pinhole imaging, and X-ray spectroscopy.

The purpose of the work was to investigate a plasma geometry that produced a single point of plasma constriction that could be accurately located before the experiment to improve the alignment of diagnostics. The resulting X-pinch geometry was found to be effective at producing localized high energy plasmas over a wide range of wire diameters and materials. Filtered pinhole images revealed a high density core with a size estimated to be less than 100 µm while emission spectra indicated a temperature not less than 1 keV. Laser images and interferometry were not able to probe the core of the X-pinch, but they did reveal the presence of plasma jets stretching from the core toward the anode and cathode along the axis of the pinch.

As X-pinches were tested on increasingly large current drivers, it became necessary to increase the mass of the pinches under study. This eventually drove the development of nested X-pinches [19]. By twisting a set of concentric wire cylinders, X-pinches were created from a variety of wire sizes and materials as, illustrated in Figure 2.1. This allowed great flexibility in the design of the X-pinch crossing point as driver currents in experiments at Cornell University rose from 500 kA on the XP generator to the 1 MA level on the COBRA generator. The performance of the nested X-pinch configuration was compared to results from two- and multi-wire X-pinches in which the organized cross point of Figure 2.1 was not

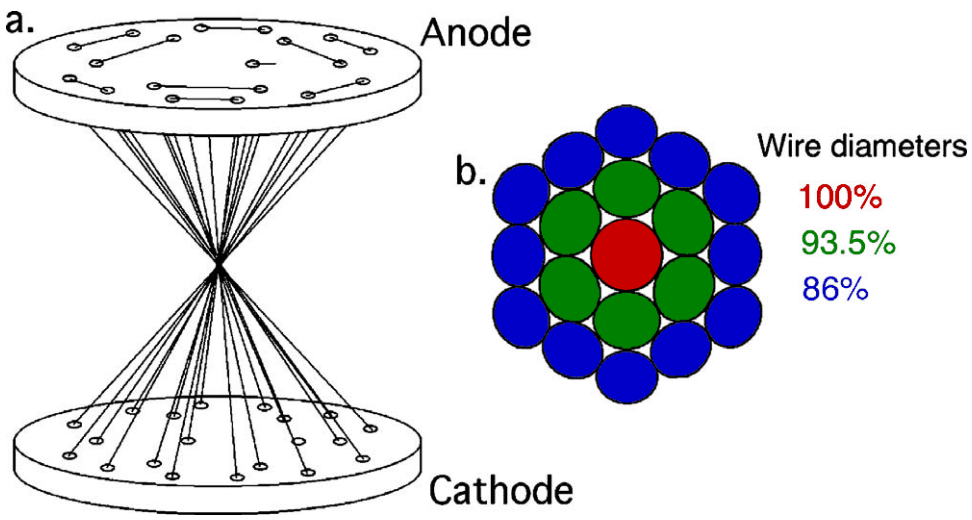

Figure 2.1: (a) Simplified nested multilayer X-pinch configuration. (b) The wire crossing region of a three-layer nested X-pinch. Image source: [19]

realized.

X-ray output power for a number of nested configurations was evaluated using PCDs filtered with Be ($E > 1\,keV$) and Ti ($2.5\,keV < E < 5\,keV$). Source size was evaluated by imaging plates containing micro-machined slits. The best configurations were defined to be those containing a single hotspot with intense emission as recorded by a Ti filtered PCD. This was consistently seen to occur in nested arrays composed of high atomic number materials surrounding materials of intermediate atomic number. X-ray output viewed through a Be foil was found to be comparable to that of standard X-pinches while Ti filtered radiation was found to be double or triple that of standard X-pinches. The best source sizes were found to be $< 3\,\mu m$.

In an effort to simplify the laborious task of building nested X-pinches, a simplified concept consisting of two conical solid electrodes bridged by a single wire was developed [20]. Tungsten alloy (95%W + 5%Cu) electrodes, each containing an axial bore, were set opposite each other in the anode-cathode gap of the XP pulsed

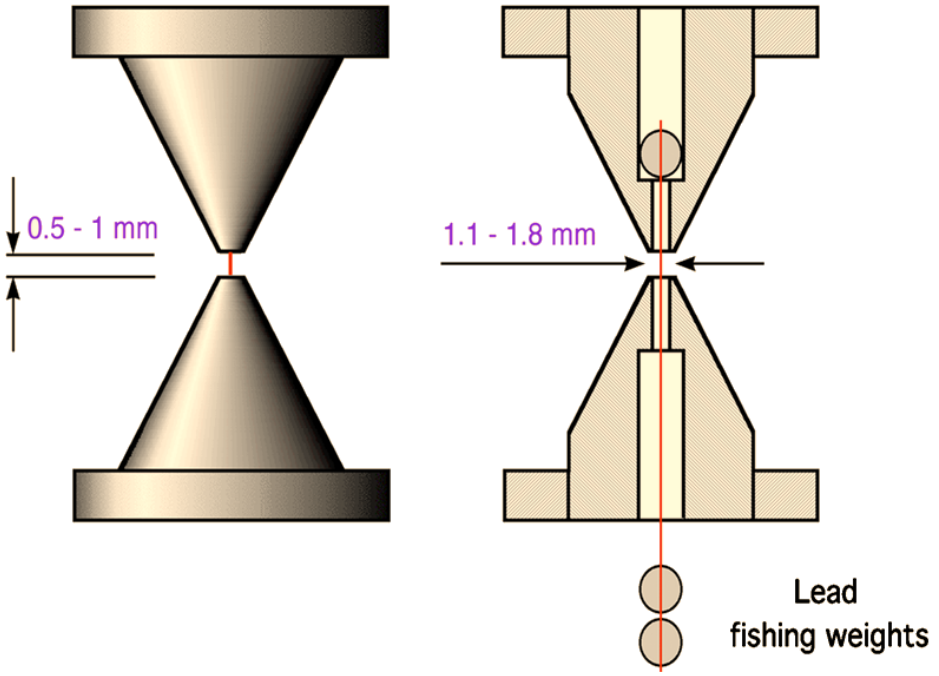

Figure 2.2: A hybrid X-pinch was made from two conical tungsten electrodes with a single wire threaded between them. Image source: [20]

power machine [7]. A wire was threaded along the axis of the configuration. This can be seen in Figure 2.2. The advantages of this geometry were twofold. First, construction was greatly simplified as only a single wire was required. Second, the solid electrodes were relatively undamaged by the experiment on XP, allowing them to be reused.

The hotspot size was evaluated by using the pinch as a point source of X-rays to image a wire mesh. The resultant edge profiles of the imaged wires revealed that the source size could be as small as 1.5 µm. In most cases, the mesh image revealed a single source of strong radiation indicating that the hybrid pinch was producing only a single burst of X-rays. It was theorized that the production of additional hotspots was suppressed due to the electrode plasma generated by UV exposure following the wire's breakdown. This was hypothesized to short out the electrode gap with plasma after the X-ray burst and prevent a second

hotspot from forming. The shorting of the gap was also surmised to be responsible for limiting the generation of radiation between 10 keV and 15 keV by preventing electron beams from forming after the X-ray burst. Peak power, as measured by Be and Ti filtered PCDs, was reproducible and comparable to that of a standard X-pinch.

2.1.2 Hotspots

The initial studies of a single X-pinch indicated that multiple bright spots of X-ray emission often formed near the original crossing point of the wires of the X-pinch. The densities and temperatures of these X-ray point sources were found to be significantly higher than the densities and temperatures of the surrounding plasma. These point sources are known as hotspots. The appearance of multiple hotspots, however, presented a problem for applications that utilized the hotspot as a source of X-rays for high resolution imaging. Early research studied the formation of multiple hotspots [12]. It was found that the formation of multiple hotspots could be controlled by the addition of a parallel shunt current path such as an additional X-pinch or wire. This often prevented a second hotspot from appearing by providing an alternate path for current after an initial X-ray burst created a gap in the X-pinch plasma channel. The size of these X-ray sources was investigated using a variety of techniques that showed the region of intense emission to be much less than 1 mm and in some cases, for >3 keV X-rays, less than 2 µm. The emission volume of a hotspot was seen to vary with X-ray energy, with higher energy X-rays coming from smaller volumes. (Source size is further discussed shortly.) The temporal duration of a single hotspot X-ray burst was found to be as short as 250 ps for <1 keV radiation and ≤100 ps for >3 keV photons.

The ability to generate a small, high density, and high temperature source of X-rays at a predetermined location prompted investigations into using the X-pinch for radiographic purposes. To this end, experiments were performed to explore the spatial, temporal, and spectral properties of the X-pinch. A number of materials including Al, Ti, NiCr, Nb, Mo, Pd, and W with a variety of wire diameters were studied over an energy range of 1 keV to >6 keV [11–13, 15, 16].

Studies of the hotspot's spatial structure have been performed using pinhole cameras to directly image the X-ray emission onto an X-ray detector which was originally X-ray sensitive film [8, 9, 11, 18]. The resulting images were time integrated and magnified by a factor dependent on the geometry of the experiment. The magnification, M, is found from the ratio of the distance from the pinhole to the detector, p, to the distance between the hotspot and the pinhole, q, *i.e.* $M = q/p$. The resulting images were time integrated and the film was exposed to X-rays over a large spectral band. More detailed studies of hotspot structure were accomplished by adding X-ray filters between the pinhole and detector. The adjustment of the filter material and thickness allowed time integrated X-ray images to be captured in specific X-ray bands. It was found that low energy X-rays were emitted from volumes larger than those of high energy X-rays. However, the resolution of a pinhole camera image is limited and dependent on the diameter of the pinhole [13], as shown in equation (2.1). This limited the accuracy of source size measurements. In equation (2.1), σ is a measure of the broadening due to the pinhole camera, which has contributions from geometric, σ_g, and diffraction, σ_d, terms.

$$\sigma^2 \approx \sigma_g^2 + \sigma_d^2 = \left[\frac{(M+1)d}{M}\right]^2 + \left[\frac{2.44\lambda p}{d}\right]^2 \qquad [\mathrm{m}^2] \quad (2.1)$$

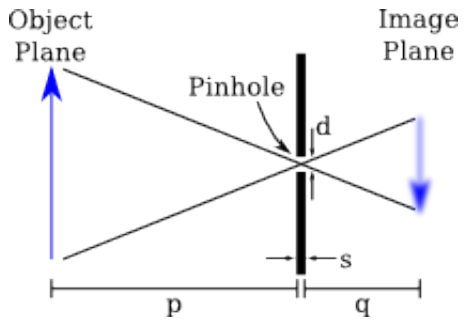

Figure 2.3: A pinhole camera provides a straight forward approach to capturing images of an object, but the finite diameter of the pinhole degrades resolution at the image plane.

An improvement in hotspot size measurements was realized by Song *et al.* in 2005 by analyzing the diffraction patterns generated by the edges of objects in point projection radiography [15]. By imaging micro-fabricated slits with a point projection geometry, the size of the hotspot became the dominant factor controlling an image's edge profiles. Theoretical edge profiles were determined by evaluating equations (2.2) - (2.4). Equation (2.2) computes $I(x_d)$, a 1D edge profile as generated by a point source passing through a 1D object with a complex transmission function $q(x)$. The distance between the source and detector is r, while r_1 and r_2 are the distance from the source to the object and the object to the detector, respectively. The variable x represents position along the transmitting object and x_d represents position along the detector. Finally, λ is the wavelength under consideration. Equation (2.3) computes I_ω, a weighting of detector intensity by the spectral composition of the X-ray source, $A(\lambda)$. Equation (2.4) then accounts for a distribution of source points to compute the final observed intensity I_s, where x_s is a position in the 1D source distribution, $B(x_s)$, which was taken to be a gaussian in the work of Song *et al.* Comparisons between experimental and theoretical edge profiles then allowed hotspot source sizes to be determined to have a gaussian

FWHM of 1 µm to a few microns with sub-micron errors.

$$I(x_d) = \left[\left(\frac{r}{i\lambda r_1 r_2}\right)^{1/2} \int e^{-\frac{i\pi}{\lambda r_2}\left(2xx_d - \frac{r}{r_1}x^2 - \frac{r_1}{r}x_d^2\right)} q(x)\,\mathrm{d}x\right]^2 \tag{2.2}$$

$$I_\omega(x_d) = \int A(\lambda) I(x_d)\,\mathrm{d}\lambda \tag{2.3}$$

$$I_s(x_d) = \int B(x_s) I_\omega(x_d + x_s(r_2/r_1))\,\mathrm{d}x_s \tag{2.4}$$

The small source size of the hotspots made them excellent candidates for radiographic X-ray sources. Thus, further investigations into the spectral emission characteristics of X-pinch hotspots were launched [9, 11, 12]. Hotspot line radiation was found to be emitted from highly ionized, in some cases He-like and H-like, ions which indicated that hotspot temperatures exceeded 1 keV. In addition to atomic line radiation from excited ions, the best X-pinches were found to produce broad band continuum emission of X-rays from 1 keV to >6 keV from the hottest and densest regions of the X-pinch. Finally, high energy X-rays (>10 keV) were also observed. These were determined to be generated by beams of electrons that were accelerated across gaps that developed near the hotspots.

In order for the X-ray burst generated by hotspots to be useful for radiographic work, an understanding of the temporal width of the pulse was required as this would set the time over which a radiograph was integrated. Initial measurements were performed using filtered photoconducting diodes (PCDs) [13,14]. While these measurements revealed that the hotspots generated a very short burst of X-rays, the measurements were limited by the bandwidth of the diodes together with the digitizing oscilloscopes to which they were connected. In order to better measure the X-ray pulse, X-ray streak cameras were employed to obtain higher resolution measurements of the burst duration [14]. The hotspots were found to emit X-rays over several hundred picoseconds for >1 keV radiation and as short as 30 ps for >3 keV continuum.

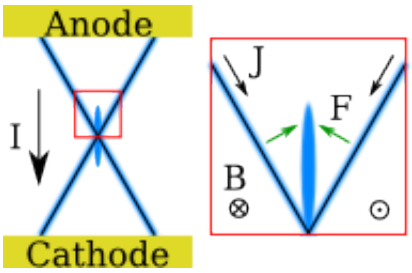

Figure 2.4: An X-pinch's jets are formed by a $\mathbf{J} \times \mathbf{B}$ force (green) in the wires' coronal plasma. The resulting flow is directed along the X-pinch axis and away from the crossing point.

The ability of an X-pinch to develop micron scale hotspots that emit broad band X-rays over sub-nanosecond time scales ideally situated them for point projection radiographic work. Small spatial scales meant that radiographs would not be blurred by the source size. Broad band emission meant that objects could easily be images in multiple wavelengths. Short burst durations meant that images of objects evolving on nanosecond time scales could be captured without blur due to object motion.

2.1.3 Jets

As current flows through the coronal wire plasma of the legs of an X-pinch, interaction with the global magnetic field produces a $\mathbf{J} \times \mathbf{B}$ force directed toward the central axis of the pinch and away from the X-pinch's cross point. This is illustrated in Figure 2.4. This flow along the axis forms a plasma jet. These jets were observed in the earliest X-pinch experiments [6] and have been studied since then as an example of plasma dynamics [9, 10, 17]. Scaling arguments have also been made to relate X-pinch jets to those found in astrophysical studies, which prompted additional experimental work [21].

The resistive MHD code GORGON has been used to study two wire X-pinches [17]. The results from that investigation were used to generate artificial radiographs that could be compared with experimentally collected data. The results were shown to be in qualitative agreement. Other results included density maps of jets appearing along the X-pinch's axis and flowing away from the central crossing point. These jets were found to be the result of wire current interacting with a global magnetic field to produce a $\mathbf{J} \times \mathbf{B}$ force toward the axis. The temperature of the jets was found to be kept low by radiative cooling, but the results from the computer simulation were not compared to experimental data.

Experimental observations of X-pinch jets have been performed using radiography and interferometry [10, 21], which are sensitive to plasma density. These have produced density maps of a jet's evolution over experimental time scales and obtained electron densities as high as $\sim 1 \times 10^{19}\,\mathrm{cm}^{-3}$. While the density of these jets is well known, temperature measurements of X-pinch jets have been elusive. This has left computer simulations as the sole means of investigating X-pinch jets but without experimental verification of the results.

2.2 Spectroscopic Notation

A number of notational schemes are used to identify the ionization states of an atom. Using magnesium as an example, Mg I refers to a neutral Mg atom. For each removed electron, the Roman numeral is incremented. Thus, Mg III is twice ionized. This is continued until the atom is fully stripped of its electrons. Ions may also be referred to using a superscript to indicate the total charge on the ion. For neutral and doubly ionized Mg, these are Mg^{+0} and Mg^{+2}, respectively. Finally,

the ion may be referred to by the neutral element which its electrons resemble. In the current example, doubly ionized Mg would be Ne-like Mg since ten electrons are bound to the nucleus, as is the case with neutral Ne. These notations refer to the number of electrons bound to the atom only. They do not describe the locations or configuration of the electrons.

The orbitals associated with each principal quantum number, n, have an alphabetical naming scheme. The $n = 1$ orbital is referred to as the K-shell. The next orbital is $n = 2$ and is called the L-shell. The orbitals for $n = 3, 4, 5$ are the M, N, and O-shells, respectively. The present research is concerned primarily with transitions into and out of the $n = 1$ orbital or K-shell.

Electronic transitions associated with the K-shell are denoted by use of the Greek alphabet. A transition between $n = 1$ and $n = 2$ is an α transition. A transition between the K-shell and $n = 3$ is a β transition. An M-shell to K-shell transition is denoted using a γ.

A final distinction is between resonance and satellite transitions. A resonance transition occurs between an excited ion and its ground state. For example, a He-like Mg ion has two bound electrons. If one of these two electrons is found in the K-shell, and the second decays into the K-shell, this is a resonance transition since the ion ends in its ground state with two electrons in the K-shell. A H-like resonance occurs in an atom containing one electron when that electron falls into the K-shell. Satellite transitions are identical to resonance transitions except that the ion has additional bound electrons at some energy levels above the ground state. For example, a Li-like ion has three bound electrons. Two electrons may be in the K-shell while the other occupies a higher orbital. The higher orbital electron then serves to screen the nuclear potential from the K-shell electrons by

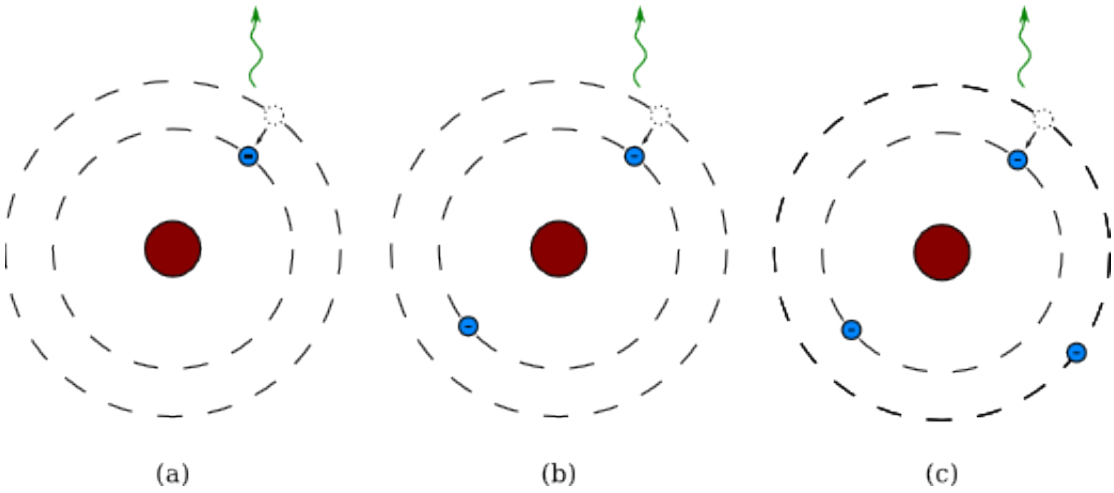

Figure 2.5: The H_α transition (a) involves a single electron falling from the n=2 to the n=1 orbital. The He_α transition (b) is similar except that an additional electron resides in the 1s orbital. The Li-like satellite transition (c) adds an extra bound electron in a higher energy orbital.

a small amount and lowers the transition energy necessary for one of the K-shell electrons to be promoted to the L-shell. The electron moves between the same orbitals as in the resonance transition, but the transition energy is lowered. When that electron drops back down to the K-shell, the X-ray photon energy is reduced by that same amount. Thus, satellite lines always appear at slightly lower energy than the associated resonance transition.

2.3 Emission Spectroscopy

The spectral characteristics of a plasma, such as which atomic transitions are excited and their relative strengths, are determined by the temperature and density of a plasma. As temperature rises, the degree of plasma ionization increases and higher energy electronic configurations are accessed. With rising density, increased collisionality also influences ionic populations and generates excited states, leading to satellites of spectral lines. Figure 2.5 depicts three common electronic transi-

tions.

The ratio of resonance lines, such as He_α to H_α, is often dominated by plasma temperature. The ratio of satellite line intensity to the parent resonance line intensity is primarily influenced by density with temperature playing a secondary role. Thus, by recording the radiation spectrum emitted by a particular plasma, an understanding of its density and temperature state can be inferred from the intensity ratio of various line pairs.

Emission spectroscopy has found application over a wide plasma parameter space from low density photoionization experiments to high energy density wire array Z-pinch experiments [22–24]. In these experiments, the X-ray emission radiation from the plasma under investigation is reflected by the lattice of a crystal according to Bragg's Law in equation (2.5) as illustrated in Figure 2.6. Here, n is the reflection order, λ is the X-ray wavelength, and d is the spacing between lattice planes. The angle θ is the angle made between an incoming X-ray and the crystal's reflecting planes, the so-called grazing angle. A thin crystal is often bent into a standard geometry, such as cylindrical or spherical, to focus X-rays onto a detector after dispersion. This permits larger bandwidths to be captured and higher X-ray fluxes to reach the detector. A discussion of common geometries is presented in section 3.4.4.

$$n\lambda = 2d\ sin(\theta) \tag{2.5}$$

The high X-ray flux emitted from X-pinch hotspots made their study by emission spectroscopy fairly straightforward. The setup for such an experiment consists of an X-ray reflecting crystal that is arranged to reflect and disperse a selected band of X-rays onto a detector as depicted in Figure 2.7. The wavelength band is se-

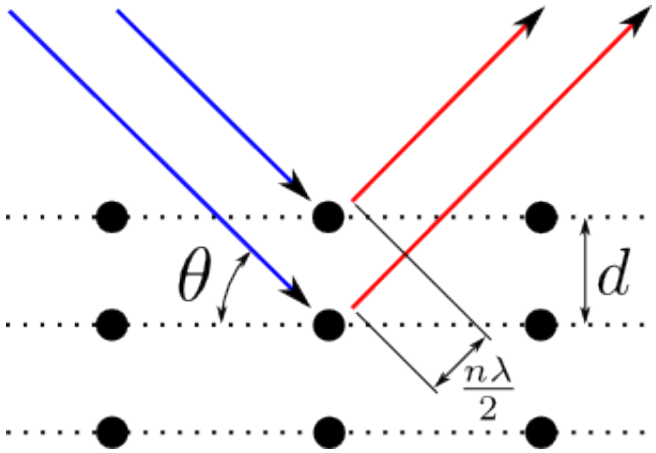

Figure 2.6: Bragg reflection occurs when path lengths differ by an integer number of wavelengths. This allows constructive interference to occur in the reflected waves.

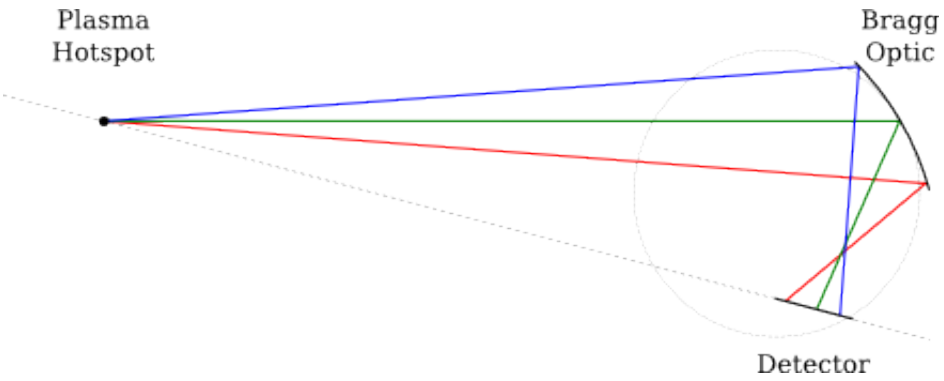

Figure 2.7: X-rays from the X-pinch hotspot are dispersed by a Bragg optic. The resultant spectrum is recorded on either film or an image plate detector.

lected by positioning the crystal such that X-rays from a hotspot satisfy equation (2.5). The results from such investigations reveal that hotspots reach temperatures and electron densities exceeding 1 keV and $1 \times 10^{23}\,\mathrm{cm}^{-3}$ respectively [14, 25, 26]. An analysis of emission spectra obtained from the axial jets of X-pinches has not been found. This is due to the low X-ray signal levels that result from the jets being relatively cold and of low density.

2.4 Absorption Spectroscopy

Emission spectroscopy collects and disperses the photons emitted as excited atoms decay to lower energy states, most often their ground states. Absorption spectroscopy, in contrast, measures the interaction between ground state atoms and a probing flux of photons. When incoming photons interact with ground state ions, the ions absorb the photon and are excited to a higher energy state. The difference in energy between the excited and ground states matches the energy of the absorbed photon. By measuring the absence of probing photons at particular wavelengths in the probing flux, information about ion populations may be obtained. This can then be related to plasma temperatures and densities [4,27,28].

This diagnostic technique is able to diagnose a lower temperature plasma in the same ionization state as emission spectroscopy. This is due to the fact that it does not rely on a large population of excited ions to generate the detected signal. Such a large population of excited ions in a given ionization state may exist only over a narrow temperature range. Additionally, densities must be sufficiently high for an emission signal to become visible above the experimental noise. Instead, only ground state ions are needed in absorption spectroscopy. Much lower plasma densities may also be detected due to the strong resonance between the probing photon and ground state ion. A cartoon depicting an absorption spectroscopy measurement is shown in Figure 2.8.

The measurements from an absorption spectroscopy experiment record a probe spectrum from which an object plasma has absorbed a fraction of the radiation. The governing relationship given in equation (2.6) describes the alterations to the probe spectrum, $I(\lambda)$ due to an absorbing plasma. Here, n is the mass density of absorbing particles and $\sigma(\lambda, \rho, T)$ is the wavelength dependent opacity of the

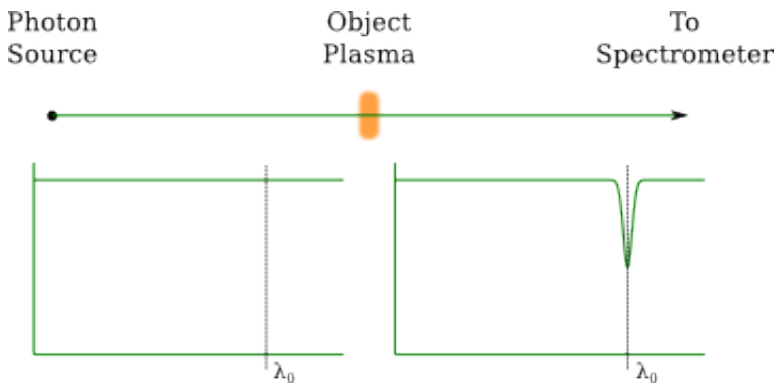

Figure 2.8: Photons at λ_0 are absorbed by the object plasma. The finite width of the absorption feature may be due to a combination of factors including the natural linewidth, Doppler broadening, or pressure broadening.

plasma with density ρ and temperature T. The quantity s is a path through the absorbing medium which is taken to be a straight line in the present work.

$$\frac{dI(\lambda)}{ds} = -n\sigma(\lambda, \rho, T)I(\lambda) \tag{2.6}$$

The solution to this equation is

$$I(\lambda) = I_0(\lambda)e^{-\tau} \tag{2.7}$$

where

$$\tau(\lambda) = \int_0^l n\sigma(\lambda, \rho, T)\,\mathrm{d}s \tag{2.8}$$

is the dimensionless optical depth of the plasma. If for a given wavelength $\tau \gg 1$, the vast majority of photons are absorbed and few reach the detector. If $\tau \ll 1$, very few photons interact with the plasma. Experimentally, it is desirable for τ to vary over a wide range throughout the bandwidth of the experiment to generate signals that are easily discernible from system noise.

If both the source spectrum, I_0, and the final spectrum, I, are known, the transmission function can be calculated as

$$T(\lambda) = \frac{I(\lambda)}{I_0(\lambda)} = e^{-\int n\sigma(\lambda,\rho,T)\,\mathrm{d}s} \tag{2.9}$$

The transmission function is then compared to the output of atomic modeling codes to determine the density and temperature of the absorbing plasma.

2.5 Elliptical Spectrometer Motivation

A particular disadvantage of absorption diagnostics is that they impose restrictions on both the geometry and properties of an object plasma under study. A key consideration when designing an absorption experiment is to ensure that each wavelength used for probing interacts with an identical plasma. In the case of X-rays, dispersion is often performed by a Bragg optic which requires the incidence angle on a crystal to vary with wavelength as given by equation (2.5). This requires that the probing X-rays are not collinear. If the rays are not collinear, they must pass through physically distinct volumes of plasma which are ideally identical in temperature and density. This is realized by restricting the object plasma to be free of significant temperature and density gradients in the plane of crystal dispersion, a difficult requirement to achieve in practice, as illustrated in Figure 2.9.

A second restriction for standard point projection absorption spectroscopy (Figure 2.9) is often placed on the temperature of the object plasma due to the arrangement of experimental components. A bright source of photons produces a uniform probing spectrum of radiation that interacts with an object plasma where it is absorbed according to the opacity of the object. Next, the modified probe spectrum is dispersed and recorded. Since the dispersive component sits between the object plasma and the recording device, any radiation emitted by the object plasma will be dispersed and recorded along with the absorption spectrum. The emitted photons are at the same energy as the absorption lines since both processes

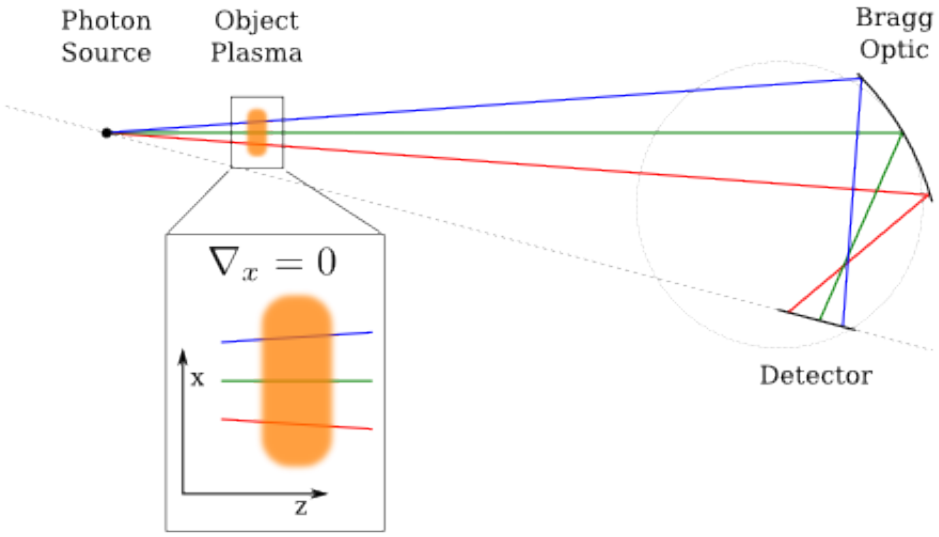

Figure 2.9: Probe photons in point projection absorption spectroscopy are not collinear, and pass through physically separate volumes of the object plasma. This requires gradients perpendicular to the direction of propagation to be small if the spectrum is to represent the object plasma as a whole.

occur between the same electronic energy levels. This can result in absorption lines being filled by photons emitted by the object plasma as shown in Figure 2.10. This obscures the true absorption spectrum. The situation is avoided by restricting the temperature of the object plasma. Since emission requires a population of excited ions, which are present at high temperature, the object plasma temperature is often restricted. The temperature must be sufficiently low so that radiation is not emitted in the desired absorption band. This restriction may preclude high energy density plasmas from being investigated by absorption techniques.

In order to overcome these limitations, a spectrometer must be able to record spectra that are spatially resolved along any non-uniform axis of a sample plasma. It must also discriminate between probing radiation emitted by the source and emission radiation from the sample. The design of such a spectrometer is presented in Chapter 4.

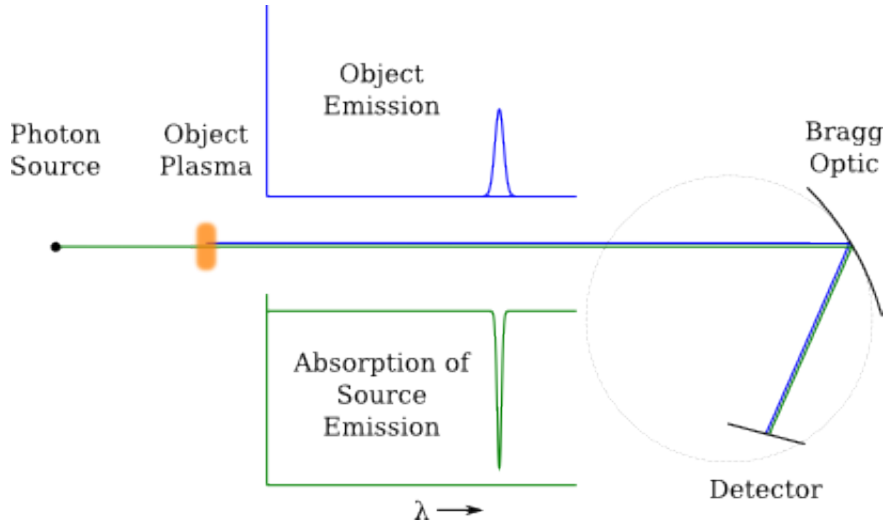

Figure 2.10: Object plasma emission (blue) is collinear with the absorption spectrum (green). The overlapping of the two spectra at the detector prevents the spectrum from being interpreted. This can be avoided by requiring the object to remain relatively cool.

CHAPTER 3

PLASMA DIAGNOSTICS

This chapter presents an overview of the diagnostic tools used in the course of this work. Photoconducting detectors determine X-ray emission timing; Rogowski coils provide current measurements; point projection radiography and X-ray spectroscopy provide details about the physical state of a plasma. These three measurement methods are discussed in detail here because they will be mentioned repeatedly throughout the remainder of this thesis.

3.1 Photoconducting Detectors (PCDs)

Photoconducting detectors (PCDs) are two-terminal devices that consist of an insulating material attached between two electrodes. A PCD is positioned so that during an experiment, a photon flux is incident upon the surface of the insulator. The insulator material has an energy gap between its valence and the conduction bands that is less than the energy of the photons to be detected. When the incident photons strike the PCD, they are able to excite electrons from the valence into the conduction band where they move more freely through the lattice. This increased mobility is manifest macroscopically as a decreased resistance between the two terminals of the device [29, 30].

To detect the resistance change, a bias voltage is applied across the device's terminals. This bias voltage may range from a few volts to hundreds of volts and depends on the chosen insulator material. Without a photon flux, this bias potential appears across the insulator, and no current flows. However, under the

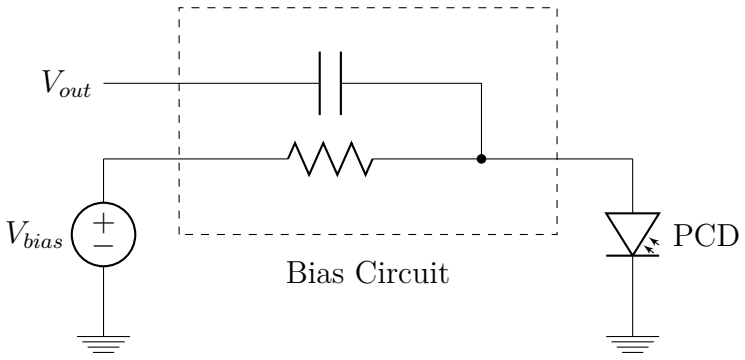

Figure 3.1: The PCD biasing circuit filters the high frequency signal from the DC bias voltage.

influence of the photons during an experiment the resistance drops and current flows. This current flow is evidence of photons in the experiment.

Biasing of the device is physically accomplished through the use of a biasing circuit consisting of only a resistor and a capacitor. The circuit has three terminals: a bias input, a signal output, and a device connection. The purpose of this circuit is two-fold. First, it allows the PCD to be biased by the voltage applied to the V_{bias} node through the resistor. Second, it acts as a high pass filter that allows the high frequency signal generated by the photon flux to pass to the recording oscilloscope. This is important since the observed signal may be small compared to the bias level. The circuit is depicted in Figure 3.1.

The PCD is restricted to the detection of a limited photon energy range. At low photon energies, a signal cannot be generated if the energy of the photon is less than the band gap of the material. In this case, an electron cannot be excited into the conduction band to cause a drop in resistance. High energy photons are not detected for a different reason. The optical depth of a material is the length over which a flux changes by a factor of e^{-1}. In general, optical depth increases with particle energy. If the optical depth rises significantly for high energy photons, the particles will pass through the material with a low probability of interaction. This

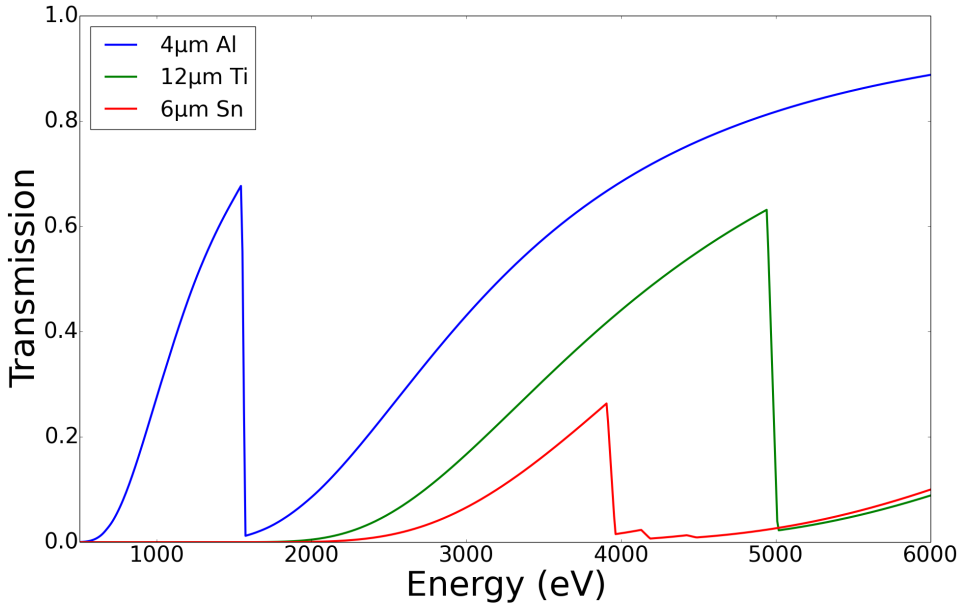

Figure 3.2: The transmission functions of three different PCD filters (Al, Ti, and Sn) are shown. Each filter exposes the underlying PCD to a different spectral band of X-rays.

prevents a significant population of electrons from entering the conduction band and reducing the material's resistance.

While the range over which a PCD can detect photons is limited, the experimentalist often wishes to further restrict the operational energy range of the PCD because restricting the detection energy range can provide useful spectral information about the photon flux. This is done by filtering the PCD. The opacity of the filter material as a function of energy along with its thickness determine the subset of photons that are able to reach the PCD. Examples of three filter transmission functions are shown in Figure 3.2.

PCDs are able to detect the appearance of an X-ray burst with a fast (sub-nanosecond) rising edge. This permits the signal peak to be used as a time marker in an experiment. However, the peak signal level is not calibrated in the present work. This means that the PCDs may be relied upon only to provide temporal

information and shot-to-shot relative X-ray flux.

3.2 Rogowski Coils

A Rogowski coil is two-terminal device that is made from a toroidal coil of wire, such as that illustrated in Figure 3.3. The device measures current flow inside the major circumference. When current flows through the central hole of the torus, a magnetic flux is generated that passes through the wire loops around the minor circumference. A voltage is generated by each wire loop that is proportional to the changing magnetic flux through and perpendicular to the plane of the loop. The sum of the voltages from all of the loops appears at the output terminals of the device. The expression relating output voltage to current flow is shown in equation (3.1).

$$V = -\frac{AN\mu_0}{l}\frac{dI}{dt} \tag{3.1}$$

The values A, N, and l are the coil's cross sectional minor area, number of turns, and major circumference respectively. The resulting voltage trace is scaled and integrated to arrive at the measured current through the coil. Direct computation of the calibration factor, $\frac{AN}{l}$, will introduce errors from the measurement of the various geometrical parameters. Instead, the calibration factor is determined empirically as described in section A.2.2.

A Rogowski coil suffers from two limitations. An ideal coil would have a large number of turns, N, in a very short length l. This would provide a large signal-to-noise ratio while measuring a very localized current flow. Unfortunately, the large $\frac{dI}{dt}$ generated by the XP pulser causes such an ideal coil to generate output voltages that exceed the breakdown voltages of connectors and signal cables between the

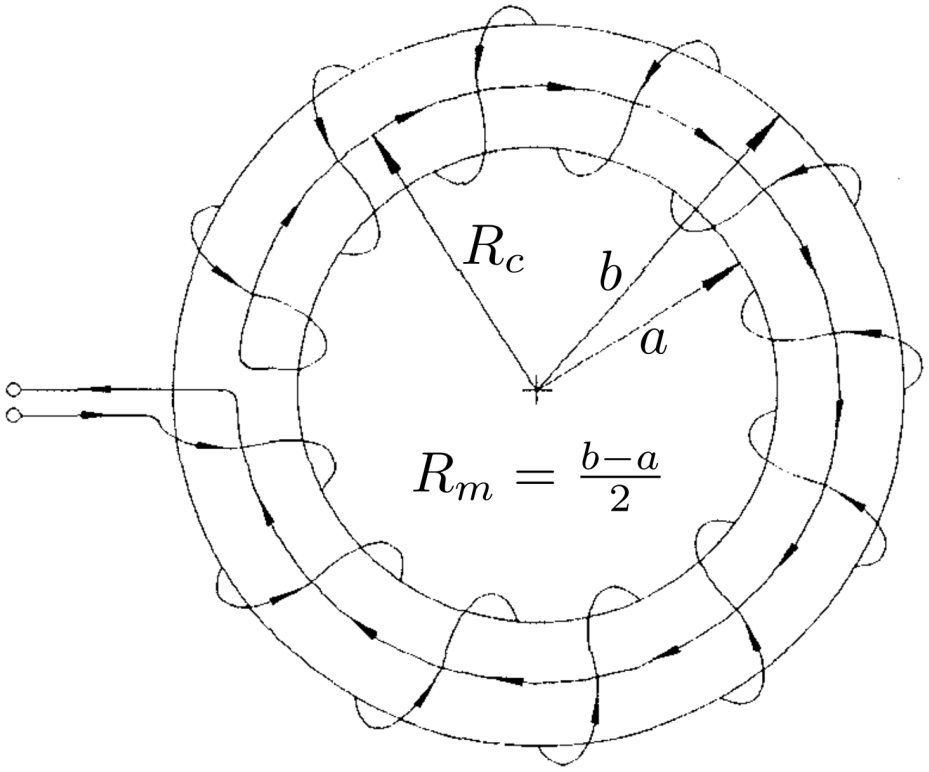

Figure 3.3: Current flowing into the page generates a magnetic flux in the plane of the page. This flux is converted to a voltage by each loop around the outside of the torus. Image source: [31]

experiment and data acquisition systems. Reduction of the minor area, A, can be done only up to a point where construction techniques fail. The final result is that Rogowski coils are often not suitable for measurement of the full machine current where $\frac{dI}{dt} \approx 5 \times 10^{12}\,\mathrm{A\,s^{-1}}$. They are limited to the measurement of fractions of the machine current.

The second limitation is caused by the inductance of the coil which is

$$L = \mu_0 N^2 \left(R_c - \sqrt{R_c^2 - R_m^2} \right) \tag{3.2}$$

where N, R_c, and R_m are the number of turns, the major radius, and minor radius as illustrated in Figure 3.3. To understand how coil inductance influences the output signal, consider the simplified schematic of Figure 3.4. The sampled signal

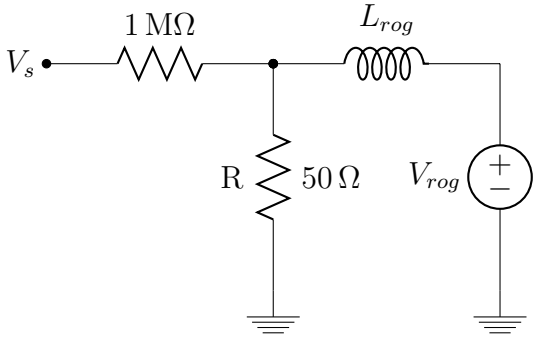

Figure 3.4: The Rogowski coil voltage appears across the Rogowski inductance, L_{rog}, and the cable termination impedance of 50 Ω. The 1 MΩ input impedance of the oscilloscope has a negligible influence on the circuit.

at the input of the oscilloscope is then

$$V_s \approx \frac{V_{rog}R}{\omega L + R} = \frac{V_{rog}}{\frac{\omega L}{R} + 1} \tag{3.3}$$

Provided $\frac{\omega L}{R} \ll 1$, the sampled voltage is approximately equal to the Rogowski voltage. However, if the inductance is allowed to rise such that $\frac{\omega L}{R} \geq 1$, the voltage at the oscilloscope begins to decrease and takes on a frequency dependence. This should be avoided. The inductance is most easily minimized by reducing the N^2 term in equation (3.1), but this conflicts with the need for a clean signal. This engineering trade-off must be well understood during the design of the coil.

3.3 Point Projection Radiography

Point projection radiography is a technique that is able to capture calibrated areal density maps of a plasma sample. This begins with a point source of photons such as an X-pinch. These photons are released isotropically and a select few impinge upon a plasma sample. Of the photons that interact with the plasma, a fraction of them are absorbed. The resulting non-uniform distribution behind the plasma contains an image of the plasma which is collected on a detector. This is illustrated

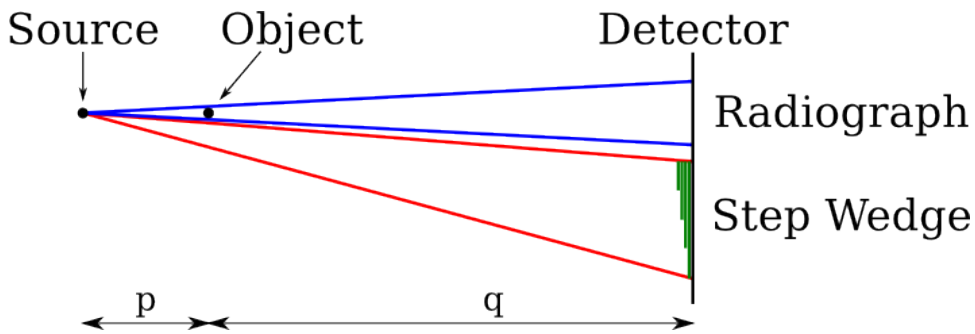

Figure 3.5: A radiograph of an object and the image of a step wedge filter are captured on the same detector. This allows the areal density of the object to be calibrated.

in Figure 3.5.

A calibration is obtained by simultaneously imaging a step-wedge made from the same material as the plasma under study. The step wedge is often placed near the detector and far away from the object plasma. When preparing to collect such an image, it is important to ensure that the image of the plasma does not overlap the step-wedge. This will cause errors during the calibration since some steps may receive a higher flux than others. An example radiograph image of a single exploding aluminum wire and a calibration step-wedge is shown in Figure 3.6.

The resolution of a point projection system with a geometry like that shown in Figure 3.5 is primarily determined by the size of the photon source. A finite source size causes the true image of the sample plasma to be blurred. This limits the image resolution to the order of the source size. The hotspot of an X-pinch provides a micron (µm) scale source size [15].

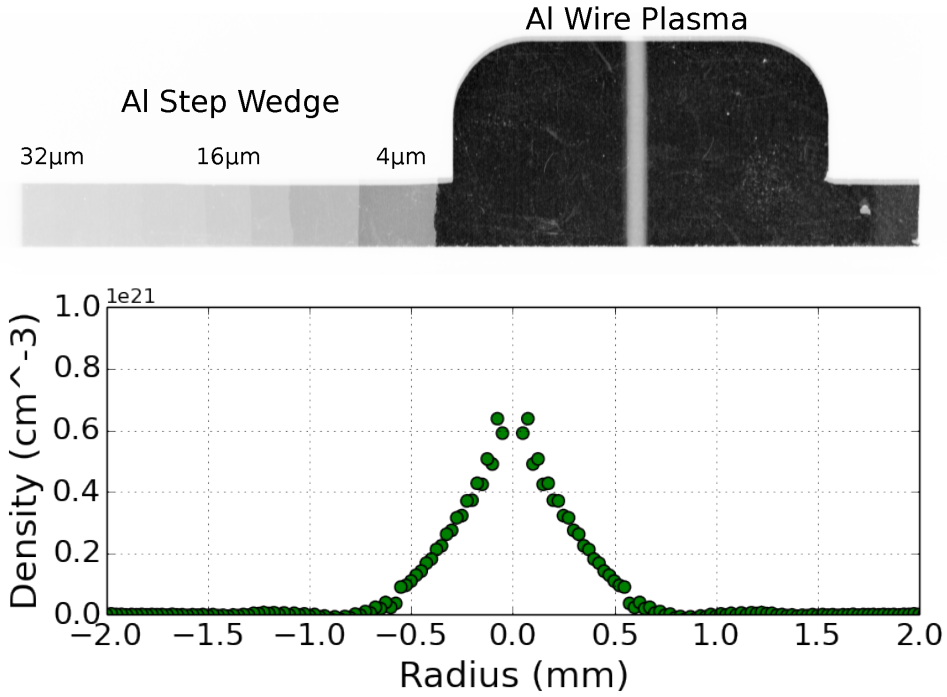

Figure 3.6: A point projection radiograph is calibrated by simultaneously imaging a step wedge of known areal density. The step wedge is made from the same material (Al) as the sample being imaged. For a cylindrical system the areal density can be Abel inverted to reveal volumetric density.

3.4 X-ray Spectroscopy

X-ray spectroscopy is concerned with the detailed spectral characteristics of a plasma. These characteristics can be either emissive or absorptive. In either case, the photon flux from or passing through the plasma contains within its spectrum details about the configuration of energy levels in the atoms and ions of the plasma. The spectral details arise from the relative populations of the various electronic energy states of the constituent atoms. Because the relative populations of these energy levels are dependent on the state of the plasma, *i.e.* its density, temperature, and ionization state, an understanding of a plasma's spectrum can lead to a diagnosis of all of these quantities.

Collection of a spectrum is performed by scattering the X-rays off of a crystalline lattice. The scattering process is governed by Bragg's Law, which considers scattering from multiple points within a lattice structure.

$$n\lambda = 2d\sin(\theta) \tag{3.4}$$

The X-ray wavelength is given by λ. The details of the crystal's lattice determine the value of d and the strength of the various reflection orders, which are given by the integer n. The result is that the scattered waves interfere constructively at an angle, θ, from the tangent of the surface (Figure 3.7). After scattering, the radiation is collected on either an image plate or photographic film detector in the present experiments.

The dispersion of a spectrum onto a detector by a crystal does not in general produce an image of the spectrum in which photon energy is a linear function of detector position. The exact details of the relationship between position and energy are dependent on the shape of the crystal and the geometric arrangement of the components of the system. Instead of computing a dispersion relation that depends on the measurement of component placement, which introduces errors, an experimentally determined polynomial relationship is often used to describe the dispersion relationship. This is done by identifying known features in the spectrum. This provides position/energy pairs which are then fit to the polynomial function. The polynomial can then be used to compute the energy of features at other film positions.

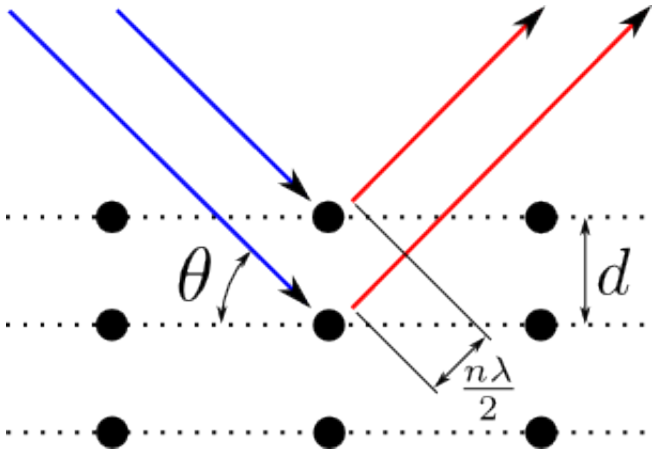

Figure 3.7: Bragg reflection occurs when path lengths differ by an integer number of wavelengths. This allows constructive interference to occur in the reflected waves.

3.4.1 Crystals

X-ray crystals work by scattering X-rays from their periodic lattice of atoms. While scattering may occur in any direction, constructive interference occurs only when equation (3.4) is satisfied. This is illustrated in Figure 3.7. Two photons are scattered by separate atoms in the lattice. When they leave the crystal, they interfere constructively only if the difference in their path lengths is a multiple of their wavelength. This criterion leads one to equation (3.4) for the reflection of X-rays from a crystalline material.

The spacing between the reflecting planes of a crystal, d, sets an upper limit for the maximum wavelength that the crystal can reflect in a given order n because θ is equal to the arcsine of a number greater than one if $\lambda > \frac{2d}{n}$. In that case, the solution to equation (3.4) is undefined for real numbers and implies that X-ray absorption by the crystal should be considered. Thus, each crystal has a maximum wavelength that it may reflect in any given order.

3.4.2 Rocking Curve

Equation (3.4) truly applies only in the ideal case of a perfect crystal. The reality is that all crystals contain lattice defects where atoms may be out of place or replaced by a different element. Such defects serve to alter the reflection properties of any crystal such that constructive interference may occur at an angle of $\theta + \Delta\theta$ instead of θ.

The deviation from perfection, $\Delta\theta$, at which significant reflected intensity may show up on the detector is described by a curve known as a Rocking curve. These curves are often, but not always, asymmetric around $\Delta\theta = 0$ [32, 33]. The width and exact details of the curve depend not only on the material of the crystal but also on the quality of the manufacturing process and geometry to which the crystal is bent. The end result is that spectra produced by real crystals have degraded spectral resolution due to X-rays being scattered with a distribution of outgoing angles. To characterize this property, a system's resolving power is described by the ratio $\frac{E}{dE}$, where dE is the width of a spectral line on film if the source line were of zero width.

3.4.3 Meridional & Sagittal References

X-ray spectroscopic systems are discussed using two reference directions. The first is the meridional direction. This is defined as the direction in which spectral dispersion occurs. The second direction is called the sagittal direction, and is perpendicular to the meridional.

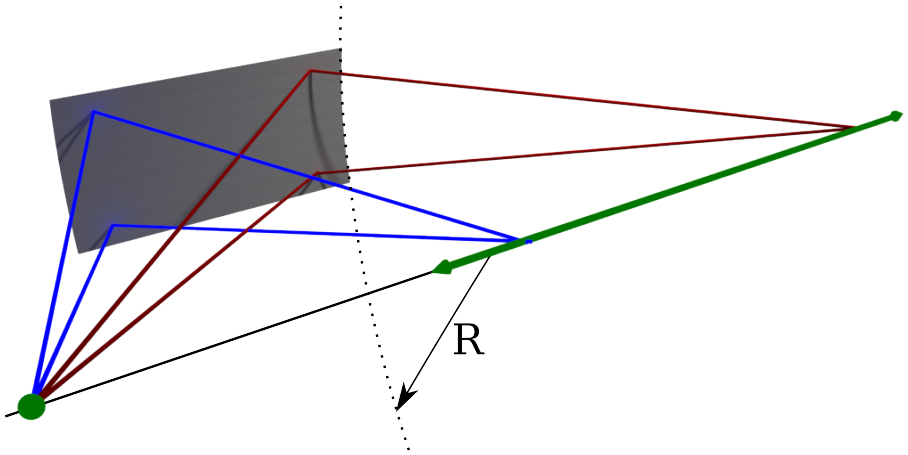

Figure 3.8: A cylindrical crystal (gray) focuses X-rays only in the sagittal direction. The X-rays are focused onto the axis of the cylinder (green line) because the source (green dot) is on the axis.

3.4.4 Geometries

The facets along which a crystal is cleaved are planes. While a flat reflector is simple, it is often desirable to alter the shape of the crystal to achieve a higher irradiance or greater dispersion at the detector. This curvature is achieved by adhering a crystal to a substrate that holds the crystal in the correct geometry.

Cylindrical

A cylindrically bent crystal functions as if it were a flat crystal in the meridional direction but adds the ability to focus in the sagittal direction, as illustrated in Figure 3.8. This preserves the bandwidth and dispersion of a flat crystal while providing additional intensity due to focusing. If the X-ray source is located on the axis of the cylinder, focusing occurs along the cylindrical axis.

Spherical

A spherical crystal is bent in two dimensions as opposed to the cylindrical crystal that is only bent in one direction [34]. The extra bend adds extra focusing power in the meridional direction, but comes at the cost of decreased dispersion and bandwidth. The focusing in general, however, contains an astigmatism. Perfect focusing from point to point is only obtainable for a specific alignment at a single wavelength. This is not easily obtainable in most experimental situations. However, it is often possible to achieve focusing in one direction with only partial focusing in the perpendicular direction. This can replicate the results of a cylindrical crystal with the addition of increased focusing power in the meridional direction.

Toroidal

Toroidal crystals relax the constraints of a spherical crystal and allow the radii of curvature in each direction to differ. This allows for greater flexibility when designing an experiment but makes the crystal specific to a single experiment alignment.

Elliptical

An elliptical geometry, like the cylindrical geometry, focuses only in a single direction. In contrast to the cylindrical geometry, focusing occurs in the meridional direction. With the source at one focal point of the ellipse, the X-rays are focused to a line through the second focal point and perpendicular to the plane of the ellipse. This is depicted in Figure 3.9.

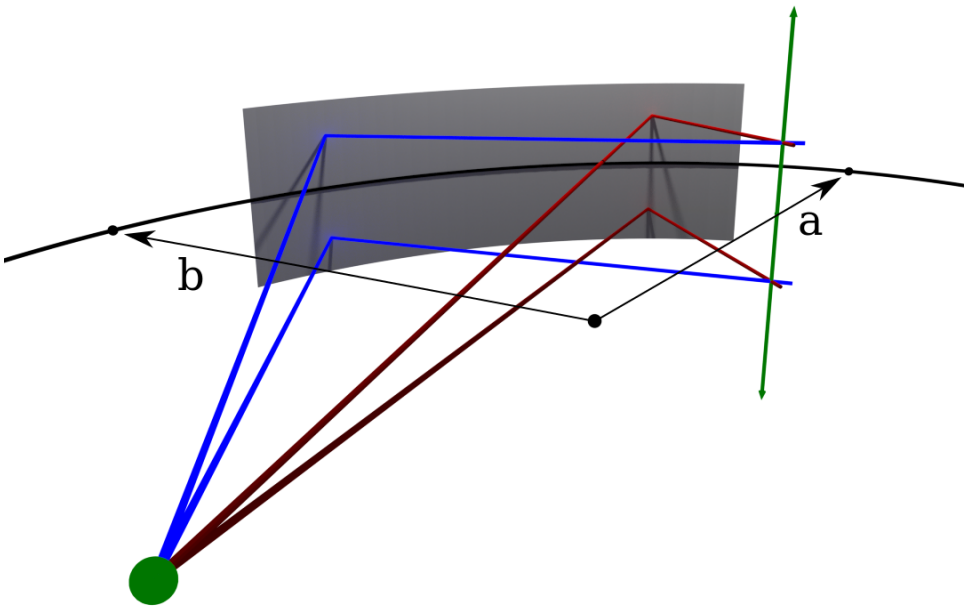

Figure 3.9: An elliptical crystal (gray) focuses X-rays only in the meridional plane. The X-rays are focused from the source at one focal point (green dot) to an axis perpendicular to the plane of the ellipse through the second focal point (green axis).

CHAPTER 4

AN ELLIPTICAL EXCOGITATION

"No battle plan ever survives contact with the enemy."

– Moltke the Elder

Intensely radiating plasmas are often surrounded by regions of cooler and lower density material which can have a significant impact on a plasma's evolution [5]. Spectra from such edge plasmas, whether they be emissive or absorptive, are often overpowered by emission spectra generated in nearby regions of high temperature and/or density, making the determination their conditions very difficult, especially in high energy density plasmas. In order to investigate conditions in such a mixed system, an X-ray spectrometer has been conceived, designed, and developed that is intended to be able to record spatially resolved absorption spectra of a plasma under study in the presence of bright emission in or close to that plasma.

The spectrometer is realized by using a novel combination of elliptical and cylindrical geometries in orthogonal planes to define the X-ray crystal's surface, together with a unique arrangement of experimental components. Contrary to a point projection absorption experiment, in which source radiation first interacts with an object plasma before dispersion by an X-ray optic, this design disperses probe radiation before interaction with the object. It is this feature that generates a resolved absorption spectrum while leaving the object plasma emission spectrum unresolved.

The spectrometer was designed to reflect X-rays in the 2^{nd} order. This design was evaluated and verified through X-ray ray tracing. Unfortunately, the strength

of 5^{th} order reflections by the chosen crystal, mica, could not be controlled as anticipated and a lengthy test program could not solve this problem. This issue is discussed in detail in section 4.5 and two solutions are presented, neither of which were considered sufficiently low risk to attempt. Thus, the absorption spectroscopy experiment discussed in Chapter 5 was undertaken to complete this thesis.

4.1 Conceptual Spectrometer Design

A point projection X-ray absorption spectroscopy experiment is depicted at the top of Figure 4.1. X-rays are generated and immediately interact with an object plasma. A spherical crystal then disperses the probe X-rays and reflects them to a focal line. A detector is placed behind this focus to allow the spectrum to defocus and recover spatial resolution. The detector image contains both spectral and spatial information. This scheme is described in detail in reference [2].

A key requirement for such an experiment is that uniformity exist along the sample's axis. Were this uniformity to not exist, long wavelength photons would interact with regions of plasma under different density and temperature conditions than those probed by shorter wavelengths. Because analysis of spectral data relies on features such as line ratios and continuum slope that span the probing bandwidth, such non-uniformity would make interpretation of the data impossible.

Another requirement for point projection absorption spectroscopy is that the object plasma is hot enough to produce ground state ions for absorption in the ionization state of interest but not so hot that those ions transition into an excited state or ionize further. If they do become excited, they will, upon falling back to the ground state, emit a photon whose energy exactly matches that of an absorption line. Should the temperature become high enough, these photons will

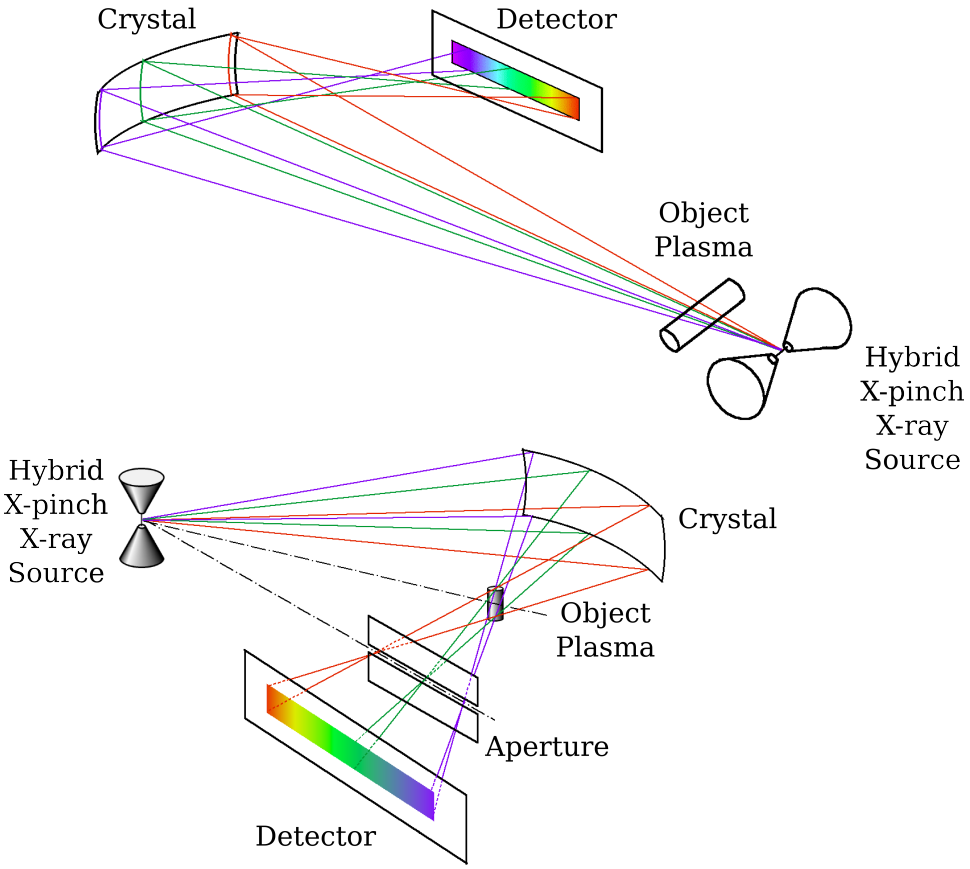

Figure 4.1: Point projection spectroscopy (top) disperses the probing radiation after interaction with the object plasma. The elliptical geometry (bottom) disperses the radiation before interaction with the object.

fill in the absorption features on the detector and emission lines will appear. This contamination by object plasma emission can lead to an erroneous interpretation of the absorption spectrum. Thus this technique is effective only over a limited range of temperatures.

In contrast, the elliptical spectrometer disperses probing X-rays before they interact with the sample, as illustrated in the bottom of Figure 4.1. This provides the opportunity to create an astigmatic focusing scheme that is not possible with the point projection setup. The crystal's geometry first focuses the X-rays onto the object's axis, shown with a vertical orientation at the bottom of Figure 4.1. At

a given position along the object's axis, all wavelengths are focused through the same localized plasma. Next, a horizontal focal line is generated behind the object in which all spatial information is compressed. As the X-rays pass this focal line and begin to defocus, spatial information is recovered and collected by a detector.

4.1.1 Geometry

The geometry of the spectrometer is designed to produce an astigmatic focusing with the meridional focus along the axis of a sample plasma and a sagittal focus in front of a detector. This is achieved by using a combination of the elliptical and cylindrical geometries discussed in section 3.4.4. The parameters of the elliptical and cylindrical curves are chosen to reflect a specific band of X-rays that probe a sample plasma.

Elliptical Curvature

The spectrometer layout is based on the geometry of an ellipse, as shown in Figure 4.2, similar to the TREX spectrometers on Sandia's Z machine [35]. Points A and D are the foci of the ellipse and lie along the major axis. Point C is the center of the ellipse and points E, B, and F lie on the elliptical surface. A defining feature of this geometry is that any ray emitted from one of the focal points in the plane of the page is reflected from the elliptical surface toward the second focal point. For example, a ray emitted along path AB is reflected along path BD.

The curve in Figure 4.2 is described by equation (4.1) and depends on the two parameters a and b, the lengths CF and CE respectively. Lengths AC and CD are both equal to the focal length f. The eccentricity of the ellipse is computed using

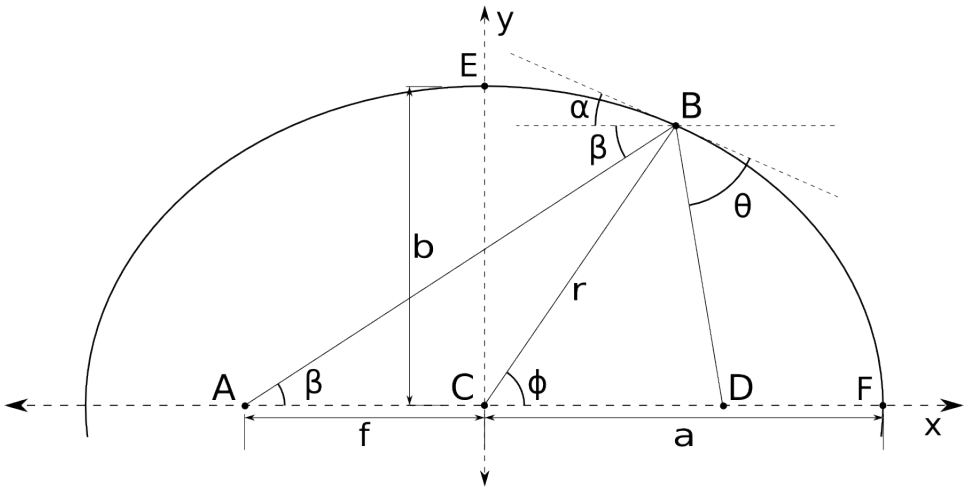

Figure 4.2: The geometry of an ellipse with $a = 8.47\,\text{cm}$ and $b = 6.77\,\text{cm}$ ($\epsilon = 0.6$). Points A and D lie at the two foci of the ellipse. The central angle BCF (ϕ) is used to parameterize X-ray reflections at point B.

the ratio of a and b in equation (4.2) and is also equal to the ratio of f to a.

$$\frac{x^2}{a^2} + \frac{y^2}{b^2} = 1 \tag{4.1}$$

$$\epsilon = \sqrt{1 - \left(\frac{b}{a}\right)^2} = \frac{f}{a} \tag{4.2}$$

To simplify the analysis of this geometry, an angle ϕ is defined to be the angle between a ray from the center of the ellipse to a point of interest on the ellipse and the major axis. This angle serves to parametrize the point of interest, B.

The length CB is a function of ϕ.

$$r(\phi) = \frac{ab}{\sqrt{(b\cos(\phi))^2 + (a\sin(\phi))^2}} \tag{4.3}$$

The coordinates of B are then

$$x = r(\phi)\cos(\phi) \tag{4.4}$$

$$y = r(\phi)\sin(\phi) \tag{4.5}$$

Two additional angles, α and β, are of importance. Angle α is defined as the

angle between the tangent at point B and the major axis. The second of the two angles, β, is the angle between a ray leaving the first focal point A and the major axis. An expression for α is found by determining the slope of the tangent line at point B from equation (4.1) and equating this to $\tan(\alpha)$.

$$\alpha = \tan^{-1}\left(\frac{-bx}{a\sqrt{a^2 - x^2}}\right) \tag{4.6}$$

The angle β is equal to

$$\beta = \tan^{-1}\left(\frac{r\sin(\phi)}{f + r\cos(\phi)}\right) \tag{4.7}$$

The reflection of X-rays at point B follows Bragg's Law.

$$n\lambda = 2d\sin(\theta) \tag{4.8}$$

Here n is the reflection order of the crystal and d is the spacing between the crystal's reflecting planes. The angle θ is between an incoming X-ray and the reflecting planes. In the present analysis these planes are taken to follow the elliptical surface. It is seen that the angle θ in equation (4.8) is equal to the sum of α and β and allows the reflected wavelength to be found as a function of the central angle ϕ.

$$\lambda(\phi) = \frac{2d}{n}\sin(\alpha(\phi) + \beta(\phi)) \tag{4.9}$$

Equation (4.9) allows an arc of the elliptical surface to be selected for X-ray reflection given the elliptical curve, crystal parameters, and a desired band of probing X-rays. For the plot in Figure 4.3, an X-ray bandwidth of 8.2 Å to 9.5 Å is selected. The ellipse of Figure 4.2 with $\epsilon = 0.6$ ($b/a = 0.8$) is used, and a mica crystal ($2d = 19.94$ Å) is assumed to be reflecting the X-rays in the 2$^{\text{nd}}$ order ($n = 2$). Second order reflections are used because they are required for a physically realizable spectrometer design. Mica cannot reflect the desired X-ray bandwidth above the 2$^{\text{nd}}$ order, and 1$^{\text{st}}$ order reflections require a very high eccentricity. The

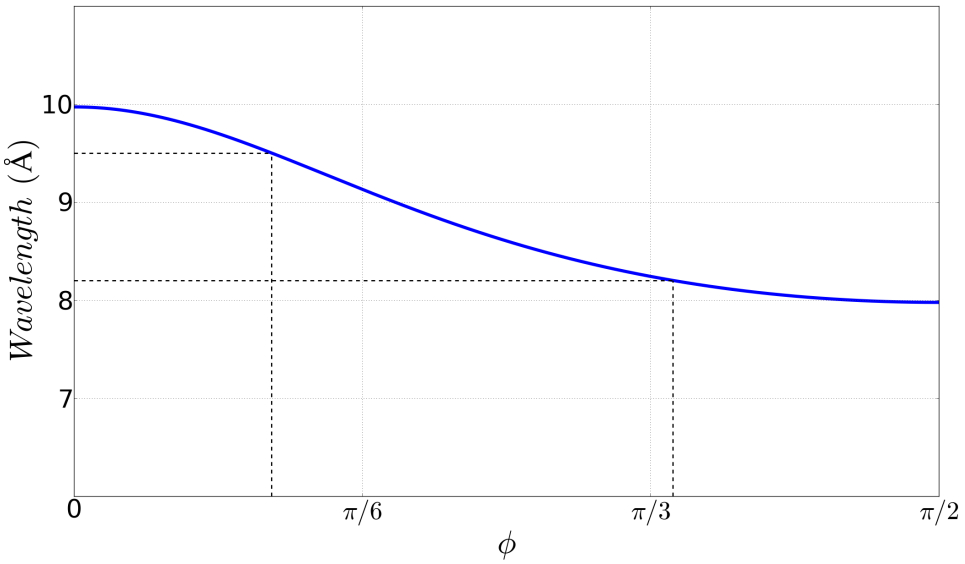

Figure 4.3: The elliptical parameters of Figure 4.2 are used with a mica crystal reflecting X-rays in the 2nd order to determine the reflected X-ray wavelength as a function of the central angle, ϕ. Limits on ϕ are determined by selecting a band of probe X-rays.

resulting radius of curvature would place excessive stress on a mica crystal. The range of ϕ is found to be [360 mrad, 1.09 rad] for this case.

Equation (4.8) enforces a limit on the maximum wavelength that a crystal may reflect. The minimum in Figure 4.3 as ϕ approaches $\frac{\pi}{2}$ is due to the nature of the elliptical geometry. A minimum eccentricity is required for the reflection of a given band of X-rays. Expressions for calculating this eccentricity are found by considering the case in which an X-ray is reflected from point E in Figure 4.2. In this case, $\phi = \frac{\pi}{2}$ and equations (4.2) and (4.3) are simplified and combined with equation (4.7). If λ_{min} is the shortest desired wavelength, then the corresponding θ, θ_{min}, and minimum required eccentricity, ϵ_{min}, are given by equations (4.10) and

(4.11), respectively.

$$\theta_{min} = \sin^{-1}\left(\frac{n\lambda_{min}}{2d}\right) \tag{4.10}$$

$$\epsilon_{min} = \sqrt{\frac{1}{1+\tan^2(\theta_{min})}} = \cos(\theta_{min}) \tag{4.11}$$

Cylindrical Curvature

The application of cylindrically bent crystals to X-ray spectroscopy has been covered extensively in the literature, such as in references [36,37]. The defining feature of a cylindrical geometry is that light emitted from a point source along the crystal's axis of revolution is focused to a line along that axis of revolution. The present work makes use of this cylindrical shape to extend the elliptical arc of the previous section out of the plane and define a two dimensional surface. This surface describes the desired geometry of the final crystal used in the system.

The remaining degree of freedom in the design of the crystal surface is the axis around which the elliptical arc is to be revolved. A standard off-axis ellipsoidal optic takes the major axis as the axis of revolution. With this choice, light from point A of Figure 4.2 is focused back to a point at D. This is undesirable as an object plasma at point D would be probed only at a single point lying in the plane of the ellipse.

Instead, an axis of revolution is chosen to focus the probing radiation into a line perpendicular to the plane of the ellipse at the second focal point D. The chosen axis intersects the first focal point of the ellipse, point A, and makes an angle of 45° with the major axis. This axis is shown in Figure 4.4.

The coordinates of the crystal's surface are obtained by applying the transfor-

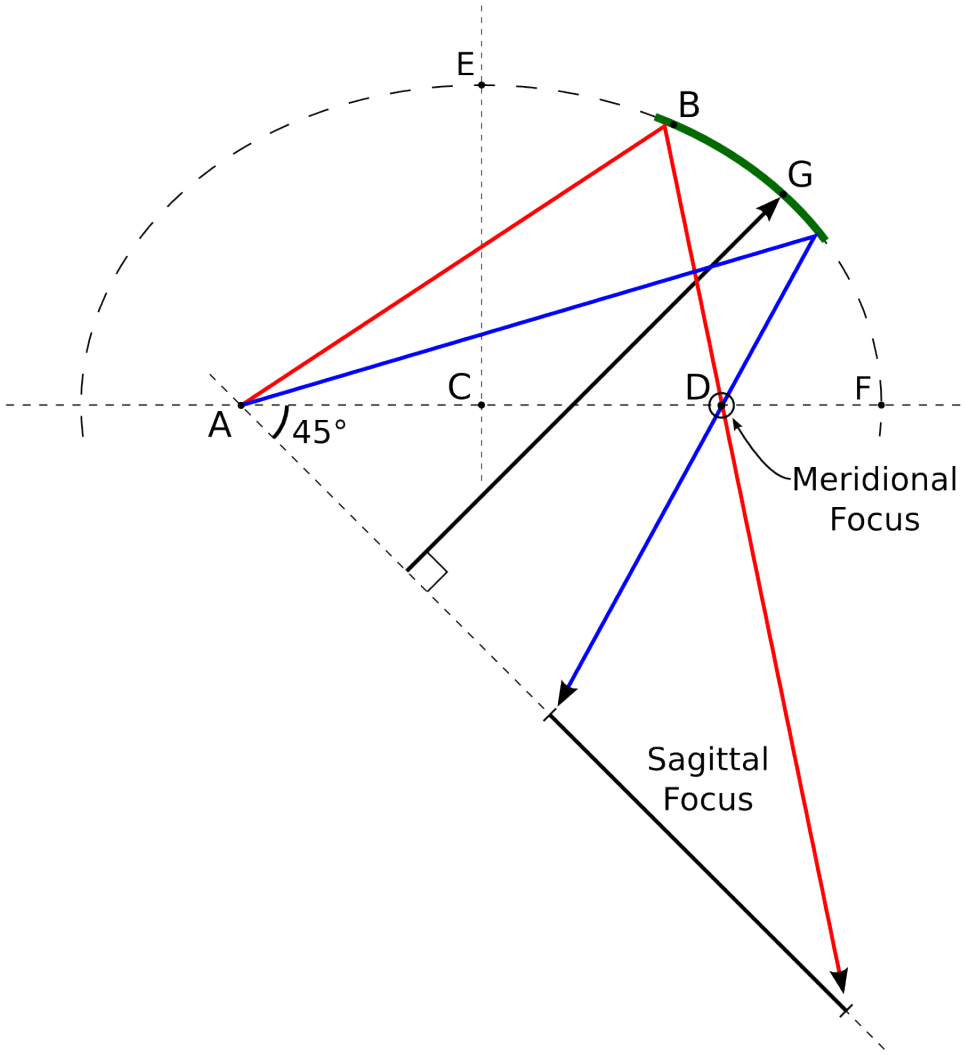

Figure 4.4: The elliptical arc is revolved around an axis containing point A and making a 45° angle with the major axis. Two focal lines are generated.

mation of equation (4.12) to the elliptical arc defined in the previous section. This extends the geometry into and out of the page. The transform proceeds by first translating the geometry so that the axis of revolution passes through the origin. This is accomplished by adding the focal length f to x ($x \rightarrow x + f$) so that the focal point at position A becomes the new origin of the system. The rotation is

then applied and the translation is removed.

$$\begin{bmatrix} x(\phi,\gamma) \\ y(\phi,\gamma) \\ z(\phi,\gamma) \end{bmatrix} = R(\gamma) \left(\begin{bmatrix} r(\phi)\cos(\phi) \\ r(\phi)\sin(\phi) \\ 0 \end{bmatrix} + \begin{bmatrix} f \\ 0 \\ 0 \end{bmatrix} \right) - \begin{bmatrix} f \\ 0 \\ 0 \end{bmatrix} \tag{4.12}$$

The rotation matrix, $R(\gamma)$, is presented in equation (4.13). The rotation angle, γ, for a given point on the elliptical arc is defined by constructing a vector through that point which is also perpendicular to the axis of revolution. This vector is shown for an arbitrary point, G, on the arc in Figure 4.4. The angle between this vector and the elliptical plane is γ, as shown in Figure 4.5. The factors of $\frac{1}{\sqrt{2}}$ in the rotation matrix arise from sine and cosine terms involving the angle between the axis of revolution and the major axis of the ellipse, which has been chosen to be 45°.

$$R(\gamma) = \begin{bmatrix} \frac{\cos(\gamma)+1}{2} & \frac{\cos(\gamma)-1}{2} & \frac{-\sin(\gamma)}{\sqrt{2}} \\ \frac{\cos(\gamma)-1}{2} & \frac{\cos(\gamma)+1}{2} & \frac{\sin(\gamma)}{\sqrt{2}} \\ \frac{\sin(\gamma)}{\sqrt{2}} & \frac{\sin(\gamma)}{\sqrt{2}} & \cos(\gamma) \end{bmatrix} \tag{4.13}$$

By requiring the axis of revolution to include the focal point A and not point D, the cylindrical bend of the crystal generates an astigmatic focusing of the X-rays. A vertical focal line perpendicular to the plane of the ellipse appears at the object plasma location. A horizontal focal line is generated along the axis of revolution. This astigmatism is introduced into the geometry to aid the separation of the emission and absorption spectra as shown in Figure 4.5. Object plasma radiation is entirely unfocused unlike the source spectrum which is reflected and focused by the crystal. This presents an opportunity to place a slit aperture on the axis of revolution and limit the detector's exposure to object plasma X-rays.

The selection of a 45° angle for the revolution axis is not tightly constrained.

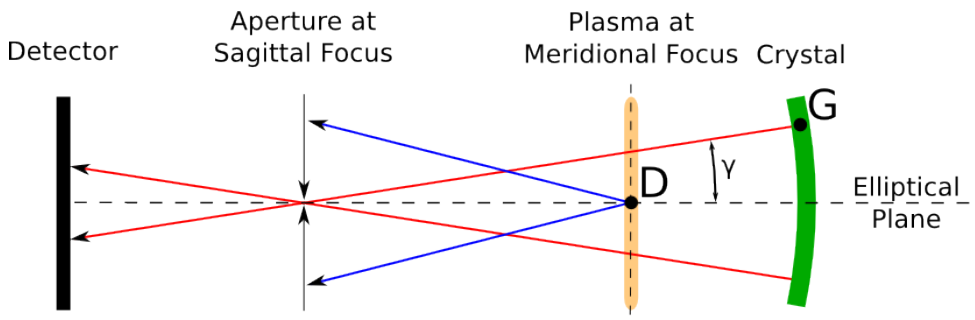

Figure 4.5: The probe X-rays (red) are focused by the crystal through the sample and then the aperture. Emission X-rays from the sample (blue) only reach the detector through the aperture. Point D is the same as is found in Figure 4.4.

Smaller angles cause a smaller portion of the object's axis to be probed and require the aperture to be placed closer to the sample. Larger angles cause spectral dispersion at the detector to become larger. The choice made here probes a reasonable amount of plasma height, 5 mm, places the aperture in a convenient location, and does not excessively disperse the absorption spectrum.

4.1.2 Spectroscopy Detector

The detectors for the spectrometer system are BAS-TR image plates. Previous studies [38] have indicated that these plates are well suited to the detection of soft X-rays due to their lack of a protective Mylar layer found on BAS-SR image plates. Images are developed using a Typhoon FLA 7000 scanner with a scanning step size of 25 µm.

With the geometric choices of section 4.1.1 and the detector placed 5 cm behind the sagittal focus, the absorption spectrum to expands out of the elliptical plane beyond the sagittal focus to a magnification of 0.7. Without this expansion, the spatial information gathered at the meridional focus would be lost. Additionally,

the dispersion of the X-rays also grows with distance behind the aperture due to meridional expansion as the X-rays pass the sample plasma.

Slit Aperture

Because a sagittal focus exists between the object plasma and the detector, a slit aperture can be placed here without affecting the absorption spectrum. This blocks a majority of the radiation emitted by the object, as shown in Figure 4.5. The emission that does pass through the slit has not interacted with the crystal and so appears as a uniform background signal and not as resolved spectral lines. This can, in principle, be subtracted from the data if the source is sufficiently bright.

4.1.3 Radiography Detector

A useful consequence of the spectrometer's elliptical geometry is an unobstructed line of sight between the source and sample, points A and D in Figure 4.4. This allows time resolved radiographs of the sample to be taken during the experiment as illustrated in Figure 3.5. The radiographs are calibrated using an aluminum step wedge. A radiograph of a single wire using this alignment was shown in Figure 3.6. Areal density information serves as an independent measurement that can be used to constrain the analysis of absorption spectra.

4.2 Material Selection

The materials chosen for the various components of the spectrometer must meet the specific requirements of the experiment. The sample to be studied contains spectral features only in specific X-ray energy bands. The source material must be able to generate continuum radiation in that band to be used as probing radiation for the sample. Additionally, the source should not generate line radiation in that band. Likewise, the crystal must be able to reflect the desired bandwidth efficiently. Finally, filters should be chosen to limit the propagation of unwanted X-rays through the system.

4.2.1 X-ray Source

Continuum X-rays were generated by a hybrid X-pinch [20] using a 50 µm diameter silver wire for calibration purposes due to its generation of lines as well as continuum in the X-ray band of interest. With calibrations completed, a gold source was substituted to produce a clean probing continuum spectrum without emission lines for the absorption experiment.

The hotspot of a hybrid X-pinch radiates continuum on sub-nanosecond time scales [20]. This is the only time during which an appreciable fluence of probing X-rays is generated. This short lifetime of the hotspot determines the time over which data is integrated on the detector, enabling time resolved data to be collected on a time integrating detector.

4.2.2 Object Plasma

The object plasma was chosen to be a two wire X-pinch. This was done because of the open geometry of the configuration. Other than a single crossing point, there are no obstructions to the propagation of the probing X-rays. Additionally, past work has documented the appearance of plasma jets above and below the hotspot of the pinch [10]. Thus, this geometry provided a good example of a hot radiating plasma, the hotspot at the crossing point, surrounded by cooler structures, the jets, that are roughly cylindrically symmetric but vary along their axis. Such a plasma is impossible to probe using point projection absorption techniques due to the emission from the crossing point and the lack of uniformity along the axis.

The material chosen for the object plasma was Al alloy 5056. The primary impurity in this alloy is magnesium at a concentration of 5%. These Mg ions were intended to serve as the absorbers in the sample, producing absorption features in the continuum spectrum of the silver or gold source. These features could then be used to determine the temperature and density of the object plasma as a function of height along its axis. The X-pinch wires were separated by about 1 mm at the crossing point to control the intensity of the hotspot.

4.2.3 Bragg Optic

Mica was the crystal of choice for this work. The crystal's proximity to both pinches raised the concern of damage to the crystal due to pinch debris. This drove the selection away from delicate crystals such as quartz. Thin sheets of mica are also relatively flexible, an important property for successfully conforming to the spectrometer's geometry.

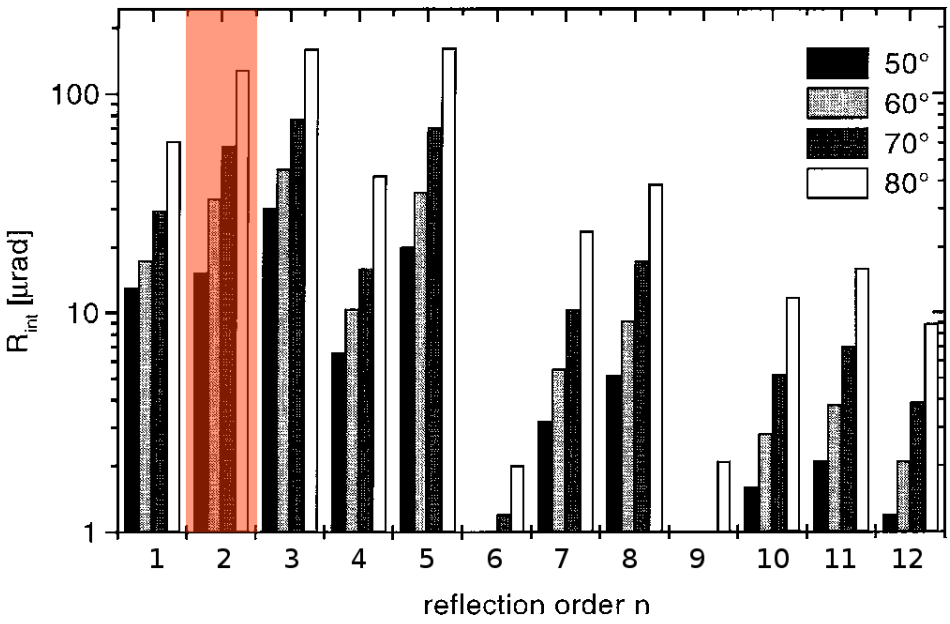

Figure 4.6: Mica reflects X-rays strongly in multiple orders. The elliptical design relies on 2nd order reflections (highlighted). Reflections for orders 1, 3, and 4 are minimized by the use of X-ray filters. Image source: [37]

The desired crystal geometry was machined into an Al substrate. An optical adhesive was applied to the machined surface, and then the crystal was pressed into the Al and held by a flexible nitrile rubber membrane using an air pressure driven press. A pressure of approximately 100 psia was maintained until an optical adhesive cured. The bonding process is described in detail in section 4.4.

The primary disadvantage of mica is its ability to reflect X-rays efficiently in multiple orders [37]. The desired X-ray bandwidth required the elliptical design to rely on X-ray reflections in the second order. However, mica reflects X-rays in the 1st, 3rd, and 5th orders with efficiencies comparable to that of 2nd order reflections. To combat this problem, X-ray filters, to be discussed below, were selected to minimize detector exposure to X-rays reflected by orders other than the 2nd. This issue is discussed further in section 4.5.

4.2.4 Filters

The XP generator was used in long pulse mode (nominal 100 ns rise time) to drive both the source and sample pinches, and so it was necessary to keep the pinches in close proximity to each other to keep the overall inductance of the load as low as possible. However, this requirement was countered by the need to keep the crystal at a safe distance from both pinches. As the distance between focal points is reduced, the distance between the crystal and the focal points also shrinks.

A focal length of 5.08 cm represented a compromise between these two competing needs. The load inductance was experimentally found to be acceptable, reducing the driver current from 500 kA to 450 kA and slowing the rise time from 100 ns to 120 ns. With this focal length, the distance between the crystal and the object plasma X-pinch was large enough to allow a 4 µm polypropylene protective filter to be installed in front of the mica and prevent catastrophic damage by debris. This represents an effective thickness of 8 µm of filter that source X-rays must pass though. This film was experimentally determined to be sufficient protection for the mica and also serves to attenuate 1^{st} order reflections. It had to be replaced after each experiment along with the hybrid X-pinch source wire and the two wires of the X-pinch object plasma.

An additional Al filter of 8 µm thickness was placed over the image plate detector. This filter serves a dual purpose. It protects the detector which lacks any protective coating of its own. It also attenuates reflections from the mica in the 1^{st} and 3^{rd} orders. The spectroscopic magnesium lines of interest have energies below the aluminum K-edge.

4.3 Ray Tracing

Due to the unique geometry of the crystal surface, it was desirable to validate the geometry of the spectrometer system before beginning construction. To accomplish this task, an X-ray ray tracing program was developed to compute the path taken by X-rays leaving one of the two elliptical foci. The geometry was that of section 4.1.1 with elliptical parameters a and b equal to 8.47 cm and 6.77 cm respectively. The aim of the program was to compute the distribution of X-rays as they intersect three key planes in the system. The first two were the object and aperture planes. The object plane contained points A and D and was perpendicular to the elliptical plane. The aperture plane included the axis of revolution from Figure 4.4 and was also perpendicular to the ellipse. The final plane investigated was that of the detector which sat behind and parallel to the aperture plane. The placement of the detector behind the aperture allowed the absorption spectrum to defocus after passing through the focal line and to recover the spatial information obtained in the object plane.

The software worked by emitting a fixed number of X-rays from an optically thin volume source at point A in Figure 4.2. The spectrum of these X-rays was taken to be of a constant intensity. The rays were directed toward the crystal surface where they were reflected. The software did not treat the Bragg reflections of X-rays in the detailed manner of some codes [32], but only considered them as specular reflections. As a consequence, modifications to the reflected spectrum, such as broadening due to the atomic structure of the crystal, were not investigated. Finally, the rays' intersections with the specified plane were computed and reported.

The first of the planes investigated was the object plane. This plane contained

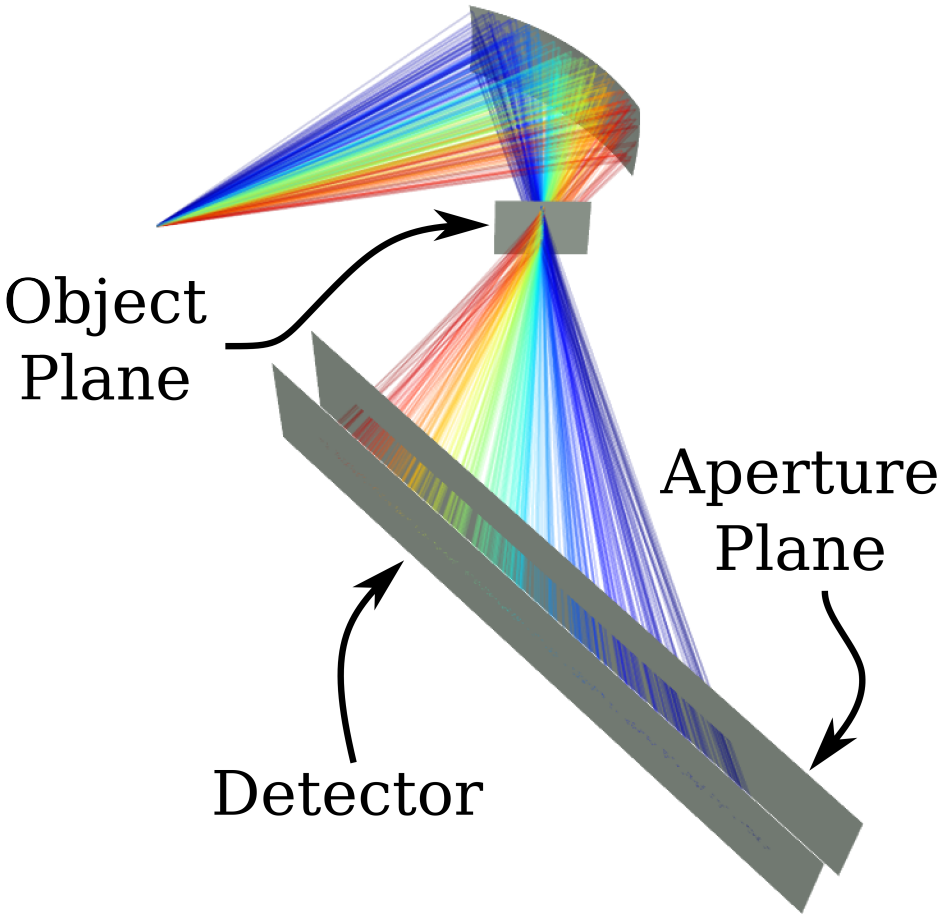

Figure 4.7: The X-ray paths through the elliptical spectrometer were investigated prior to fabrication. The distribution of X-rays in three planes were considered.

the axis of the object plasma and the major axis of the ellipse. The results are shown in Figure 4.8. All wavelengths of X-rays are seen to be tightly grouped around a focal line. The horizontal scale is greatly exaggerated compared to the vertical scale. The finite width of the focus is due to two factors. Near the center of the plot, the width is due to the finite size of the source emitting the X-rays, which was set to a radius of 10 µm. Near the ends of the focal region, the observed defocussing is due to the cylindrical curvature of the crystal. If the angle between the axis of revolution and the major axis is decreased, both the defocussing and

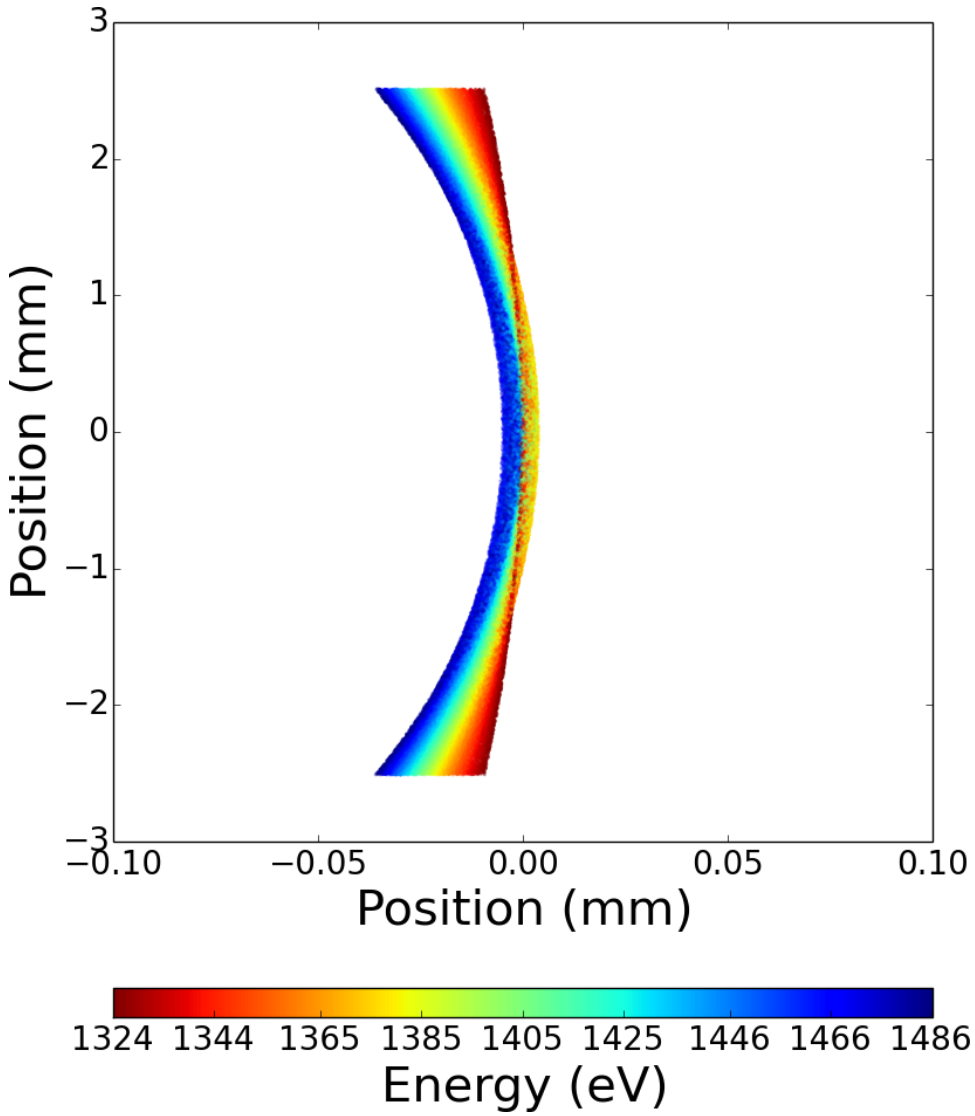

Figure 4.8: The X-rays are distributed along a curved focal line in the object plane. This provides spatial resolution at the object location to the spectrometer. Notice the difference in horizontal and vertical scales.

height of this distribution decrease. The expanded horizontal axis of Figure 4.8 also accentuates the spectral spread of the X-rays as they pass through this plane. In an experimental setting, the deviations from a perfect focal line were much smaller than the object plasma and were of no consequence.

The focus in the aperture plane is shown in Figure 4.9. X-rays are spectrally dispersed while passing through a horizontal focus. The finite height of the focus

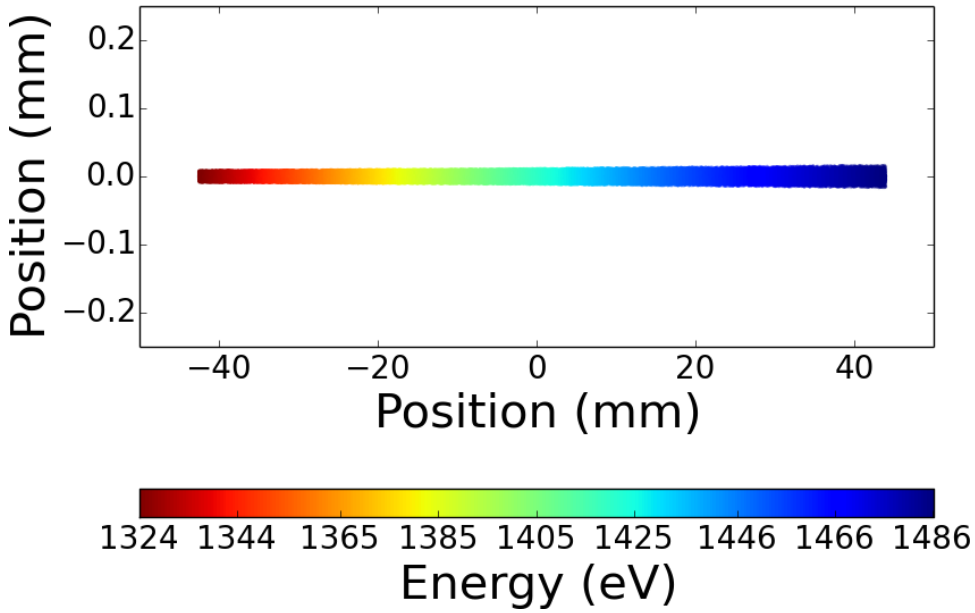

Figure 4.9: The X-rays are distributed along a horizontal focal line in the aperture focal plane.

is due to the 10 µm radius of the source.

Figure 4.10 presents the X-ray distribution at the detector plane. In contrast to Figure 4.8 and 4.9, Figure 4.10 provides two dimensions of resolution. Each point on the detector plane contains information about the absorption of a given wavelength at a specific height along the object plasma's axis. A demagnification of 67% is calculated by comparing the distribution heights in Figures 4.8 and 4.10. The magnification can be adjusted by varying the distance between the aperture and detector planes.

4.4 Crystal Construction

The unique nature of the proposed spectrometer meant that the desired crystal geometry was not readily available. As such, the task of producing the crystal was

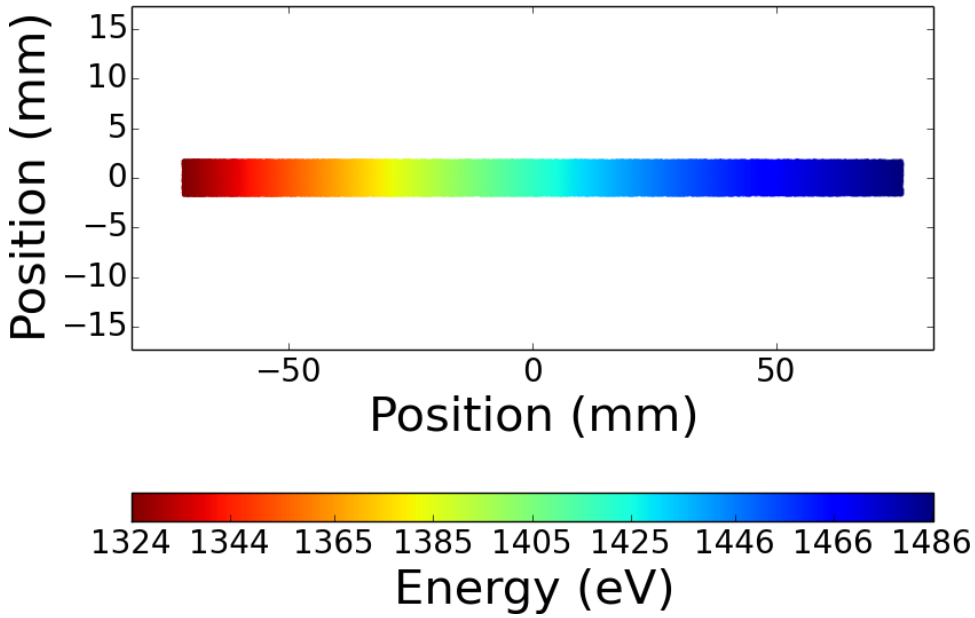

Figure 4.10: The absorption spectrum seen at the detector plane has both spatial (vertical) and spectral (horizontal) resolution.

undertaken in-house. The process began with sourcing a suitable substrate and raw crystal. The crystal was then bonded to the substrate to achieve the desired geometry.

4.4.1 Substrate

The substrate began as an aluminum block into which the desired crystal geometry was machined. Two mounting holes were located outside of the elliptical surface that allow the crystal to be placed accurately in the experimental system. The final shape is rendered in Figure 4.11.

The substrate was first fabricated in our own machine shop using a CNC lathe with a reported spatial resolution of 12.7 µm. This was done by first aligning the axis of revolution in Figure 4.4 with the rotational axis of the lathe. The same transformation was then applied to the elliptical surface to generate a tool path

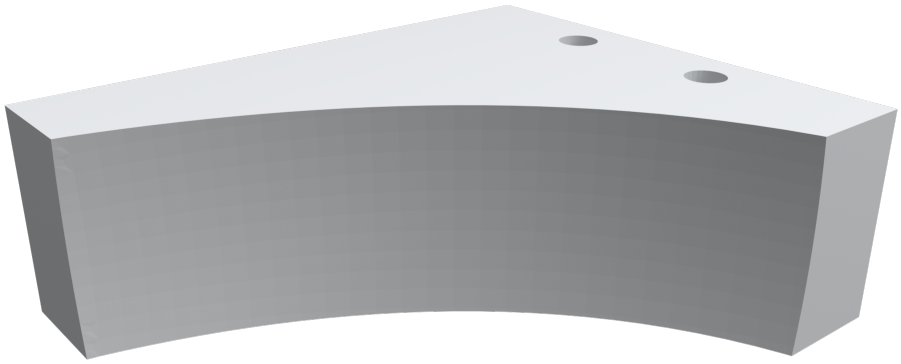

Figure 4.11: The crystal geometry is cut into an aluminum block. Two mounting holes are placed outside the elliptical surface.

for the lathe. To balance the mechanical load on the spindle, a second substrate was placed on the opposite side of the spindle axis. The tool path is illustrated in Figure 4.12.

Unfortunately, this machining process was not able to reproduce the specified geometry adequately. As the tool moved down the z-axis, the radius was adjusted to follow the tool path. At a certain portion of the cut, $\frac{dr}{dz}$ became very small and eventually changed sign. During this period of time, $\Delta r = \frac{dr}{dz}\Delta z$ fell below the resolution of the lathe. Thus, instead of following the specified path, a flat feature was cut into the aluminum. This prevented the substrate from performing as intended.

A solution was found by outsourcing the fabrication of the substrate. Machining techniques beyond those available in-house were able to control the precision of the tool tip with a much higher resolution. A single point diamond turning process was employed to produce the optical substrate by Diverse Optics of Rancho Cucamonga, CA. The final RMS roughness of the machined surface was less than

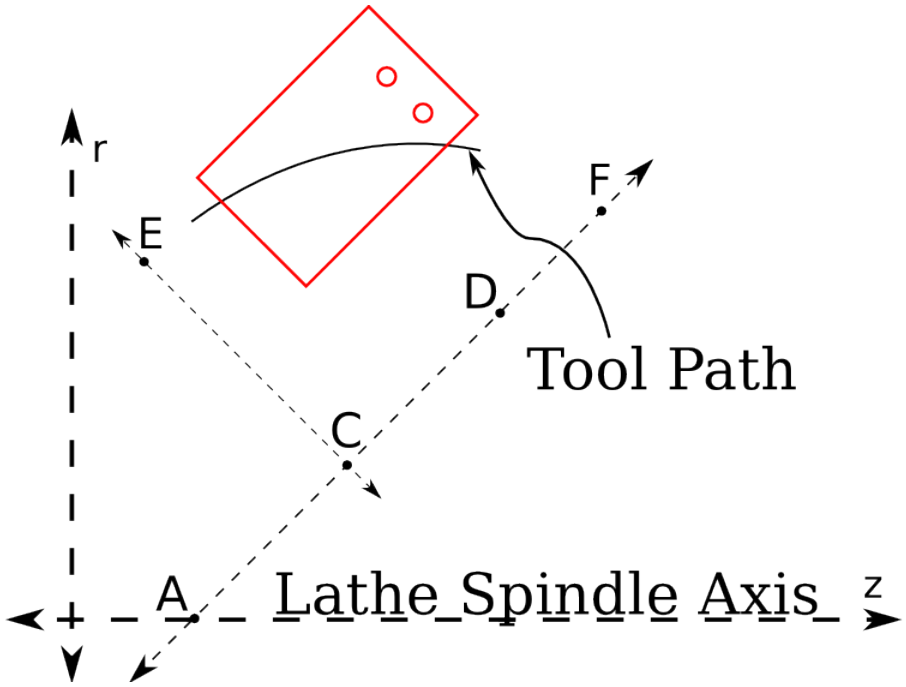

Figure 4.12: The axis of revolution is aligned with the lathe's spindle. The points A, C, D, E, and F correspond with those in Figure 4.4. The CNC lathe follows the tool path to cut the aluminum substrate (red). A second substrate (not shown) is cut opposite the first to balance the lathe.

1 µm.

4.4.2 Crystal

As already state, mica was selected as the Bragg optic for the system. The crystals were V-1 quality superfine scratch free muscovite mica. The dimensions were 10 mm x 40 mm x 50 µm.

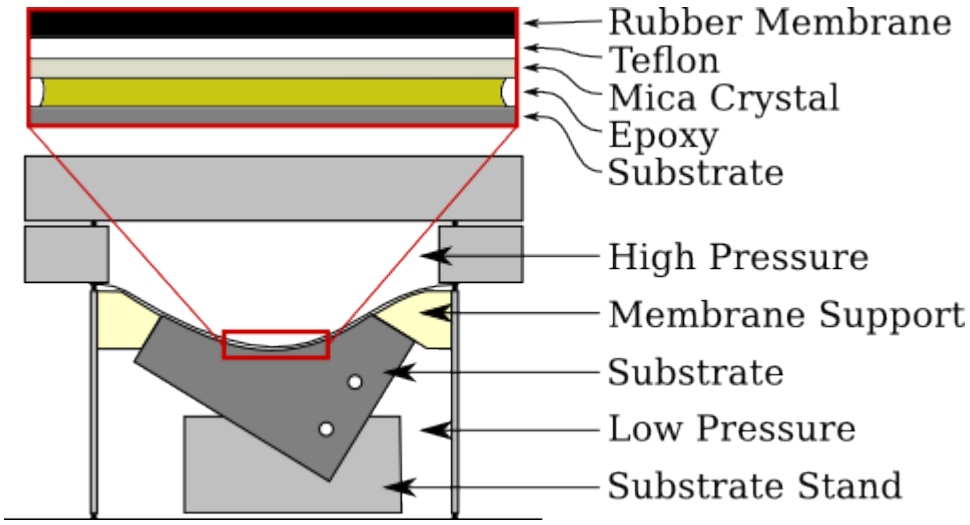

Figure 4.13: A combination of vacuum and high pressure air was used to hold the crystal to the substrate while the epoxy was given time to cure.

4.4.3 Bonding

A custom crystal press utilizing a combination of vacuum and high pressure air was used to bond mica crystals to the substrate. The arrangement of the press can be seen in Figure 4.13. A low pressure chamber at the bottom of the press was separated from a chamber of high pressure air by a nitrile rubber membrane. The substrate sat in the vacuum portion of the press with the face that defined the crystal geometry facing the pressure barrier. The surface geometry of the substrate was extended to the walls of the chamber with the addition of a plastic insert. This was found to reduce the stretching of the rubber membrane and improve the final quality of the crystal's bond. During operation, it was this barrier that applied the force that held the crystal against the substrate while the epoxy cured.

The crystal press was fabricated from aluminum stock. The pressure barrier was made using a 1 mm sheet of nitrile rubber. This was chosen for its elasticity and ability to resist puncture. The epoxy used to bond the mica to the substrate was type F-65 from Summers Optical and was thinned using monomeric styrene.

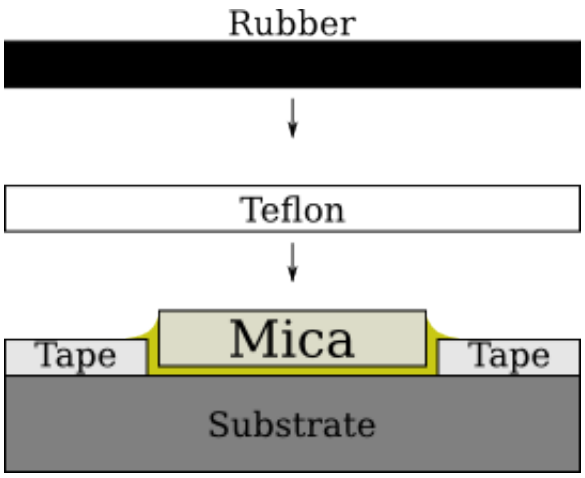

Figure 4.14: A thin tape was used locate the crystal on the substrate. The thickness of the tape was less than that of the crystal to ensure firm contact across the crystal's surface area.

To prevent the rubber barrier from bonding to the substrate a 30 µm sheet of Teflon was placed over the substrate after the mica crystal had been positioned on its surface. Extension of the substrate's geometry to the chamber walls was accomplished using Delrin. To allow the vacuum to establish on either side of the Delrin extension, *i.e.* everywhere below the rubber membrane, a periodic series of holes were drilled. These were sufficiently small so as to not distort the rubber barrier during operation.

Once the rubber membrane was in place, it was impossible to determine the position of the crystal visually. To ensure correct crystal placement and prevent shifting during assembly or curing, strips of 3M Scotch tape were applied to the substrate to define the boundaries of the crystal. The thickness was less than that of the crystal's thickness of 50 µm. This allowed the membrane to make contact with the crystal over its entire surface area. A thicker tape prevented the rubber from making contact with the edges of the crystal and led to poor bonding.

The presence of dust or other particulates between the substrate and crystal

produced visible distortions in the surface of the bonded mica crystals. To minimize these defects, great care was taken during assembly of the crystal press to ensure that all surfaces were free from foreign particles. Cleaning of the surfaces was done using an alcohol solvent and dusting was performed using a bulb duster.

Mixing of the epoxy's components was done using a clean plastic stir rod. The rod was cleaned using alcohol and allowed to dry prior to mixing. Stir rods made from other materials were found to introduce debris into the epoxy which caused defects to appear in the crystal's surface. The recommended ratio of 3 mL of epoxy to 2 drops of curing agent was used. To this mixture, 2 mL of monomeric styrene were added. A thinned epoxy was found to reduce the appearance of small bubbles under the crystal.

Assembly began by defining the final location of the crystal's edges on the substrate using 3M Scotch tape. It was then located in the center of the press. The Delrin support structure was then inserted around the substrate. The surface was cleaned, dusted, and covered with a clean cloth to prevent accumulation of dust. The mixture of epoxy, curing agent, and thinner was then prepared, mixed, and applied to the exposed substrate surface. The crystal was then set in place and covered with a Teflon sheet. The crystal was then manually pressed into the location defined by the tape and held in place by the surface tension of the adhesive. The nitrile rubber membrane was then installed and sealed over the assembly.

The low pressure chamber of the press was then evacuated which caused the rubber to force the crystal into its final location. The final vacuum pressure was not monitored. Manual pressure was applied starting from the center of the crystal toward the outward edges. This was found to help remove any remaining bubbles under the crystal. The high pressure chamber was then sealed and pressurized

with air ranging between 80 and 100 psi.

The recommended curing time for the adhesive was 36 hours. Bonding of a crystal was often performed over a weekend and so sat under pressure in excess of 48 hours. Spontaneous release of the crystal was never observed after a 36 hour cure.

Following a cure time, the pressures in the press were released in the reverse order that they were applied. The high pressure was slowly vented and the upper chamber opened. The vacuum was then slowly released and the lower chamber unsealed. Venting was done slowly to prevent any accidental damage to the crystal by the moving rubber membrane as pressures changed. The nitrile rubber and Teflon were then removed to expose the crystal surface.

Due to the static pressures, epoxy was consistently found between the mica and Teflon sheet. This was removed by gently cleaning the crystal with an acetone soaked optical cleaning cloth. The acetone acted to dissolve any exposed epoxy while the optical cloth prevented scratches. The tape defining the crystal's location was then removed and a final cleaning was performed.

The area of the crystal was smaller than that of the substrate. This left a portion of the carefully machined substrate surface exposed during an experiment. To prevent damage during an experiment, the exposed aluminum of the substrate and the edges of the mica crystal were covered with vinyl electrical tape. This served as a protective layer and also masked the crystal edges which were the most prone to defects.

In the event that debris from an experiment was not stopped by the protective filters around the crystal, mechanical damage to the mica surface could occur.

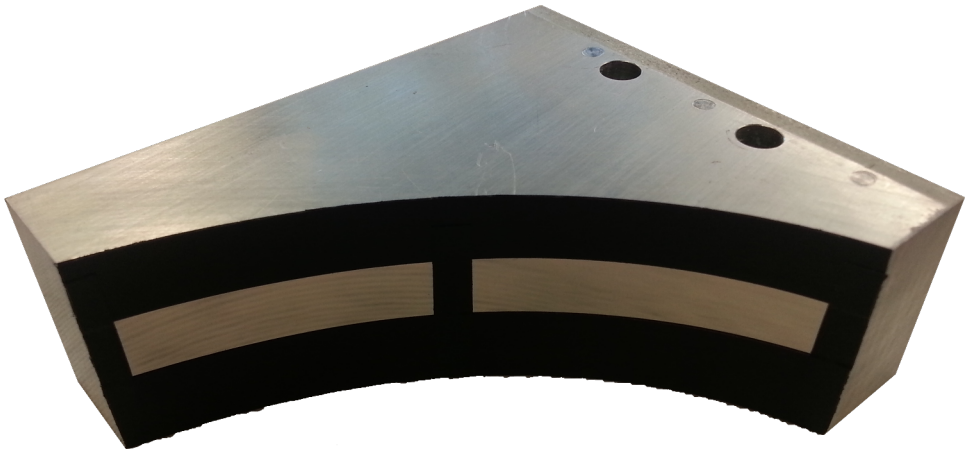

Figure 4.15: Two mica crystal were tiled onto the elliptical substrate. The edges of the crystal were masked with vinyl electrical tape to mask defects.

Over the course of multiple experiments, this damage could become visible as artifacts in the recorded X-ray spectra. This damage could not be repaired, and so it became necessary to remove the mica from the substrate. This was accomplished by removing the protective electrical tape and submerging the crystal in a acetone bath in an ultra-sonic cleaner. Over time the acetone would find its way between the crystal and substrate and eventually break the bond between the two. The crystals were then discarded and the substrate prepared for a new pressing.

4.5 Results

Section 4.2.3 presented the characteristic of mica to reflect X-rays in multiple orders. The ideal design of the spectrometer specified that X-rays should be reflected only in the 2^{nd} order. This potential issue was identified while the elliptical spectrometer was under design. It was anticipated that careful selection of the source and filter materials could reduce the intensity of reflection orders other than the 2^{nd} order.

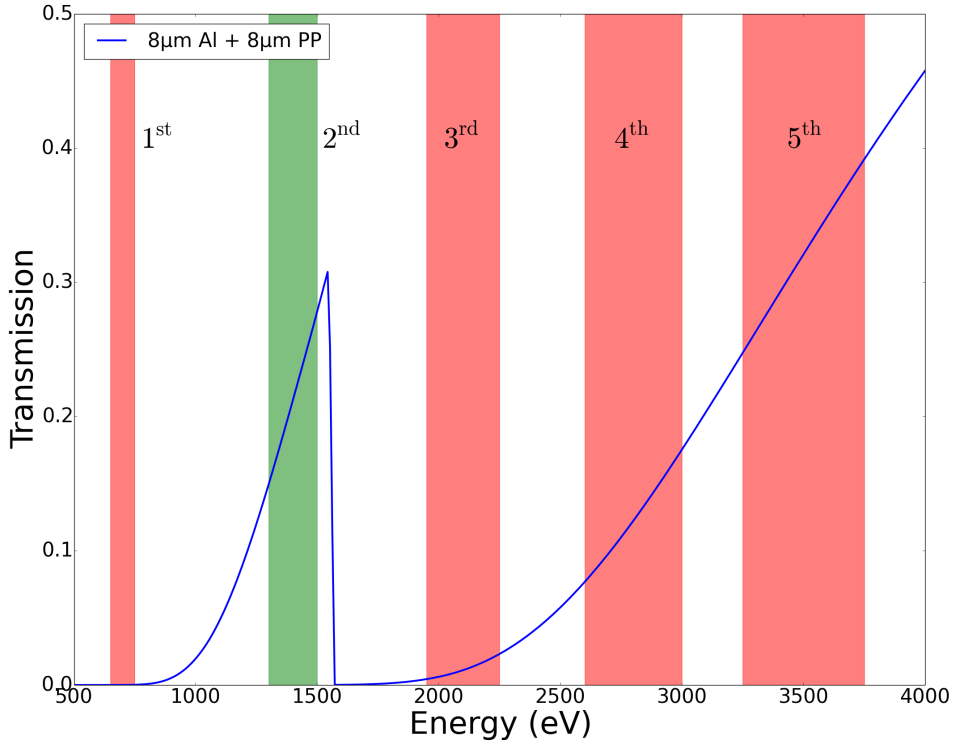

Figure 4.16: The design bandwidth is highlighted in green. Reflections from 1st, 3rd, 4th, and 5th orders are highlighted in red. The combination of filters (blue) is designed to attenuate most of the unwanted X-rays.

The design bandwidth of 8.2 Å to 9.5 Å corresponds to an energy band from 1300 eV to 1500 eV. This bandwidth is shown in green in Figure 4.16 along with the cumulative transmission through all of the X-ray filters in the system. This includes a double pass through 4 µm of polypropylene used for crystal protection and 8 µm of aluminum used to protect the detector. Reflections in the 1st order (650 eV to 750 eV) and 3rd order (1950 eV to 2250 eV) are seen to be heavily attenuated. Fourth order reflections from mica occur with low efficiency compared to the 2nd order (see Figure 4.6) and are not expected to contribute to the signal appreciably. Unfortunately, the 5th order contribution, if there is one, will be attenuated to a lesser degree than the 2nd order (Figure 4.16).

The 5th order was believed to be controllable by careful selection of the X-ray

source material. The available modeling software, PrismSPECT [39], was limited to performing spectroscopic simulations of elements with $Z \leq 36$. This prevented many common X-pinch source materials in rows 5 and 6 of the periodic table from being simulated. As such, experience guided the search for a suitable source. Molybdenum ($Z = 42$) had been successfully used to probe aluminum ($Z = 13$) in past work [4]. Since the target ion was Mg ($Z = 12$), Zr ($Z = 40$) and Nb ($Z = 41$) were tried. The recorded spectra with a Mo source contained strong continuum radiation, but no absorption features from the sample were observed. Likewise, many of the transition metals were tried with the same result. Low Z elements such as C and F (PTFE thread) were also tried, but their low mass makes them poor X-pinch source materials. They did not produce strong X-rays in any band. As such, no absorption spectra were observed using the low Z material sources.

To confirm the suspicion that 5^{th} order X-rays were obscuring the absorption data, the 8 µm Al filter in front of the detector was replaced with 12 µm of Ti. A comparison between the transmission functions of Al and Ti is shown in Figure 4.17. With the only significant difference between the filters in the bandwidth of interest being the elimination of the 2^{nd} order mica reflection by the Ti filter, any exposure observed through that filter can be attributed to unwanted X-rays in the spectrometer system. Strong exposure was observed with every source material, indicating that filtering and material selection alone were insufficient to control the unwanted X-rays.

A grazing incidence X-ray mirror was proposed as a final attempt to solve the 5^{th} order problem. As shown in Figure 4.18, a mirror with an incidence angle of 1° would serve to eliminate the problematic X-rays. A blank Si wafer was cut to a size of 10 cm x 2.5 cm and positioned behind the sagittal focus and nominally

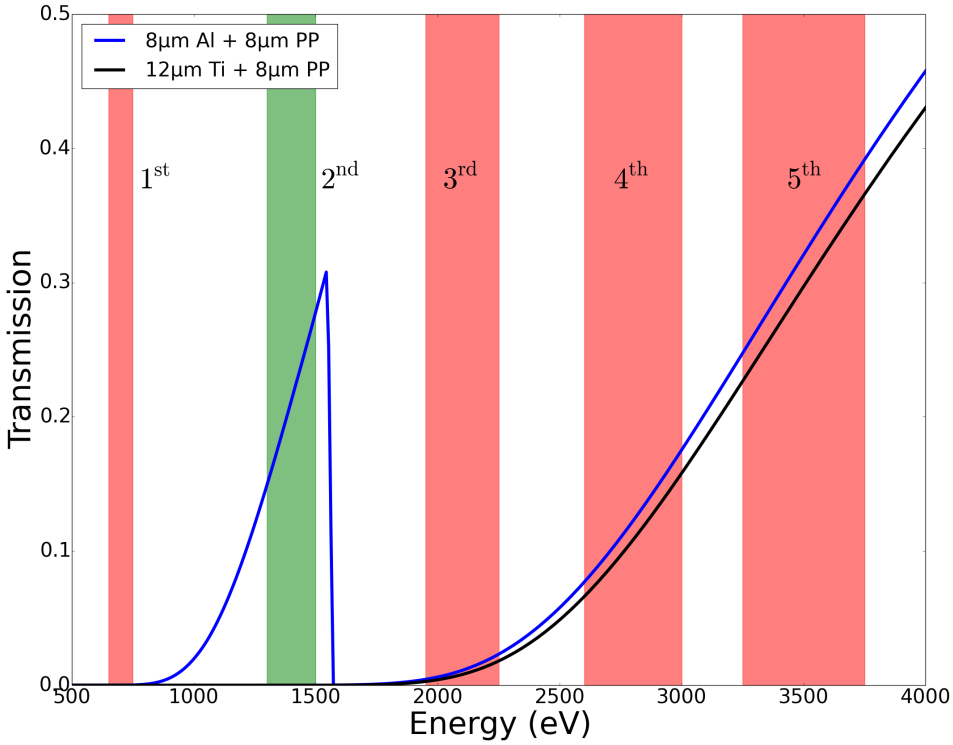

Figure 4.17: The transmission of X-rays through 8 µm of Al (blue) and 12 µm of Ti (black) only differ significantly in the 2nd order.

aligned at an incidence angle of 1°. Unfortunately, X-rays were never observed to be reflected by the mirror. This could be due to the mirror's surface roughness, but was more likely due to the sensitivity of the reflectivity function to angle. A difference of only 0.5° is seen in Figure 4.18 to be sufficient to radically alter the reflectivity of the mirror. An inability to align the mirror sufficiently accurately is suspected to be the dominant cause of the mirror's failure.

A second potential solution is to replace the mica crystal with another material known to reflect X-rays only in the desired bandwidth. If aluminum lines were chosen for study, the X-ray band would shift to slightly higher energies and allow a quartz 1010 crystal to perform the X-ray dispersion. Quartz 1010 is prevented from working between 1.3 keV and 1.5 keV due to the spacing of it's atomic structure. The spectrometer could be redesigned to observe aluminum lines using quartz 1010

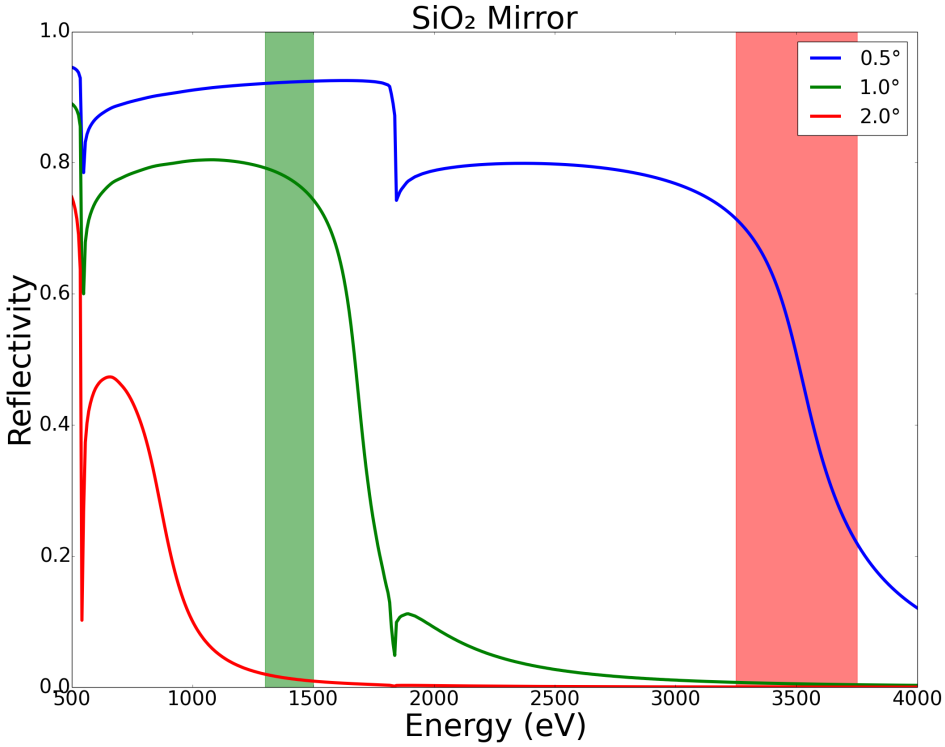

Figure 4.18: The reflectivity of an SiO_2 mirror is shown for three different grazing angles of incidence. The 2^{nd} order band is shown in green while the 5^{th} order appears in red.

in the first reflection order. However, it is not known if a quartz crystal can be bent to the required elliptical shape due to its increased fragility compared to mica. This was considered to be a high risk path to completion of this thesis.

The design of the elliptical spectrometer can be made to work if and only if the proper band of X-rays can be isolated from the continuum of photons produced by the source. Two solutions have been proposed for this. The first is to rebuild the spectrometer with the objective of adding and aligning a silicon dioxide mirror behind the sagittal focus to better than 0.5°. The second is to use quartz as the dispersive element in the system. Both of these solutions were considered unlikely to succeed in a timely manner.

Finally, mica can continue to be used as the dispersing crystal if a sample mate-

rial can be identified that contains diagnostic spectral features that are accessible using 5^{th} order reflections. The accessible X-ray bandwidth can also be increased beyond that shown in Figure 4.18 by considering alternate elliptical parameters. An attempt was made to find such a material by using PrismSPECT [39] to generate theoretical absorption spectra, but this effort was limited by the number of available atomic models ($Z \leq 36$). Ultimately, a suitable candidate was not identified.

CHAPTER 5

SPHERICAL SPECTROSCOPY

A primary requirement of the elliptical spectrometer's successful operation was to discriminate between the many reflection orders of mica. Since satisfying this requirement was unlikely to occur in a timely manner, the expertise gained during the spectrometer's development and implementation was leveraged to study the absorption spectrum of single exploding wires in a point projection scheme [34, 40]. Such an object is nearly uniform along its length making it a suitable target for a point projection absorption experiment. The work now focuses on studying the K-edge absorption properties of aluminum in detail from a time sequence of spectroscopic data from a single exploding wire over 60 ns - 110 ns of the XP current pulse after the moment of wire explosion. The goal of these experiments was to provide dynamical data that contributes to understanding the transformation of solid material into dense plasma. These data will add to the existing literature [41–43] and provide a benchmark for dynamical codes [44, 45] that attempt to simulate the development of exploding wire plasmas. In Chapters 8 and 9, we will see that this goal was achieved.

5.1 Material Selection

In order to avoid the troubles that plagued the elliptical spectrometer design, the spectral bandwidth of interest was changed to study the aluminum K-edge using a quartz crystal. The bandwidth of interest extends from approximately 1540 eV to 1580 eV, with the aluminum K-edge sitting in the middle of this range at 1559 eV. The bandwidth change allowed the crystal material to be changed to quartz 1010,

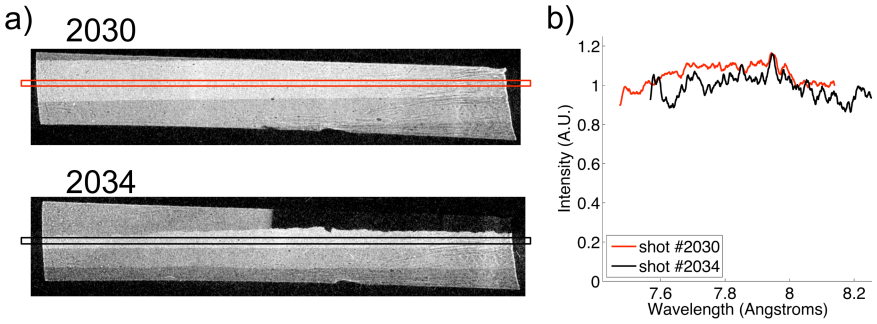

Figure 5.1: Lineouts from two Molybdenum spectra taken on the COBRA pulsed power platform illustrate the uniformity of the X-ray source spectrum from 7.5 Å (1650 eV) to 8.2 Å (1510 eV). Image source: [40]

which reflects X-rays only in the first order, unlike the mica crystal used in Chapter 4. The remaining material selections, mainly filters, were adjusted to accommodate this bandwidth change.

5.1.1 X-ray Source

The study of aluminum spectral features in this bandwidth has been accomplished previously with a molybdenum hybrid X-pinch source [40]. The Mo spectrum was shown to be uniform throughout the chosen bandwidth and to provide a sufficiently large X-ray flux for absorption spectroscopy. As such, the X-ray source was changed to a molybdenum hybrid X-pinch. The diameter of the molybdenum wire was left as a free parameter that could be adjusted to control the timing of the X-ray burst.

5.1.2 Object Plasma

The change of the spectral bandwidth meant that the 5% magnesium content of the Al 5056 alloy used in the elliptical design was no longer diagnostic. A change was made to Al 1199 which is 99.99% pure. This removed any ambiguity as to the source of observed spectral features.

With the change from the elliptical spectrometer to a point projection scheme, it became important to consider the uniformity of the plasma sample. This necessitated a change in the geometry of the object plasma. A single exploding wire was chosen to replace the two wire X-pinch of Chapter 4. This provided near axial uniformity, but structure in the radial direction. At small radii, a cold dense wire core was expected to generate a spectrum with characteristic K-edge absorption. At large radii, a hotter and lower density corona was expected to generate line absorption.

5.1.3 Bragg Optic

The Bragg optic changed from elliptical mica to spherical quartz 1010 which reflects X-rays well only in the 1^{st} order. This addressed the primary difficulty of mica. The spherical shape is a standard geometry that was already available and had been obtained from a spectroscopic crystal manufacturer. The quartz crystal was 15 mm x 50 mm x 50 µm. The crystal's radius of curvature was 180 mm.

5.1.4 Filters

Studying spectral features around aluminum's K-edge meant that aluminum could no longer be used as a filter. This would have added a K-edge to the spectrum and absorbed any photons in a broad band above the K-edge's energy of 1559 eV. Instead, a 10 µm beryllium filter is used to protect the detector from both debris and stray light. The Be filter begins to pass X-rays around 1 keV and is devoid of spectral features at higher energies.

The crystal must be protected from the debris generated by the source and sample pinches. This was done with a 2 µm thick Mylar film which also served as a filter for X-rays below 1 keV. It was placed at a convenient location between the sample plasma and quartz crystal. The Mylar filter was large enough to cover the solid angle of the quartz crystal as seen by the source. Neither filter was damaged during the execution of these experiments.

5.2 Component Layout

The layout of the components of the spectroscopy system is shown in Figure 5.2. Detailed measurements of component placements are presented in section 6.4.2 and illustrated in Figure 6.1.

5.2.1 Sample Plasma

The sample plasma was a single aluminum wire that lay in the meridional plane. It was placed perpendicular to the propagation direction of the probing X-rays. This

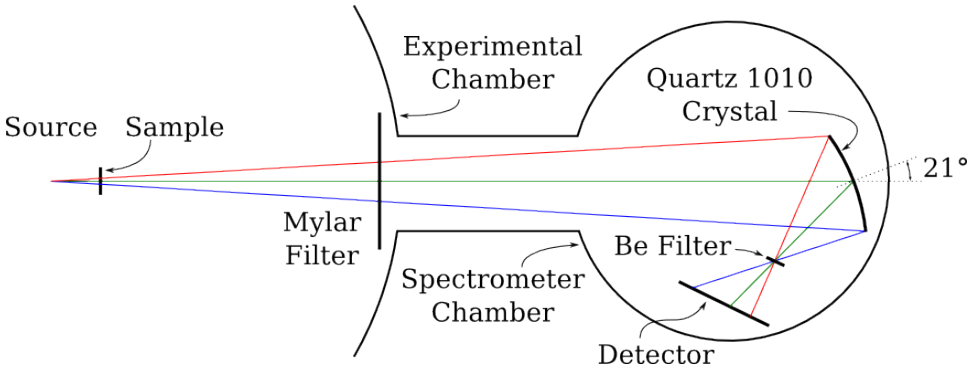

Figure 5.2: The quartz crystal was placed outside of the main experimental chamber and protected by a Mylar filter. The crystal was rotated 21° about its center. This set the Bragg angle to the required 69° for a central wavelength of 7.95 Å.

aligned the spatially uniform wire with the dispersion of crystal. The radial variations in the wire were then visible in the sagittal plane in which spatial resolution is retained.

The wire served as one of three return current paths. The remaining two paths were constructed from 12.7 mm diameter steel posts. The distance between the source and sample was approximately 44 mm, which is comparable to the distance between the source and the axes of the return current posts. This proximity carried two advantages. First, since the distance from the source to any return current path was almost the same, the inductance of each return current path was almost the same as that of the wire portion. Thus, each path carried a similar current. The wire path took a slightly smaller percentage of the current than the two posts due to the additional inductance of the Al wire (25 µm radius). The result was that the sample plasma carried a measured peak current of approximately 120 kA.

The second advantage was the high magnification afforded by the close placement of the object plasma to the source (44 mm). This ensured that radial variations in the plasma structures surrounding the wire covered a large portion of the

crystal's face in the sagittal direction. This made such variations easy to observe. Additionally, the high magnification meant that a very small portion of the wire's length (3 mm) was projected onto the surface of the crystal. This minimized the potential for plasma instabilities along the wire's length to disrupt the uniformity necessary for point projection spectroscopy.

5.2.2 Quartz Crystal

For quartz 1010, $2d = 8.5096\,\text{Å}$. This leads to a Bragg angle of 69° to reflect radiation at the aluminum K-edge (1559 eV) in the 1st order. This is the angle between the incident photons and the surface of the crystal. In practice, it was easier to measure the angle between the incident photons and the surface normal. This angle of 21° is shown in Figure 5.2.

The crystal was placed 730 mm from the X-ray source. This large distance contributed to the large magnification discussed in the previous section. It also placed the crystal outside of the main experimental chamber, within which damage was more likely to occur.

5.2.3 Detector and Filters

The X-ray detector was placed as far from the crystal as the spectrometer chamber allowed (144 mm). This maximized the spectral dispersion at the detector plane. This was beyond both the meridional and sagittal focal distances of the spherical crystal, which allowed both spectral and spatial information to appear on the detector.

There were two filters in the system. The first was a protective film between the sample plasma and the Bragg optic. This was placed inside the wall of the experimental chamber over the port connected to the spectrometer. This prevented debris from entering the spectrometer and damaging the quartz crystal.

The second filter was composed of 10 µm beryllium. It was placed between the meridional and sagittal focal planes of the crystal. This allowed the filter to be as small as possible while still covering the entire spectrum. It also worked in combination with the rest of the detector housing to create a light tight environment. This was not important for image plate detectors, but was critical for film detectors.

5.3 Ray Tracing

The ray tracer used to investigate the elliptical design in section 4.3 was also utilized to examine the spherical spectrometer design. The components were arranged as shown in Figure 5.2. In addition to the source, optic, and detector, a sample plasma was approximated as a cold, 4 µm thick aluminum filter. The filter's size was set to 250 µm x 12.7 mm, which is much larger than the sample wire. This was done to show the position of aluminum's K-edge at the detector plane. The protective Mylar and beryllium filters were not simulated since they did not significantly alter the recorded spectrum.

The only plane of interest in this configuration was that of the detector. Thus, the distributions of X-rays in the meridional and sagittal focal planes were not investigated. The results are shown in Figure 5.3.

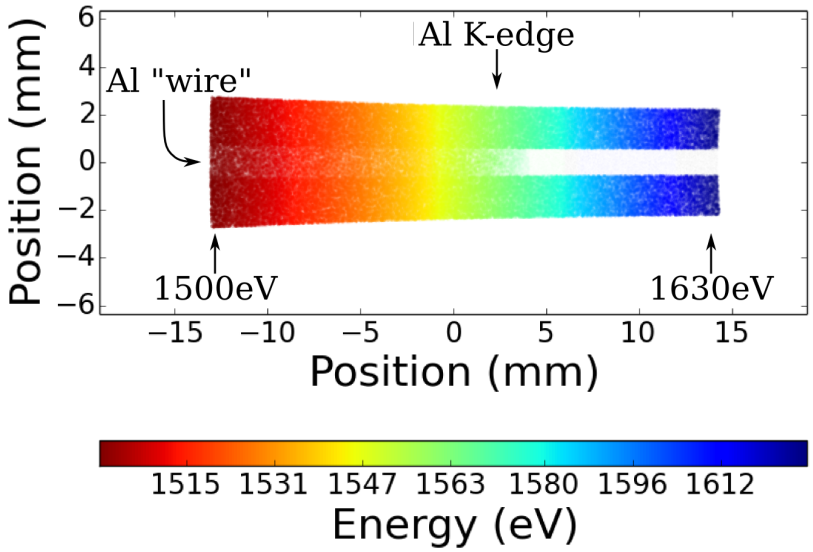

Figure 5.3: The X-ray flux was computed at the detector location. An aluminum filter served as a surrogate for an aluminum plasma. The resulting absorption can be seen along the spectral axis. The aluminum K-edge appears near the middle of the detector.

The image demonstrates that spectral resolution appears along the horizontal axis of the detector. Spatial resolution appears in the vertical direction. This is evidenced by the appearance of the top and bottom edges of the cold aluminum filter that represents a sample plasma. In an experimental setting, the core is expected to be much smaller in width and surrounded by line absorption. Finally, the aluminum K-edge is seen near the center of the detector with an energy near 1559 eV.

CHAPTER 6

SOURCES OF ERROR

Errors in measurements are an inevitable consequence of working in the real world. If they are going to present themselves in data, they must be understood so that data may be interpreted in the proper context. The sources of error considered here include the spectral characteristics of the X-ray source spectrum, film noise, electrical noise, temporal resolution, and spectral resolution.

6.1 Source X-ray Spectrum

The transmission of X-rays through a plasma with energy E, $T(E)$, can be computed assuming both the recorded spectrum, $I(E)$, and the probing spectrum, $I_0(E)$, are known.

$$T(E) = \frac{I(E)}{I_0(E)} \tag{6.1}$$

This deceptively simple equation contains the implicit assumption that the X-ray source spectral intensity does not fall below the noise level of the recorded spectrum from all sources. If the transmission function is rewritten to include noise sources as an independent term, instead of $I(E)$, it becomes:

$$T(E) = \frac{I(E) + n}{I_0(E)} = \frac{I}{I_0} + \frac{n}{I_0} \tag{6.2}$$

If at any energy, the intensity of the probing spectrum, I_0, drops below the noise level, the first term remains bounded ($\frac{I}{I_0} \in [0,\, 1]$) while the second term can become very large and dominate the transmission function. This hides data contained in the first term.

The molybdenum emission spectrum from the hotspot of an X-pinch has been studied in detail [40]. That study found that the emission spectrum from a Mo source in the bandwidth around the aluminum K-edge is featureless. As such, there is no danger of a dip in the source intensity that would cause noise to dominate the data at any energy of interest if it does not dominate at all energies of interest.

6.2 Photographic Film

After chemical development and digitization, the photographic film used to record the experimental spectra contains speckle. The source of this noise is due to non-uniformities in the sensitivity of film grains. This noise source introduces uncertainties into the recorded spectra and hence to the inferred values of density and temperature. The noise is characterized by examining a portion of the film in which the signal level was known to be zero. The noise value is taken as the standard deviation of the grayscale values in this region.

The relative importance of this noise measurement is given by the signal-to-noise ratio (SNR). To compute this quantity, an estimation of the signal level is necessary. This was obtained by identifying two regions of the image with one containing 0% transmission and the other containing 100% transmission. The difference between the mean values in each of these regions defined the signal level. The SNR was then calculated for each spectrum, and provided a measure of the cleanliness of the data. A strong X-pinch produced SNR values that ranged from 5 to 15. A complete list of SNR values as defined here is presented in Table B.1.

6.3 Object Plasma Current

The measurement of the current running through a plasma sample was also prone to measurement errors. These errors were introduced by electrical noise. This noise was a combination of electrical pickup by long signal cables and noise internal to the analog-to-digital converters (ADCs) in the oscilloscopes used for data acquisition. The error was estimated by first integrating the voltage signal from the Rogowski coil and scaling by a calibration factor to obtain the current measurement. Finally, the standard deviation of fluctuations in the baseline of the measured current for 20 ns before current flowed in the experiment was computed. This was taken as the error in the current measurement. The error due to electrical noise was never found to exceed 40 A. It is very likely that this error is inconsequential when compared to the error in the Rogowski coil's calibration factor. Unfortunately, this error is not known, but can be reasonably be assumed to be 10%.

6.4 Resolution

Instrument response functions affect the resolution of any measurement. In matters of timing, degradation of resolution is caused by the finite sampling rate of an oscilloscope and the rise time of a PCD in response to X-rays. Spectral resolution is degraded by three factors: a source's size, a crystal's rocking curve, and a digitizer's spatial resolution.

6.4.1 Temporal

Temporal resolution was affected by two factors. The first was the accuracy of the determination of $t = 0$. The second was the accuracy of the X-ray source timing as measured by PCDs. The first was limited by the sampling rate of the recording oscilloscopes, 2.5 GHz. The second was limited by the rise time of the PCD signal. The 10% to 90% rise time of the PCDs was measured to be approximately 1.2 ns. The two sources of error were uncorrelated and added in quadrature to provide an estimate of the error in experimental timing. The overall timing error is found to be less than 1.3 ns.

$$\frac{1}{2.5\,\mathrm{GHz}} = 400\,\mathrm{ps} \tag{6.3}$$

$$\Delta t = \sqrt{(400\,\mathrm{ps})^2 + (1.2\,\mathrm{ns})^2} \approx 1265\,\mathrm{ps} \tag{6.4}$$

$$\Delta t \leq 1.3\,\mathrm{ns} \tag{6.5}$$

6.4.2 Spectral

There were three independent sources of spectral resolution degradation: the source size, the rocking curve, and the digitizer resolution. Each of these was modeled by a Gaussian kernel that was convolved with a noise free image with infinite resolution. The final image was then the successive convolution of all the noise kernels with a true image. Noise sources were considered individually and then combined to arrive at an estimate of the final spectral resolution.

Since the resolution in the spectral direction was desired, the system was considered only in the meridional plane. The system is depicted in Figure 6.1. The finite source size and rocking curve width, Δx_s and $\Delta\phi$ respectively, were mapped

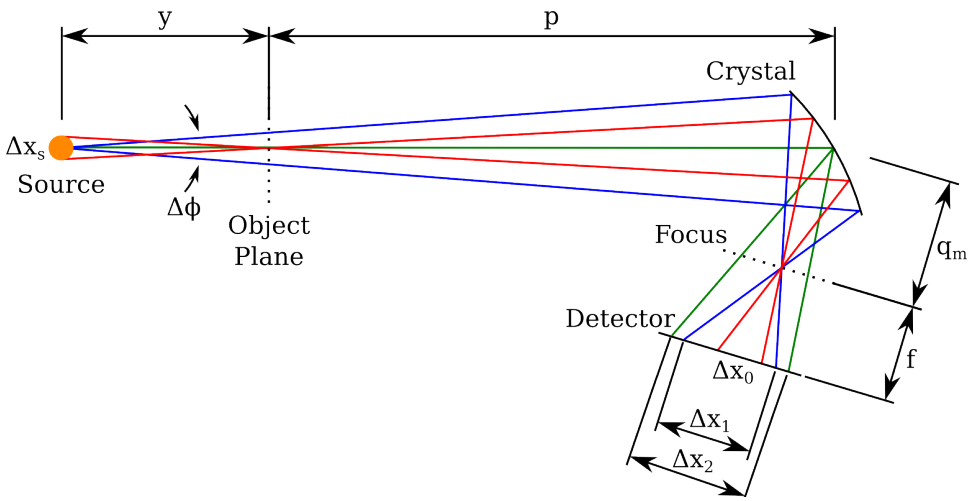

Figure 6.1: Spectral errors appear in the meridional plane of the system. The blue ray path represents errors in the acceptance of incident X-rays due to the finite width of the rocking curve, $\Delta\phi$. Likewise, the green path depicts errors in the reflection of an X-ray due to the rocking curve. The red path shows an error due to a finite source size Δx_s.

to errors in the film plane. To compute the errors in the plane of the film, the lens equation was used to determine the meridional focal length, q_m [34]. The Bragg angle, the crystal's radius of curvature, and the distance between the object and crystal were known: $\theta_B = 69°$, $R = 180\,\text{mm}$, and $p = 686\,\text{mm}$.

$$\frac{1}{p} + \frac{1}{q_m} = \frac{2}{R\sin(\theta_B)} \rightarrow q_m \approx 96\,\text{mm} \tag{6.6}$$

The source to crystal distance and the crystal to film distance were 730 mm and 144 mm respectively. This gives values for y and f in Figure 6.1 of 44 mm and 48 mm, completing the specification of the system.

The hybrid X-pinch hotspot generates the X-ray source that is used for absorption spectroscopy. The size of this hotspot has been previously studied [20]. By analysis of the diffraction pattern generated by the edge of a carbon fiber, the source was identified to have a diameter of 1.5 µm. This is scaled by the magnifi-

cation of the system to arrive at the source size in the detector plane.

$$\Delta x_0 = \Delta x_s \left(\frac{p}{y}\right)\left(\frac{f}{q_m}\right) \approx 12\,\mu\text{m} \tag{6.7}$$

The error represented by Δx_1 accounts for the acceptance of incident X-rays with energies differing from that selected by the Bragg angle. This error is characterized by the width of the crystal's rocking curve. In an ideal case, a monochromatic X-ray source would only be reflected by an infinitesimally small width of the crystal's surface which satisfies Bragg's law for a given wavelength. However, imperfections in the crystal cause that region to be of a finite size. The size of the reflecting region was computed by considering the illumination of the crystal with a photon beam which has a divergence equal to the width of the rocking curve. The size in the plane of the film was computed using the magnification between the crystal and film.

An exact rocking curve for the quartz crystal was not available. However, the manufacturer did quote that the rocking curve width was of the order of $10''$, which was assumed to be for a flat crystal. The act of bending the crystal into the spherical geometry caused the rocking curve to broaden [32,33]. The degree of broadening could not be determined, but was conservatively taken to be a factor of 2. Thus, a value of $20''$ was used as an approximation of $\Delta\phi$. The small angle approximation was used to compute Δx_1.

$$\Delta x_1 = \Delta\phi\,(y+p)\left(\frac{f}{q_m}\right) \approx 37\,\mu\text{m} \tag{6.8}$$

Additionally, a photon may be reflected from the crystal's surface imperfectly. This error is represented by Δx_2. Again, the degree of imperfection was taken as the width of the rocking curve. This is illustrated as the green path in Figure 6.1.

$$\Delta x_2 = \Delta\phi\,(q_m+f) \approx 14\,\mu\text{m} \tag{6.9}$$

The last source of error came from the digitization of the spectral films. This process convolved an instrument response function with the film being scanned. Digitization was performed at 3200 dpi. The inverse of this value was used to estimate the error due to the scanning process.

$$\Delta x_{scan} = \frac{1}{3200\,\mathrm{dpi}} \approx 8\,\mu\mathrm{m} \tag{6.10}$$

All of these error sources were independent of each other. Thus, they were combined in quadrature to estimate the positional deviation of an X-ray from its ideal location on the detector.

$$\Delta x = \sqrt{\Delta x_0^2 + \Delta x_1^2 + \Delta x_2^2 + \Delta x_{scan}^2} \approx 42\,\mu\mathrm{m} \tag{6.11}$$

The spectral resolving power of a spectroscopic system is a figure of merit that describes the fidelity of a recorded spectrum. It is computed as $\frac{E}{dE}$, where dE is the apparent width of a line on film that has a nominal width of zero. The third order polynomial spectral calibration obtained in section 7.2.2 is used to calculate the resolving power of the present system. The value is computed at the center of the spectrum (E = 1559 eV).

$$\frac{E}{dE} = E\left(\frac{dE}{dx}\Delta x\right)^{-1} \tag{6.12}$$

$$= \frac{a_0 + a_1 x + a_2 x^2 + a_3 x^3}{\left(a_1 + 2a_2 x + 3a_3 x^2\right)\Delta x} \tag{6.13}$$

$$\approx 5600 \tag{6.14}$$

CHAPTER 7

DATA ANALYSIS

A total of 22 experimental trials are presented and analyzed in this thesis. Each shot consists of three primary data elements. The first is the current through the sample aluminum wire. This is detected by a non-integrating Rogowski coil and recorded by a TDS 644B oscilloscope at a sampling rate of 2.5 GHz and a bandwidth of 500 MHz. The timing of the X-ray burst from the hybrid pinch source is detected by a PCD biased with approximately 300V. This is also recorded by a TDS 644B at 2.5 GHz. Finally, the absorption spectrum taken of the aluminum sample is collected on BioMax MS film. The film is developed for 6 min in a 1:1 solution of Ilford Microphen Developer then scanned at a resolution of 3200 dpi. A complete accounting of the experimental data is available in appendix B.

7.1 A Zero Dimensional Model

An examination of the current derivative in Figure 7.1 reveals a rapid rise approximately 30 ns after current begins to flow. Before this time, the current is flowing in a well defined wire. This characteristic change is present in every experimental trial and indicates the formation of a low resistivity coronal plasma around the wire core. The time of this change defines $t = 0$ for each pulse in this chapter's analysis. This plasma channel is expected to carry a majority of the sample current and limit the addition of energy to the core after $t = 0$. Testing this hypothesis requires an estimate of energy deposition into the core at the time of the corona's formation. An X-pinch cannot develop a hotspot early enough in the current pulse to probe the core spectroscopically at $t = 0$, so a computational approach is adopted to

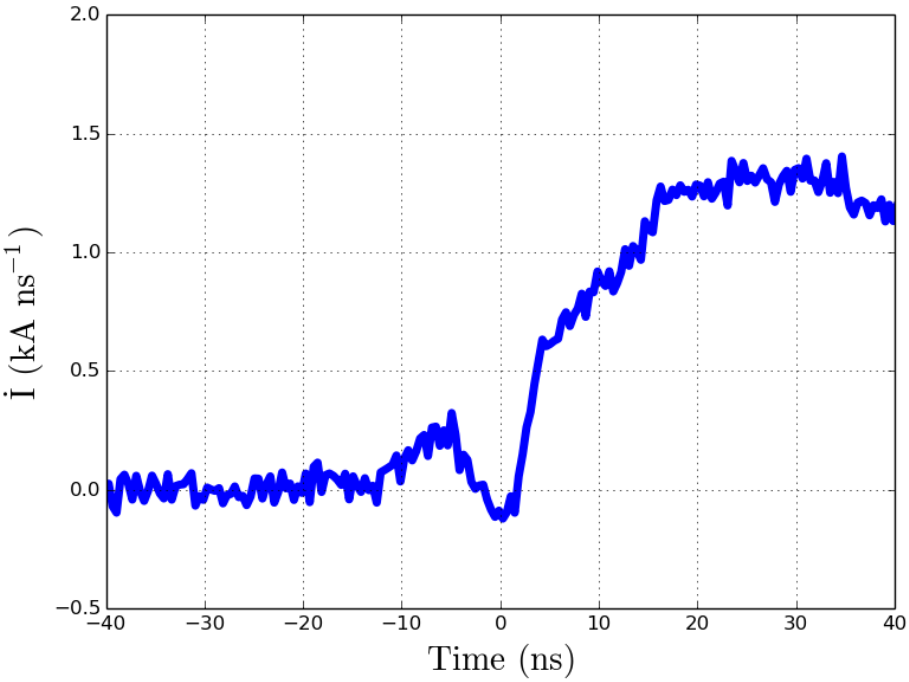

Figure 7.1: The derivative of the current in the sample aluminum wire exhibits a rapid rise after current begins to flow. This feature defines $t = 0$.

arrive at an estimate of the total energy deposition at $t = 0$ and determine if the wire should have exploded by then. The system to be modeled is initially a solid aluminum wire with a diameter of 25 µm and a length of 12.7 mm.

A zero dimensional model is assumed in which both pressure and current are uniform throughout the wire. The justifications for these assumptions are presented in section 7.1.1. The model uses the SESAME equation of state (EOS) 3720 [46] and tabulated conductivity values [47, 48]. Each of these data sources has been validated over four orders of magnitude in density and six orders of magnitude in temperature [48, 49]. The computation is performed over a time domain defined from the start of current flow until plasma formation as witnessed by the Rogowski coil as discussed above. This is typically 30 ns, but occasionally shorter as noted in appendix B. The experimental input to the model is the derivative of

the sample current. The output of the model is the current in the wire along with the temperature and density of the wire as functions of time.

The number of variables is reduced by the introduction of a constraint on the pressure of the system. The system pressure, $P(\rho, T)$, is specified by the SESAME EOS table and assumed to be the sum of the magnetic pressure generated by the current flowing through the wire and the thermal motion of the aluminum atoms.

$$P(\rho, T) = P_{mag} + P_{therm} \tag{7.1}$$

The magnetic pressure is written as a function of density (ρ) and current (I).

$$B = \frac{\mu_0 I}{2\pi r} \tag{7.2}$$

$$P_{mag} = \frac{B^2}{2\mu_0} \tag{7.3}$$

$$= \frac{\mu_0 I^2}{8\pi^2 r^2} \tag{7.4}$$

$$= \frac{\mu_0 l \rho I^2}{8\pi M} \tag{7.5}$$

The wire length, l, and mass, M, are constants. The expression for the thermal pressure is

$$P_{therm} = \frac{nm\overline{\nu^2}}{3} \tag{7.6}$$

$$= \frac{2}{3}\left(\frac{1}{2} nm\overline{\nu^2}\right) \tag{7.7}$$

$$= \frac{2}{3}\rho U(\rho, T) \tag{7.8}$$

where the energy density, $U(\rho, T)$, is taken from the SESAME EOS. The values n, m, and ν are number density, atomic mass, and thermal velocity respectively.

The resulting pressure expression relates current, density, and temperature which allows one of the variables to become dependent on the remaining two. Density is chosen to become dependent leaving current and temperature as the

remaining independent variables. Thus, given the current and temperature at any time during the solution, the density can be found by solving for the roots of:

$$\frac{2}{3}\rho U(\rho,T)+\frac{\mu_0 l\rho I^2}{8\pi M}-P(\rho,T)=0 \tag{7.9}$$

Since $P(0,T)=0$ in the SESAME EOS table, the trivial root at $\rho=0$ is ignored.

A numerical solver evolves the state of the system, $y(t)$, given expressions for the time derivative and initial value of each quantity. The derivative of the current is recorded directly during each experiment and the rate of change of temperature is assumed to be due to joule heating of the wire.

$$\frac{dT}{dt}=\frac{1}{cM}I^2R \tag{7.10}$$

$$=\frac{1}{cM}I^2\left(\frac{l}{\sigma A}\right) \tag{7.11}$$

$$=\frac{l^2}{c\sigma M^2}\rho I^2,\quad \frac{1}{A}=\frac{l\rho}{M} \tag{7.12}$$

The specific heat, c, is computed from the SESAME EOS as $\frac{dU}{dT}$ and σ is a tabulated conductivity value. The initial values are set as:

$$y_0=\begin{bmatrix}0\text{A}\\ 300\text{K}\end{bmatrix} \tag{7.13}$$

The full system of equations is then:

$$y_0=\begin{bmatrix}0\,\text{A}\\ 300\,\text{K}\end{bmatrix} \tag{7.14}$$

$$\frac{dy}{dt}=\begin{bmatrix}\frac{dI}{dt}\ \text{data}\\ \frac{l^2}{c\sigma M^2}\rho I^2\end{bmatrix} \tag{7.15}$$

$$\frac{2}{3}\rho U(\rho,T)+\frac{\mu_0 l\rho I^2}{8\pi M}-P(\rho,T)=0 \tag{7.16}$$

7.1.1 Rationale for 0D

A zero dimensional model is justified by showing that neither the current nor the pressure vary significantly in the radial direction. For a uniform current to exist, the skin depth must be larger than the wire size. A uniform pressure requires that pressure waves transit the system on time scales short compared to the computational time. This transit time is computed by comparing the sound speed to the size of the system.

The expression for skin depth, δ, requires an estimate of the current frequency. The current rise time of 30 ns is taken as one quarter of a full cycle to give an angular frequency, ω, of approximately $52.4 \times 10^6\,\mathrm{s}^{-1}$. The conductivity, σ, is approximately $39 \times 10^6\,\Omega\,\mathrm{m}$. The skin depth of the current is then

$$\delta = \sqrt{\frac{2}{\mu_0 \omega \sigma}} \approx 28\,\mu\mathrm{m} \tag{7.17}$$

The pressure wave transit time, t_p, is the time required for a sound wave to traverse the radius of the wire. The sound speed, c_s, is computed from the SESAME table using the Newton-Laplace equation (7.18) and evaluates to approximately $5250\,\mathrm{m\,s}^{-1}$. The radius is 12.7 µm.

$$c_s = \sqrt{\frac{K_s}{\rho}} = \sqrt{\frac{\partial P}{\partial \rho}} \tag{7.18}$$

$$t_p = \frac{r}{c_s} \approx 2\,\mathrm{ns} \tag{7.19}$$

Since the skin depth is larger than the wire radius (12.7 µm) and the transit time is much smaller than the computational time domain (30 ns), the use of a zero dimensional model is justified.

7.1.2 Error Propagation

The inputs to the model are the SESAME EOS [46], the resistivity table from Sandia [47,48], and the time derivative of the current. Errors in the two tables are not available. The remaining source of error is present in the measurement of $\frac{dI}{dt}$. The error in $I(t)$, is estimated by first integrating the signal to obtain a current trace. Then, the 1-σ error, ΔI, is calculated using the 20 ns preceding current start. Across the set of all experiments, ΔI is found to be less than ± 40 A. This value is used to propagate errors throughout the model.

The expression for the derivative of temperature with time is expanded to include errors in the measurement of the current. This provides an expression for the growth of error in the temperature calculation.

$$\frac{dT}{dt} = \frac{l^2}{c\sigma M^2}\rho I^2 \tag{7.20}$$

$$\frac{dT}{dt} + \frac{d\Delta T}{dt} = \frac{l^2}{c\sigma M^2}\rho \left(I + \Delta I\right)^2 \tag{7.21}$$

$$= \frac{l^2}{c\sigma M^2}\rho \left(I^2 + 2I\Delta I + \Delta I^2\right) \tag{7.22}$$

$$\frac{d\Delta T}{dt} = \frac{l^2}{c\sigma M^2}\rho \left(2I\Delta I + \Delta I^2\right) \tag{7.23}$$

This temperature error is appended to the system of equations to solve and given

an initial value of 0 K.

$$y_0 = \begin{bmatrix} 0\,\mathrm{A} \\ 300\,\mathrm{K} \\ 0\,\mathrm{K} \end{bmatrix} \tag{7.24}$$

$$\frac{dy}{dt} = \begin{bmatrix} \frac{dI}{dt}\ \text{data} \\ \frac{l^2}{c\sigma M^2}\rho I^2 \\ \frac{l^2}{c\sigma M^2}\rho\left(2\Delta I I + \Delta I^2\right) \end{bmatrix} \tag{7.25}$$

$$\frac{2}{3}\rho U(\rho, T) + \frac{\mu_0 l \rho I^2}{8\pi M} - P(\rho, T) = 0 \tag{7.26}$$

Finally, $\Delta\rho$ is estimated by

$$\Delta\rho = \sqrt{\frac{\partial\rho}{\partial T}\Delta T + \frac{\partial\rho}{\partial I}\Delta I} \tag{7.27}$$

With tabulated data existing as functions of T and ρ, estimates of any quantity, x, can now be calculated as

$$\Delta x = \sqrt{\frac{\partial x}{\partial T}\Delta T + \frac{\partial x}{\partial \rho}\Delta\rho} \tag{7.28}$$

An example of a simulation with a full error analysis is shown in Figure 7.2. Errors are represented as a semi-transparent patch behind each trace.

7.2 Image Processing

Each absorption spectrum is calibrated to account for the non-linear dispersion of the spherical quartz crystal and the non-linear process of chemical film development. Timing information is obtained from PCD signals. The spectra are then further processed to obtain the product of density and opacity as a function of

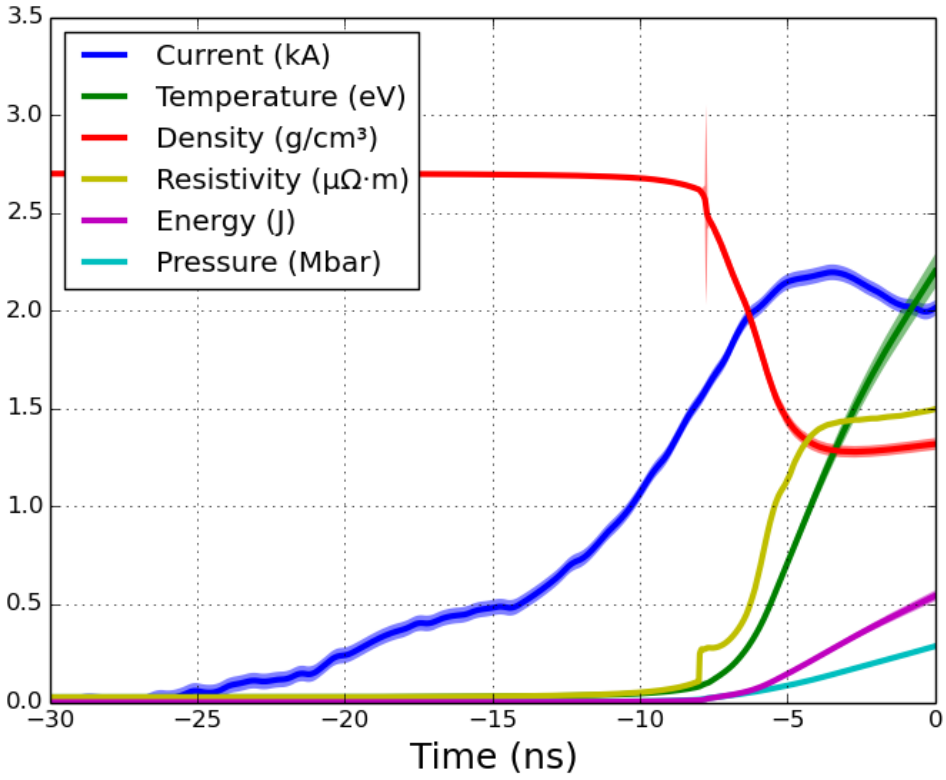

Figure 7.2: A zero dimensional simulation of XP shot #7446. Energy deposition, shown in magenta, reaches a value of 540 mJ.

radius and photon energy. This data is then compared to the output of the spectral opacity code SCRAM [50] to determine plasma density and temperature as functions of radius.

7.2.1 Signal to Noise Ratio

Signal to noise ratios (SNRs) are computed for each spectrum. The signal level is estimated as the difference between the mean values of the regions containing 100% and 0% transmission as shown in Figure 7.5. The noise level is estimated as the standard deviation of the values contained in the 0% transmission region. Signal to noise ratios range from approximately 2.7 for the weakest X-ray sources

to 18.8 for the strongest sources. The shot log in appendix B.1 contains a complete listing of SNR values.

7.2.2 Spectral Calibration

The dispersion of a spherical crystal is both non-linear and sensitive to the alignment of the spectroscopic system. To begin the calibration process, a spectrum that possesses strong line absorption is selected from the set. Shot #7448 is chosen to be a reference spectrum. Because the K-edge of the aluminum filter is constant in every spectrum, the K-edges of all other spectra are aligned with the K-edge of the reference spectrum by translation. This is demonstrated for shot #7361 in Figure 7.3. Rather than attempt to develop an exact analytical expression for the dispersion of the system based on the system's geometry, line energies are identified in the reference spectrum by comparison with simulations. The comparison is shown in Figure 7.4. The resulting position/energy pairs are then fit to a third order polynomial which is applied to all spectra.

7.2.3 Noise Reduction

The field of view in each spectrum is sufficiently wide to view both the top and bottom halves of the aluminum wire sample. Due to cylindrical symmetry, each half contains the same diagnostic information, but different realizations of noise. By averaging both halves of the wire, the noise levels are reduced by $\sqrt{2}$ without a loss of data.

In a select few spectra, the wire sample was not accurately centered in the

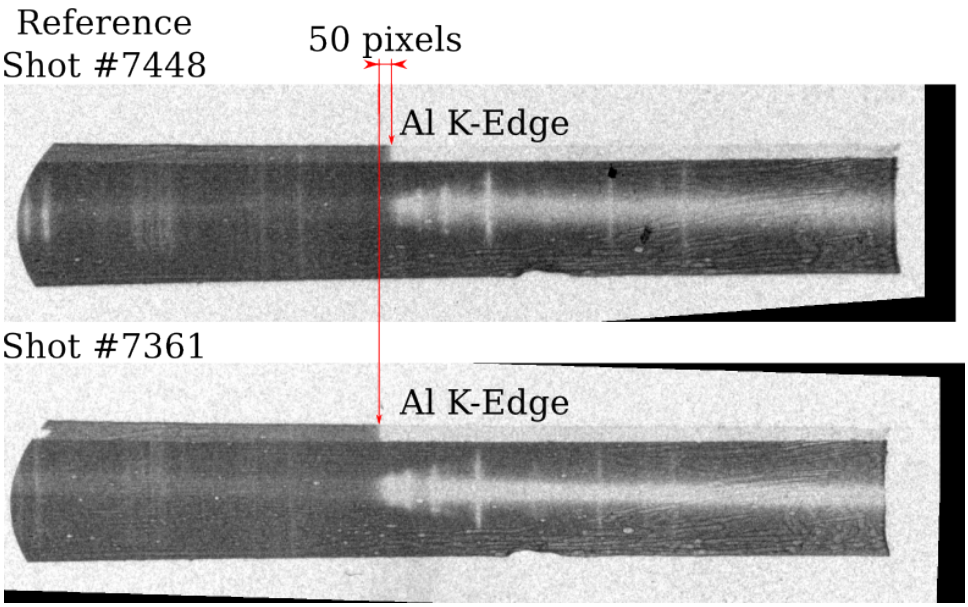

Figure 7.3: The K-edge of shot #7361 is shifted 50 pixels to the right to align with the K-edge of shot #7448.

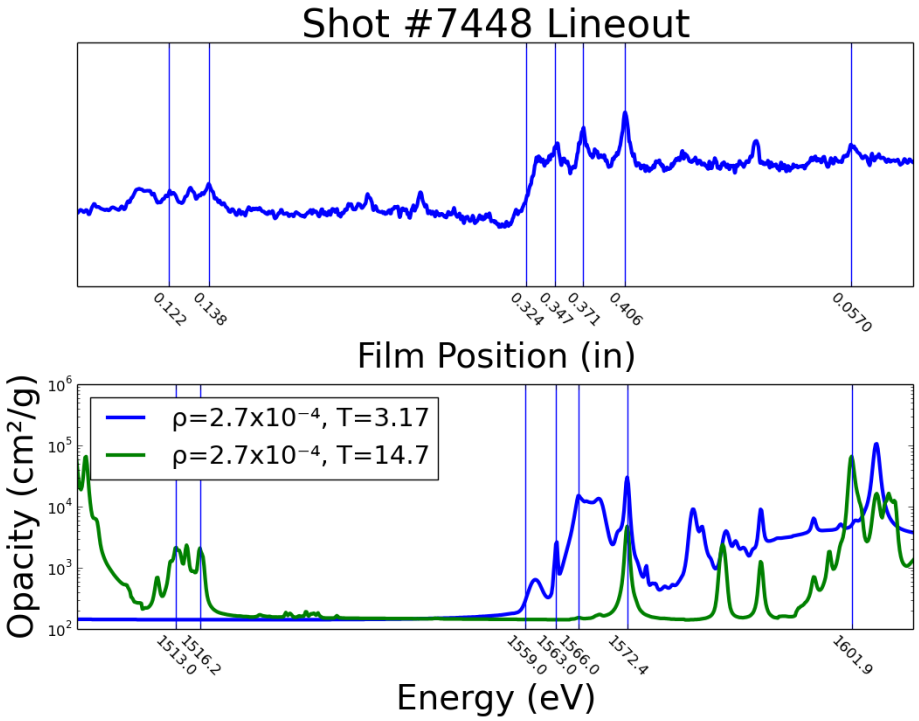

Figure 7.4: The lineout from shot #7448 is taken over a wide spatial extent that covers a range of plasma parameters. It is calibrated against two opacity curves simulated by the SCRAM code [50]. Densities are reported in $\mathrm{g\,cm^{-3}}$. Temperatures are reported in eV.

Position	Energy	Residual
0.122	1513.0	0.830
0.138	1516.2	-0.994
0.324	1559.0	0.158
0.335	1561.0	0.362
0.347	1563.0	0.296
0.371	1566.0	-0.541
0.406	1572.0	-0.150
0.570	1601.9	0.041

Table 7.1: Eight points are used to map film position to photon energy. The residual is the error between the specified energy and that found from the third order polynomial fit.

$$E(x) = a_0 + a_1 x + a_2 x^2 + a_3 x^3 \tag{7.29}$$

a_0	a_1	a_2	a_3
1462.59	499.93	-860.57	723.05

Table 7.2: The final calibration is a third order polynomial that maps film position to photon energy.

crystal's field of view. In these cases, no averaging is performed and only the fully visible half of the wire is used.

7.2.4 Grayscale Calibration

Exposure to an X-ray flux causes the BioMax MS film to darken while unexposed regions remain transparent. However, the mapping from photon flux to film opacity is not necessarily a linear function. Each film is then scanned by a Epson

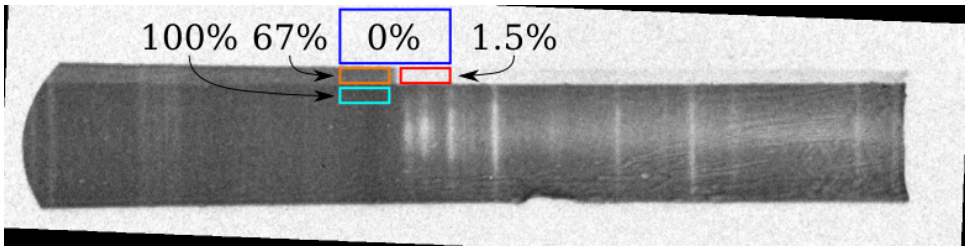

Figure 7.5: Four regions representing 0, 1.5, 67, and 100 percent transmission are selected to calibrate the grayscale values for each shot. Shot #7364 is shown.

Perfection V700 photo scanner at 3200 dpi to produce a 16-bit grayscale TIFF file. During the conversion, regions of the film exposed to high photon fluxes are mapped to low grayscale values and vice versa. Like the chemical development, this digitization cannot be relied upon to provide a linear mapping from film opacity to grayscale value. To extract quantitative data from the films, it is necessary to define a function that can convert grayscale values ($G \in [0, 2^{16}]$) back to the X-ray transmission through the sample ($T \in [0, 1]$). Due to variability in source X-ray intensity and the development process, each film is calibrated individually.

Grayscale calibration values are extracted from four regions of each film. These regions are: above the Al filter, through the Al filter above the K-edge, through the Al filter below the K-edge, and below the Al filter below the K-edge. They are shown in Figure 7.5. These regions are selected to sample the full range of transmission values while avoiding significant absorption. The mean grayscale value in each region is used for calibration, which minimizes the potential influence of nearby lines.

An offset exponential function is chosen for the calibration. The offset is necessary because the mean grayscale value in the 0% region is never observed to be 0. The calibration for shot #7364 in Figure 7.5 is shown in Table 7.3. The full list of grayscale calibration fits are available in appendix B.3.

$$T(x) = ae^{-bx} + c \tag{7.30}$$

a	b	c
3.57	5.43×10^{-5}	-0.124

Table 7.3: The offset exponential function maps a recorded grayscale value to an X-ray transmission value. Fit values for shot #7364 are shown.

7.3 Abel Inversion

The transmission values in the calibrated spectra are not the result of the source X-rays passing through a uniform plasma. Instead the cylindrical nature of the wire causes each ray to sample plasma conditions at multiple radii before reaching the detector film. The process of sampling a cylindrically symmetric plasma with parallel probes is described by the Abel Transform. An expression for the transform is shown in equation (7.31). The standard analytical expression of equation (7.32) is found through a change a variables. The transform is illustrated graphically in Figure 7.6.

$$F(y) = \int_{-\infty}^{\infty} f\left(\sqrt{x^2 + y^2}\right) \, \mathrm{d}x \tag{7.31}$$

$$F(y) = 2\int_{y}^{\infty} \frac{f(r)r \, \mathrm{d}r}{\sqrt{r^2 - y^2}} \tag{7.32}$$

The expression for the transmission values, first presented in equation (2.9), is now manipulated to arrive at a function that is identified as the Abel transform of

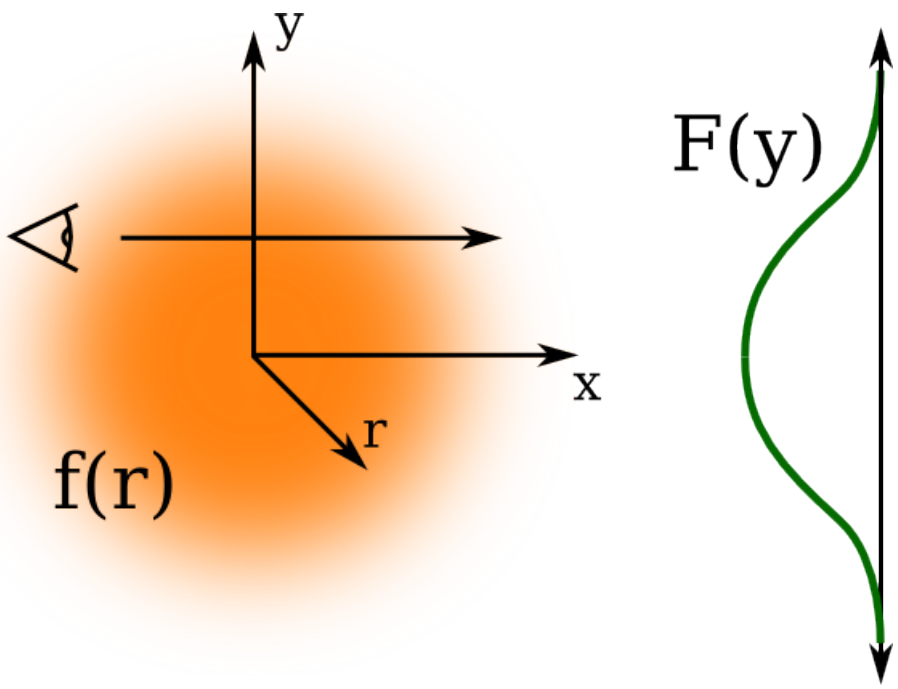

Figure 7.6: The result of sampling a cylindrical function, $f(r)$, along parallel lines of sight is the Abel transform of the function, $F(y)$.

the product of opacity and density.

$$T = e^{-\int \rho(r)\sigma(r)\,\mathrm{d}x} \tag{7.33}$$

$$F = -\ln(T) \tag{7.34}$$

$$= \int_{-\infty}^{\infty} \rho(r)\sigma(r)\,\mathrm{d}x \tag{7.35}$$

Where T is the calibrated spectral transmission and F is the Abel transform. Plasma density and opacity are represented by ρ and σ respectively.

The product of density and opacity can be obtained by use of the inverse Abel transform. The analytical expression is given in equation (7.36). Any decent experimentalist should feel his or her skin crawling at the mention of a numerical derivative. This is because the noise inherent in any experimental data is greatly amplified by numerical differentiation. Direct evaluation of this integral is ill-

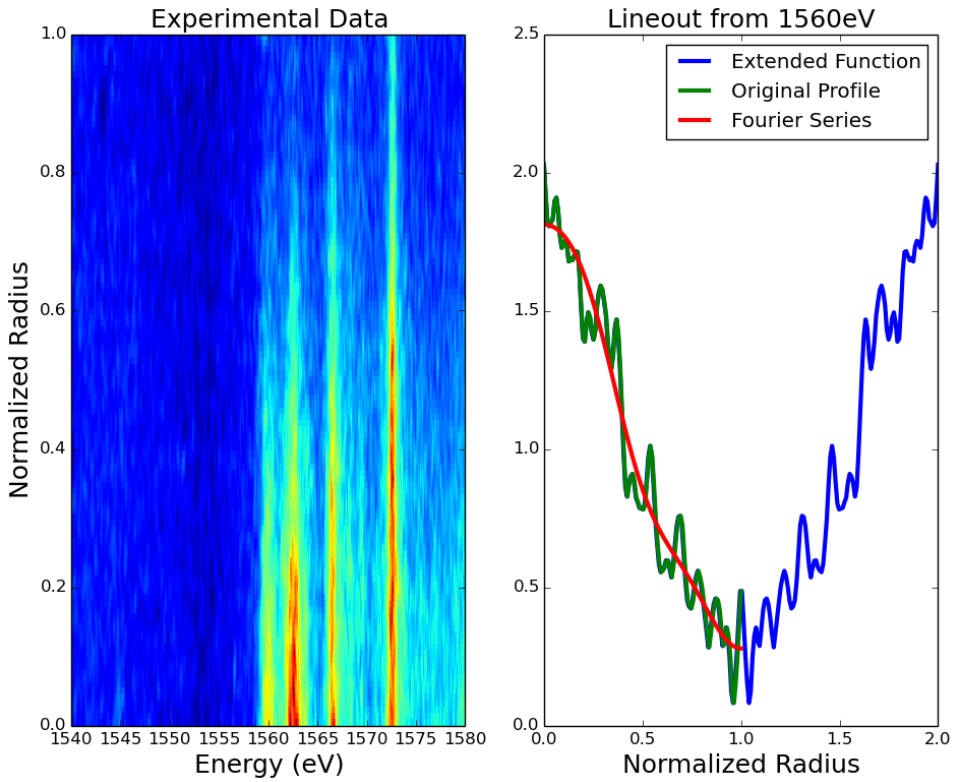

Figure 7.7: A Fourier series expansion of the lineout from shot #7364 at 1560 eV is used to approximate the experimental data.

advised!

$$f(r) = -\frac{1}{\pi}\int_r^\infty \frac{dF}{dy}\frac{\mathrm{d}y}{\sqrt{y^2 - r^2}} \tag{7.36}$$

To avoid the menagerie of problems that come with numerical differentiation of noisy data, the inversion is approached by a less direct route. Without loss of generality, the process is illustrated using the radial profile found in shot #7364 at a photon energy of 1560 eV after the procedure in section 7.2.3 has been performed. A full analysis requires that this process be repeated for each photon energy in every spectrum.

While the Abel inverse is problematic for noisy data, pairs of analytical transforms do exist [51]. The two transform pairs of relevance to the present work are reproduced in Table 7.4. Note that there does not exist a transform pair containing

$f(r)$	$F(y)$	conditions
$(a^2 - r^2)^{-1/2} \Pi_a(r)$	π	$0 < y < a$
$J_0(\omega r)$	$\frac{2\,cos(\omega y)}{\omega}$	$\omega > 0$

$$\Pi_a(x) = \begin{cases} 1 & \text{for } 0 < \text{x} < \text{a} \\ 0 & \text{otherwise} \end{cases}$$

Table 7.4: Two pairs of analytical Abel transforms allow a Fourier series representation of data to be easily inverted. J_0 is a Bessel function of the first kind and Π_a is the rectangle function defined above.

a sine function. To avoid the use of a sine function, the lineout is first mirrored about a normalized radius value of $r = 1.0$. This is the extended function in Figure 7.7. This forces the experimental data to become an even function, which won't contain any sine terms in a Fourier expansion.

A Fourier series expansion of the extended function is now computed. The present work uses $N = 4$, which approximates the data well while providing smoothing for the data. The series is then evaluated over the domain of $r = [0, 1]$. With the coefficients of the Fourier series in hand, the Abel inversion is a straight forward matter of reading the transform table. The inverted data from shot #7364 is shown in Figure 7.8.

$$f(x) = \frac{1}{2}\int_0^2 f(x)\,\mathrm{d}x + \sum_{n=1}^{N} a_n cos\left(\frac{2\pi n x}{2}\right) \tag{7.37}$$

$$a_n = \int_0^2 f(x) cos\left(\frac{2\pi n x}{2}\right) \tag{7.38}$$

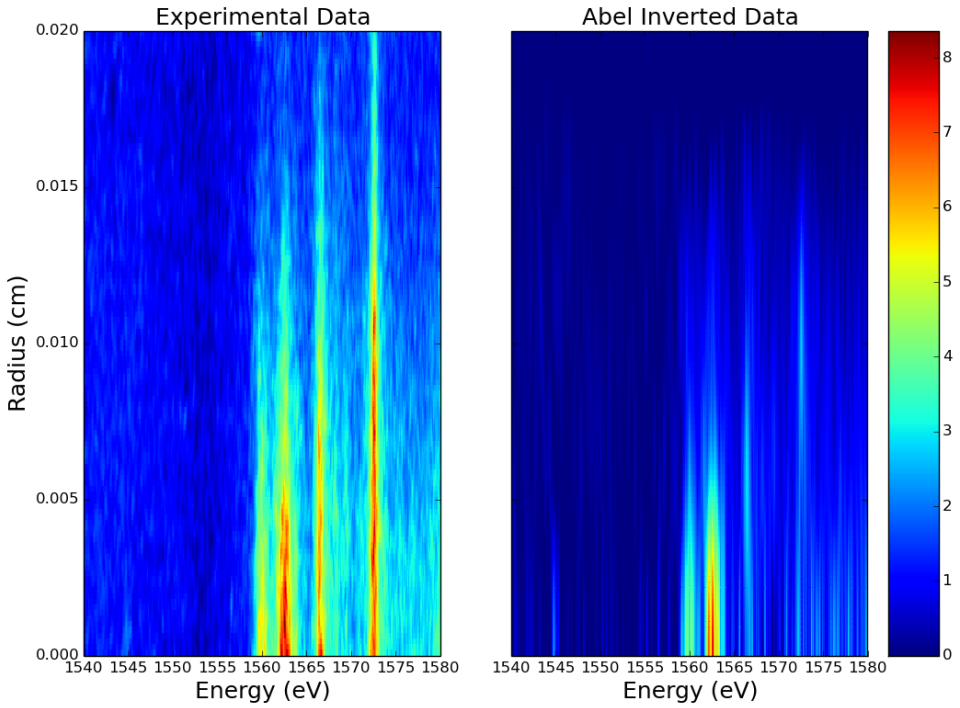

Figure 7.8: The experimental data on the left is inverted to produce the image on the right. The colorbar provides a scale for optical depth in the inverted data image. Both vertical axes describe radial position.

Inpainting

The transmission function maps grayscale values to X-ray transmission, but the presence of noise ensures that transmission values will occasionally fall outside of zero to one. This is problematic for equation (7.34) and results in NaN (not a number) values appearing in F. These values will persist and contaminate later calculations if they are not addressed and corrected.

These invalid values are corrected with an iterative process called inpainting. To begin a loop, the location of every NaN in the data is identified and replaced with a zero. Next, temporary data is constructed as the two dimensional convolution of the original data with a 3x3 pixel kernel. The values of the kernel's pixels are all one except for the center pixel which is zero. For the purpose of convolution, the

$$A_0 = \begin{bmatrix} 1 & 1 & 2 & 2 \\ 1 & 2 & N & 3 \\ 2 & N & N & N \\ 3 & N & N & N \end{bmatrix} \rightarrow \begin{bmatrix} 1 & 1 & 2 & 2 \\ 1 & 2 & 0 & 3 \\ 2 & 0 & 0 & 0 \\ 3 & 0 & 0 & 0 \end{bmatrix}$$

$$C = \begin{bmatrix} 1 & 1 & 1 & 1 \\ 1 & 1 & 0 & 1 \\ 1 & 0 & 0 & 0 \\ 1 & 0 & 0 & 0 \end{bmatrix} \quad k = \begin{bmatrix} 1 & 1 & 1 \\ 1 & 0 & 1 \\ 1 & 1 & 1 \end{bmatrix}$$

$$\frac{A_0 \otimes k}{C \otimes k} = \frac{\begin{bmatrix} 9 & 10 & 13 & 16 \\ 10 & 7 & 10 & 9 \\ 12 & 8 & 5 & 6 \\ 13 & 8 & 0 & 0 \end{bmatrix}}{\begin{bmatrix} 8 & 7 & 7 & 7 \\ 7 & 5 & 5 & 4 \\ 6 & 4 & 2 & 2 \\ 5 & 3 & 0 & 0 \end{bmatrix}} \approx \begin{bmatrix} 1.125 & 1.429 & 1.857 & 2.286 \\ 1.429 & 1.4 & 2 & 2.25 \\ 2 & 2 & 2.5 & 3 \\ 2.6 & 2.667 & N & N \end{bmatrix}$$

$$A_1 = \begin{bmatrix} 1 & 1 & 2 & 2 \\ 1 & 2 & 2 & 3 \\ 2 & 2 & 2.5 & 3 \\ 3 & 2.667 & N & N \end{bmatrix}$$

Figure 7.9: A single loop of the inpainting process is demonstrated for example data, A_0. The array C represents the location of valid data with a 1 and invalid data with a 0. The kernel is array k. Convolution is represented by $\otimes$ and boundaries are assumed to be symmetric. Division in line three is performed element-wise. Only the invalid elements in array A_0 are replaced by their counterparts from line three to form array A_1.

borders are considered to be symmetric. The temporary data is then normalized by the number of valid pixels included in the convolution of each point. The result is an image in which NaN values adjacent to valid data are replaced with a weighted sum of that valid border data. Invalid pixels that don't border valid data remain invalid. The final step is to replace only the NaN values in the original data with the corresponding pixels from the convolution. This only changes the invalid border pixels and completes the loop. This process is repeated until no NaN values remain. A single iteration of this process is illustrated in 7.9.

7.4 Genetic Algorithm

The remaining task is to determine the density and temperature profiles that give rise to the Abel inverted data. Lineouts from each Abel inversion are taken at seven radial positions: 0, 25, 50, 75, 100, 125, and 150 µm. A density and a temperature are found at each radius by comparing a synthetic spectrum to the experimental data. The comparison is done by evaluating a function that reaches a minimum when a solution is found. Taken together, the seven density and seven temperature values form the desired radial profiles.

Many techniques exist to find the minimum of a function, but most require the function to be smooth. An explicit expression for the function's gradient is also often used to aid in the search for a minimum. Unfortunately, the opacity table is neither smooth nor easily differentiable. This limits the number of possible solution methods to brute force or non-linear methods. While a brute force technique is possible, it is not feasible due to the extremely large parameter space which is discussed in section 7.4.1. The non-linear technique chosen for the problem at hand is the genetic algorithm [52].

The framework of a genetic algorithm uses terminology that parallels that of biological evolution. The individual is the basic building block of the algorithm. It contains the information necessary to describe a solution to a problem. The quality of this solution is determined by a metric that is specific to the problem at hand. The metric allows a fitness value to be assigned to the individual. In the present work, the individual is a multi-dimensional numerical vector and the fitness value is also numerical. Individuals exist as members of a population and can be ranked according to their respective fitness values. As in biological systems, the best individuals pass their traits to the next generation. This is done by selecting

individuals from the population and mixing them together to create new solutions. The terms mix, blend, breed, and crossover can be used interchangeably. Finally, mutations are random changes to an individual's solution that have the potential to access new regions of the solution space. The basic genetic algorithm is run many times just as biological evolution occurs over many generations. For this reason, a cycle through the algorithm is called a generation.

A genetic algorithm begins with a population of individuals, each of which encodes a possible solution to the given problem. Each individual in the population is evaluated to determine how well the encoded solution solves the problem. The evaluation allows the individuals to be ranked according to the accuracy of their solution (section 7.4.2). The individuals in the population are now mixed with one another with preference given to highly ranked individuals. This process creates new individuals that are inserted into the population. The method of mixing and the probability of its occurrence are described in section 7.4.4. Random mutations are then probabilistically applied to each individual. This completes one cycle or generation of the algorithm as illustrated in Figure 7.10. By running the algorithm for many generations, the best solutions come to dominate the pool of individuals and hopefully converge to the same solution.

It should be noted that, unlike some linear solution methods, convergence even to a local minimum is not guaranteed. This can be due to a number of factors including, but not limited to, small population sizes, infrequent mixing, excessively large mutations, or a small number of generations. These factors are determined at the discretion of the user and do not have optimum values for all problem types.

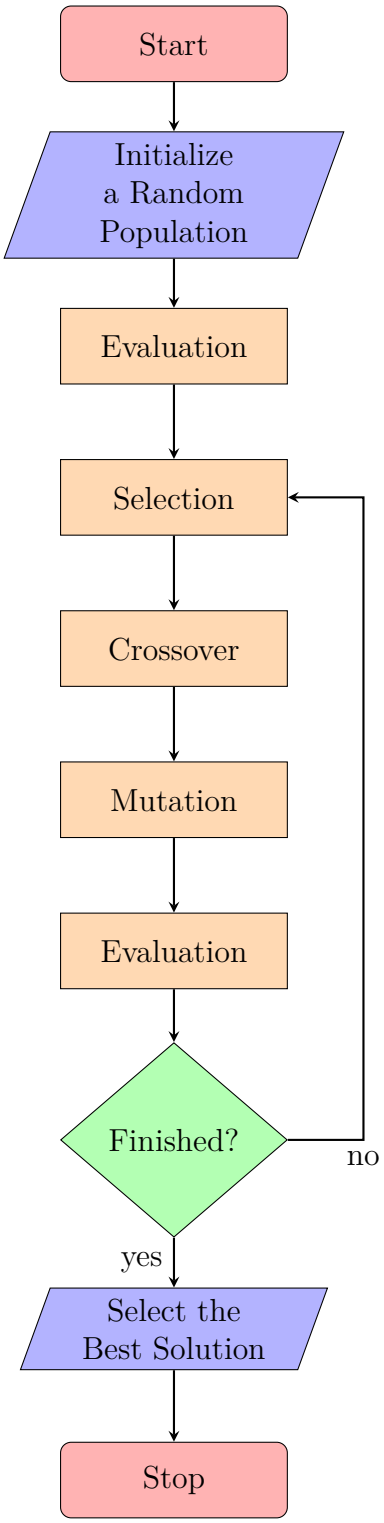

Figure 7.10: The genetic algorithm consists of four basic operations: selection, crossover, mutation, and evaluation. These are repeated for a fixed number of generations. Ten generations are used in the present work.

7.4.1 Population

The individuals comprising the population of candidate solutions need to encode a solution to the problem at hand. This is done with a list of five floating point numbers. The first and second are the density and temperature respectively. These correspond to values found in the opacity table. The third and fourth values describe the shape of the K-edge which is not well captured in the opacity table. Since the opacity table doesn't describe the K-edge well, it is fit using an analytical function based on a Fermi-Dirac distribution [53, 54]. This function is given in equation (7.40).

$$f = \frac{1}{e^{(E-E_f)/kT_f} + 1} \tag{7.39}$$

$$\kappa = \kappa_L + \kappa_K(1 - f) \tag{7.40}$$

The values of κ_K and κ_L are the mass absorption coefficients above and below the K-edge respectively. These values are tabulated for aluminum [55]. The final value determines the energy at which the spectrum switches from the Fermi function to the opacity table. For $E < p_2 + p_3 \times p_4$, the Fermi model is used; otherwise, values are taken from the opacity table.

The individuals of the first generation are initialized by randomly selecting a value for each parameter from a uniform distribution. The distribution for each parameter is defined by a minimum and a maximum that is unique to that parameter. These bounds are shown in Table 7.5. The first generation is initialized with 1000 individuals. This is empirically found to provide a reasonable trade-off between computational time and the time required for convergence to a solution.

	p_0 (cm^{-3})	p_1 (eV)	p_2 (eV)	p_3 (eV)	p_4
MIN	6×10^{16}	0.025	1556	0.0	0.0
MAX	6×10^{21}	10.0	1562	1.5	5.0

Table 7.5: Each parameter is initialized from a uniform distribution defined by a unique minimum and maximum.

7.4.2 Evaluation

The encoded profiles are used to construct synthetic spectra of the plasma at each radial position in the data. There is no density or temperature variation along the energy axis. The opacity as a function of energy is generated using the encoded temperature and density. Finally, the opacity is multiplied element-wise with the density to produce a synthetic spectrum. The synthetic spectrum will match the experimental data under the assumptions that the density and temperature profiles were chosen correctly and that the opacity function accurately represents reality.

To determine the quality of the match between the experimental and synthetic data, χ^2 is computed as shown in equation (7.41).

$$\chi^2 = \frac{1}{N} \sum^{N} [\kappa\rho - d]^2 \tag{7.41}$$

Here, κ is the opacity function. The experimental data is represented by d. Each spectrum contains a total of N pixels over which the summation is taken. A perfect solution, $\chi^2 = 0$, is extremely unlikely due to the presence of noise in the data. Since a solution is found when χ^2 is minimized, the fitness of an individual is computed as $\frac{1}{\chi^2}$.

7.4.3 Selection

Mixing members of the population is done to arrive at new potential solutions. In order for this to happen, an algorithm is needed to determine which individuals will be selected for crossover. This work uses a tournament to determine the list of breeding individuals. The process begins by randomly selecting k individuals from the current population. The current work uses $k = 3$. Of these three members, the individual with the best solution is selected and added to a list. The tournaments continue until the number of selections is equal to the size of the population, $N = 1000$ in this case. It is possible that some individuals are selected more than once and that some individuals are not selected at all. This is advantageous as it means that the worst solutions are forgotten and the best solutions pass their characteristics onto the next generation. The new list is used in the crossover operation.

7.4.4 Crossover & Mutation

The crossover operation works pair-wise on the list generated by the selection process. Individuals in the present work are only comprised of numerical data and so a numerical crossover is utilized. Two breeding individuals and a controlling parameter, α, are used to produce two new individuals. In the present work, $\alpha = 0.2$ is empirically found to work well. The crossover occurs in place to produce two new individuals that replace the original two. This keeps the overall size of the population constant. The algorithm to crossover a given parameter, p_n, from

	p_0 (cm^{-3})	p_1 (eV)	p_2 (eV)	p_3 (eV)	p_4
μ	0	0	0	0	0
σ	1×10^{19}	1.0	1.0	1.0	0.5

Table 7.6: The mutation of each parameter is controlled by a Gaussian distribution that is unique to that parameter. The mean and standard deviation are represented by μ and σ respectively.

two input individuals is

$$\gamma = (1 + 2\alpha)R - \alpha \tag{7.42}$$

$$p_n^1 = (1 - \gamma)p_n^1 + \gamma p_n^2 \tag{7.43}$$

$$p_n^2 = \gamma p_n^1 + (1 - \gamma)p_n^2 \tag{7.44}$$

In the notation used above, p_n^i represents the n^{th} parameter of the i^{th} individual being considered. Thus, $n \in [0, 1, 2, 3, 4]$ and $i \in [1, 2]$. The variable R is a random number drawn from a uniform distribution between zero and one.

Mutation occurs for every individual in the population after the crossover process. Each parameter of each individual is mutated with an independent probability which is set to a constant value of 0.2. A random number, β, is drawn from a uniform distribution in the range of zero to one during every mutation. If $\beta < 0.2$, the parameter is mutated by adding it to a number drawn from a Gaussian distribution. The Gaussian distributions are uniquely defined for each parameter by Table 7.6. The choice of these values represents a balance between the speed of convergence and the algorithm's ability to settle on a solution. If mutations occur too often or are too large, a potential solution may be lost. On the other hand, mutations encourage new regions of the solution space to be explored so they must be allowed to occur.

Parameter Bounds

The processes of crossover and mutation have the potential to adjust parameters outside of the bounds defined by Table 7.5. To counter this possibility, the parameters of each individual are checked after each crossover and mutation. If any parameter is found to lie outside of the allowable range, it is replaced with the nearest bound. This prevents individuals from wandering off into parameter space where solutions may be less likely or non-physical ($T < 0$).

7.4.5 Convergence

There is no universal criterion to detect the convergence of a genetic algorithm. The present work runs the algorithm for 10 generations before terminating. Convergence of the algorithm is monitored by tracking the average value of χ^2. If the algorithm does not appear to have converged on a solution after 10 generations, it is restarted from its final state. The solution is taken from the individual with the highest fitness (lowest χ^2) at the end of the last generation.

7.4.6 Error Estimation

At the termination of the genetic algorithm, a large majority of the population is well suited to describe the experimental data. Any variation in the parameters of the population is due to the presence of noise in the experimental data. The weighted standard deviation of each parameter is taken across the entire population as a measure of the uncertainty in the final solution. Since the fitness function (χ^2) is designed for minimization, the weights, w_i, are computed as the inverse of the

fitness value for each individual. This gives the greatest weight to the best solutions and minimizes the contribution from the surviving poor solutions.

$$w_i = \frac{(\chi_i^2)^{-1}}{\sum_{i=1}^{N} (\chi_i^2)^{-1}} \tag{7.45}$$

$$\mu_n = \frac{1}{N} \sum_{i=1}^{N} w_i p_n^i \tag{7.46}$$

$$\sigma_n = \sqrt{\frac{\sum_{i=1}^{N} w_i \left(\mu_n - p_n^i\right)^2}{N}} \tag{7.47}$$

The individuals in the population are indexed by the variable i which runs from 1 to $N = 1000$. The weighted mean value for the n^{th} parameter, μ_n is found first. As before, p_n^i represents the n^{th} parameter of the i^{th} individual. The weighted standard deviation of the n^{th} parameter is then computed as σ_n. This is taken to be the error in the n^{th} parameter.

7.5 Opacity Table Modifications

The theoretical opacity table that is being used to interpret the experimental data requires modifications before use. The table's lower temperature limit is 1 eV. This temperature is potentially greater than those found in the experiment especially in the core of the aluminum wire. This limit exists because of numerical convergence problems while generating the table at low temperatures. Since extrapolation off of the table is possible during analysis, a room temperature opacity curve is added at 25 meV [56]. This addition allows the table to be interpolated down to known values at room temperature instead of relying on extrapolation.

The tabulated opacity values are free from any of the broadening mechanisms that degrade the results of an experiment. In order to make a meaningful comparison between experimental and theoretical data, the theoretical data must be

broadened in the same manner as occurs in the experiment. An estimate of the spectral resolution is found in section 6.4.2. The opacity table is broadened by convolution with a Gaussian kernel with a width equal to that of the spectral resolution. This allows the table to match the experimental data.

CHAPTER 8

RESULTS

The analytical techniques described in Chapter 7 are applied to the collected experimental data. The results of that analysis are presented here. A discussion of these results is reserved for Chapter 9.

8.1 0D Model

The current through the sample aluminum plasma was recorded by a non-integrating Rogowski coil. That data was input into the 0D model which tracked the state of the wire from the time current began to flow up to the time of coronal plasma formation. At termination, the model reported the total energy deposited into the wire sample and the final density of the sample. The density was converted to the radius of the wire assuming a fixed length and no mass loss. The final energy and radius values are reported in Table 8.1. The mean value and standard deviation of these outputs are presented in last two rows as μ and σ respectively.

In order to compute the final energy and radius of the aluminum wire, it was necessary for the model to track other physical values describing the wire's state. The parameters of wire current, temperature, density, resistivity, and pressure are plotted in Figure 8.1 for Shot #7446. Error bars for each parameter appear as a transparent patch behind each trace. Figure 8.1 is representative of the 0D model results for all shots.

Shot #	Energy (mJ)	Radius (µm)
7357	820	17.4
7360	470	18.0
7361	770	17.5
7362	720	17.6
7363	340	18.2
7364	630	17.7
7370	230	18.0
7371	290	18.2
7373	640	17.7
7377	590	17.8
7444	390	18.2
7446	540	17.9
7447	350	18.2
7448	640	17.7
7449	420	18.1
7450	1040	17.1
7452	870	17.3
7453	420	18.1
7454	480	18.0
7455	400	18.1
7457	380	18.2
7458	400	18.1
μ	538	17.87
σ	209	0.33

Table 8.1: This table lists the output of the 0D model for the 22 analyzed shots. The energy deposited into the core and radius of the wire are reported at the time that current switches from the wire core into the coronal plasma. The final two rows present the mean (μ) and standard deviation (σ) of the calculations.

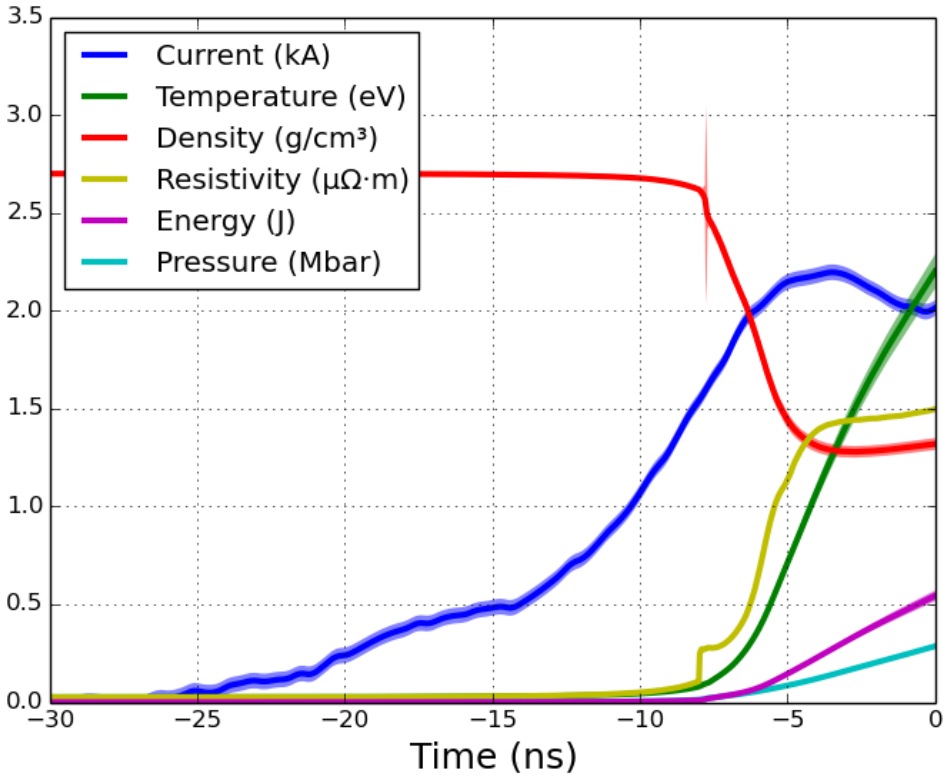

Figure 8.1: A zero dimensional simulation of XP shot #7446. In addition to total energy deposition and radius, the values of current, temperature, density, resistivity, and pressure are tracked through time.

8.2 Radiography

A portion of the genetic algorithm's task is to determine a value for density which best describes a given spectrum. This value comes into play directly as a factor in the product $\sigma\rho$ and as an independent variable of the opacity table, $\sigma(\rho, T)$. While the genetic algorithm is capable of performing this task, an additional measurement of the wire core's density is performed by point projection radiography. This serves as a consistency check on the genetic algorithm's results.

Radiographic images were captured and Abel inverted to measure volumetric density. Due to the low absorption in the corona of the wire, density values can

only be gathered by this technique in the wire core. An image taken at a time of 75 ns into the current pulse indicates that the peak density is below $1 \times 10^{20}\,\mathrm{cm}^{-3}$. This peak value and the radial profile are both consistent with densities found at this time by the genetic algorithm.

Radiographs captured before 75 ns indicate that wire core densities exceed $1 \times 10^{20}\,\mathrm{cm}^{-3}$. Densities above this value are never reported by the GA. The performance of X-pinches as a source of X-rays is poor for times early in the current pulse, and a low X-ray flux increases the relative contribution of noise to the signal. The GA cannot be expected to perform well when it is feed a diet of noisy data. It is likely that density profiles reported by the GA for early times underestimate reality.

8.3 Absorption Spectra

Of the 22 shots analyzed with the 0D model, the spectra of only 14 are examined in detail. The eight rejected spectra are excluded because of major inconsistencies with the remaining data set, or in the case of shot #7360, the spectral film recorded a very low signal-to-noise ratio, which rendered analysis pointless. Any results obtained from shot #7360 were accompanied by error bars of similar size to the values of interest.

For shot #7450, the wire was aligned with the edge of the dispersing crystal, causing a portion of the wire core to be clipped. Without a view of the entire wire core, determination of $r = 0$ was not possible. Thus, this spectrum was also rejected.

The spectra of shots #7444, #7446, and #7452 show wire core radii that don't fit into the time sequence of the other spectra. Their radii are similar to those of spectra taken approximately 50 ns later. This is illustrated in Figure 8.3. The current waveforms for these three shots are not different from those of other data points. It is speculated that the wires' surfaces were inadvertently contaminated during handling, which could have altered their dynamics.

The remaining three excluded spectra are the results of shots #7364, #7371, and #7455. These spectra do not present a well defined K-edge or wire core for analysis. Since the spectra from these three shots contain the same line absorption as the other spectra, it is not believed that another material was inadvertently inserted into the experiment. It is possible that a smaller wire diameter was inadvertently used, which would explain the presence of the correct absorption lines while accounting for the missing K-edge as a result of a lower areal density.

Each spectrum is analyzed at seven radial positions: 0, 25, 50, 75, 100, 125, and 150 µm ± 3 µm. At each radial position, a density and a temperature are found along with the position and slope of the K-edge. These values allow synthetic spectra to be generated which are compared to the experimental data. This is done for shot #7448 as an example in Figure 8.2.

The top left of the figure presents the acquired spectrum with a bandwidth of ±20 eV around the aluminum K-edge. False color is used to indicate optical depth with blue indicating minimal absorption and red indicating peak absorption. The horizontal red lines indicate the locations at which the lineouts in the right half of the figure are taken. These lineouts are vertically offset for clarity. A vertical black line at 1559 eV indicates the location of the K-edge for solid density aluminum at room temperature. Synthetic spectra, generated from the solutions found by the

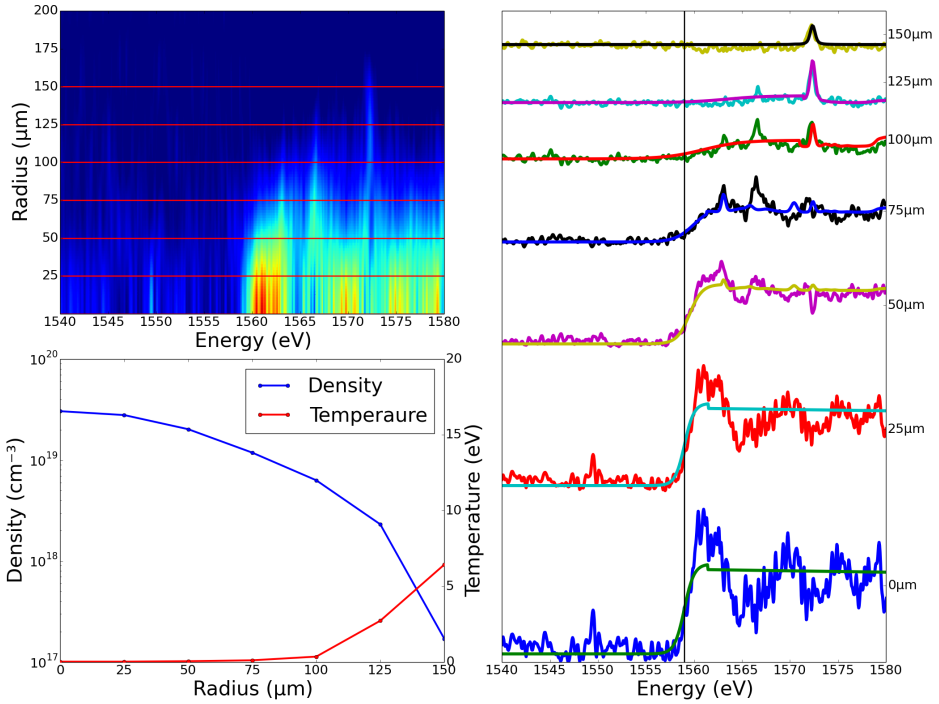

Figure 8.2: The spectrum from shot #7448 (top left) is analyzed at seven different radial positions. Comparisons are made to synthetic spectra (right). The resultant radial density (blue) and temperature (red) profiles are show in the bottom left.

genetic algorithm, are overlaid with the experimental data. Finally, the resultant atomic number density and temperature profiles are plotted in the bottom left of the image. Numerical data from this analysis is presented in Table 8.2. The detailed results from the analysis of all of the spectra appear in Appendix B.4.

	SCRAM		K-Edge	
Radius (µm)	ρ (cm^{-3})	T (eV)	E_f (eV)	T_f (eV)
0	3.1×10^{19} ±3.3%	0.025±18%	1559.00±0.06%	0.51±72%
25	2.8×10^{19} ±2.6%	0.025±25%	1559.02±0.05%	0.49±60%
50	2.0×10^{19} ±2.3%	0.054±39%	1559.54±0.05%	0.66±50%
75	1.2×10^{19} ±4.3%	0.11±47%	1559.98±0.04%	0.98±42%
100	6.3×10^{18} ±5.4%	0.36±19%	1561.00±0.04%	2.00±17%
125	2.3×10^{18} ±9.6%	2.7± 6%	1563.38±0.18%	2.00±31%
150	1.7×10^{17} ±11%	6.4±11%	1555.19±0.19%	0.14±462%

Table 8.2: The numerical results from shot #7448 are presented along with relative error estimates. The error is estimated from the population of candidate solutions generated by the genetic algorithm. The variables E_f and T_f are defined in equation (7.39).

8.3.1 Wire Core Radius

Density profiles are used to determine the radius of the wire cores at the time that each spectrum is captured. This is done by computing the radius at which the density falls to half of the density found at a radius of 0 µm. These wire core radii are plotted against the time at which the spectra are captured in Figure 8.3. The radii computed from shots #7444, #7446, and #7452 are included to illustrate the inconsistency of their radii with respect to the remainder of the data set.

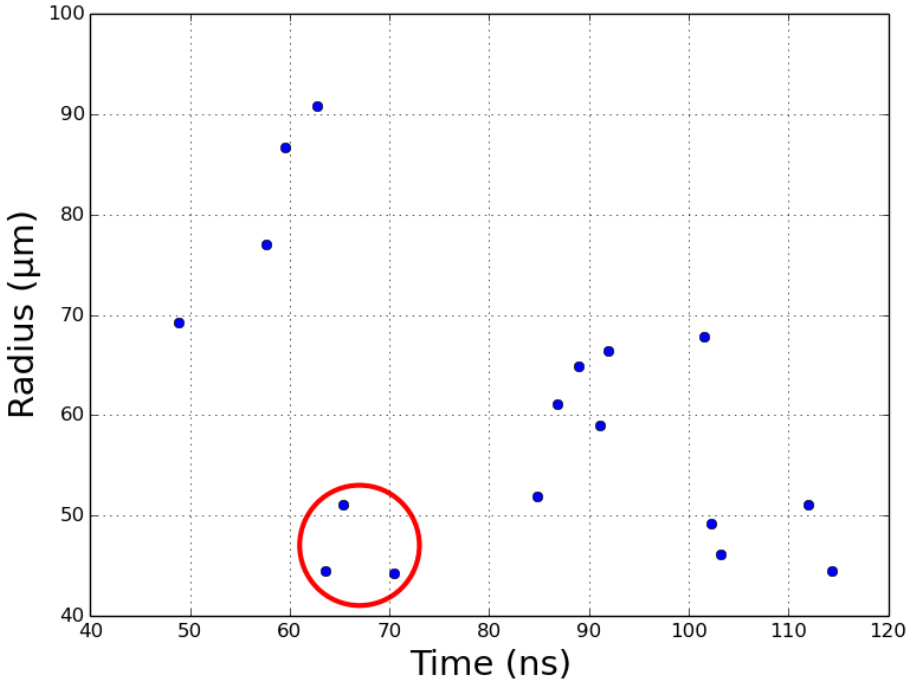

Figure 8.3: The wire core radii are plotted against the time of spectra capture. Three data points (circled) are found to deviate from the trend established by the remainder of the data set. These shots are identified as outliers.

8.3.2 K-Edge Position

A close examination of the absorption spectra reveals that the energy of the aluminum K-edge increases as density decreases. The position of the K-edge is taken half way up the transition. The K-edge energy is plotted against density for several shots in Figure 8.4. This subset of spectra is composed of data points with signal-to-noise ratios greater than 10. Only data points with densities higher than $1 \times 10^{19}\,\mathrm{cm}^{-3}$ are plotted. This cutoff is selected because a K-edge is not consistently apparent in the experimental data at lower densities.

The exact energy of the K-edge on the y-axis should not be considered absolutely correct due to errors in the spectral calibration. The calibration is obtained

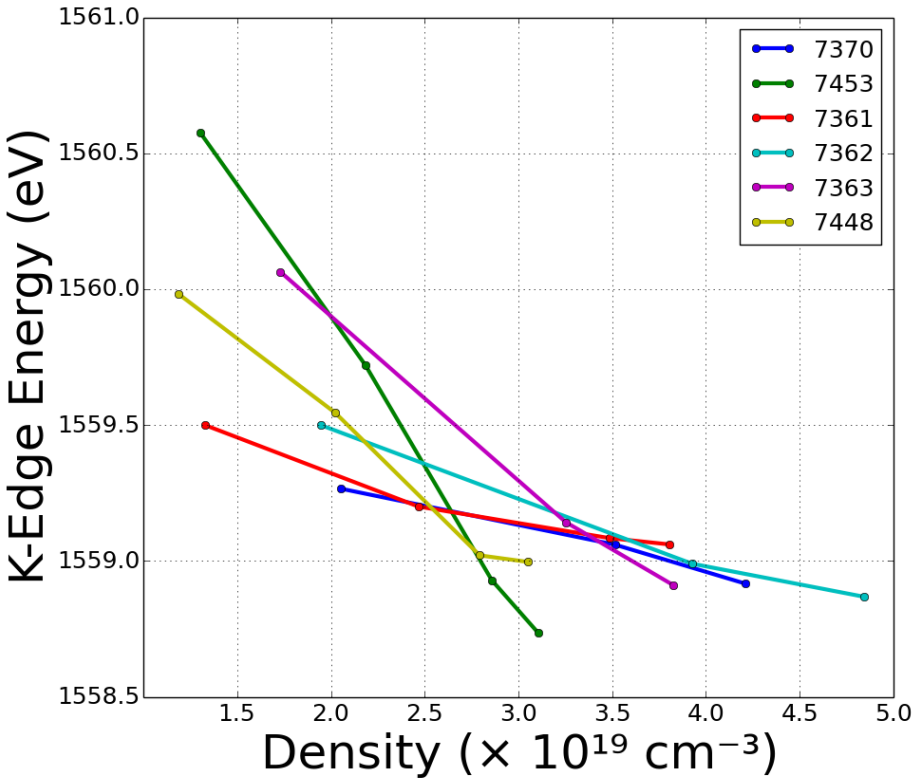

Figure 8.4: The position of the aluminum K-edge is plotted against density for six shots. The spread in the data at low density occurs because the K-edge becomes less prominent as density decreases.

by identifying known absorption lines over a large bandwidth. These points are fit to a third order polynomial by minimizing the calibration error at each known data point. This error is not reduced to zero by the fitting procedure. Near the cold aluminum K-edge energy of 1559 eV, this error is ≈400 meV. This error is inconsequential when compared to the full bandwidth of the spectra being examined. However, the position of the K-edge is found to shift by only 1.5 eV for which the calibration error is significant. Should this error be added to the data points in Figure 8.4, the curves would shift upward by 400 meV. This error does not change the trend identified in the data.

8.3.3 K-Edge Oscillations

A consistent spectroscopic feature is found in the wire core that is not captured by the opacity tables or Fermi model. It appears as variations in the strength of X-ray absorption above the K-edge. This is evident in the lineout through $r = 0\,\mu m$ of Figure 8.2. The theoretical opacity is flat for X-ray energies above the K-edge, but this is not observed in the experimental data. The oscillations are seen to persist for the length of the current pulse from 60 ns through >110 ns. This may point to physics that is not yet included in the SCRAM opacity code.

To illustrate this feature, Fourier transforms of eight absorption spectra are presented in Figure 8.5. These spectra are selected to cover a wide range of sampling times. The absorption spectra are averaged over the radial dimension for $0\,\mu m < R < 25\,\mu m$ to ensure that only the wire core is sampled even at late times (see Figure 8.3).

The process of computing a Fourier transform places the data in reciprocal space. Since the absorption spectra exist in energy space, the transforms are computed in reciprocal energy space. The x-axis is scaled by the product of the Planck constant, $\hbar$, and the speed of light, c, to convert the abscissa to units of length [57].

The transforms are computed for energies greater than the K-edge energy of 1559 eV. This limits the bandwidth to ≈30 eV. In turn, the resolution of the transform is limited to ≈1 nm. This cannot resolve peaks well, but it is sufficient to indicate the presence of peaks corresponding to features noticed in the absorption spectra.

The Fourier transforms of the wire core for all 14 analyzed spectra are now

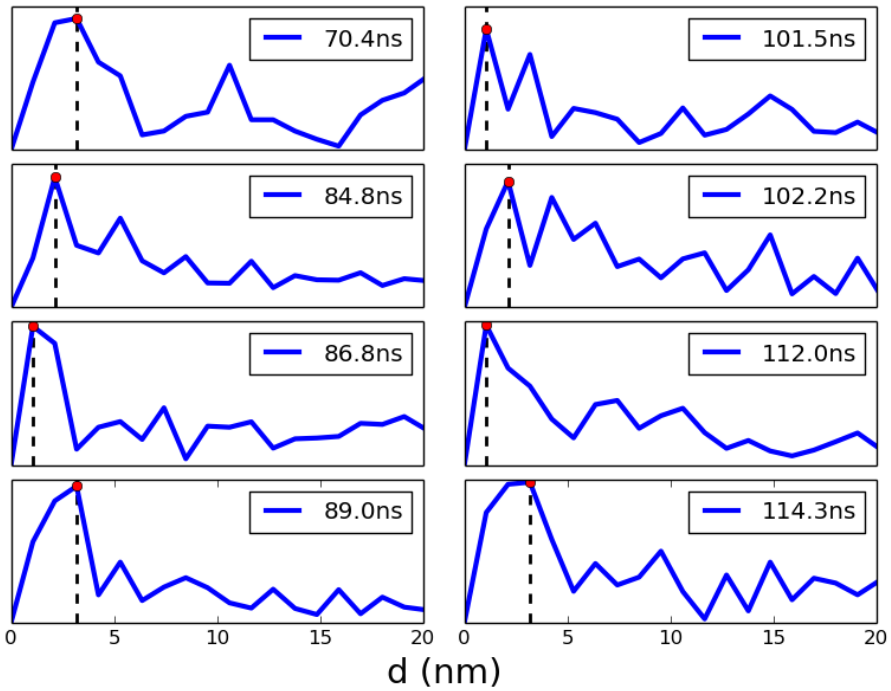

Figure 8.5: A Fourier transform is taken of the wire core absorption spectra for eight shots. Each graph shows a peak at or slightly below 3 nm. A red dot indicates the peak value of each transform.

averaged together. The result is plotted in Figure 8.6. This is done to improve the signal-to-noise level. By averaging the transforms together, noise is reduced to allow less prominent peaks to appear. The location of the first peak is believed to lie between the data points of the transform due to the low resolution of the transform. The possible physical meaning of these oscillations will be discussed in Chapter 9.

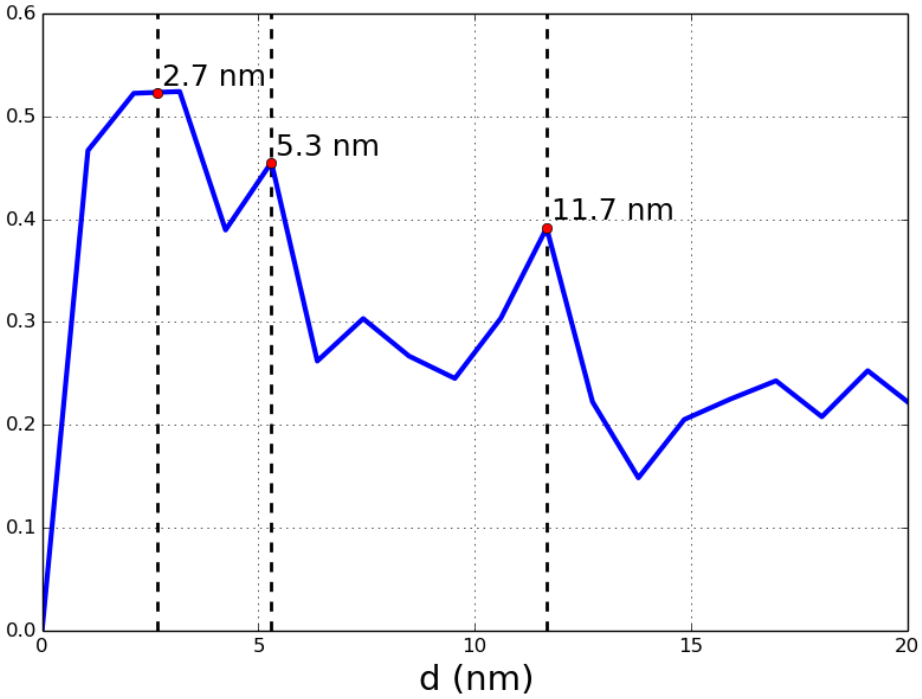

Figure 8.6: The wire core transforms is averaged over all shots and the magnitude is presented. The first peak is believed to lie between the data points of the transform. The resolution is limited by the finite bandwidth of the K-Edge spectrum.

CHAPTER 9

DISCUSSION

The content of Chapter 8 is the result of the physical processes that play a role in the development of exploding aluminum wires. These results are discussed as a unified whole to shine light on the inner workings of aluminum Z-pinches. They are also placed in the context of past published works.

9.1 0D Model

The output of the zero dimensional model described in section 8.1 determines the evolution of six variables: current, temperature, density, resistivity, energy, and pressure as the wire heats prior to voltage breakdown in the surrounding gas. Of these, only current changes appreciably until the last 10 ns of the 30 ns computation. The low resistivity of solid aluminum keeps the energy deposition from ohmic heating (I^2R) low even though the current is rising rapidly. This also prevents the remainder of the variables from changing appreciably during this time.

At $t \approx$ -8 ns relative to voltage breakdown, the temperature reaches ≈930 K and the aluminum undergoes a phase change into a liquid. This is witnessed by a rapid decrease in density and an increase in the resistivity of the aluminum in Figure 9.1. At this time, energy deposition begins to increase appreciably due to the continuing current increase and the increased resistivity of liquid aluminum. This, in turn, drives the temperature and pressure to increase rapidly.

These changes continue until approximately $t =$ -4.5 ns. At this point, the resistivity and density stop changing and become nearly constant. This may indicate

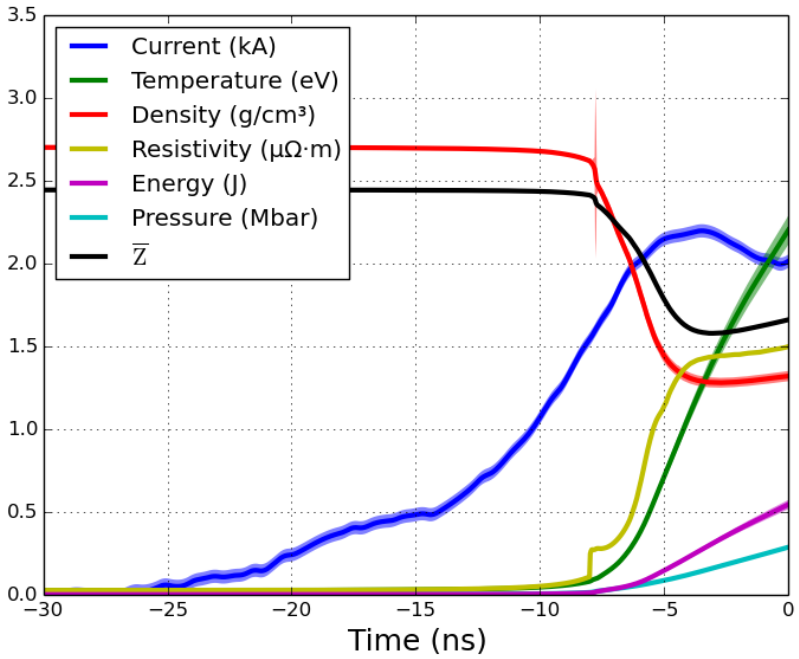

Figure 9.1: The average ionization state (black) is added to the results from XP shot #7446 previously shown as Figure 8.1.

a second phase change. The temperature at this time is 8000 K, well in excess of aluminum's boiling point, but the pressure has reached 100 kbar which could be responsible for an elevation of the boiling temperature in a 0D model.

A more interesting observation occurs at an earlier time when energy deposition in the model reaches 200 mJ. The enthalpy of atomization for aluminum is $326\,\mathrm{kJ\,mol^{-1}}$. This is converted to energy given the initial mass of the aluminum wire. The mass of the aluminum, m, is 16.8 µg and the atomic weight, A_w, is $26.98\,\mathrm{kg\,mol^{-1}}$.

$$H = \frac{326\,\mathrm{kJ}}{\mathrm{mol}} \frac{m}{A_w} \approx 200\,\mathrm{mJ} \tag{9.1}$$

At this time sufficient energy has been added to the aluminum to completely atomize the material and overcome the bonds between atoms. Every experimental trial is observed to cross this threshold a few nanoseconds before the termination

of the computation.

It is interesting to note that the current profile also changes at this time. Instead of continuing to rise, the current becomes constant for the remainder of the simulation. An expression for the current derivative is found from the voltage of an inductive load.

$$V = \frac{d}{dt}(LI) \tag{9.2}$$

$$= L\frac{dI}{dt} + I\frac{dL}{dt} \tag{9.3}$$

$$\frac{dI}{dt} = \frac{1}{L}\left(V - I\frac{dL}{dt}\right) \tag{9.4}$$

If the current derivative is approximately zero, the voltage must be approximately equal to $I\frac{dL}{dt}$. While the voltage of the experimental load cannot be monitored on the XP platform, V is unlikely to be zero during the discharge. The current is also measured to be nonzero. Thus, the only way for $\frac{dI}{dt}$ to be zero is if the current path is rearranging and the inductance is changing during the final 4.5 ns. This would be the case if the plasma column is expanding and carrying the current.

Thus, atomization of the aluminum must be followed by the ionization of the aluminum atoms and the rearrangement of the current path. This is seen in Figure 9.1 as an increase in $\overline{\mathrm{Z}}$ at t = -4 ns in the 0D model. The value of $\overline{\mathrm{Z}}$ is the result of QMD calculations performed by M. Desjarlais *et al.* [48]. If this process proceeds in a nonuniform manner, the current may deviate from a uniform path through the aluminum. The ionization continues until a low resistivity coronal plasma forms that is able to carry the current around the wire core.

The rapid rise of current at t = 0 ns triggers the end of the simulation. The time required to switch current from the wire core to the coronal plasma can be estimated from the ratio of wire inductance to resistance, $\frac{L}{R}$. This ratio is estimated

to be less than 1 ns, which cannot account for the full time between atomization and current switching. Instead, the delay is thought to allow sufficient energy to be deposited for a current carrying population of coronal ions to appear and to expand. This ion population must build to a level and expand to a large enough cross sectional area to be capable of carrying the current with a resistance much lower than that of the wire core.

9.2 Spectral Fitting

The agreement between the experimental data and the synthetic spectra is not expected to be perfect. The experimental data contains noise from a variety of sources that won't appear in theoretical opacity tables or analytical functions. It is also possible that theoretical calculations do not completely capture every aspect of reality. Mean opacities, the K-edge structure, and its position may be misrepresented. Additionally, absorption lines may be predicted with the incorrect location, strength, or width. The differences between experimental data and theoretical calculations can point to physics missing from simulation codes and suggest avenues for refinement.

9.2.1 Similarities

The average optical depth both above and below the K-edge is matched very well in the synthetic spectra. Since optical depth is a product of opacity and density, it is possible that an overestimation of the opacity could be countered by an underestimation of the density and *vice versa*. The density values are corroborated

by measurements taken from radiographic images. This in turn corroborates the average opacity values predicted by the SCRAM code.

The position and shape of the K-edge are found to be well captured in the synthetic spectra. This structure is entirely due to the analytical expression found in equation (7.40). The equation is found to provide sufficient flexibility to describe the K-edge in all of the analyzed spectra.

The spectra at radii larger than the wire core's radius become dominated by line absorption. At the low densities found in the corona, the K-edge is no longer apparent and the genetic algorithm relies exclusively on the opacity data contained in the SCRAM tables. When this occurs, values for the K-edge structure are still generated. However, without a K-edge to fit, no set of values is preferred over another and they become randomly distributed. This is evidenced by K-edge parameter errors that increase with radius.

The spectral line at 1563 eV appears in both the synthetic and experimental datasets. This line is generated by a 1s-2p transition in a B-like ion. The ionization level indicates that it should be visible at relatively low temperatures. Indeed, this is observed in the experimental data. The line is observed only at radii just outside of the wire core where densities are too low for a K-edge to appear. Additionally, it is not found at large radii where the corona is carrying a majority of the drive current and the temperature is high.

The line at 1572 eV appears only in regions of high temperature and is produced by a 1s-2p transition in a Be-like ion. This is found in the coronal plasma where the drive current keeps the temperature elevated. At large radii, this line is often the only spectral feature available for fitting purposes. The width of this line is

strongly dependent on density [54]. The strength of this line relative to that of the 1563 eV line allows the GA to determine a temperature.

9.2.2 Discrepancies

While some agreement is found between the experimental and synthetic spectra, there are features present in each that are not found in the other. The experimental data consistently shows an absorption line at 1566 eV. This line appears near the wire core like the 1563 eV line, but it extends to larger radii where temperatures are higher. It does not extend to the furthest radii as the line at 1572 eV does. The amplitude of this absorption line increases as that of the 1563 eV line decreases. Likewise, absorption at 1566 eV decreases as absorption at 1572 eV increases. This indicates that the the absorption line at 1566 eV dominates the spectrum for a range of temperatures between those near the wire core and those in the corona.

Since matches to both of these bracketing lines are found in the opacity table, it is certain that the temperature at which this 1566 eV line dominates the spectrum lies inside the bounds of the table. However, the synthetic spectra do not contain this feature. A close inspection of the synthetic spectrum at a radius of 75 µm in shot #7448 (Figure 8.2) reveals a small absorption feature at a slightly reduced energy. If this feature is the line seen in the experimental data, its energy is slightly too low and its strength is computed as a fraction of that observed in the data.

Examining the same spectrum, a feature is seen to appear at 1570 eV that is not found in the experimental data. This line appears only with the 1572 eV line, and its intensity is always equal to or less than that of its companion. At large radii where the temperature becomes elevated, it is seen to disappear and the

match to the experimental data is again very good. It should be noted that it is possible that this feature corresponds to the unidentified experimental signal at 1566 eV. However, the experimental amplitude ratio of the two lines is never found in the opacity table. This suggests that both its position and amplitude are being calculated incorrectly.

In addition to the discrepancies of individual absorption lines, the position and slope of the K-edge are not captured accurately by SCRAM. This is a known shortcoming of the code (S. Hansen, personal communication, October 2, 2015). To generate the K-edge in the synthetic spectra calculated here, it was necessary to use an analytical function for the opacity. This function is based on a Fermi distribution and given in equation (7.40). The transition from the analytical to computational opacities introduces a discontinuity into the synthetic spectra which can be seen near the top of the K-edge in Figure 8.2.

The final discrepancy in the synthetic spectra occurs in the wire core where densities are high ($>1 \times 10^{19}\,\mathrm{cm}^{-3}$) and the temperature is low ($<1\,\mathrm{eV}$). Due to numerical convergence problems at low temperature, the lowest temperature in the computational opacity table is 1 eV (S. Hansen, personal communication, September 13, 2015). To extend the table down to room temperature, the opacity of solid density aluminum is artificially added to the bottom of the table. The data is then interpolated down to this lower limit. The opacity of the cold aluminum is constant aside from the transition at the K-edge. This contrasts with the experimental data in which large variations in opacity are observed above the K-edge energy. These variations are not found anywhere in the opacity table. An interpretation of this feature is presented in section 9.3.2.

9.3 Wire Core Physics

The density profiles determined by the genetic algorithm do not reveal a step transition from the dense wire core to the low density corona. Instead, a smooth transition in density is observed. To define the boundary of the wire core without a sharp transition, a change of 50% from the density at $r = 0$ is used to define the edge. This criterion is applied to each analyzed spectrum to generate Figure 8.3. The wire core is defined as existing at radii less than this boundary.

Spectra taken late in the current pulse show smaller wire cores than those taken at early times. This is due to radiation driven ablation [58]. The current deposits energy into the corona which is released as radiation. This radiation carries energy into the wire core which heats the material and causes it to ablate into the corona. This results in a mass loss and applies an ablation pressure radially inward. These both act to reduce the radius over time.

Magnetic field pressure is not believed to be a driving factor in reducing the radius of the wire core. Little current flows in the wire core once the coronal plasma forms because of the reduced resistivity of the corona. This statement is supported by the rapid current increase observed by the Rogowski coil around the sample wire, which is interpreted as evidence of a current shift from the core to the low resistivity corona on an $\frac{L}{R}$ timescale. The low core current in turn generates a minimal azimuthal magnetic field at the core/corona boundary which cannot apply sufficient pressure to compress the core. For example, if the wire core has a density of $1 \times 10^{19}\,\mathrm{cm}^{-3}$ and a temperature of 0.5 eV, the kinetic pressure is 60 kbar. If the wire core is assumed to retain a relatively large 10% of the peak drive current, the magnetic pressure is only 24 kbar. Under such conditions, the wire would be expected to expand until a pressure balance is reached. This is contrary to the

observation of a decreasing wire core radius and implies that magnetic pressure is not a dominant force near the wire core.

The plasma coupling parameter, Γ, is the ratio of Coulomb energy to thermal energy and is shown in equation (9.5) where the Wigner-Seitz radius has been used in the calculation of the Coulomb energy. Here, q, T, and n are the charge, temperature, and density in the wire core respectively. To estimate the coupling parameter in the wire core, the density at $r = 0$ is taken from Table 8.2 ($3.1 \times 10^{19}\,\mathrm{cm}^{-3}$). The temperature reported by the GA in the wire core (25 meV) is suspected to be erroneous for reasons discussed above, thus a temperature estimate of 2 eV is taken from the results of the 0D model. Finally, PrismSPECT [39] is used to estimate that the aluminum plasma is singly ionized.

$$\Gamma = \frac{E_C}{k_B T} = \frac{q^2}{4\pi\epsilon_0 k_B T}\sqrt[3]{\frac{4\pi n}{3}} \approx 0.4 \tag{9.5}$$

Similarly, the number of particles in a Debye sphere, N_D, can also be used as a measure of coupling in a plasma.

$$N_D = \frac{4\pi}{3} n \lambda_D^3 = \frac{4\pi(\epsilon_0 k_B T)^{3/2}}{3 n^{1/2} q^3} \approx 0.8 \tag{9.6}$$

Since both Γ and N_D are of the order of one, the wire core plasma cannot be classified as either weakly or strongly coupled.

9.3.1 K-Edge Position

In a 1998 publication, Hall *et al.* described an experiment designed to study the effects of compression on aluminum's K-edge [59]. The experimental target was a 2 µm thick aluminum foil sandwiched between 5 µm sheets of e-parylene. Compression of the target was achieved by laser irradiation of both sides of the target, which

shocked the aluminum sample to densities above solid density. Varying degrees of compression were achieved by varying the laser's intensity. A probing spectrum of X-rays was produced by irradiation of a uranium source. The absorption spectrum was dispersed by a Thallium Acid Phthalate (TlAP) crystal onto an X-ray CCD detector.

The results of the experiment revealed that the position of the K-edge shifted to lower energy under compression. The degree of compression was estimated using the MEDUSA code. A shift of $\Delta E = -4\,\mathrm{eV}$ was found to accompany compression to twice solid density. The relationship between the K-edge position and compression is shown in Figure 9.2. The conclusion was that the energy of the K-edge is primarily dependent on material density while the width of the K-edge is a function of temperature.

An investigation reported by Benuzzi-Mounaix *et al.* in 2011 extended Hall's work using a similar experiment [60]. A key difference is that range of probed densities extended to nearly three times solid density, $8\,\mathrm{g\,cm^{-3}}$. The results from this paper are in quantitative agreement with those of Hall *et al.* and are reproduced in Figure 9.3. It should be noted that the position of the K-edge appears to be measured at the base of the transition. Measuring the edge at this location records changes due to both the center and slope of the K-edge. The results presented in this thesis have measured the K-edge at the center of the transition (50% amplitude) which is not affected by the slope. This definitional difference does not carry physical meaning.

The results extracted from exploding wires on the XP platform access a very different parameter space. While temperatures are generally similar ($<5\,\mathrm{eV}$), the densities recorded in the wire cores are three orders of magnitude lower than solid.

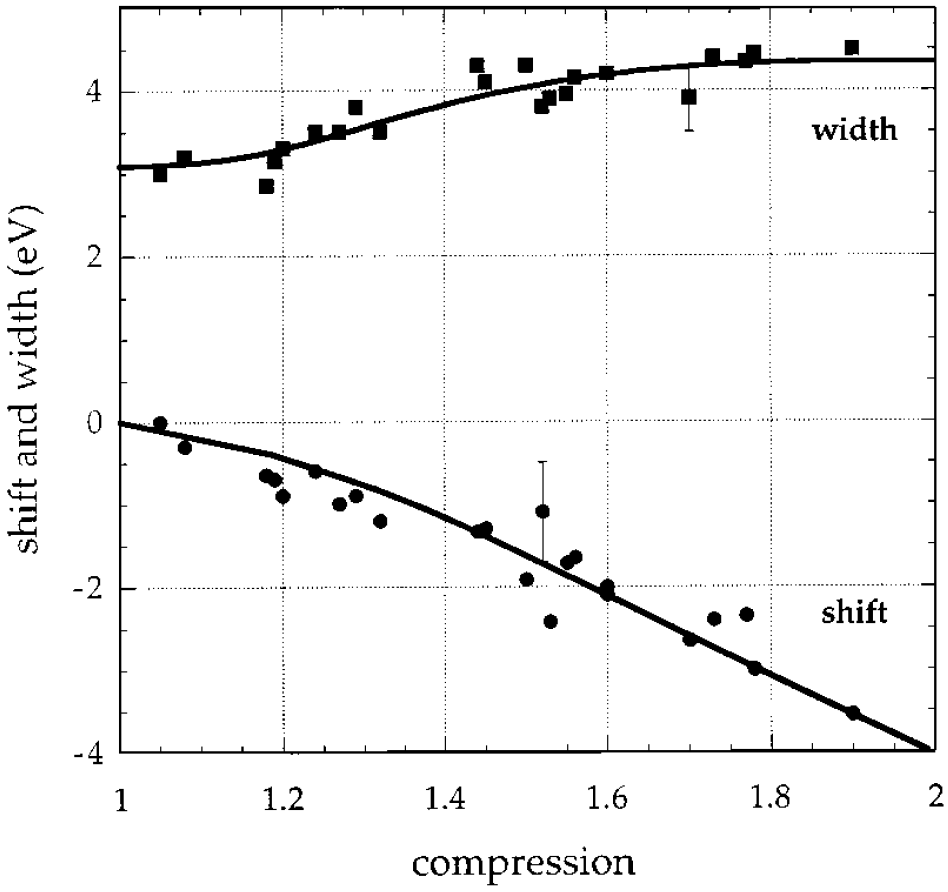

Figure 9.2: Hall *et al.* observed that the energy of the K-edge decreases with increasing density relative to solid density. The trend is approximately linear. Image source: [59]

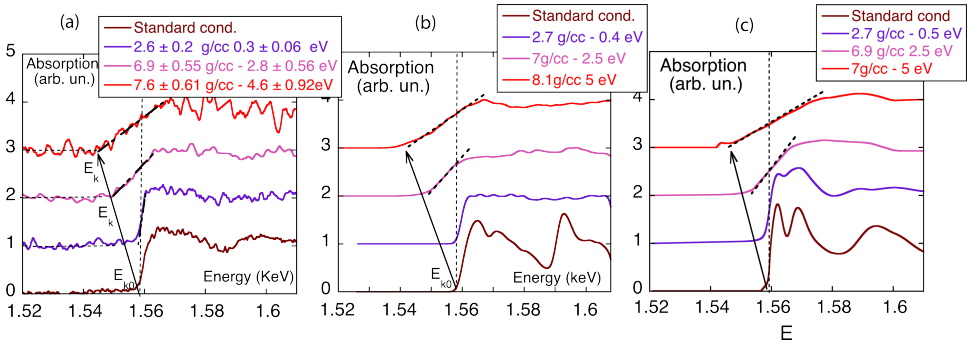

Figure 9.3: The experimental position of the K-edge (a) continues to move to lower energy with compression up to $7.6\,\mathrm{g\,cm^{-3}}$. Plots (b) and (c) show *ab initio* and dense plasma model calculations respectively. Image source: [60]

This is probing a region of parameter space that has not been found reported in the literature and adds data points to the left of the y-axis in Figure 9.2. The trend in the data is consistent: the K-edge energy falls with increasing density. This is hypothesized to be due to a lowering of the continuum level as density increases [60].

9.3.2 K-Edge Oscillations

Oscillations in the absorption of X-rays are consistently observed in the wire core at energies above the K-edge. These variations do not appear to be due to line absorption because of their periodic nature. They also encompass wavelength ranges which are much larger than the widths of absorption lines. These features are not found in the opacity table, which indicates that they are the result of physical processes that are not considered by the SCRAM model.

A clue to their origin is found in the work of Epstein *et al.* [57]. This work examined the structural properties of aluminum after flash melting. The experiment melted an aluminum sample using a focused laser. After a delay of 30 ns, another laser pulse generated a spectrum of probing X-rays. The arrangement of the experiment was such that three absorption spectra were captured simultaneously for each test: the unattenuated probe spectrum, the melted aluminum spectrum, and the solid aluminum spectrum.

The extended X-ray absorption fine structure (EXAFS) of solid aluminum contained oscillations above the K-edge. The FFT of these oscillations contained peaks with locations corresponding to the distance between atoms in crystalline aluminum. These results were shown to agree with X-ray diffraction results to

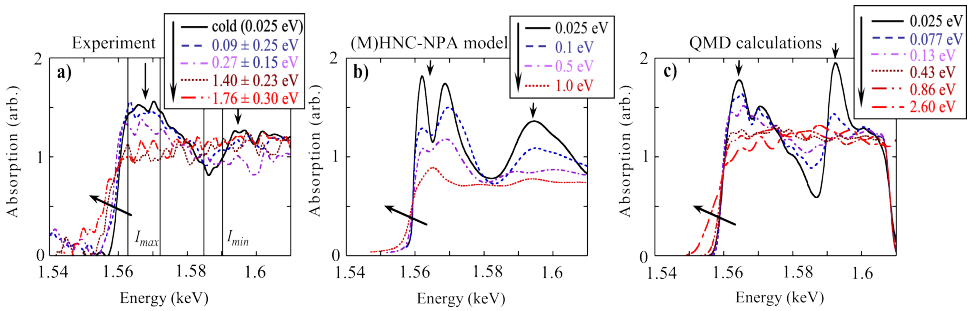

Figure 9.4: The oscillations observed in experimental data of the literature (a) are of a longer wavelength than those found in the XP data. The (M)HNC-NPA (b) and QMD (c) calculations both reproduce oscillations above the K-edge. Image source: [61]

better than 0.1 Å. The spectrum collected from the melted aluminum also showed oscillations. The FFT of these oscillations revealed weaker peaks that had been shifted to larger atomic spacings. This result was interpreted as evidence of residual local structure in the melted aluminum. The temperature and density of the melted aluminum were not reported. It should be noted that the X-ray bandwidth over which the spectra were collected was ≈280 eV. This provided a higher FFT resolution than is possible using the XP data.

A 2010 paper reported an investigation into the disordering of heated solid density aluminum [61]. Part of this work presented simulations of aluminum absorption in the vicinity of the K-edge. These calculations showed oscillations that are reminiscent of those found the XP data. The oscillations are shown to persist up to temperatures of 0.5 eV. These results are reproduced in Figure 9.4

In light of the results found in the literature, the oscillations observed in the XP experimental data might be interpreted to represent residual structure from the solid phase. However, the peaks in the FFT's presented in Chapter 8 are located at wavelengths too long to agree with data for solid aluminum. Instead, the absorption peaks are hypothesized to be generated by clusters of relatively low

density aluminum atoms suspended in the plasma of the wire core.

The zero dimensional model cannot account for a nonuniform sample and so could not predict the environment necessary for such oscillations. In its predictions of energy deposition into an aluminum wire for 22 recorded current traces, in each case, the deposited energy was found to exceed the energy required for complete atomization of the aluminum. In some cases, this threshold was exceeded by a factor of 4. If the model's assumption of uniformity is relaxed, the wire need not change phase uniformly. This would alter the resistivity of the wire, cause nonuniform energy deposition, and invalidate the model's results after the solid-liquid phase change. A full three dimensional simulation of an exploding wire from a cold start is beyond the scope of this thesis, but it could become nonuniform even before the formation of a coronal plasma occurs due to the grain structure of solid aluminum.

The Fourier transform peaks of the experimental XP data in Figure 8.5 suggest the presence of structures on spatial scales of 3 nm. It is not immediately clear if this represents the average size of an aluminum cluster or the average spacing between clusters. If the clusters are formed during the initial heating of the wire core, the number of clusters should be approximately fixed after current switches into the corona with potential mass loss due to radiation driven ablation. The volume of the wire core is directly related to its radius, which has been shown to decrease with time. With a fixed number of clusters, a decreasing radius would increase the cluster density and decrease the average distance between the clusters. However, the time sequence of FFTs shown in Figure 8.5 suggests that this feature is not dependent on time. Thus, it is hypothesized that this is a measurement of the average spacing between aluminum atoms in clusters which were formed during

the initial heating of the wire. This small size could not have been observed by previous work that used radiographic imaging to determining the inner structure of exploding aluminum wires [62].

The question of the K-edge's origin in a given spectrum now arises. It is not clear if the observed K-edge is a result of absorption by the fully averaged bulk plasma or by a collection of aluminum clusters. If it is caused by the bulk plasma, the SCRAM opacity model would be expected to provide reasonable results. Indeed, an edge is found in the opacity table, but the location is not consistent with the experimental data. This suggests that aluminum clusters could play a role in the establishment of the K-edge in the experiments.

Atomic spectroscopy codes, such as SCRAM, compute the spectral properties of a plasma based on a given density and temperature. If the experimental conditions are not uniform, but instead composed of clusters in a plasma environment, it is not surprising that some experimental spectral features are missing. This interpretation also makes sense in the context of aluminum shock compression experiments [59,60]. Indeed, oscillations above the K-edge were not observed in these experiments. It is much more reasonable to expect a heterogeneous environment to form below solid density during expansion of material that starts out with a nonuniform structure.

An accurate replication of the experimental observations is expected to require an opacity code that readily handles physical conditions from condensed matter to plasma relevant regimes. This would avoid the need to anchor the opacity table with a cold aluminum opacity curve. Additionally, it would be necessary to incorporate heterogeneity into such a model. A model able to span such a large parameter space while accounting for a heterogeneous environment is expected to

require a herculean effort.

CHAPTER 10

CONCLUSIONS

10.1 Elliptical Spectrometer

The initial concern that spectroscopic absorption measurements could be contaminated by sample emission motivated the design of a novel elliptical spectrometer. The goal of the design was to construct a spectrometer capable of discriminating an absorption signal from any self emission generated by a plasma sample. This was done by using an elliptical crystal to disperse and focus the probing radiation onto the plasma under study. This is in contrast with point projection schemes in which the radiation is dispersed after interaction with the sample. Additionally, an astigmatism was included to focus the probing radiation through a slit aperture that further limited the influence of self emission. The details of this design are presented in Chapter 4.

Due to the novel design of the spectrometer and the unique geometry of the crystal, a ray tracing code was written to investigate the propagation of X-rays through the spectrometer. The spatial and spectral distribution of the X-rays were computed in three planes of interest in the spectrometer. The first two planes verified the astigmatism of the X-ray crystal and that the X-rays were being focused onto the plasma sample. The third plane was that of detector. The calculations in this plane confirmed that the spectrometer would record both spatially and spectrally resolved information about the plasma under study.

The spectrometer was then fabricated and experimentally tested. This was done by using the spectrometer to record the emission spectrum of magnesium

which contained spectral features in the bandwidth of interest. The experimental results matched the ray tracing results and verified the alignment of the spectrometer.

Unfortunately, experimental measurements of absorption spectra revealed a significant design flaw in the spectrometer. The design called for a mica crystal to disperse X-rays in the second order, but it is known to reflect X-rays well in many orders. It was believed that the reflection of X-rays from these other orders could be suppressed through tailoring of the X-ray source spectrum and filter selection. A variety of source materials and filters were evaluated, but reflections from the mica crystal in the fifth order could not be suppressed below the signal level in the second order.

With the root cause of the failure identified, two potential solutions were presented to alleviate signal contamination from fifth order reflections. The first was to change the crystal material. Quartz is well known for its ability to reflect X-rays in the first order only. With this this in mind, the design of the spectrometer could be adjusted to account for dispersion by a quartz crystal and successfully realized. This solution requires a quartz crystal which is more brittle than mica and may not be able to conform to the elliptical geometry of the spectrometer. It is for this reason that quartz was not initially used as the dispersing medium in the design.

A second solution that continues to use the mica crystal but adds an X-ray mirror to the spectrometer's design was tested. The mirror was situated directly in front of the detector to deflect the X-rays by 1°. If the grazing angle of the mirror could be controlled to better than 0.5°, the X-rays from the fifth order could be suppressed while allowing the absorption signal to propagate to the detector. Unfortunately, the necessary alignment tolerances could not be achieved, which

prevented the successful application of this solution.

10.2 Point Projection Spectroscopy

While discrimination between second and fifth order reflections from mica was not achieved in the elliptical spectrometer's design, the skills developed during its development and testing could be applied to investigate the behavior of aluminum's K-edge in a point projection absorption experiment. This was done by probing the K-edge generated by aluminum in single wire explosions. The details of this experiment are presented in Chapter 5. The results of the experiment were captured in high resolution and time resolved spectra that were taken over a series of experiments. These spectra have been calibrated and analyzed to investigate the behavior of aluminum under the experimental conditions.

The spectra presented a set of opacity features that were not predicted by a single theory. To explain the majority of the spectral features observed in the data, a hybrid opacity model was adopted. An analytical function could describe the shape of the K-edge, but it could not account for line absorption. The opacity code SCRAM could predict line absorption, but its performance near the K-edge was poor. Thus, each solution was used over a limited spectral range with a transition between the two occurring at the top of the K-edge.

The position and shape of aluminum's K-edge was modeled using a function based on the Fermi distribution. The position and slope of the function's edge were allowed to change to match the data. This was found to provide a good fit to the aluminum K-edge inside the wire's core. In the corona surrounding the wire, the line integrated density of neutral aluminum was too low to observe a K-edge.

Line absorption features were matched using opacity predictions generated by SCRAM. Due to numerical convergence issues, the predictions could be made only as low as a temperature of 1 eV. Since temperatures below this level could exist in the wire core, the opacity table was modified to include the opacity of solid density aluminum at room temperature. This allowed interpolation instead of extrapolation to occur in the event that temperatures below 1 eV were believed to exist in the sample. The quality of the match between the experimental data and the opacity predictions is discussed in detail in section 9.2.

The analysis of the spectra has identified a relationship between the energy of aluminum's K-edge and the material's density. In room temperature solid aluminum, the K-edge appears at an energy of 1559 eV. As density decreases, the position of the K-edge is observed to move to higher energies. This trend is consistent with observations of laser shocked aluminum in which the K-edge shifts to lower energies under compression. The energy shift is caused by a change in the continuum level inside the aluminum. As density falls, atoms move further from and perturb each other less. This allows the continuum level to rise. The higher continuum level increases the energy required to eject a K-shell electron from a neutral atom. This is manifest spectroscopically as a shift in the K-edge energy. While this phenomenon has previously been observed in higher than solid density aluminum, this work adds new data at sub-solid densities against which theoretical explanations of K-edge shifts may be evaluated.

Of the spectral features not captured by the hybrid opacity model, the most prominent is the oscillation in opacity that is observed above the K-edge in the wire core. This feature is only observed in the wire core where the density is high and the temperature is relatively low. This is a manifestation of X-ray absorption

fine structure (XAFS). This is striking because the appearance of an XAFS signal depends on long range atomic ordering in a sample that is typically found in solid materials. After passing through the liquid and gas phases into a plasma, one may expect that any ordering from the solid phase would be lost. However, this does not appear to be the case. This structure is consistently found in the wire core of multiple experimental trials.

This data highlights the role that mesoscale physics might play in the evolution of plasmas. The atomic ordering that gives rise to the XAFS signal exists in an intermediate spatial scale which is larger than the atomic scale considered by plasma opacity codes such as SCRAM. The mesoscale is also too small to be considered by codes that predict bulk material properties such as equations of state. Thus, it is believed that the physics giving rise to the observed spectral structure may be absent in many cold start plasma calculations. Experimental evidence has been presented that suggests the need for mesoscale physics to be included in those detailed plasma physics simulations. The challenge now lies with the computational community to reproduce these experimental findings by simulating the relevant physics across all spatial scales. The data presented in this thesis is submitted as a benchmark against which such efforts may be validated.

CHAPTER 11

CONTINUED WORK

The results presented in this thesis required the use of simulated opacity tables for interpretation of the experimental data. The results of Chapter 8 depend on the validity of these simulations. It would be of scientific value to develop a platform on which opacity data could be directly extracted. This has been recently demonstrated by results indicating that iron opacities are currently being underestimated by atomic modeling codes [63]. This could provide a benchmark for atomic simulation codes that guide the interpretation of spectra. Such a change requires an inversion of the thought process used throughout the analysis presented in Chapter 7. Instead of considering density and temperature to be variables dependent on opacity, opacity could be viewed as the dependent variable. This is accomplished by determining both density and temperature through diagnostics that are independent of spectra. They can then be used to extract experimental opacity data from the collected spectra.

11.1 Independent Measurements

Opacity can be extracted from a spectrum only if all other relevant plasma parameters are known through other means. The relevant parameters are X-ray transmission, density, and temperature. Each of these must be determined by an independent diagnostic tool. Then, the results can be combined to infer the opacity values of the plasma structure under study.

11.1.1 X-ray Transmission

X-ray transmission can be determined through the same technique used in this thesis. The point projection technique has already been demonstrated to be capable of obtaining well resolved spectra, which can be converted to calibrated transmission values. The quality of the conversion between image grayscale values and transmission, however, could be improved. A cold aluminum step wedge could replace the aluminum filter that was used to provide an energy fiducial. By varying the thickness, the number of points used to fit the offset exponential in equation (7.30) can be increased. The energy fiducial will remain so long as the material is not changed.

An alternative would be to leave the single thickness aluminum filter and add a second crystal. This crystal would be tuned to the same energy bandwidth of the spectroscopic crystal. The original filter would remain to provide the energy fiducial on the spectral crystal while the second crystal would be covered by an aluminum step wedge to provide as many calibration points as possible. Both crystals should be imaged onto the same film to prevent any differences in the chemical development from influencing the results.

11.1.2 Density

Two techniques can be employed to determine the radial density distribution of an exploding wire accurately. The first is calibrated point projection radiography as discussed in section 3.3. If the magnification of the spectroscopic system is such that only a small portion of the wire's length is required to generate the absorption spectrum, the remaining length of the wire will generate a radiographic

image beyond the edges of the spectroscopic crystal. This image can be collected, calibrated with a step wedge, and analyzed to reveal density. As long as the wire can be considered uniform along its length, the inferred density will provide a good representation of the density found in the spectrograph.

The second technique is laser interferometry. Laser interferometry is a well documented technique used to measure areal densities [64]. While radiography is well suited to probing high densities, interferometry is better suited to probing the lower densities found in a wire's corona. The combination of both measurements should provide an unambiguous measurement of plasma density across all radii of the wire.

11.1.3 Temperature

The remaining necessary data is temperature as a function of radius. Radially resolved Thomson scattering off of plasmas provides such a measurement [65]. The analysis of such data provides a wealth of information including density and temperature. With density independently determined by both radiography and interferometry, this provides an independent measurement of plasma temperature at discrete radii. An interpolation of these data points will likely be necessary to obtain a radial temperature profile.

11.2 Opacity Validation

The measurements of X-ray transmission and density provide an experimental measurement of opacity. The final detail of temperature provides the theoretician

with a set of data containing opacity over an X-ray bandwidth at known density and temperature. This can be compared to opacity modeling codes to either validate the output or to guide work aimed at generating improved simulations. It is believed that such an experiment could be used to provide valuable scientific data across a wide X-ray bandwidth for a number of elements.

APPENDIX A

THE XP PULSED POWER GENERATOR

The generation of high energy density plasmas requires energy to be deposited into a sample on short time scales. These short time scales minimize energy dissipation to the surrounding environment. To achieve these conditions, energy is stored over a long period of time and released on the time scale of the experiment. While this can be accomplished by a number of methods, the present work utilizes the XP pulsed power generator to develop the necessary experimental conditions [7].

A.1 Mechanical Description

The XP pulsed power machine was designed to deliver up to 500 kA with a rise time of 50 ns to an experimental load. Initially, energy is stored in a 10 capacitor Marx bank. When triggered, the bank's energy is compressed in time by transfer to an intermediate storage capacitor on a 1 µs time scale. A main switch then passes the energy to the pulse forming line in ≈125 ns. Finally, the near simultaneous closing of eight water gap switches transfers the electrical pulse into the experimental load in ≈50 ns where it is used to generate plasmas for study.

A.1.1 Marx Bank

The XP pulsed power machine is driven by a Marx bank containing 10 1.8 µF capacitors. The topology of the circuit is such that all capacitors are charged in parallel and they are switched into a series configuration to initiate the discharge.

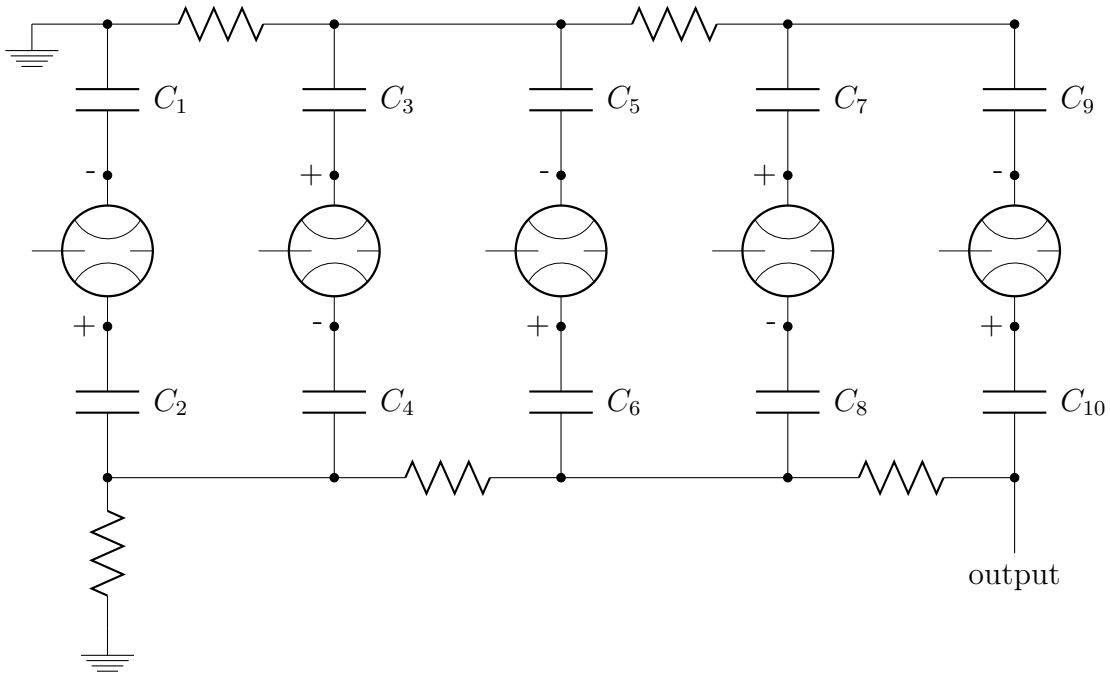

Figure A.1: Symmetric charging of the Marx bank occurs at the terminals labeled '+' and '-'. Triggering the bank shorts the five gas switches. The voltage on the output is the sum of the individual capacitor voltages.

This results in a ten fold voltage increase at the output of the Marx bank. A schematic of the bank is shown in Figure A.1.

Charging is performed through a resistor network (not shown) that limits the current from the high voltage power supplies flowing into the capacitors. The resistors shown in Figure A.1 hold one terminal of each capacitor at ground while the bank is charging. During discharge, the impedance of these resistors is much larger than that of the series connections between the capacitors. Thus, they may be considered as open circuits during this time.

The connections between the capacitors used during discharge incorporate five sulfur hexafluoride (SF_6) gas switches. These switches act as open circuits while the bank is charging. To initiate a discharge of the bank, a trigger pulse is applied to the mid-plane electrode of the first two switches. This causes them to become

short circuits and increase the voltage across the remaining three switches. The higher voltage causes the final three switches to self break and deliver ten times the charging voltage to the output of the Marx bank. The gas pressure in the switches is adjusted to ensure hold off of the charging voltage and reliable break down due to triggering during discharge.

For the purposes of this work, a charging voltage of 40 kV is applied to each of the capacitors. Assuming zero losses, the Marx bank output voltage applied to the intermediate storage capacitor is 400 kV and the total energy storage is then 13 kJ. Charging to higher voltages is possible and has been done in the past; however, this places extra electrical stress on the machine and leads to more frequent failures.

A.1.2 Intermediate Storage Capacitor

The intermediate storage capacitor (ISC) is composed of four concentric steel cylinders submerged in a deionized water dielectric. Two of these are connected to the high voltage output of the Marx bank while the remaining two are held at ground potential. Starting from the center and moving radially outward, the first and third cylinders are at high voltage while the second and fourth are connected to ground. The total capacitance of the geometry is 80 nF which is less than the series capacitance of the Marx bank. The lower capacitance requires less charging time and contributes to the time compression of the pulse. The surfaces of the cylinders are perforated to prevent air bubbles from becoming trapped and encouraging breakdown in the ISC.

The ISC serves as the first stage of pulse compression for the charge stored in the Marx bank. The Marx bank discharges its capacitors into the ISC over a

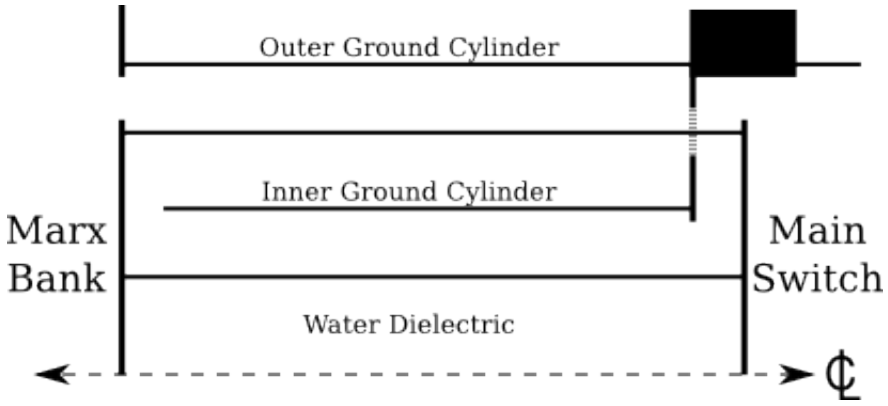

Figure A.2: The intermediate storage capacitor is built from four concentric cylinders and uses deionized water as the dielectric. Perforations in the cylinders (not shown) allow bubbles to rise to the surface.

time period of 700 ns. The output of the ISC is connected to the main switch which presents an open circuit during this time. Slightly before the ISC reaches full charge, the voltage becomes sufficiently high to break down the main switch SF_6 dielectric and cause it to conduct. The charge flows through the main switch and into the pulse forming line (PFL) on a 100 ns time scale.

A.1.3 Main Switch

The main switch is positioned between the intermediate storage capacitor and the pulse forming line. Two opposing hemispherical electrodes are enclosed in a plastic housing and separated by a gap. The cavity formed around the electrodes is filled with SF_6 gas that is fed to the switch along the axis of the ISC. Aluminum plates seal the ends of the switch and make the connections to the ISC and pulse forming line.

In contrast to the switches found in the Marx bank, the main switch is not triggered. Instead, closing of the switch is accomplished by the breakdown of

the SF_6 fill gas due to the high voltage on the ISC. The voltage at which the breakdown occurs is controlled by the gas pressure in the switch according the dielectric breakdown curve for SF_6 [66]. Increasing this pressure results in a higher gas breakdown voltage.

The gas fill pressure is chosen to determine the charging limit of the ISC. It is not set to break down at the peak output voltage of the Marx bank. Instead, the pressure is set to allow the switch to break down slightly before the peak voltage is reached. This ensures that the switch will close given the statistical uncertainty of the breakdown voltage or if some charge is lost in the Marx bank or ISC. If the switch does not close, power will be reflected back into the Marx bank where it could cause damage. The typical operating pressure is 9 psig.

Conduction of current causes energy to be deposited inside the switch cavity. This energy can cause material to be ablated from the surface of the electrodes, the SF_6 to dissociate, and other chemical compounds to form. The resulting collection of unwanted material is colloquially referred to as 'switch dust'. While gaseous matter can be removed by periodically evacuating and refilling the switch cavity with clean SF_6, solid particles can collect along the inner walls of the switch. This eventually leads to the formation of an alternate current path along the switch's housing that cannot be controlled by gas pressure. This presents itself as an inability to control ISC charging time by adjusting gas pressure since the gas is no longer the primary conducting medium of the switch. Removal and cleaning of the switch housing is then required.

A.1.4 Pulse Forming Line

The pulse forming line (PFL) is connected to the main switch opposite the ISC. The construction of the PFL imitates that of the ISC but it is composed of three concentric steel cylinders. The inner- and outer- most cylinders are held at ground potential while the middle cylinder is connected to the main switch. Deionized water is used as the dielectric in the PFL as in the ISC. The capacitance of the PFL is lower than that of the ISC. This is due to a reduced number of concentric cylinders and a reduction in length, although a portion of this is compensated by a smaller spacing between the cylinders. As a result, the charging time of the PFL is shorter than that of the ISC and the current pulse is further compressed.

A.1.5 Water Gap Switches

At the end of the pulse forming line, eight water gap switches are arranged around the circumference of the high voltage cylinder. Normally, each switch consists of a pair of stainless steel electrodes with a 1 to 2cm gap between them. The space is filled with the same deionized water that serves as the dielectric for the ISC and PFL lines. These switches are not triggered and operate by self break in a manner similar to the main switch. Switching is intended to occur simultaneously to lower the overall inductance of the switch. The switching of the PFL into the load also provides a final stage of pulse compression. The potential required for breakdown is adjusted by changing the length of the gap between a switch's electrodes. Larger gaps require larger breakdown voltages.

The spacing of the water gap switches may be used to affect the rise time of the final current pulse delivered to the load. With a small gap, the voltage and

time required to form a current channel in the water can become negligible. Under these circumstances, the derivative of the load current closely follows the voltage of the PFL. This is equivalent to bridging the high voltage of the PFL to ground with an inductive load. As a result, little pulse compression takes place due to the water switches and the rise time can exceed 100 ns. This mode of operation is used in the present work.

A.2 Machine Diagnostics

Diagnosis of machine performance is primarily evaluated by three monitors. Voltage monitors on the ISC and PFL provide information about compression and timing of the pulse as it moves through the machine. Near the experimental load, a $\dot{\mathrm{B}}$ probe detects the flow of current. Together, these three sensors allow machine health to be evaluated on a shot-to-shot basis.

A.2.1 Voltage Monitors

Voltage monitors are installed in the intermediate storage capacitor and the pulse forming line. Each is located approximately half way down the respective machine segment and is submerged in the same deionized water used as the dielectric for the ISC and PFL. A schematic diagram of a voltage monitor is shown in Figure A.3. The geometry of the monitor forms a capacitive voltage divider which is followed by a resistive divider. These work together to attenuate the high voltage to a safe level that can be easily transported by cable to a digitizing oscilloscope and recorded.

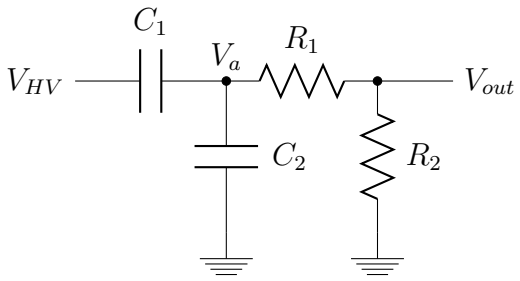

Figure A.3: A capacitive voltage divider, followed by a resistive divider, is used to measure the high voltages on the ISC and the PFL.

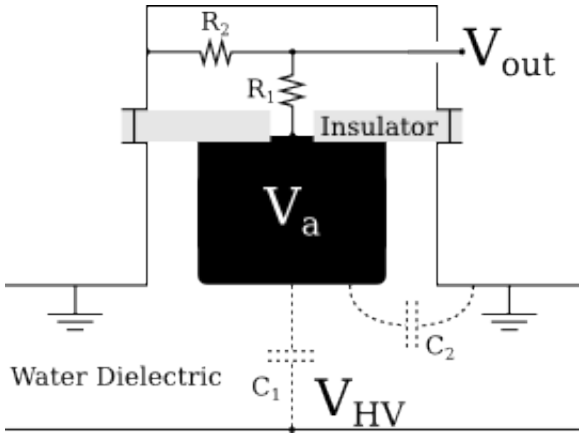

Figure A.4: A voltage monitor is built into the wall of the outer ground plane. Capacitors C_1 and C_2 are formed by the geometry of the monitor using deionized water as a dielectric.

The outer cylinder of both the ISC and PFL are held at ground potential while the next layer in the design works at high voltage. The voltage monitor is used to detect a fraction of the high voltage capacitively. A solid isolated electrode is inserted flush with the outer ground plane. This geometry forms the capacitors C_1 and C_2 of Figure A.4. An additional resistive divider is potted in epoxy behind the electrode to further attenuate the signal. The design can be seen in Figure A.4. The transfer function, with $s = i\omega$, is given by

$$\frac{V_{out}}{V_{HV}} = \frac{sR_2C_1}{s(R_1 + R_2)(C_1 + C_2) + 1} \tag{A.1}$$

Typical voltage monitor signals are presented in Figure A.5. The charge on

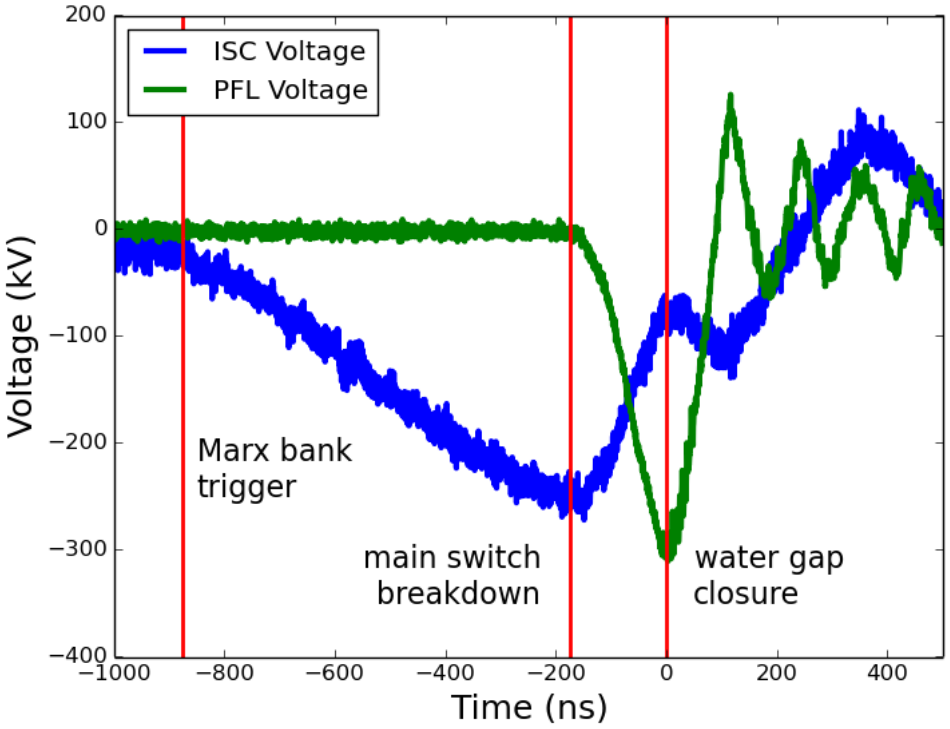

Figure A.5: The ISC (blue) and PFL (green) voltage traces are shown. The rise time of the PFL voltage pulse has been decreased due to pulse compression by the main switch.

the ISC begins to rise as the Marx bank is discharged. This occurs approximately 900 ns before the time $t = 0$, which is defined as the time current begins to flow through the load. After charging for 700 ns, the voltage on the ISC is sufficiently high that the SF_6 gas in the main switch breaks down and begins to conduct charge into the PFL. At this point, the voltage on the ISC begins to fall. With the PFL now connected, the characteristic charging time of this element is significantly shorter than the ISC, which is seen in the rise time of the PFL voltage monitor signal. If the water switches are not shorted as the PFL reaches full charge, the water gap switches break down and begin to conduct current into the experimental load.

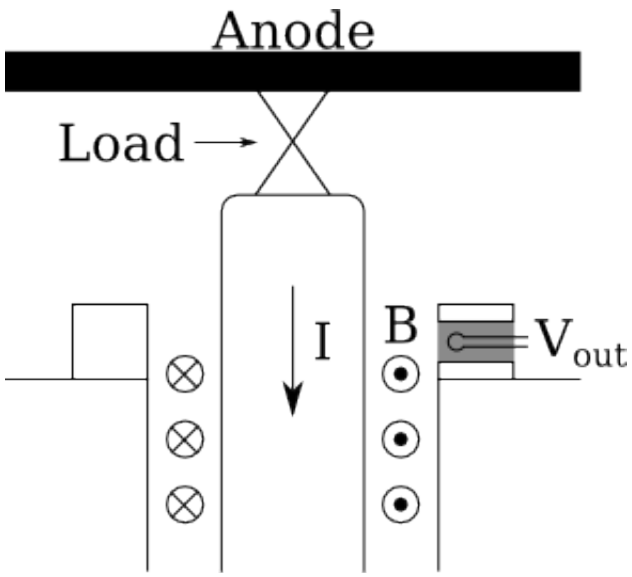

Figure A.6: A loop of wire monitors the current pulse by generating a voltage from the changing magnetic field in the power feed.

A.2.2 Current Monitor

The current pulse is monitored in the power feed immediately preceding the experimental load. This is done by mounting a loop of wire inside the coaxial power feed which is electrically isolated from rest of the machine. This isolation is necessary to prevent any direct pick up of the main machine current. The loop of wire responds by generating a voltage signal proportional to the changing magnetic flux ($\dot{\mathrm{B}}$) in the power feed. This voltage is recorded, scaled, and integrated to reveal the experimental current waveform.

The output signal of the $\dot{\mathrm{B}}$ probe is dependent on position relative to the machine current. To prevent shot-to-shot variation, the probe is potted with epoxy into an aluminum ring that sits around the current feed. This maintains the probe's position and provides electrical isolation as shown in Figure A.6. The output voltage of this probe is determined by combining Ampère's and Faraday's Laws

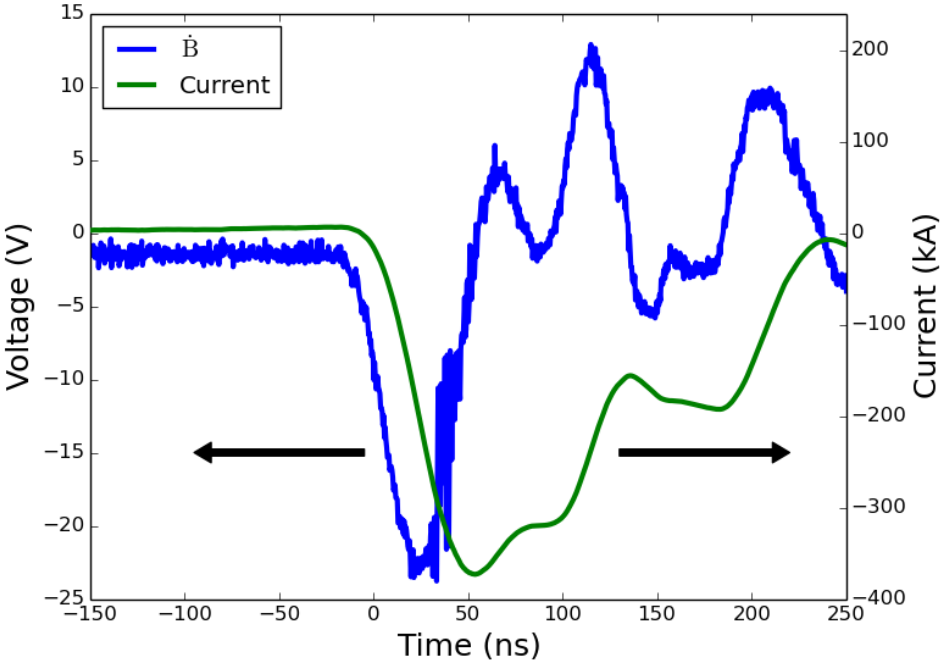

Figure A.7: A plot of the $\dot{B}$ voltage signal (blue) and the resulting current waveform (green).

in equations (A.2) - (A.4) where the surface integral is over the area of the probe. The voltage signal can then be integrated as shown in equation (A.5) to produce a waveform that is proportional to the current. The proportionality constant, C, is determined by calibrating the $\dot{B}$ probe using an independent current pulser.

$$B = \frac{\mu_0 I}{2\pi r} \tag{A.2}$$

$$\phi = \int B \cdot \mathrm{d}A = I \int \frac{\mu_0}{2\pi r}\, \mathrm{d}A \tag{A.3}$$

$$V = -\frac{\mathrm{d}\phi}{\mathrm{d}t} = \frac{1}{C}\,\frac{\mathrm{d}I}{\mathrm{d}t} \tag{A.4}$$

$$I(t) = C \int V(\tau)\, \mathrm{d}\tau \tag{A.5}$$

Calibration

As just stated, the proportionality constant, C, in equation (A.5) is found by measuring the current on an independent current pulser. The pulser's current is simultaneously measured by a calibrated integrating Rogowski coil. The current used for calibration is of the order of 18 kA with a rise time of approximately 300 ns. Since the constant, C, is only a function of geometric properties, it is not affected by the magnitude or rise time of the current pulse. An arrangement similar to that in Figure A.6 is used with the load replaced by a solid aluminum rod. The signal from the $\dot{B}$ loop is integrated and compared with that of the integrating Rogowski coil. The scaling constant is calculated as the ratio of the two signal peaks. This constant is then used to compute the current from signals acquired during an experiment.

APPENDIX B

EXPERIMENTS AND DATA

B.1 Shot Log

All of the shots performed during the course of the present work are listed in Table B.1. Shots with missing data were not analyzed due to poor pinch performance. The configuration refers to the arrangement of wires in the hybrid pinch. A value of NxM indicates that N wires were loaded into the pinch each with a diameter of M µm. The gap refers to the space left between the two cones of the hybrid pinch. The values t_{start} and t_x record the times of current start and X-ray burst respectively.

Shot #	Source	Configuration	Gap (mm)	t_{start} (ns)	t_x (ns)	SNR
7356	Mo	3x40	2			
7357	Mo	3x40	2	-30	91.1	2.78
7358	Mo	3x40	2			
7359	Mo	2x40	1.75			
7360	Mo	2x40	1.75	-30	83.4	3.16
7361	Mo	2x40	1.75	-30	86.8	15.37
7362	Mo	3x40	2	-30	114.3	15.05
7363	Mo	3x40	2	-25	103.2	10.45
7364	Mo	1x40	1.5	-30	105.4	18.84
7365	Mo	1x40	2			
7366	Mo	1x40	1.75			
7367	Mo	1x40	1.25			
7368	Mo	1x40	1			
7369	Mo	1x40	1			
7370	Mo	1x40	1	-30	112.0	14.05
7371	Mo	1x40	1	-15	84.9	7.79
7372	Mo	1x40	1			
7373	Mo	1x25	1	-20	48.9	6.07
7374	Mo	1x25	0.75			
7375	Mo	1x30	1			
7376	Mo	1x30	1			
7377	Mo	1x40	1.5	-30	57.7	4.92
7444	Mo	1x40	1.5	-30	70.4	4.69
7445	Mo	1x40	1.5			13.27
7446	Mo	1x40	1.5	-30	63.6	8.43
7447	Mo	1x40	1.5	-30	84.8	9.91
7448	Mo	1x40	1.5	-20	89.0	13.93
7449	Mo	1x40	1.5	-15	62.8	3.63
7450	Mo	1x40	1.5	-30	92.3	8.95
7451	Mo	1x40	1.5			
7452	Mo	1x40	1.5	-30	65.4	8.56
7453	Mo	1x40	1.5	-20	101.5	10.07
7454	Mo	1x40	1.5	-20	59.5	6.83
7455	Mo	1x40	1.5	-15	80.2	9.70
7456	Mo	1x40	1.5			15.75
7457	Mo	1x40	1.5	-30	102.2	10.64
7458	Mo	1x40	1.5	-15	91.9	8.65
7459	Mo	1x40	1.5			

Table B.1: This is a complete list of experimental shots performed for the present work. Shots with missing data were not analyzed due to poor pinch performance.

B.2 Absorption Spectra

The catalog of collected absorption spectra appears here. These images have been rotated so that the image of the exploding wire is horizontal. A translation has been applied to most of the images to align the position of the K-edge generated by the cold aluminum filter seen above the wire.

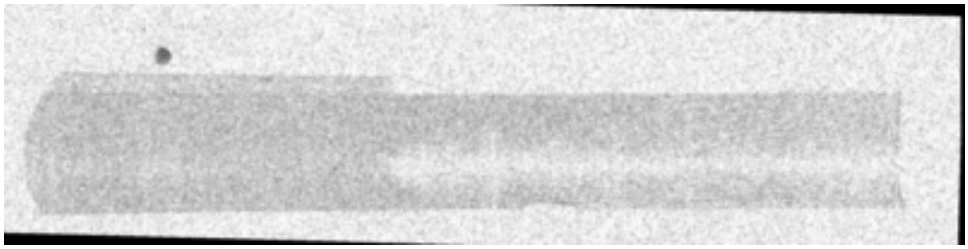

Figure B.1: Shot #7357 spectrum

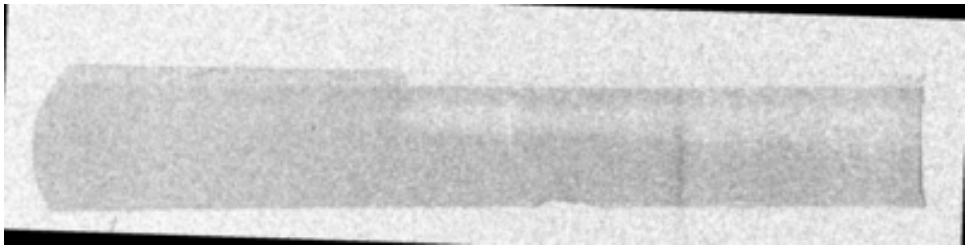

Figure B.2: Shot #7360 spectrum

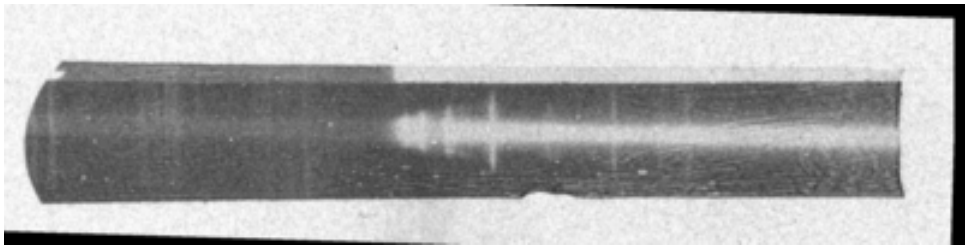

Figure B.3: Shot #7361 spectrum

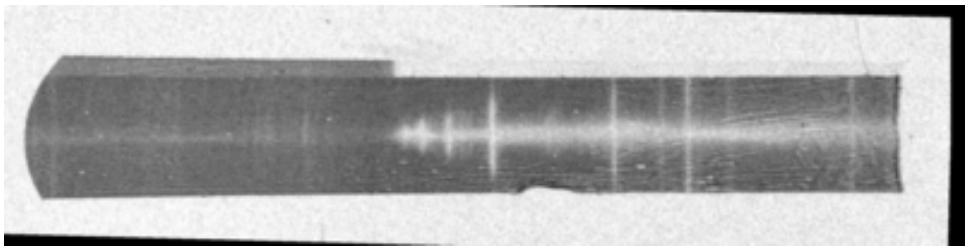

Figure B.4: Shot #7362 spectrum

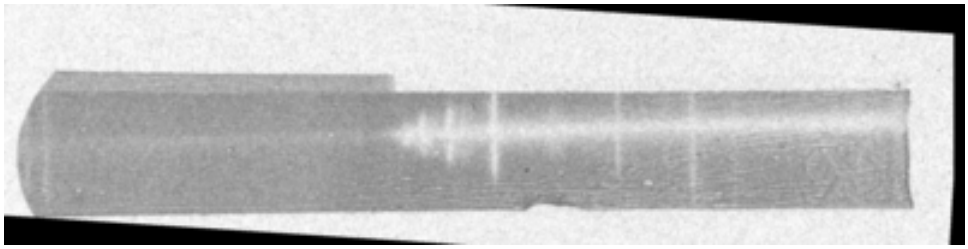

Figure B.5: Shot #7363 spectrum

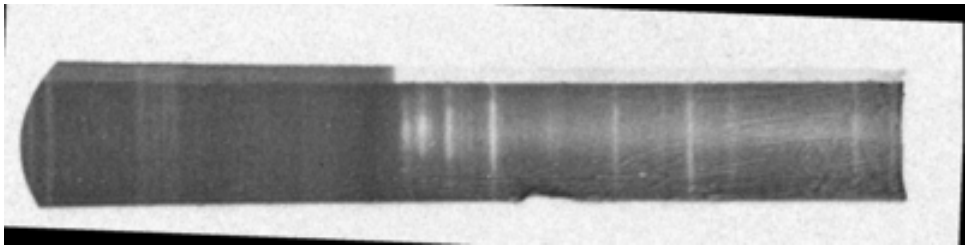

Figure B.6: Shot #7364 spectrum

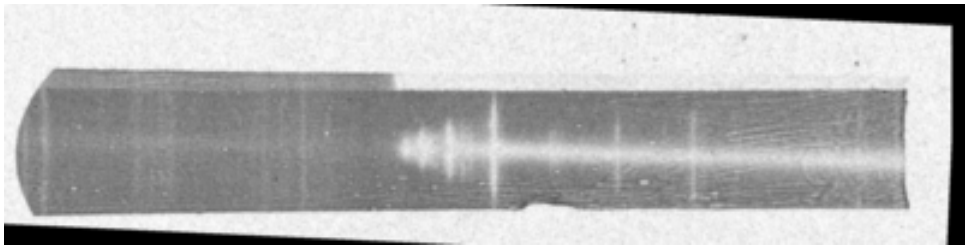

Figure B.7: Shot #7370 spectrum

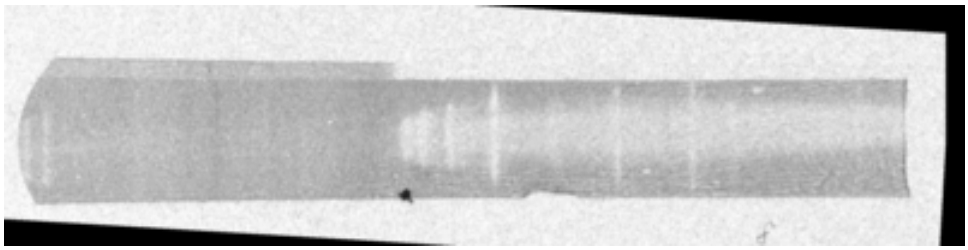

Figure B.8: Shot #7371 spectrum

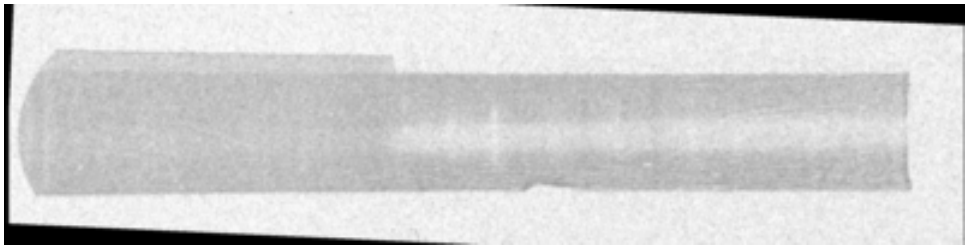

Figure B.9: Shot #7373 spectrum

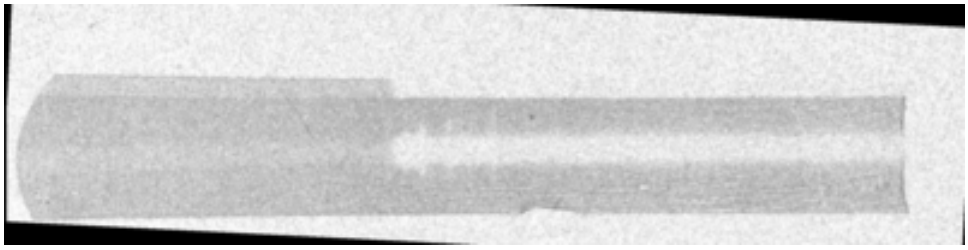

Figure B.10: Shot #7377 spectrum

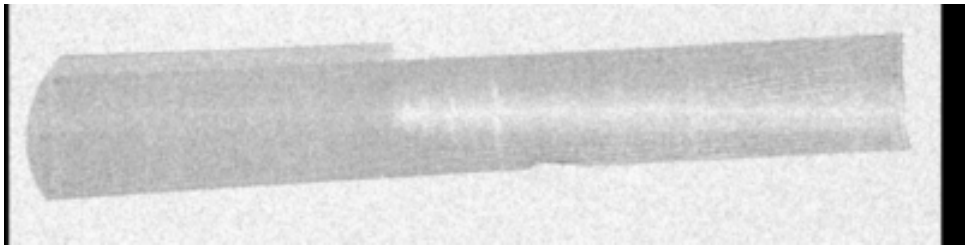

Figure B.11: Shot #7444 spectrum

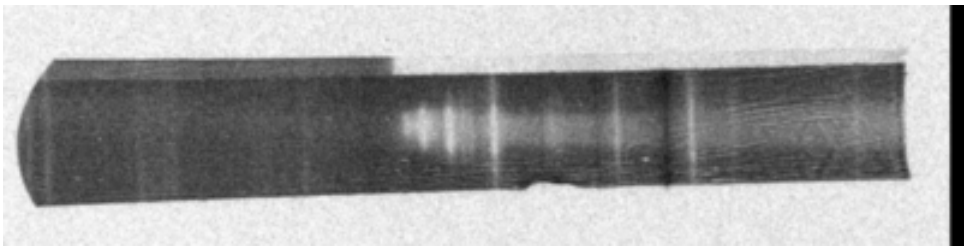

Figure B.12: Shot #7445 spectrum

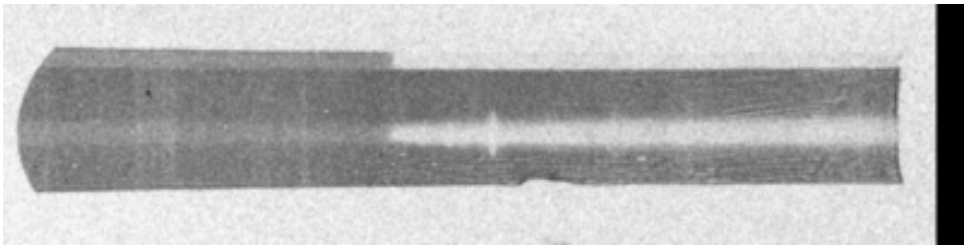

Figure B.13: Shot #7446 spectrum

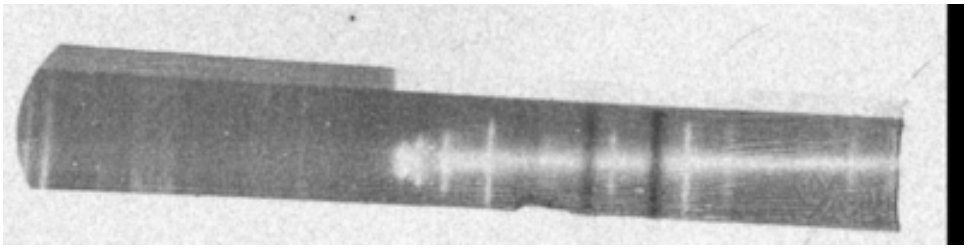

Figure B.14: Shot #7447 spectrum

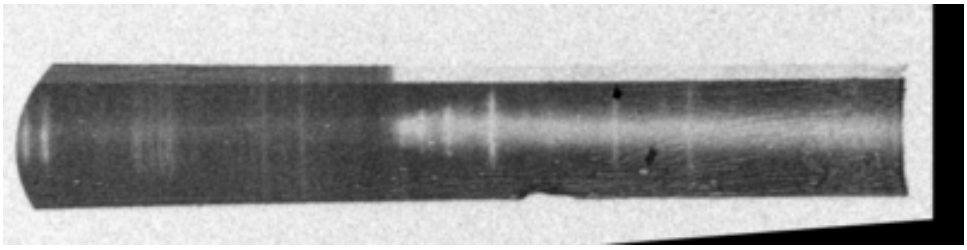

Figure B.15: Shot #7448 spectrum

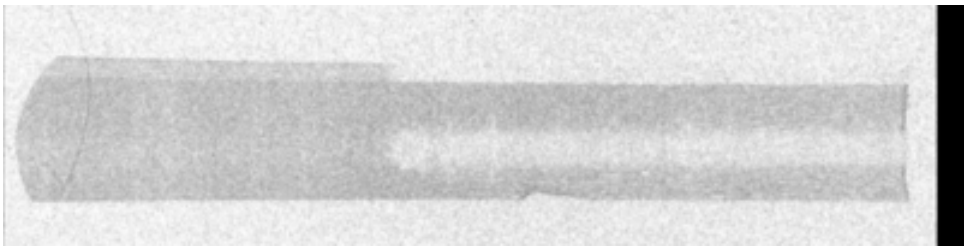

Figure B.16: Shot #7449 spectrum

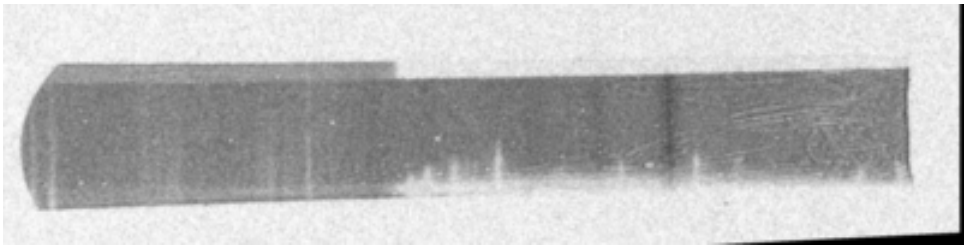

Figure B.17: Shot #7450 spectrum

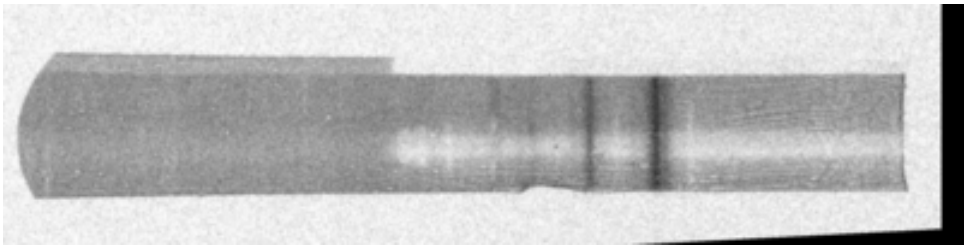

Figure B.18: Shot #7452 spectrum

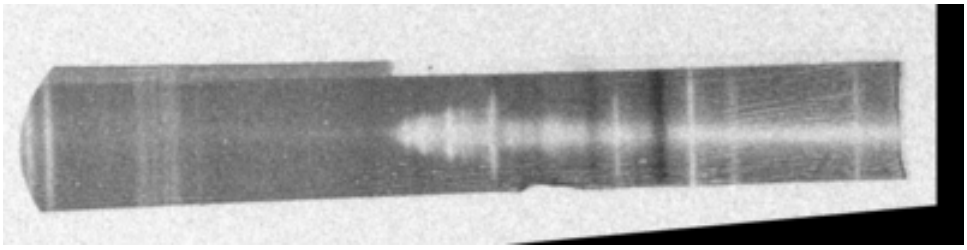

Figure B.19: Shot #7453 spectrum

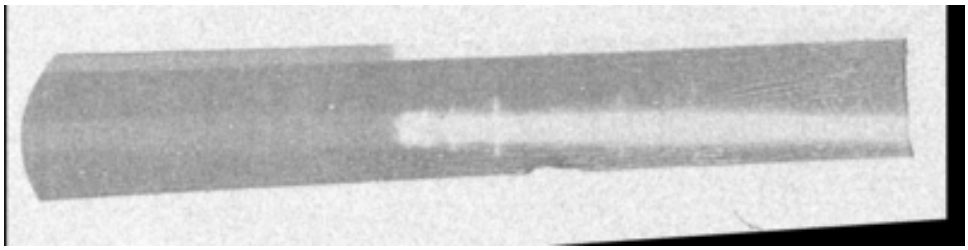

Figure B.20: Shot #7454 spectrum

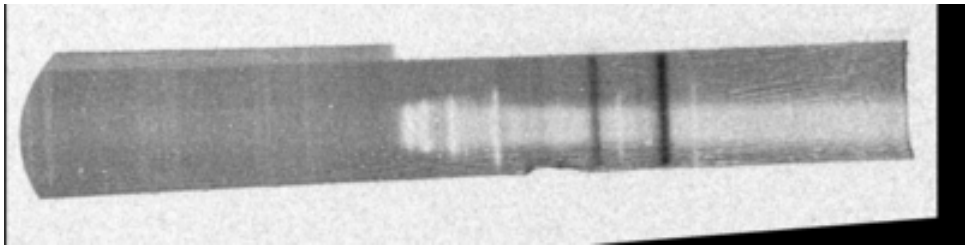

Figure B.21: Shot #7455 spectrum

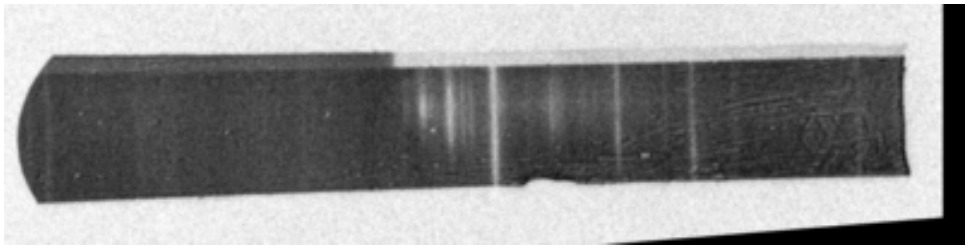

Figure B.22: Shot #7456 spectrum

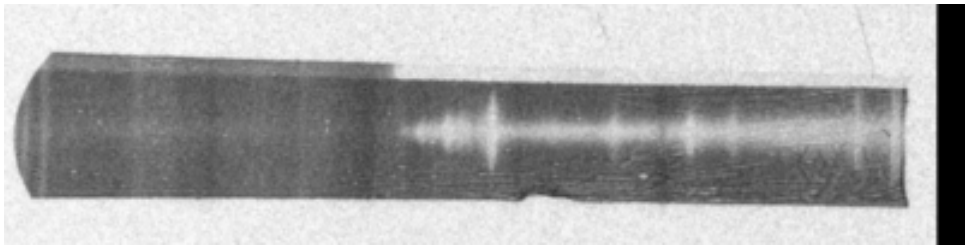

Figure B.23: Shot #7457 spectrum

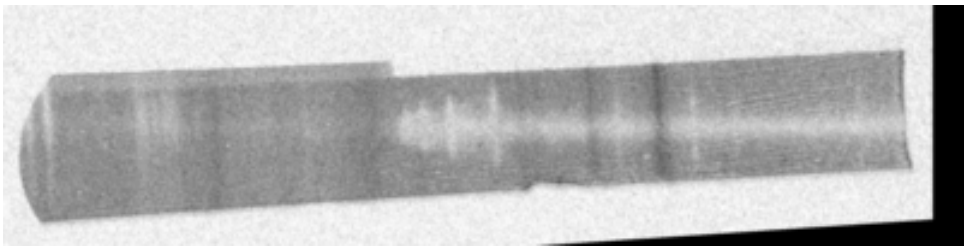

Figure B.24: Shot #7458 spectrum

B.3 Grayscale Mappings

Table B.2 lists the parameters defining the functions used to translate grayscale values to X-ray transmission.

$$T(x) = ae^{-bx} + c \tag{B.1}$$

Shot #	a	b	c
7357	169	9.37×10^{-5}	-0.57854
7360	28.24883	4.2×10^{-6}	-21.98186
7361	2.91645	3.05×10^{-5}	-0.47985
7362	4.02186	4.56×10^{-5}	-0.25685
7363	6.00098	2.48×10^{-5}	-1.30449
7364	3.56869	5.43×10^{-5}	-0.12421
7370	5.50867	4.35×10^{-5}	-0.12421
7371	9.09996	2.95×10^{-5}	-1.49318
7373	14.12502	2.94×10^{-5}	-2.27854
7377	-5.32563	-8.93×10^{-5}	9.19747
7444	247.24374	3.04×10^{-7}	-242.64627
7446	4.38012	3.09×10^{-5}	-0.72489
7447	3.69036	3.52×10^{-5}	-0.46009
7448	2.355	4.02×10^{-5}	-0.22117
7449	109.88125	8.34×10^{-7}	-104.4177
7450	5.08985	3.70×10^{-5}	-0.54506
7452	5.358	2.02×10^{-5}	-1.54247
7453	4.15226	3.96×10^{-5}	-0.38634
7454	6.54042	1.93×10^{-5}	-2.01478
7455	4.81106	3.48×10^{-5}	-0.56618
7457	3.12818	3.45×10^{-5}	-0.39761
7458	5.20211	2.91×10^{-5}	-0.86586

Table B.2: This table lists the parameters used to define the transfer function between grayscale and X-ray transmission values.

B.4 Genetic Algorithm Results

The results from the genetic algorithm are presented here in both a graphical and numerical format. The results of the GA are occasionally adjusted manually to correct solutions that are found to be incorrect by visual comparison with the experimental data. This is most often necessary near the center of the wire core. This is indicated by an asterisk following the radial position in the numerical results. In the graphical data, the spectrum (top left) is analyzed at seven different radial

positions. Comparisons are made to synthetic spectra (right) and the resultant radial density (blue) and temperature (red) profiles are show in the bottom left.

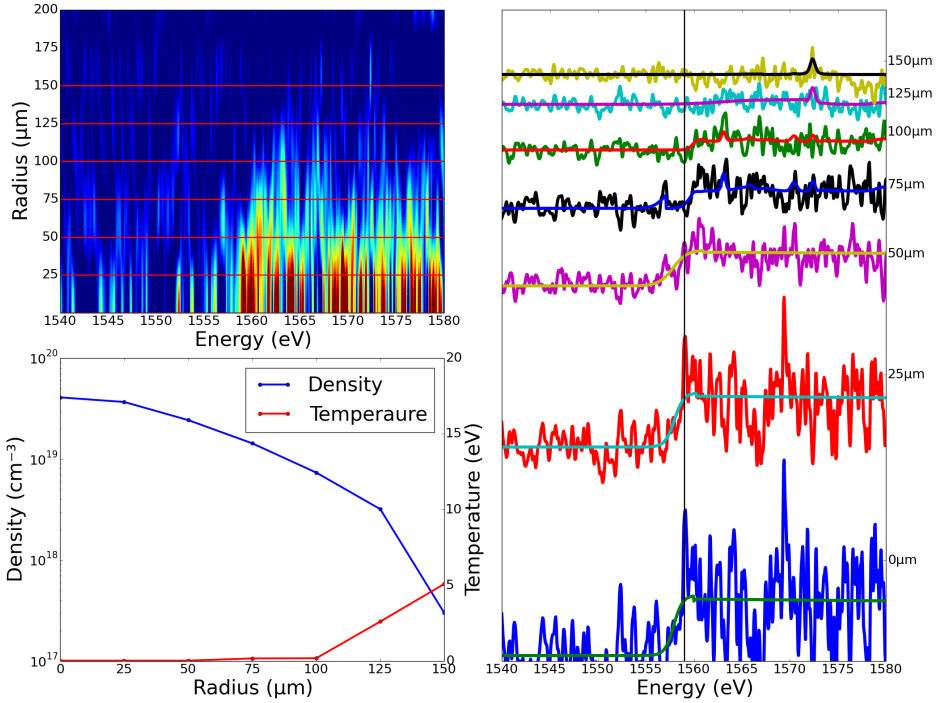

Figure B.25: Shot #7357 graphical comparison

	SCRAM		K-Edge	
Radius (μm)	ρ (cm^{-3})	T (eV)	E_f (eV)	T_f (eV)
0	4.1×10^{19} ±5.2%	0.025±35%	1557.89±0.02%	0.46±43%
25	3.7×10^{19} ±4.9%	0.025±40%	1557.96±0.03%	0.49±79%
50	2.4×10^{19} ±3%	0.025±37%	1557.82±0.02%	0.73±29%
75	1.4×10^{19} ±3.9%	0.17±33%	1556.83±0.07%	0.57±104%
100	7.3×10^{18} ±5.5%	0.18±33%	1559.85±0.12%	0.25±64%
125	3.2×10^{18} ±32%	2.6± 8%	1562.72±0.13%	1.81±29%
150	3.0×10^{17} ±6.8%	5.1±16%	1564.43±0.20%	0.54±105%

Table B.3: Shot #7357 numerical data

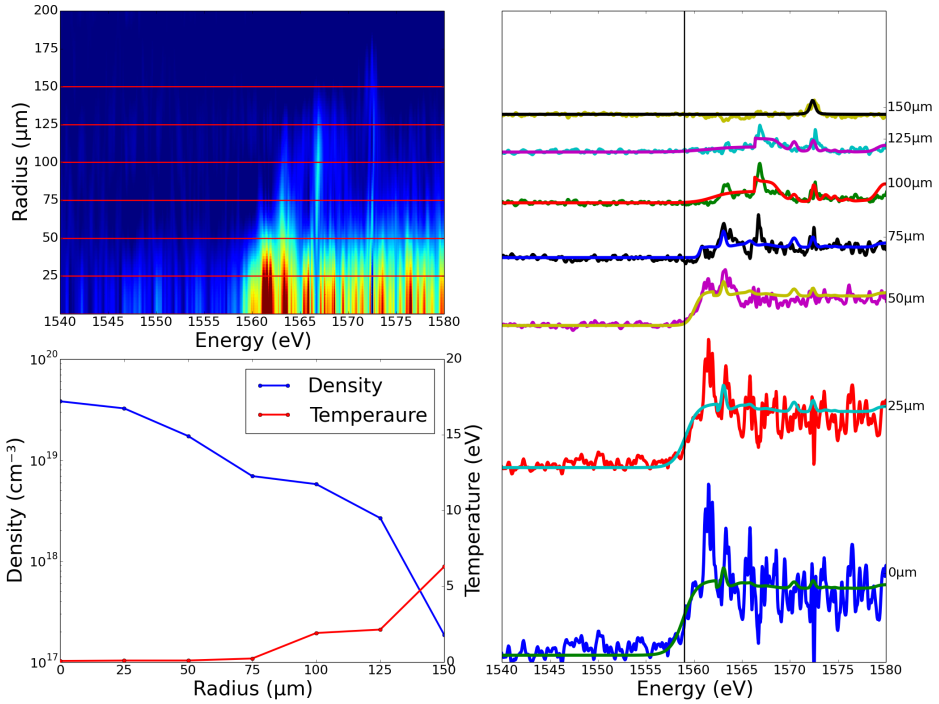

Figure B.26: Shot #7363 graphical comparison

	SCRAM		K-Edge	
Radius (µm)	ρ (cm^{-3})	T (eV)	E_f (eV)	T_f (eV)
0	3.8×10^{19} ±2.1%	0.071±28%	1558.91±0.02%	0.68±30%
25	3.3×10^{19} ±1.9%	0.097±25%	1559.14±0.02%	0.66±35%
50	1.7×10^{19} ±3.2%	0.099±37%	1560.06±0.08%	0.39±92%
75	6.9×10^{18} ±5.2%	0.23±24%	1560.62±0.03%	0.14±188%
100	5.8×10^{18} ±14%	1.9± 9%	1562.00±0.08%	0.94±53%
125	2.7×10^{18} ±11%	2.1± 7%	1561.32±0.06%	1.47±19%
150	1.8×10^{17} ±8%	6.3±11%	1557.98±0.09%	0.17±248%

Table B.4: Shot #7363 numerical data

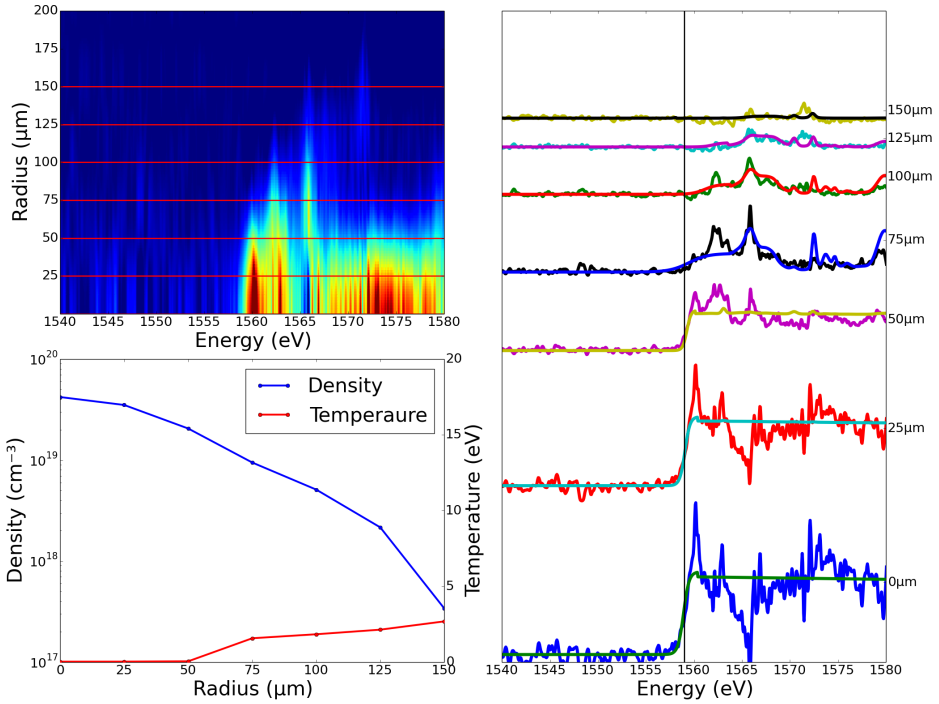

Figure B.27: Shot #7370 graphical comparison

	SCRAM		K-Edge	
Radius (µm)	ρ (cm^{-3})	T (eV)	E_f (eV)	T_f (eV)
0	4.2×10^{19} ±2.4%	0.025±19%	1558.92±0.01%	0.29±32%
25	3.5×10^{19} ±3.2%	0.027±23%	1559.06±0.03%	0.27±82%
50	2.1×10^{19} ±2.2%	0.047±43%	1559.27±0.07%	0.22±99%
75	9.5×10^{18} ±13%	1.6±31%	1559.46±0.05%	1.00±28%
100	5.1×10^{18} ±11%	1.8± 9%	1561.13±0.04%	0.65±37%
125	2.2×10^{18} ±7.4%	2.1± 5%	1562.00±0.13%	0.49±94%
150	3.4×10^{17} ±23%	2.7±10%	1557.85±0.11%	0.08±527%

Table B.5: Shot #7370 numerical data

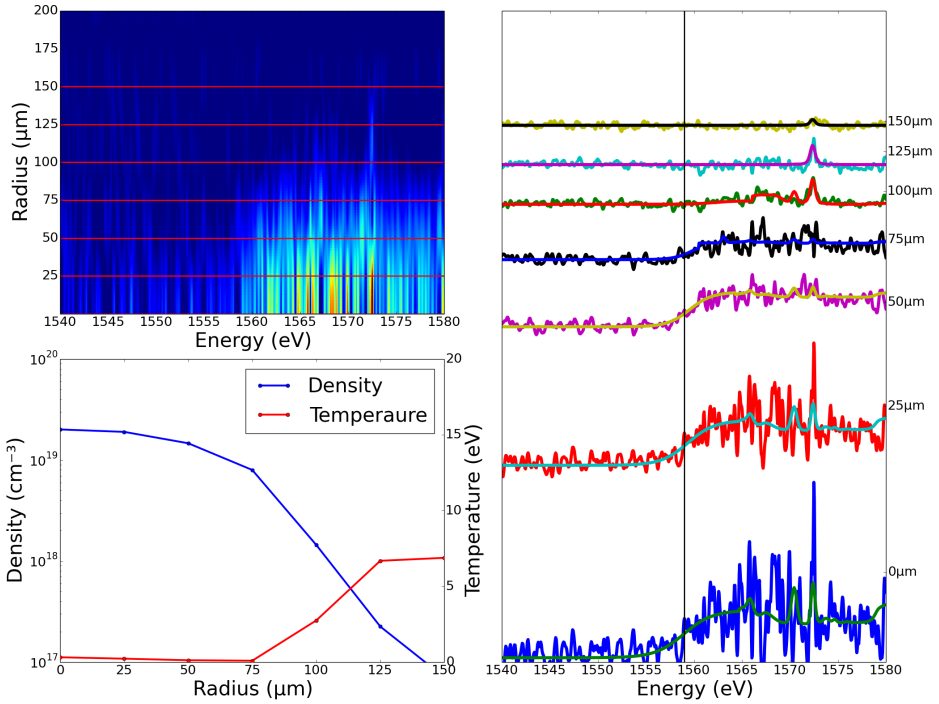

Figure B.28: Shot #7373 graphical comparison

	SCRAM		K-Edge	
Radius (µm)	ρ (cm^{-3})	T (eV)	E_f (eV)	T_f (eV)
0	2.0×10^{19} ±4.4%	0.31±24%	1558.94±0.03%	1.50±11%
25	1.9×10^{19} ±3.1%	0.22±25%	1559.37±0.02%	1.39±10%
50	1.5×10^{19} ±2.1%	0.12±28%	1559.57±0.02%	1.16±21%
75	8.0×10^{18} ±3.4%	0.086±44%	1559.96±0.04%	1.00±38%
100	1.4×10^{18} ±13%	2.7± 4%	1562.00±0.11%	1.11±41%
125	2.2×10^{17} ±13%	6.7±11%	1557.35±0.10%	0.11±210%
150	7.1×10^{16} ±5.9%	6.9± 4%	1559.79±0.07%	0.21±125%

Table B.6: Shot #7373 numerical data

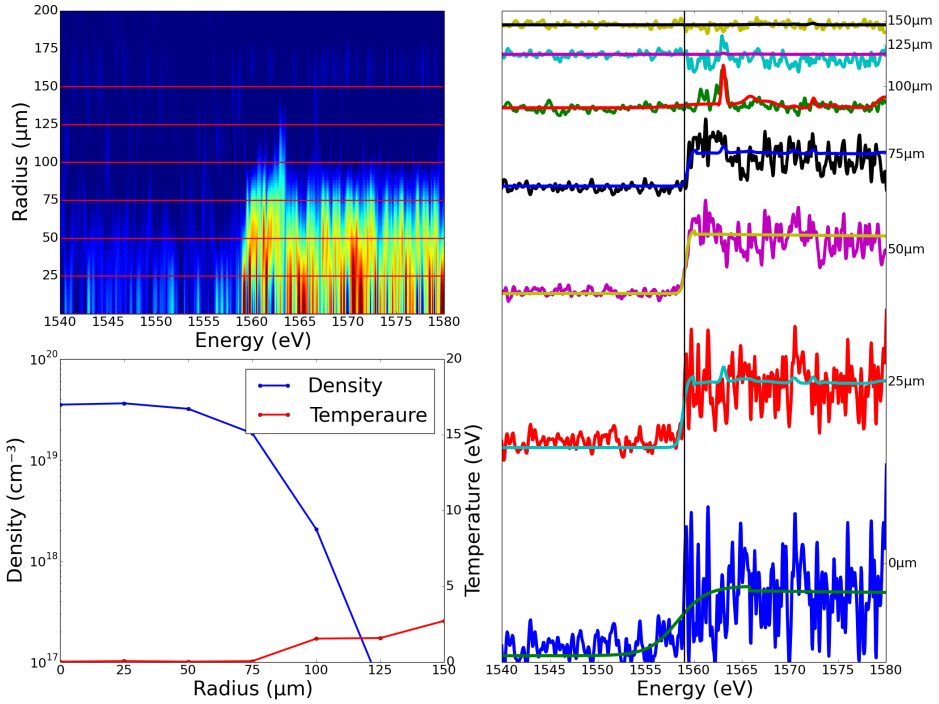

Figure B.29: Shot #7377 graphical comparison

	SCRAM		K-Edge	
Radius (μm)	ρ (cm^{-3})	T (eV)	E_f (eV)	T_f (eV)
0	3.5×10^{19} ±2%	0.025±126%	1558.30±0.02%	1.50±13%
25	3.7×10^{19} ±2.5%	0.063±49%	1558.86±0.02%	0.25±143%
50	3.2×10^{19} ±2.9%	0.025±35%	1559.15±0.04%	0.20±118%
75	1.8×10^{19} ±2.5%	0.059±23%	1559.38±0.06%	0.19±59%
100	2.1×10^{18} ±12%	1.5± 6%	1558.10±0.11%	1.18±33%
125	6.0×10^{16} ±1.7e-14%	1.6± 1%	1556.26±0.07%	0.61±71%
150	9.1×10^{16} ±11%	2.7± 5%	1557.86±0.04%	0.23±143%

Table B.7: Shot #7377 numerical data

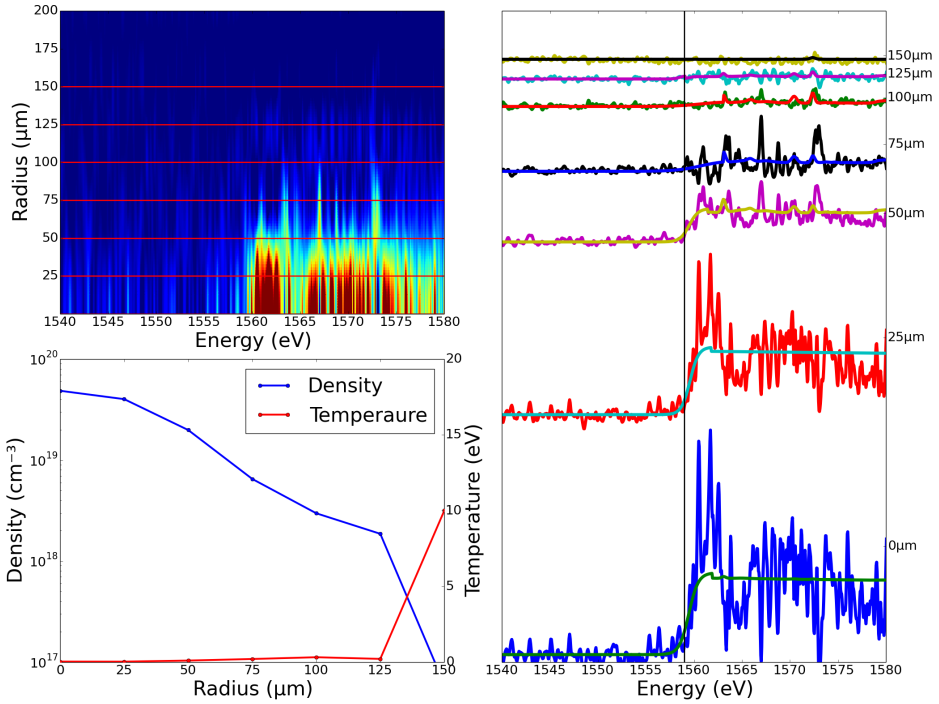

Figure B.30: Shot #7444 graphical comparison

	SCRAM		K-Edge	
Radius (μm)	ρ (cm^{-3})	T (eV)	E_f (eV)	T_f (eV)
0	4.9×10^{19} ±1.8%	0.029±11%	1559.47±0.06%	0.49±46%
25	4.0×10^{19} ±2.2%	0.025±28%	1559.58±0.04%	0.44±62%
50	2.0×10^{19} ±2.2%	0.095±24%	1559.50±0.06%	0.47±71%
75	6.5×10^{18} ±7.1%	0.2±76%	1560.73±0.08%	1.31±31%
100	3.0×10^{18} ±7.3%	0.31±25%	1560.65±0.10%	1.33±25%
125	1.9×10^{18} ±6.2%	0.21±18%	1558.47±0.08%	0.27±152%
150	6.0×10^{16} ±8.2e-14%	10± 0%	1559.79±0.10%	0.14±58%

Table B.8: Shot #7444 numerical data

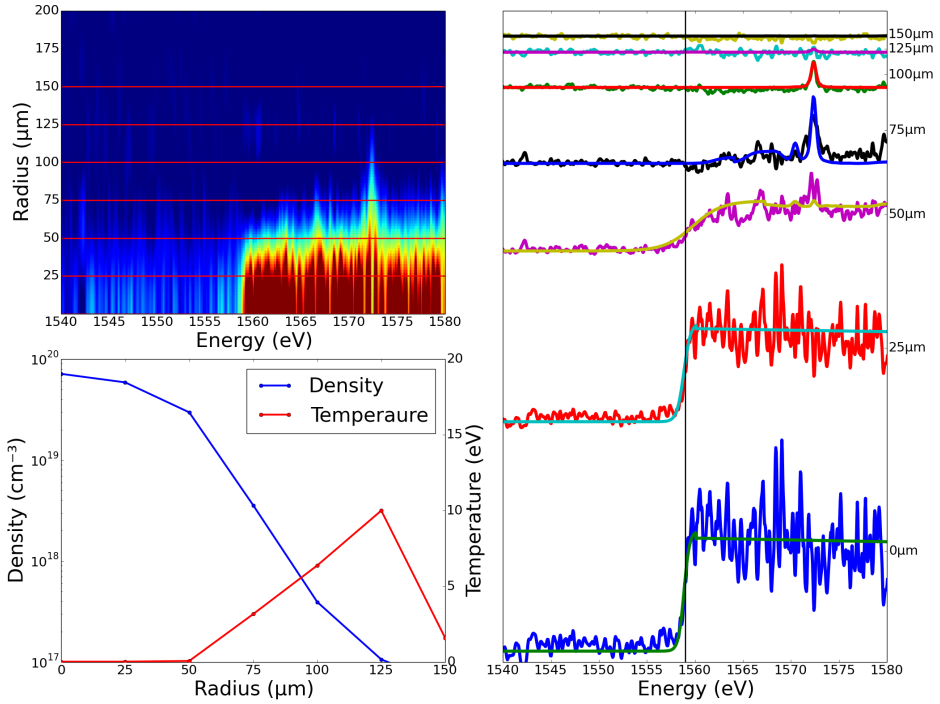

Figure B.31: Shot #7446 graphical comparison

	SCRAM		K-Edge	
Radius (µm)	ρ (cm^{-3})	T (eV)	E_f (eV)	T_f (eV)
0	7.1×10^{19} ±2.3%	0.025±34%	1558.86±0.01%	0.29±54%
25	5.9×10^{19} ±1.8%	0.025±36%	1558.84±0.01%	0.36±42%
50	3.0×10^{19} ±1.8%	0.07±28%	1559.80±0.01%	1.50±13%
75	3.6×10^{18} ±58%	3.2±43%	1562.00±0.14%	0.56±90%
100	3.9×10^{17} ±29%	6.4±20%	1556.87±0.10%	0.02±1682%
125	1.1×10^{17} ±1.9%	10± 5%	1557.85±0.05%	1.25±21%
150	6.0×10^{16} ±0.044%	1.6± 6%	1561.89±0.00%	1.13±45%

Table B.9: Shot #7446 numerical data

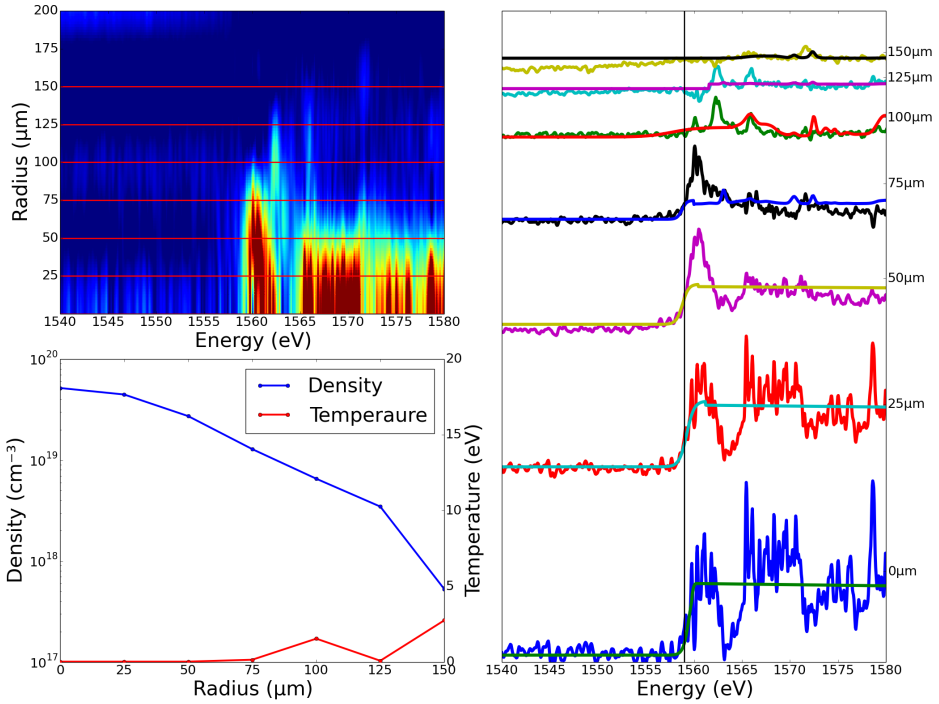

Figure B.32: Shot #7447 graphical comparison

	SCRAM		K-Edge	
Radius (µm)	ρ (cm^{-3})	T (eV)	E_f (eV)	T_f (eV)
0*	5.2×10^{19} ±2.1%	0.025± 6%	1559.50±0.01%	0.30±23%
25	4.5×10^{19} ±2.5%	0.025± 7%	1559.25±0.05%	0.39±58%
50	2.7×10^{19} ±4.2%	0.025±58%	1558.80±0.03%	0.32±82%
75*	1.3×10^{19} ±5.5%	0.15±29%	1558.75±0.04%	0.25±33%
100	6.5×10^{18} ±5.2%	1.5± 9%	1557.69±0.05%	1.31±22%
125	3.5×10^{18} ±14%	0.082±972%	1561.57±0.03%	0.00±inf%
150	5.3×10^{17} ±17%	2.8± 7%	1556.48±0.10%	0.00±inf%

Table B.10: Shot #7447 numerical data

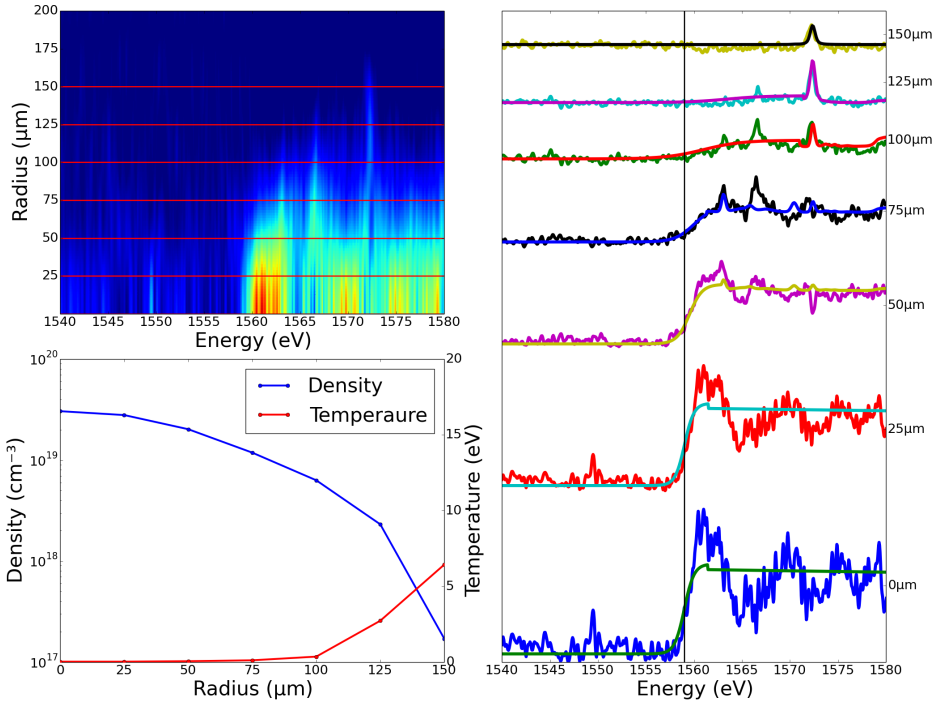

Figure B.33: Shot #7448 graphical comparison

	SCRAM		K-Edge	
Radius (µm)	ρ (cm^{-3})	T (eV)	E_f (eV)	T_f (eV)
0	3.1×10^{19} ±3.3%	0.025±18%	1559.00±0.06%	0.51±72%
25	2.8×10^{19} ±2.6%	0.025±25%	1559.02±0.05%	0.49±60%
50	2.0×10^{19} ±2.3%	0.054±39%	1559.54±0.05%	0.66±50%
75	1.2×10^{19} ±4.3%	0.11±47%	1559.98±0.04%	0.98±42%
100	6.3×10^{18} ±5.4%	0.36±19%	1561.00±0.04%	2.00±17%
125	2.3×10^{18} ±9.6%	2.7± 6%	1563.38±0.18%	2.00±31%
150	1.7×10^{17} ±11%	6.4±11%	1555.19±0.19%	0.14±462%

Table B.11: Shot #7448 numerical data

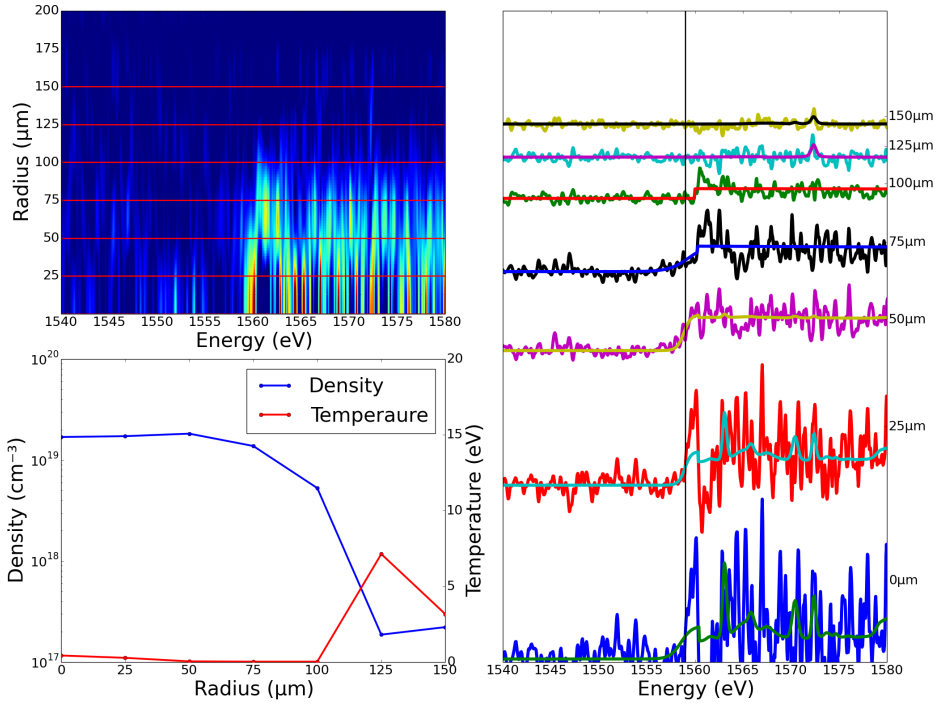

Figure B.34: Shot #7449 graphical comparison

	SCRAM		K-Edge	
Radius (µm)	ρ (cm^{-3})	T (eV)	E_f (eV)	T_f (eV)
0	1.7×10^{19} ±8.9%	0.43±21%	1558.54±0.11%	0.58±64%
25	1.7×10^{19} ±5%	0.27±24%	1558.95±0.06%	0.33±130%
50	1.8×10^{19} ±2.5%	0.042±50%	1558.85±0.01%	0.37±61%
75	1.4×10^{19} ±2.8%	0.025±32%	1559.31±0.06%	1.02±37%
100	5.3×10^{18} ±4.8%	0.025±154%	1559.99±0.04%	0.00±inf%
125	1.9×10^{17} ±22%	7.1±19%	1562.00±0.11%	1.04±54%
150	2.2×10^{17} ±6.2%	3.2±22%	1558.06±0.06%	0.01±2216%

Table B.12: Shot #7449 numerical data

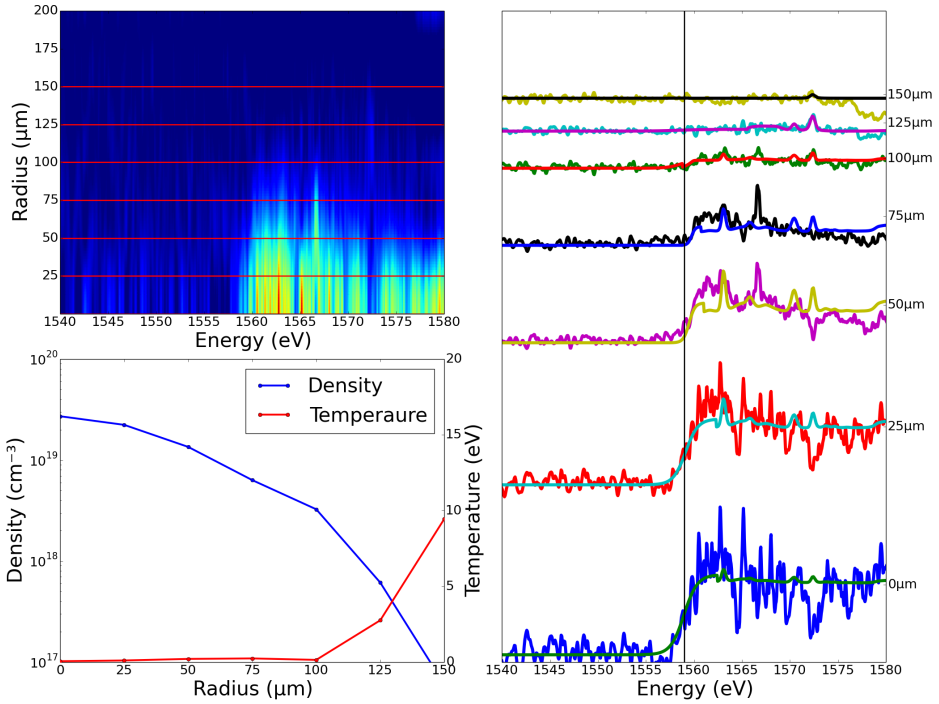

Figure B.35: Shot #7452 graphical comparison

	SCRAM		K-Edge	
Radius (µm)	ρ (cm^{-3})	T (eV)	E_f (eV)	T_f (eV)
0	2.7×10^{19} ±2.4%	0.052±29%	1558.96±0.01%	0.70±21%
25	2.2×10^{19} ±2.2%	0.1±21%	1559.13±0.01%	0.64±22%
50*	1.4×10^{19} ±3.3%	0.2±20%	1559.50±0.02%	0.30±28%
75*	6.3×10^{18} ±4.9%	0.24±23%	1559.75±0.07%	0.20±41%
100	3.3×10^{18} ±5.6%	0.14±37%	1558.80±0.08%	0.75±64%
125	6.1×10^{17} ±18%	2.8±16%	1558.55±0.09%	1.41±32%
150	6.0×10^{16} ±0.2%	9.5± 4%	1557.49±0.05%	0.43±73%

Table B.13: Shot #7452 numerical data

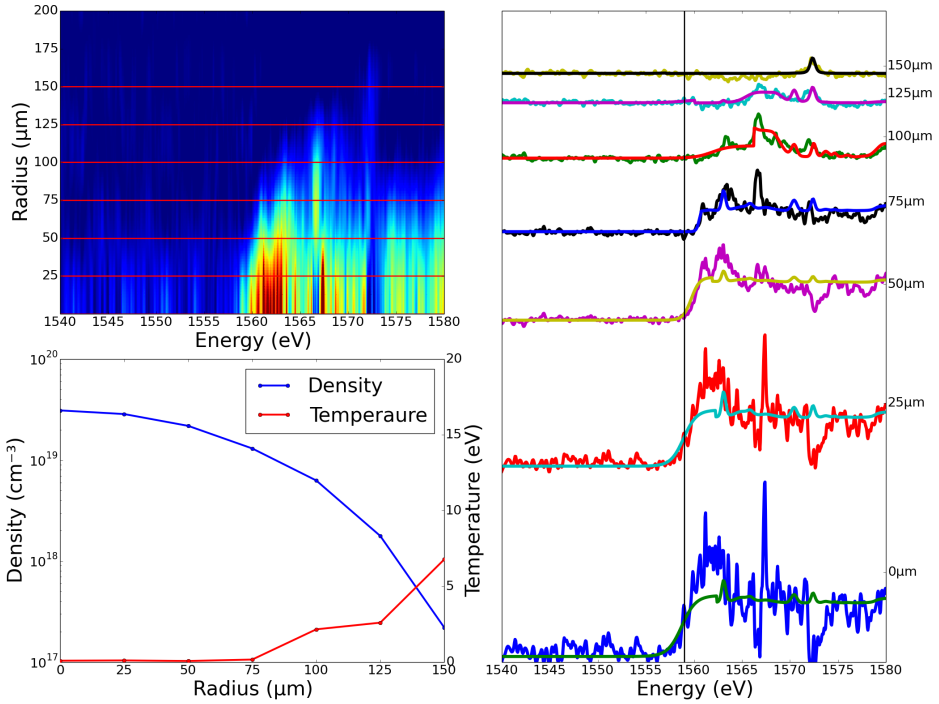

Figure B.36: Shot #7453 graphical comparison

	SCRAM		K-Edge	
Radius (µm)	ρ (cm^{-3})	T (eV)	E_f (eV)	T_f (eV)
0	3.1×10^{19} ±2.3%	0.088±18%	1558.73±0.02%	0.74±41%
25	2.9×10^{19} ±2.3%	0.1±23%	1558.93±0.02%	0.67±39%
50	2.2×10^{19} ±2.6%	0.068±59%	1559.72±0.05%	0.43±61%
75	1.3×10^{19} ±3.5%	0.16±27%	1560.57±0.01%	0.16±129%
100	6.3×10^{18} ±8.4%	2.2± 7%	1561.94±0.03%	0.90±26%
125	1.8×10^{18} ±8.4%	2.6± 2%	1559.08±0.09%	1.12±39%
150	2.2×10^{17} ±29%	6.8±17%	1556.33±0.10%	0.43±98%

Table B.14: Shot #7453 numerical data

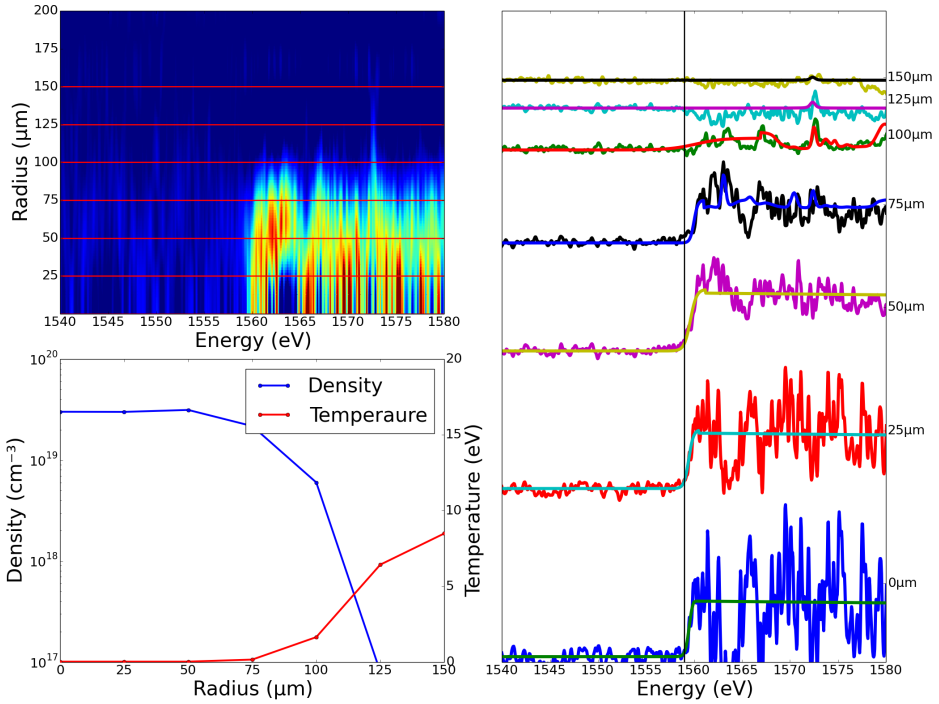

Figure B.37: Shot #7454 graphical comparison

	SCRAM		K-Edge	
Radius (µm)	ρ (cm^{-3})	T (eV)	E_f (eV)	T_f (eV)
0*	3.0×10^{19} ±4.8%	0.025±65%	1559.50±0.10%	0.20±44%
25	3.0×10^{19} ±2.5%	0.025± 5%	1559.46±0.07%	0.24±60%
50	3.1×10^{19} ±2.3%	0.025±48%	1559.63±0.08%	0.32±78%
75*	2.2×10^{19} ±3%	0.16±23%	1560.00±0.04%	0.20±39%
100	6.0×10^{18} ±8.2%	1.6±31%	1560.20±0.05%	1.37±36%
125	8.0×10^{16} ±10%	6.4± 7%	1556.42±0.08%	1.38±24%
150	6.0×10^{16} ±0.35%	8.5± 2%	1558.31±0.04%	0.36±59%

Table B.15: Shot #7454 numerical data

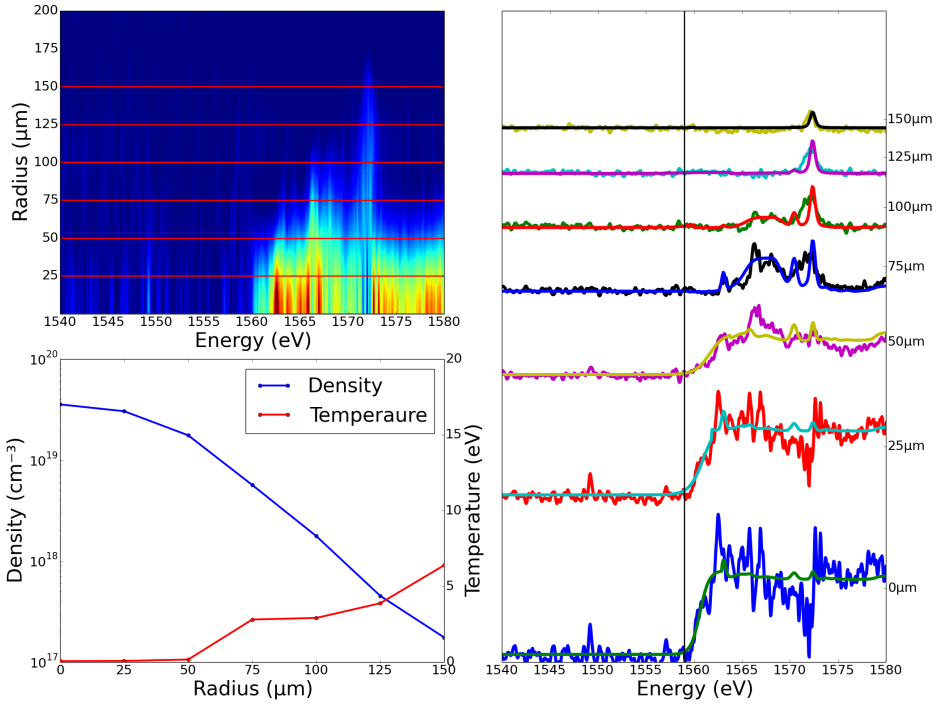

Figure B.38: Shot #7457 graphical comparison

	SCRAM		K-Edge	
Radius (µm)	ρ (cm^{-3})	T (eV)	E_f (eV)	T_f (eV)
0	3.6×10^{19} ±2.2%	0.063±48%	1560.63±0.02%	0.48±37%
25	3.0×10^{19} ±2.7%	0.072±42%	1560.97±0.02%	0.72±22%
50	1.8×10^{19} ±2.7%	0.16±27%	1561.63±0.01%	0.75±31%
75	5.7×10^{18} ±5.7%	2.8± 1%	1559.45±0.10%	0.00±inf%
100	1.8×10^{18} ±8.3%	2.9± 1%	1559.49±0.10%	0.81±43%
125	4.5×10^{17} ±22%	3.9±42%	1558.12±0.08%	1.13±27%
150	1.7×10^{17} ±11%	6.4±15%	1559.56±0.08%	0.11±304%

Table B.16: Shot #7457 numerical data

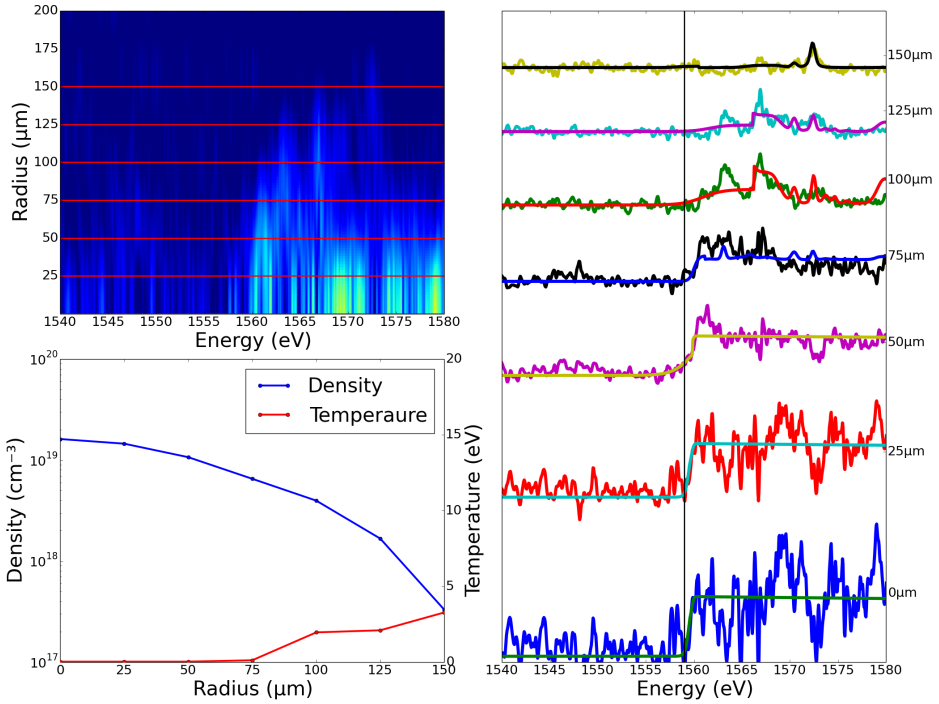

Figure B.39: Shot #7458 graphical comparison

	SCRAM		K-Edge	
Radius (µm)	ρ (cm^{-3})	T (eV)	E_f (eV)	T_f (eV)
0*	1.6×10^{19} ±2.5%	0.025± 7%	1559.50±0.04%	0.20±55%
25*	1.5×10^{19} ±2.4%	0.025±14%	1559.50±0.05%	0.20±55%
50	1.1×10^{19} ±3.2%	0.025±21%	1559.84±0.06%	0.99±36%
75*	6.5×10^{18} ±4.5%	0.12±39%	1560.00±0.06%	0.25±53%
100	4.0×10^{18} ±11%	2± 6%	1560.93±0.05%	1.06±27%
125	1.7×10^{18} ±9.6%	2.1± 3%	1561.59±0.12%	0.91±53%
150	3.3×10^{17} ±18%	3.3±38%	1558.18±0.11%	0.55±80%

Table B.17: Shot #7458 numerical data

APPENDIX C

CODES

The programs used to analyze data and compute results presented in this thesis are provided here. They are written in the Python programming language and were run using Python version 2.7.6. Comments are provided to detail the operation of specific regions of code. These programs are provided as-is and are not guaranteed to be free of errors.

C.1 X-ray Tracer

The X-ray ray tracer is composed of three separate files that work together to build the geometry of a spectroscopic system and compute the intersection of X-rays with planes of interest.

C.1.1 Geometry

The 'Geometry.py' file is responsible for defining all of the geometrical objects needed to describe a spectroscopic system. This includes cylindrical and spherical source geometries that are capable of emitting uniformly over a given bandwidth or as described by an input file. Optical elements include the elliptical and spherical geometries used in this thesis. An extension to include both cylindrical and toroidal optics is trivial. Detectors are modeled as infinitely thin planes with uniform response to all photon energies. Filters are also included. They are defined identically to a detector, but adjust an X-ray's intensity by a transmission value.

The transmission value is determined by the composition of the filter which is a collection of materials layers and their respective thicknesses. A filter may be composed of any number of material layers. Finally, circular, rectangular, and mesh apertures are implemented. Transmission through theses objects is modeled in a binary manner with photons either passing through the aperture unaffected or being completely stopped.

A 'Scene' object is also defined in this file. It serves as a container to hold the source, optic, detector, filters, and apertures that have been defined. This container is passed to the ray tracing engine for calculations.

```
1  class RayTracerObject(object):
2      def __init__(self, g, n, hlim, vlim, seed=0):
3          from numpy import matrix
4          '''
5          The function g(h, v) takes two equally sized 1D arrays 'h' and 'v'
6              and returns a 3xN array of vectors pointing to the surface.
7          The function n(h, v) takes two equally sized 1D arrays 'h' and 'v'
8              and returns a 3xN array of surface normal vectors.
9          The inputs 'hlim' and 'vlim' are each two element lists providing
10             upper and lower bounds for the arguments of 'g' and 'n'.  These
11             are taken to be closed intervals.
12         '''
13         # Store variables used for surface evaluation before any transforms.
14         self.g = g
15         self.n = n
16         self.hlim = hlim
17         self.vlim = vlim
18         self.seed = seed
```

```
19          # Generate an identity transform.
20          self.T = matrix([[1, 0, 0, 0], \
21                           [0, 1, 0, 0], \
22                           [0, 0, 1, 0], \
23                           [0, 0, 0, 1]])
24          self.Tinv = self.T.I

25      def translate(self, vector):

26          from numpy import matrix

27          '''
28          The three values of 'vector' define the object's
    displacement as dx,
29              dy, and dz respectively.
30          '''

31          # Update the object transform matrix with the
    translation vector 'vector'.
32          D = matrix([[1, 0, 0, vector[0]], \
33                      [0, 1, 0, vector[1]], \
34                      [0, 0, 1, vector[2]], \
35                      [0, 0, 0,         1]])

36          # Compute and update the inverse transform matrix.
37          self.T = D * self.T
38          self.Tinv = self.T.I

39      def rotate(self, point, vector, phi):

40          from numpy import cos, matrix, sin, sqrt

41          '''
42          The inputs 'point' and 'vector' are three element
    arrays that describe the
43              rotation axis.
44          The 'phi' input describes the degree of rotation around
     the defined axis
45              according to the right hand rule.
46          '''

47          # Ensure that 'vector' is a unit vector.
48          vector /= sqrt((vector * vector).sum())

49          # Translate the object so that 'point' is moved to the
    origin.
50          self.translate(-1 * point)
```

```
51          # Update the object transform matrix with a rotation of
     'phi' radians around
52          #    the axis defined by 'point' and 'vector'.
53          R = matrix([[0.0, 0.0, 0.0, 0.0], \
54                      [0.0, 0.0, 0.0, 0.0], \
55                      [0.0, 0.0, 0.0, 0.0], \
56                      [0.0, 0.0, 0.0, 1.0]])

57          R[0, 0] = cos(phi) + vector[0] * vector[0] * (1 - cos(
    phi))
58          R[0, 1] = vector[0] * vector[1] * (1 - cos(phi)) -
    vector[2] * sin(phi)
59          R[0, 2] = vector[0] * vector[2] * (1 - cos(phi)) +
    vector[1] * sin(phi)

60          R[1, 0] = vector[1] * vector[0] * (1 - cos(phi)) +
    vector[2] * sin(phi)
61          R[1, 1] = cos(phi) + vector[1] * vector[1] * (1 - cos(
    phi))
62          R[1, 2] = vector[1] * vector[2] * (1 - cos(phi)) -
    vector[0] * sin(phi)

63          R[2, 0] = vector[2] * vector[0] * (1 - cos(phi)) -
    vector[1] * sin(phi)
64          R[2, 1] = vector[2] * vector[1] * (1 - cos(phi)) +
    vector[0] * sin(phi)
65          R[2, 2] = cos(phi) + vector[2] * vector[2] * (1 - cos(
    phi))

66          # Apply the rotation.
67          self.T = R * self.T

68          # Remove the initial translation.
69          self.translate(point)

70          # Update the transformation inverse.
71          self.Tinv = self.T.I

72      def get_random_surface_points(self, npts, exclude=None):

73          from numpy import array, hstack, invert, ones, random,
    vstack, zeros

74          '''
75          Generate arrays of surface points and normals using '
    npts' random (h,v) pairs
```

```
76              in the closed 'hlim' and 'vlim' intervals.
77          The 'exclude' variable is a list of four element tuples
    .  Each tuple specifies
78              an 'hlim' and 'vlim' range in which no points may
    be generated.
79          '''

80          # If an exclusion interval isn't specified, set the
    values so that it doesn't
81          #    affect the rest of the computations.
82          if exclude == None: exclude = [(self.hlim[0], self.hlim
    [0], self.vlim[0], self.vlim[0])]

83          VettedPts = 0

84          random.seed(self.seed)
85          h = self.hlim[0] + random.random_sample(npts) * (self.
    hlim[1] - self.hlim[0])
86          v = self.vlim[0] + random.random_sample(npts) * (self.
    vlim[1] - self.vlim[0])

87          while VettedPts < npts:

88              mask = zeros(npts, dtype='bool')

89              for interval in exclude:

90                  mask += (h > interval[0]) * (h <= interval[1])
    * (v > interval[2]) * (v <= interval[3])

91              h = h[invert(mask)]
92              v = v[invert(mask)]

93              VettedPts = len(h)

94              hnew = self.hlim[0] + random.random_sample(npts -
    VettedPts) * (self.hlim[1] - self.hlim[0])
95              vnew = self.vlim[0] + random.random_sample(npts -
    VettedPts) * (self.vlim[1] - self.vlim[0])

96              h = hstack((h, hnew))
97              v = hstack((v, vnew))

98          # Apply the object transform to the surface points and
    normals.
99          # Translations do not affect normals and so are omitted
     by only using a subset
```

```
100         #    of the transformation matrix 'T'.
101         # Since 'T' is a matrix the result must be cast back to
     an array.
102         points  = array(self.T * vstack([self.g(h, v), ones(
    npts)]))
103         normals = array(self.T[0:3, 0:3] * self.n(h, v))
104 
105         return points[0:3, :], normals[0:3, :]
106 
107     def get_mesh(self, npts, exclude=None):
108 
109         from numpy import array, linspace, meshgrid, nan, ones,
     vstack, where, zeros
110 
111         '''
112         Generate arrays of surface points and normals using '
    npts' uniform (h,v) pairs
113             in the closed 'hlim' and 'vlim' intervals.
114         The 'exclude' variable is a list of four element tuples
    .  Each tuple specifies
115             an 'hlim' and 'vlim' range in which no points may
    be generated.
116         '''
117 
118         if exclude == None: exclude = [(self.hlim[0], self.hlim
    [0], self.vlim[0], self.vlim[0])]
119 
120         h = self.hlim[0] + linspace(0.0, 1.0, npts) * (self.
    hlim[1] - self.hlim[0])
121         v = self.vlim[0] + linspace(0.0, 1.0, npts) * (self.
    vlim[1] - self.vlim[0])
122 
123         H, V = meshgrid(h, v)
124 
125         [X, Y, Z] = self.g(H, V)
126 
127         mask = zeros((npts, npts))
128 
129         for interval in exclude:
130 
131             mask += (H > interval[0]) * (H <= interval[1]) * (V
     > interval[2]) * (V <= interval[3])
132 
133         X = where(mask, nan, X)
134         Y = where(mask, nan, Y)
135         Z = where(mask, nan, Z)
```

```
124         P = vstack([X.reshape(npts * npts), \
125                     Y.reshape(npts * npts), \
126                     Z.reshape(npts * npts), \
127                     ones(npts * npts)])

128         # Apply the object's transform.
129         # Since 'T' is a matrix the result must be cast back to
        an array.
130         P = array(self.T * P)

131         X = P[0, :].reshape((npts, npts))
132         Y = P[1, :].reshape((npts, npts))
133         Z = P[2, :].reshape((npts, npts))

134         return X, Y, Z

135     def get_reference_point(self):

136         return self.T[0:3, 3]

137     def get_intersections(self, point, vector):

138         '''
139         This is a placeholder function that raises a fatal
        error.  It must be overridden
140             with a subclass function or never called.
141         '''

142         raise NotImplementedError, 'check_intersections() not
        overridden in subclass'

143     def set_seed(self, seed):

144         self.seed = seed

145 class Aperture(RayTracerObject):

146     def __init__(self, g, n, hlim, vlim, seed=0, exclusion=None
        ):

147         '''
148         Initialization variables 'g', 'n', 'hlim', and 'vlim'
        are described
149             in the parent class 'RayTracerObject' __init__()
        method.
150         Inputs 'hpass' and 'vpass' define parametric ranges
        that should allow
```

```
151             xrays to pass through the aperture.
152         '''
153         # Initialize the parent class.
154         super(Aperture, self).__init__(g, n, hlim, vlim, seed)
155         # Store the parametric limits describing the aperture opening.
156         self.exclusion = exclusion
157     def get_random_surface_points(self, npts):
158         # Call the parent class get_random_surface_points() while excluding
159         #    the aperture.
160         return super(Aperture, self).get_random_surface_points(npts, exclude=self.exclusion)
161     def get_mesh(self, npts):
162         # Call the parent class get_mesh() while excluding the aperture.
163         return super(Aperture, self).get_mesh(npts, exclude=self.exclusion)
164 class Detector(RayTracerObject):
165     def __init__(self, g, n, hlim, vlim, seed=0):
166         '''
167         Initialization variables 'g', 'n', 'hlim', and 'vlim' are described
168             in the parent class 'RayTracerObject' __init__() method.
169         '''
170         # Initialize the parent class.
171         super(Detector, self).__init__(g, n, hlim, vlim, seed)
172     def get_intersections(self, point, vector):
173         from numpy import abs, array, vstack, ones
174         '''
175         This method computes the location of a ray's intersection with the
176             object.  The returned arrays contain intersection
```

```
    points in the
177             plane of the object and boolean values indicating
    intersection
178             with the object.
179         '''

180         # How many ray intersections are we computing?
181         npts = point.shape[1]

182         point = array(self.Tinv * vstack((point, ones(npts))))
    [0:3, :]
183         vector = array(self.Tinv[0:3, 0:3] * vector)

184         # The vector is parameterized using 't'.  Calculate the
     value of
185         #    't' in the XZ plane (y = 0).
186         t = -1.0 * point[1, :] / vector[1, :]

187         # Compute intersections with the XZ plane.
188         plane_int = point + vector * t

189         # Does the ray intersect the object?
190         object_int = (abs(plane_int[0, :]) < self.g(self.hlim
    [1], 0.5)[0]) * \
191                      (abs(plane_int[2, :]) < self.g(0.5, self.
    vlim[1])[2])

192         # Apply the object transformation to the intersection
    points.
193         plane_int = array(self.T * vstack((plane_int, ones(npts
    ))))[0:3, :]

194         return plane_int, object_int

195 class Filter(RayTracerObject):

196     def __init__(self, width=1.0, height=1.0, seed=0, settings
    =[('Al', 0.004)]):

197         from numpy import array, zeros

198         '''
199         The first two inputs 'width' and 'height' describe the
    shape of the
200             filter.  It is assumed to start in the XZ plane and
     be centered
201             around the origin.
```

```
202         The last input 'settings' allows the filter material
    and thickness
203             to be specified during initialization.
204         '''
205         # Prepare variables for parent class initialization.
206         g = lambda h, v: array([-1.0 * width / 2.0 + h  * width
    , \
207                                 h * 0.0, \
208                                 -1.0 * height / 2.0 + v *
    height])
209         n = lambda h, v: array([0.0 * h, h / h, 0.0 * h])
210         # Initialize the parent class.
211         super(Filter, self).__init__(g, n, (0.0, 1.0), (0.0,
    1.0), seed)
212         # Define a dictionary relating each element to an array
     position.
213         self.ZDict = {'Li': 0, 'Be': 1, 'B' : 2, 'C' : 3, 'Na':
     4, \
214                       'Mg': 5, 'Al': 6, 'Si': 7, 'P' : 8, 'S' :
     9, \
215                       'K' :10, 'Ca':11, 'Sc':12, 'Ti':13, 'V'
    :14, \
216                       'Cr':15, 'Mn':16, 'Fe':17, 'Co':18, 'Ni'
    :19, \
217                       'Cu':20, 'Zn':21, 'Ga':22, 'Ge':23, 'As'
    :24, \
218                       'Se':25, 'Rb':26, 'Sr':27, 'Y' :28, 'Zr'
    :29, \
219                       'Nb':30, 'Mo':31, 'Tc':32, 'Ru':33, 'Rh'
    :34, \
220                       'Pd':35, 'Ag':36, 'Cd':37, 'In':38, 'Sn'
    :39, \
221                       'Sb':40, 'Te':41, 'Cs':42, 'Ba':43, 'La'
    :44, \
222                       'Ce':45, 'Pr':46, 'Nd':47, 'Pm':48, 'Sm'
    :49, \
223                       'Eu':50, 'Gd':51, 'Tb':52, 'Dy':53, 'Ho'
    :54, \
224                       'Er':55, 'Tm':56, 'Yb':57, 'Lu':58, 'Hf'
    :59, \
225                       'Ta':60, 'W' :61, 'Re':62, 'Os':63, 'Ir'
    :64, \
226                       'Pt':65, 'Au':66, 'Hg':67, 'Tl':68, 'Pb'
    :69, \
```

```
227                         'Bi':70, 'Po':71, 'At':72, 'Ra':73, 'Ac'
    :74, \
228                         'Th':75, 'Pa':76, 'U' :77, \
229                         'Polyimide':78, 'BN': 79, 'Si3N4':80, \
230                         'Polypropylene':81, 'PMMA':82, \
231                         'Polycarbonate':83, 'Mylar':84, 'Teflon'
    :85, \
232                         'Parylene-C':86, 'Parylene-N':87, 'SiO'
    :88}

233         # Invert the dictionary keys and values to enable a
    reverse lookup.
234         # This allows the dictionary to return the material
    name when given an array index.
235         # Using a copy of ZDict in the loop maintains Python 3
    compatibility.
236         for k in self.ZDict.copy().keys():
237             value = self.ZDict[k]
238             self.ZDict[str(value)] = k

239         # Define an initial thickness of 0 microns for each
    filter material.
240         self.l0 = zeros(len(self.ZDict) / 2)

241         # Import the valid energy range and the 2D sigma*n
    array.
242         [self.energy, self.sigma_n] = self.__import_sigma_n(
    self.ZDict, './sigma*n')

243         # Set given argument thicknesses.
244         for m in settings:
245             self.set_material_thickness(m[0], m[1])

246     def __import_sigma_n(self, dictionary, directory='./sigma*n
    '):

247         from numpy import loadtxt, ndarray, isinf
248         from os import listdir

249         files = listdir(directory)

250         # Get the shape of sigma_n.
251         # Since reverse lookups have been added to the
    dictionary, the number of columns
252         #    needs to be divided by two.
253         data = loadtxt(directory+'/Li.dat')
254         energy = data[:, 0]
```

```
255         sigma_n = ndarray((len(energy), len(dictionary) / 2))

256         for f in files:
257             element = f[:-4]
258             sigma_n[:, dictionary[element]] = loadtxt(directory
    + '/'+ f)[:, 1]

259         # There may be INF in the data sets.
260         # Set these to a stupid large number to avoid errors.
261         sigma_n[isinf(sigma_n)] = 1e99

262         return [energy, sigma_n]

263     def __interpolate_transmission(self):

264         from numpy import exp, sum

265         '''
266         Create an interpolating function for the filter's
    transmission curve.
267         '''

268         from scipy.interpolate import interp1d

269         sigma_n_l = sum(self.sigma_n * self.l0, axis=1)
270         trans = exp(-1 * sigma_n_l)

271         self.transmission = interp1d(self.energy, trans, kind='
    linear', \
272                                      bounds_error=False,
    fill_value=0.0)

273     def get_intersections(self, point, vector):

274         from numpy import abs, array, ones, vstack

275         '''
276         This method computes the location of a ray's
    intersection with the
277             object.  The returned arrays contain intersection
    points in the
278             plane of the object and boolean values indicating
    intersection
279             with the object.
280         '''

281         # How many ray intersections are we computing?
```

```
282         npts = point.shape[1]

283         point = array(self.Tinv * vstack((point, ones(npts))))
    [0:3, :]
284         vector = array(self.Tinv[0:3, 0:3] * vector)

285         # The vector is parameterized using 't'.  Calculate the
     value of
286         #    't' in the XZ plane (y = 0).
287         t = -1.0 * point[1, :] / vector[1, :]

288         # Compute intersections with the XZ plane.
289         plane_int = point + vector * t

290         # Does the ray intersect the object?
291         object_int = (abs(plane_int[0, :]) < self.g(self.hlim
    [1], 0.5)[0]) * \
292                      (abs(plane_int[2, :]) < self.g(0.5, self.
    vlim[1])[2])

293         # Apply the object transformation to the intersection
    points.
294         plane_int = array(self.T * vstack((plane_int, ones(npts
    ))))[0:3, :]

295         return plane_int, object_int

296     def set_material_thickness(self, material, thickness):

297         '''
298         Change the thickness of the given material.
299         Material thicknesses are assumed to be given in mm.
300         '''

301         self.l0[self.ZDict[material]] = thickness / 1000.0
302         self.__interpolate_transmission()

303     def get_transmissions(self, energy):

304         '''
305         Return the filter transmission values at the given
    energies.
306         '''

307         return self.transmission(energy)

308 class Optic(RayTracerObject):
```

```
309     def __init__(self, _2d, order, g, n, hlim, vlim, seed=0,
    name=None):

310         '''
311         Input '_2d' provides the crysta's 2d spacing in
    angstroms.
312         Input 'order' is an array-like object containing
    crystal reflection
313             order.
314         Initialization variables 'g', 'n', 'hlim', and 'vlim'
    are described
315             in the parent class 'RayTracerObject' __init__()
    method.
316         Input 'name' is an optional input used to identify the
    crystal.
317         '''

318         # Initialize the parent class.
319         super(Optic, self).__init__(g, n, hlim, vlim, seed)

320         # Store optic variables.
321         self._2d = _2d
322         self.order = order
323         self.name = name

324 class Source(RayTracerObject):

325     def __init__(self, g, n, hlim, vlim, seed=0, spectrum=None)
    :

326         # Initialize the parent class.
327         super(Source, self).__init__(g, n, hlim, vlim, seed)

328         # Specify a default uniform spectrum.
329         self.set_spectrum(spectrum)

330     def set_spectrum(self, spectrum=None):

331         from numpy import array, loadtxt, max, ndarray
332         from scipy.interpolate import interp1d

333         '''
334         Set the spectrum output for the X-ray source.
335         The spectrum argument may be one of four types:
336             1) a list:
337                 The list is converted to a 1D NumPy array and
```

```
    treated as
338                 described in (3).
339             2) a string:
340                 This is a path to a file containing spectra
    data.  The data
341                 file contains two columns.  Each row contains
    one energy and
342                 one intensity value.  Comment lines start with
    '#'.
343             3) a 1D NumPy array:
344                 These are taken to be discreet energies emitted
     by the source.
345                 The intensity of each energy is one.
346             4) a 2D NumPy array:
347                 The first column is treated as the 1D NumPy
    array in (3).  The
348                 second column contains energy intensities.
349         If no spectrum data is given, the default is to set all
     energies between
350         1000 and 10000 to an intensity of one.  All spectra
    data is interpolated.
351         Energies outside the bounds of the interpolation are
    set to an intensity of
352         zero.
353         '''

354         # Use a flag to indicate that a default spectrum is
    being used.
355         self.defaultspectrum = False

356         if isinstance(spectrum, list):

357             # We've been given a list, convert it to an ndarray
     first.
358             spectrum = array(spectrum)

359         if isinstance(spectrum, str):

360             # A spectrum file has been provided, use this to
    determine photon intensity.
361             self.spectrum = loadtxt(spectrum)

362             # Normalize the intensity data and interpolate.
363             # Photons outside the energy range provided by the
    file are of zero intensity.
364             self.spectrum[:, 1] /= max(self.spectrum[:, 1])
```

```
365         elif isinstance(spectrum, ndarray) and spectrum.ndim ==
     1:

366             # We have been given a 1D array of energies to use
    for the spectrum.
367             # Assume all energies are emitted with an intensity
     of one.
368             self.spectrum = ndarray((spectrum.shape[0], 2))
369             self.spectrum[:, 0] = spectrum
370             self.spectrum[:, 1] = 1.0

371         elif isinstance(spectrum, ndarray) and spectrum.ndim ==
     2:

372             # We have been given a 2D array of energies and
    intensities to use for the spectrum.
373             self.spectrum = spectrum

374         else:

375             # If no spectrum is given, use a default band from
    100 to 10000.
376             # All photons in the band are given an intensity of
     one.
377             self.spectrum = array([[100, 1.0], [10000, 1.0]])
378             self.defaultspectrum = True

379         self.intensity = interp1d(self.spectrum[:, 0], self.
    spectrum[:, 1], \
380                                   kind='linear', bounds_error=
    False, fill_value=0.0)

381     def get_intensities(self, energy):

382         '''
383         Return the source intensity at a given energy.
384         '''

385         return self.intensity(energy)

386     def get_random_volume_points(self, npts):

387         from numpy import array, ones, random, vstack

388         '''
389         Generate an array of volume points using 'npts' random
    (h,v) pairs
```

```
390             in the closed 'hlim' and 'vlim' intervals.
391         '''
392         # The values in 's' are in the range [0, 1).  Since the points g(h, v) are
393         #    surface points, s * g(h, v) will be a collection of volume points.
394         random.seed(self.seed)
395         h = self.hlim[0] + random.random_sample(npts) * (self.hlim[1] - self.hlim[0])
396         v = self.hlim[0] + random.random_sample(npts) * (self.vlim[1] - self.vlim[0])
397         s = random.random_sample(npts)
398         # Apply the object transform to the surface points.
399         # Since 'T' is a matrix the result must be cast back to an array.
400         # The final row is removed before returning.
401         return array(self.T * vstack([s * self.g(h, v), ones(npts)]))[0:3, :]
402 class CircularAperture(Aperture):
403     def __init__(self, rstop, rpass, seed=0):
404         from numpy import array, cos, pi, sin
405         '''
406         The first input 'rstop' describes the radius of the aperture stop.
407         The second input 'rpass' describes the radius of the aperture opening.
408         '''
409         g = lambda h, v: array([h * cos(v), \
410                                 h * 0.0, \
411                                 h * sin(v)])
412         n = lambda h, v: array([0.0 * h, h / h, 0.0 * h])
413         # Initialize the parent class.
414         super(CircularAperture, self).__init__(g, n, (0.0, rstop), (0.0, 2.0 * pi), seed,
415                                                exclusion=[(0.0, rpass, 0.0, 2.0 * pi)])
416     def get_intersections(self, point, vector):
```

```
417         from numpy import array, ones, sqrt, vstack

418         '''
419         This method computes the location of a ray's intersection with the
420             object.  The returned arrays contain intersection points in the
421             plane of the object and boolean values indicating intersection
422             with the object.
423         '''

424         # How many ray intersections are we computing?
425         npts = point.shape[1]

426         point = array(self.Tinv * vstack((point, ones(npts))))[0:3, :]
427         vector = array(self.Tinv[0:3, 0:3] * vector)

428         # The vector is parameterized using 't'.  Calculate the value of
429         #    't' in the XZ plane (y = 0).
430         t = -1.0 * point[1, :] / vector[1, :]

431         # Compute intersections with the XZ plane.
432         plane_int = point + vector * t

433         # Does the ray intersect the object?
434         # Only one exclusion region should be defined.  Any others are ignored.
435         r = sqrt(plane_int[0, :] ** 2 + plane_int[2, :] ** 2)
436         object_int = ((r > self.hlim[0]) * (r < self.exclusion[0][0]) + (r > self.exclusion[0][1]) * (r < self.hlim[1]))

437         # Apply the object transformation to the intersection points.
438         plane_int = self.T * vstack((plane_int, ones(npts)))
439         plane_int = array(plane_int)

440         return plane_int, object_int

441 class RectangularAperture(Aperture):

442     def __init__(self, wstop, hstop, wpass, hpass, seed=0):

443         from numpy import array
```

```
444         '''
445         The first two inputs 'wstop' and 'hstop' describe the
    shape of the
446             aperture.  It is assumed to start in the XZ plane
    and be centered
447             around the origin.
448         The last inputs 'wpass' and 'hpass' define the size of
    the opening.
449         '''

450         g = lambda h, v: array([-1.0 * wstop / 2.0 + h * wstop,
     \
451                                 0.0 * h, \
452                                 -1.0 * hstop / 2.0 + v * hstop
    ])
453         n = lambda h, v: array([0.0 * h, h / h, 0.0 * h])

454         # Initialize the parent class.
455         super(RectangularAperture, self).__init__(g, n, (0.0,
    1.0), (0.0, 1.0), seed,
456                                                   exclusion
    =[(0.5 * (1 - wpass / wstop),
457
    0.5 + wpass / (2.0 * wstop),
458
    0.5 * (1 - hpass / hstop),
459
    0.5 + hpass / (2.0 * hstop))])

460     def get_intersections(self, point, vector):

461         from numpy import array, invert, ones, vstack

462         '''
463         This method computes the location of a ray's
    intersection with the
464             object.  The returned arrays contain intersection
    points in the
465             plane of the object and boolean values indicating
    intersection
466             with the object.
467         '''

468         # How many ray intersections are we computing?
469         npts = point.shape[1]

470         point = array(self.Tinv * vstack((point, ones(npts))))
```

```
    [0:3, :]
471         vector = array(self.Tinv[0:3, 0:3] * vector)

472         # The vector is parameterized using 't'.  Calculate the
     value of
473         #    't' in the XZ plane (y = 0).
474         t = -1.0 * point[1, :] / vector[1, :]

475         # Compute intersections with the XZ plane.
476         plane_int = point + vector * t

477         x = plane_int[0, :]
478         z = plane_int[2, :]

479         # Does the ray intersect the object?
480         obj_bounds = (x > self.g(0.0, 0.5)[0]) * (x < self.g
    (1.0, 0.5)[0]) * \
481                      (z > self.g(0.5, 0.0)[2]) * (z < self.g
    (0.5, 1.0)[2])

482         # Map XZ intersection points back HV coordinates.
483         h = (x - self.g(0.0, 0.5)[0]) / (2 * self.g(1.0, 0.5)
    [0])
484         v = (z - self.g(0.5, 0.0)[2]) / (2 * self.g(0.5, 1.0)
    [2])

485         # Do these values pass through the exclusion?
486         exc_int = (h > self.exclusion[0][0]) * (h < self.
    exclusion[0][1]) * \
487                   (v > self.exclusion[0][2]) * (v < self.
    exclusion[0][3])

488         object_int = obj_bounds * invert(exc_int)

489         # Apply the object transformation to the intersection
    points.
490         plane_int = self.T * vstack((plane_int, ones(npts)))
491         plane_int = array(plane_int)

492         return plane_int, object_int

493 class Mesh(Aperture):

494     def __init__(self, wmesh, hmesh, wpmm, open_area, seed=0):

495         from numpy import array, sqrt
```

```
496         '''
497         The first two inputs 'wmesh' and 'hmesh' describe the
    shape of the
498             mesh.  It is assumed to start in the XZ plane and
    be centered
499             around the origin.
500         The input 'wpmm' defines the number of wires per
    millimeter.  It is
501             a tuple containing horizontal and vertical wires
    per millimeter.
502         The input 'openarea' defines the percentage of the
    surface area
503             occupied by the openings. It is in the range [0, 1)
    .
504         '''
505         self.delta = 1.0 / wpmm
506         g = lambda h, v: array([-1.0 * wmesh / 2.0 + h * wmesh,
     \
507                                 0.0 * h, \
508                                 -1.0 * hmesh / 2.0 + v * hmesh
    ])
509         n = lambda h, v: array([0.0 * h, h / h, 0.0 * h])
510         # Compute opening locations in terms of 'h' and 'v'.
511         # Add these to the exclusion list.
512         # The 'delta' value is needed for intersection
    calculations.
513         exclusions = []
514         numholes = (wpmm * [wmesh, hmesh]).round().astype('int'
    )
515         hstart = self.delta[0] * (1 - sqrt(open_area)) / (2.0 *
     wmesh)
516         vstart = self.delta[1] * (1 - sqrt(open_area)) / (2.0 *
     hmesh)
517         for i in range(0, numholes[0]):
518             for j in range(0, numholes[1]):
519                 e = (hstart + i * self.delta[0] / wmesh, hstart
     + self.delta[0] * (i + sqrt(open_area)) / wmesh,
520                      vstart + j * self.delta[1] / hmesh, vstart
     + self.delta[1] * (j + sqrt(open_area)) / hmesh)
521                 exclusions.append(e)
522         # Initialize the parent class.
523         super(Mesh, self).__init__(g, n, (0.0, 1.0), (0.0, 1.0)
```

```
    , seed,
524                                     exclusion=exclusions)

525     def get_intersections(self, point, vector):

526         from numpy import array, invert, mod, ones, vstack

527         '''
528         This method computes the location of a ray's
    intersection with the
529             object.  The returned arrays contain intersection
    points in the
530             plane of the object and boolean values indicating
    intersection
531             with the object.
532         '''

533         # How many ray intersections are we computing?
534         npts = point.shape[1]

535         point = array(self.Tinv * vstack((point, ones(npts))))
    [0:3, :]
536         vector = array(self.Tinv[0:3, 0:3] * vector)

537         # The vector is parameterized using 't'.  Calculate the
     value of
538         #    't' in the XZ plane (y = 0).
539         t = -1.0 * point[1, :] / vector[1, :]

540         # Compute intersections with the XZ plane.
541         plane_int = point + vector * t

542         x = plane_int[0, :]
543         z = plane_int[2, :]

544         # Does the ray intersect the object (inside hlim and
    vlim)?
545         obj_bounds = (x > self.g(0.0, 0.5)[0]) * (x < self.g
    (1.0, 0.5)[0]) * \
546                      (z > self.g(0.5, 0.0)[2]) * (z < self.g
    (0.5, 1.0)[2])

547         # Map XZ intersection points back HV coordinates.
548         # Then map back to the first exclusion and check for
    intersections there.
549         h = (x - self.g(0.0, 0.5)[0]) / (2 * self.g(1.0, 0.5)
    [0])
```

```
550         v = (z - self.g(0.5, 0.0)[2]) / (2 * self.g(0.5, 1.0)
    [2])

551         h = mod(h, self.delta[0] / (2 * self.g(1.0, 0.5)[0]))
552         v = mod(v, self.delta[1] / (2 * self.g(0.5, 1.0)[2]))

553         # Do these values pass through the first exclusion?
554         exc_int = (h > self.exclusion[0][0]) * (h < self.
    exclusion[0][1]) * \
555                   (v > self.exclusion[0][2]) * (v < self.
    exclusion[0][3])

556         object_int = obj_bounds * invert(exc_int)

557         # Apply the object transformation to the intersection
    points.
558         plane_int = self.T * vstack((plane_int, ones(npts)))
559         plane_int = array(plane_int)

560         return plane_int, object_int

561 class Film(Detector):

562     def __init__(self, width, height, seed=0):

563         from numpy import array

564         '''
565         The two inputs 'width' and 'height' describe the shape
    of the film.
566             It is assumed to start in the XZ plane and be
    centered around
567             the origin.
568         '''

569         g = lambda h, v: array([-1.0 * width / 2.0 + h * width,
     \
570                                 h * 0.0, \
571                                 -1.0 * height / 2.0 + v *
    height])
572         n = lambda h, v: array([0.0 * h, h / h, 0.0 * h])

573         # Initialize the parent class.
574         super(Film, self).__init__(g, n, (0.0, 1.0), (0.0, 1.0)
    , seed)

575 class EllipticalSpectrometer(Optic):
```

```
576     def __init__(self, _2d, order, a, b, point, axis, theta,
    phi, seed=0, name=None):
577         from numpy import arctan2, array, cos, sin, sqrt
578         '''
579         Input '_2d' is the atomic spacing of the crystal.
580         Input 'order' is the reflection orders of the crystal
    to consider.
581         The inputs 'a' and 'b' are the semi-major and semi-
    minor axes.
582         The arrays 'point' and 'axis' describe an axis around
    which the
583             ellipse is revolved.
584         Input 'theta' lists the angular limits of the ellipse
    in the XY
585             plane.  Input 'phi' lists the angular limits of
    revolution
586             around the axis defined by 'axis' and 'point'.
587         '''
588         # Normalize 'axis'.
589         axis /= sqrt((axis * axis).sum(axis=0))
590         def g(h, v):
591             # Precompute for speed.
592             CosH = cos(h)
593             SinH = sin(h)
594             CosV = cos(v)
595             SinV = sin(v)
596             # Define the elliptical arc in the XY plane.
597             x0 = a * b * CosH / sqrt((b * CosH) ** 2 + (a *
    SinH) ** 2)
598             y0 = a * b * SinH / sqrt((b * CosH) ** 2 + (a *
    SinH) ** 2)
599             z0 = 0.0
600             # Translate the arc so that the axis passes through
     the origin.
601             x0 -= point[0]
602             y0 -= point[1]
603             z0 -= point[2]
604             # Revolve the arc around the axis.
```

```
605             X = x0 * (CosV + axis[0] * axis[0] * (1 - CosV)) +
    \
606                 y0 * (axis[0] * axis[1] * (1 - CosV) - axis[2]
    * SinV) + \
607                 z0 * (axis[0] * axis[2] * (1 - CosV) + axis[1]
    * SinV)
608             Y = x0 * (axis[1] * axis[0] * (1 - CosV) + axis[2]
    * SinV) + \
609                 y0 * (CosV + axis[1] * axis[1] * (1 - CosV)) +
    \
610                 z0 * (axis[1] * axis[2] * (1 - CosV) - axis[1]
    * SinV)
611             Z = x0 * (axis[2] * axis[0] * (1 - CosV) - axis[1]
    * SinV) + \
612                 y0 * (axis[2] * axis[1] * (1 - CosV) + axis[0]
    * SinV) + \
613                 z0 * (CosV + axis[2] * axis[2] * (1 - CosV))

614             # Undo translation operation.
615             X += point[0]
616             Y += point[1]
617             Z += point[2]

618             return array([X, Y, Z])

619         def n(h, v):

620             # Precompute for speed.
621             CosH = cos(h)
622             SinH = sin(h)
623             CosV = cos(v)
624             SinV = sin(v)

625             # Define the elliptical arc normals in the XY plane
    .
626             x0 = a * b * CosH / sqrt((b * CosH) ** 2 + (a *
    SinH) ** 2)
627             y0 = a * b * SinH / sqrt((b * CosH) ** 2 + (a *
    SinH) ** 2)
628             gamma = arctan2(a ** 2 * y0, b ** 2 * x0)
629             nx = cos(gamma)
630             ny = sin(gamma)
631             nz = 0.0

632             # Revolve the arc around the axis.
633             X = nx * (CosV + axis[0] * axis[0] * (1 - CosV)) +
    \
```

```
634                 ny * (axis[0] * axis[1] * (1 - CosV) - axis[2]
    * SinV) + \
635                 nz * (axis[0] * axis[2] * (1 - CosV) + axis[1]
    * SinV)
636             Y = nx * (axis[1] * axis[0] * (1 - CosV) + axis[2]
    * SinV) + \
637                 ny * (CosV + axis[1] * axis[1] * (1 - CosV)) +
    \
638                 nz * (axis[1] * axis[2] * (1 - CosV) - axis[1]
    * SinV)
639             Z = nx * (axis[2] * axis[0] * (1 - CosV) - axis[1]
    * SinV) + \
640                 ny * (axis[2] * axis[1] * (1 - CosV) + axis[0]
    * SinV) + \
641                 nz * (CosV + axis[2] * axis[2] * (1 - CosV))

642             return array([X, Y, Z])

643         # Initialize the parent class.
644         super(EllipticalSpectrometer, self).__init__(_2d, order
    , g, n, theta, phi, seed, name)

645 class SphericalSpectrometer(Optic):

646     def __init__(self, _2d, order, width, height, radius, seed
    =0, name=None):

647         from numpy import arcsin, array, cos, pi, sin

648         '''
649         Input '_2d' is the atomic spacing of the crystal.
650         Input 'order' is the reflection orders of the crystal
    to consider.
651         The inputs 'width', 'height', and 'radius' describe the
     shape of the
652             crystal.  It is assumed to start along the x-axis
    with width
653             measured in the y- direction and height in the z-
    direction.
654         '''

655         g = lambda h, v: array([radius * sin(v) * cos(h), \
656                                 radius * sin(v) * sin(h), \
657                                 radius * cos(v)])
658         n = lambda h, v: array([-1.0 * sin(v) * cos(h), \
659                                 -1.0 * sin(v) * sin(h), \
660                                 -1.0 * cos(v)])
```

```
661         hmax = arcsin((width / 2.0) / radius)
662         vmax = arcsin((height / 2.0) / radius)
663         # Initialize the parent class.
664         super(SphericalSpectrometer, self).__init__(2d, order,
    g, n, \
665                                                     (-1.0 *
    hmax, hmax), \
666                                                     (pi / 2.0 -
    vmax, pi / 2.0 + vmax), seed, name)
667 class CylindricalSource(Source):
668     def __init__(self, radius, height, seed=0, spectrum=None):
669         from numpy import array, cos, pi, sin
670         '''
671         The source is assumed to be centered on the origin and
    aligned
672             with the z-axis.
673         '''
674         g = lambda h, v: array([radius * cos(h), \
675                                 radius * sin(h), \
676                                 -1.0 * height / 2.0 + v *
    height])
677         n = lambda h, v: array([cos(h), \
678                                 sin(h), \
679                                 0.0 * v])
680         # Initialize the parent class.
681         super(CylindricalSource, self).__init__(g, n, (0.0, 2.0
    * pi), (0.0, 1.0), seed, spectrum)
682 class SphericalSource(Source):
683     def __init__(self, radius, seed=0, spectrum=None):
684         from numpy import array, cos, pi, sin
685         '''
686         The source is assumed to be centered on the origin.
687         '''
688         g = lambda h, v: array([radius * sin(v) * cos(h), \
```

```
689                                     radius * sin(v) * sin(h), \
690                                     radius * cos(v)])
691         n = lambda h, v: array([-1.0 * sin(v) * cos(h), \
692                                 -1.0 * sin(v) * sin(h), \
693                                 -1.0 * cos(v)])
694         # Initialize the parent class.
695         super(SphericalSource, self).__init__(g, n, (0.0, 2.0 *
    pi), (0.0, pi), seed, spectrum)
696 class Scene(object):
697     def __init__(self, source, optic, detector, filters=[],
    apertures=[]):
698         # Store the objects in the scene.
699         self.source = source
700         self.optic = optic
701         self.detector = detector
702         self.filters = filters
703         self.apertures = apertures
704 if __name__ == '__main__':
705     print 'geometry'
```

C.1.2 Engine

The 'Engine.py' file is responsible for taking a 'Scene' object as defined in 'Geometry.py' and tracing X-rays from the source to the detector. X-rays originate at a random location from within the volume of the source and travel toward a random point on the surface of the X-ray optic. Each ray is assigned an intensity according to the source's spectrum. The reflection unit vector from the surface of the optic is computed from the incident unit vector and the optic's normal unit vector according to

$$\hat{r_s} = 2\left(\hat{r_n} \cdot \hat{r_i}\right)\hat{r_n} - \hat{r_i} \tag{C.1}$$

where $\hat{r_s}$ is the specularly reflected unit vector. The variables $\hat{r_i}$ and $\hat{r_n}$ represent the incident and normal unit vectors respectively. No broadening mechanisms such as a rocking curve for the crystal are simulated. The angle between the incident and normal vectors is used to compute the energy of each ray according to Bragg's law. Once the energy is known, each ray is checked for intersections with any filter or aperture before the optic and intensity values are updated accordingly. The reflected rays are then rechecked for intersections with apertures and filters. Finally, the intersection with the detector is computed.

Plotting routines are also included in 'Engine.py'. These can either provide a 3D rendering of the scene or a 2D plot of X-ray intersection locations with the detector. A 3D rendering is used to check for gross errors during setup. A 2D plot of the detector reveals the expected experimental X-ray signal. Each X-ray intersection is shown as a single point with color being used to indicate X-ray energy and opacity used to indicate relative intensity. Relative intensity is used since a model for detector response has not been included.

```
1  class XRayBurst(object):
2      def __init__(self, source, optic, n, seed):
3          from numpy import zeros
4          '''
5          Acquire and store 'n' rays originating in the 'source'
       and
6              directed toward the 'optic'.
7          '''
8          # Update source and optic seed values.
9          source.set_seed(seed)
10         optic.set_seed(seed)
11         # Get ray vectors and start points.
12         # Surface normals are saved for later convenience.
```

```
13          self.points = zeros((3, n, 2))
14          self.points[:, :, 0] = source.get_random_volume_points(
    n)
15          self.points[:, :, 1], self.normals = optic.
    get_random_surface_points(n)

16          # Leave unknowns empty until they can be computed.
17          self.energy = []
18          self.intensity = []
19          self.filmint = []

20      def __add__(self, other):

21          from numpy import hstack

22          self.points = hstack((self.points, other.points))
23          self.normals = hstack((self.normals, other.normals))
24          self.energy = hstack((self.energy, other.energy))
25          self.intensity = hstack((self.intensity, other.
    intensity))
26          self.filmint = hstack((self.filmint, other.filmint))

27          return self

28      def __iadd__(self, other):

29          return self + other

30  def RayTracer(scene, nrays, seed, queue=None):

31      from scipy.constants import physical_constants
32      from numpy import abs, arccos, array, insert, ones, pi, \
33                        sin, sqrt, vstack, where
34      from numpy.random import choice

35      # Define some physical constants.
36      c = physical_constants["speed of light in vacuum"][0]
37      h = physical_constants["Planck constant in eV s"][0]

38      # Create an x-ray burst.
39      XRays = XRayBurst(scene.source, scene.optic, nrays, seed)

40      # Compute bragg angles and assign photon energies.
41      # Photon energies are computed in units of eV.
42      Rays = XRays.points[:, :, 1] - XRays.points[:, :, 0]
43      NormalCosines = (Rays * XRays.normals).sum(axis=0) / sqrt((
    Rays * Rays).sum(axis=0))
```

```
44      BraggAngles = pi / 2.0 - arccos(abs(NormalCosines))
45      Wavelength = scene.optic._2d * sin(BraggAngles) / choice(
        scene.optic.order, nrays, replace=True)
46      XRays.energy = (h * c) / (Wavelength * 1e-10)

47      # Get starting photon intensities from source spectrum.
48      XRays.intensity = scene.source.get_intensities(XRays.energy
        )

49      # Check for aperture or filter intersections before the
        crystal.
50      #    Update intensity values.
51      for f in scene.filters:

52          _, b = f.get_intersections(XRays.points[:, :, 0], Rays)
53          XRays.intensity = where(b, XRays.intensity * f.
        get_transmissions(XRays.energy), XRays.intensity)

54      for a in scene.apertures:

55          _, b = a.get_intersections(XRays.points[:, :, 0], Rays)
56          XRays.intensity = where(b, 0.0, XRays.intensity)

57      # Compute reflected vectors.
58      Rays = 2.0 * (Rays * XRays.normals).sum(axis=0) * XRays.
        normals - Rays

59      # Check for aperture or filter intersections after the
        crystal.
60      #    Update intensity values.
61      for f in scene.filters:

62          _, b = f.get_intersections(XRays.points[:, :, 1], Rays)
63          XRays.intensity = where(b, XRays.intensity * f.
        get_transmissions(XRays.energy), XRays.intensity)

64      for a in scene.apertures:

65          _, b = a.get_intersections(XRays.points[:, :, 1], Rays)
66          XRays.intensity = where(b, 0.0, XRays.intensity)

67      # Compute film intersection points.
68      i, b = scene.detector.get_intersections(XRays.points[:, :,
        1], Rays)
69      XRays.points = insert(XRays.points, 2, i, axis=2)

70      # Return film intersection points to the XZ plane.
```

```
71      # Write intersection points, energies, and intensities to
        file.
72      XRays.filmint = array(scene.detector.Tinv * vstack((i, ones
        (XRays.points.shape[1]))))[0:3, :]

73      # Push results to the queue.
74      if not queue == None:

75          queue.put(XRays)

76      else:

77          return XRays

78  def ThreadedTracer(scene, nrays):

79      from copy import deepcopy
80      from time import time
81      from numpy import random, round
82      import multiprocessing as mul

83      # Start the timer.
84      tstart = time()

85      rayspercore = round(nrays / mul.cpu_count())
86      seeds = random.random_integers(0, 1000000, size=mul.
        cpu_count())
87      queue = mul.Queue()

88      processes = [mul.Process(target=RayTracer, args=(deepcopy(
        scene), rayspercore, s, queue)) for s in seeds]
89      for p in processes: p.start()

90      # Collect results here.
91      result = queue.get()
92      for _ in seeds[1:]:
93          result += queue.get()

94      for p in processes: p.join()

95      queue.close()

96      # Stop the timer and print elapsed time.
97      tstop = time()
98      print 'Traced', rayspercore * mul.cpu_count(), 'rays.'
99      print 'Elapsed time =', tstop - tstart, 's.'
```

```
100     SaveOutput(result)

101     return result

102 def Display(scene, results, show2d=False, show3d=False):

103     from mayavi import mlab
104     import matplotlib as mplot

105     mplot.use('WXAgg')

106     import matplotlib.pyplot as plt
107     from scipy.constants import physical_constants
108     from numpy import arange, arccos, delete, linspace, pi,
    repeat, round, s_, sin, sqrt, vstack

109     c = physical_constants["speed of light in vacuum"][0]
110     h = physical_constants["Planck constant in eV s"][0]

111     # Colors are set according to energies in the first given
    reflection order.
112     Rays = results.points[:, :, 1] - results.points[:, :, 0]
113     NormalCosines = (Rays * results.normals).sum(axis=0) / sqrt
    ((Rays * Rays).sum(axis=0))
114     BraggAngles = pi / 2.0 - arccos(abs(NormalCosines))
115     Wavelength = scene.optic._2d * sin(BraggAngles) / scene.
    optic.order[0]
116     Energy = (h * c) / (Wavelength * 1e-10)

117     if show2d:

118         if show3d:  plt.ion()

119         cm = mplot.cm.ScalarMappable()
120         cm.set_cmap('jet_r')
121         color = cm.to_rgba(Energy, bytes=False)
122         color[:, 3] = results.intensity

123         numbars = len(scene.optic.order)
124         barheight = 0.25
125         aspect = 7.0 / 1.375
126         aspect = 2
127         boarder = 1.25
128         width = 7 + 2.0 * boarder
129         height = 7 / aspect + 2.0 * boarder + numbars * (
    barheight + boarder)
130         fig = plt.figure(figsize=(width, height))
```

```
131         ax1 = fig.add_axes([(boarder) / width, \
132                             (boarder + numbars * (barheight +
    boarder)) / height, \
133                             1.0 - (2.0 * boarder) / width, \
134                             1.0 - (2.0 * boarder + numbars * (
    barheight + boarder)) / height])
135         s = ax1.scatter(results.filmint[0, :], results.filmint
    [2, :], c=color, marker='.', edgecolors='none', \
136                         vmin=min(results.energy), vmax=max(results.
    energy))
137         ax1.set_xlim(scene.detector.g(scene.detector.hlim[0],
    0.5)[0], \
138                      scene.detector.g(scene.detector.hlim[1],
    0.5)[0])
139         ax1.set_ylim(scene.detector.g(0.5, scene.detector.vlim
    [0])[2], \
140                      scene.detector.g(0.5, scene.detector.vlim
    [1])[2])
141         ax1.set_xlabel('Position (mm)', fontsize=30)
142         ax1.set_ylabel('Position (mm)', fontsize=30)
143         for label in ax1.get_xticklabels() + ax1.
    get_yticklabels():
144             label.set_size(20)

145         # Add colorbars.
146         for o in range(0, numbars):

147             cb_ax = fig.add_axes([(boarder) / width, \
148                                   (boarder + o * (barheight +
    boarder)) / height, \
149                                   1.0 - (2.0 * boarder) / width
    , \
150                                   (barheight) / height])
151             #cb_ax.set_ylabel(str(scene.optic.order[o]),
    fontsize=15)
152             Wavelength = scene.optic._2d * sin(BraggAngles) /
    scene.optic.order[o]
153             Energy = (h * c) / (Wavelength * 1e-10)
154             norm = mplot.colors.Normalize(vmin=Energy.min(),
    vmax=Energy.max())
155             cb = mplot.colorbar.ColorbarBase(cb_ax, cmap='jet_r
    ', norm=norm, orientation='horizontal')
156             ticks = linspace(Energy.min(), Energy.max(), 9)
157             ticks = round(ticks, 0)
158             cb.set_ticks(ticks)
159             cb.ax.tick_params(labelsize=20)
160         cb_ax.set_xlabel('Energy (eV)', fontsize=30)
```

```
161         plt.show()

162     if show3d:

163         # Setup the mlab plot.
164         mlab.figure(bgcolor=(1, 1, 1))

165         # Plot the ray paths.
166         x = results.points[0, :, :].flatten()
167         y = results.points[1, :, :].flatten()
168         z = results.points[2, :, :].flatten()
169         s = repeat(Energy, 3)
170         connections = vstack([arange(0, results.points.shape[1]
    * 3 - 1, 1.0), \
171                               arange(0, results.points.shape[1]
    * 3 - 1, 1.0) + 1.0]).T
172         connections = delete(connections, s_[2::3], 0)

173         src = mlab.pipeline.scalar_scatter(x, y, z, s)
174         src.mlab_source.dataset.lines = connections
175         lines = mlab.pipeline.stripper(src)  #
    @UndefinedVariable
176         mlab.pipeline.surface(lines, colormap='jet', line_width
    =1.0)

177         # Plot the source, crystal, and film.
178         s = scene.source.get_mesh(100)
179         o = scene.optic.get_mesh(100)
180         d = scene.detector.get_mesh(100)

181         mlab.mesh(s[0], s[1], s[2], color=(0, 0, 1))
182         mlab.mesh(o[0], o[1], o[2], color=(0, 0, 1))
183         mlab.mesh(d[0], d[1], d[2], color=(0, 0, 1))

184         # Plot any filters.
185         for f in scene.filters:

186             m = f.get_mesh(100)
187             mlab.mesh(m[0], m[1], m[2], color=(0.465, 0.531,
    0.598))

188         # Plot any apertures.
189         for a in scene.apertures:

190             m = a.get_mesh(100)
191             mlab.mesh(m[0], m[1], m[2], color=(0, 0, 0))
```

```
192         # Display the plot.
193         mlab.show()

194 def SaveOutput(results):

195     from numpy import savetxt, vstack

196     savetxt('output.rt5', vstack((results.filmint, results.
        energy, results.intensity)).T)

197 if __name__ == '__main__':

198     print 'engine'
```

C.1.3 Elliptical Spectrometer

The code used to run the elliptical ray tracing calculations in section 4.3 is presented here for completeness.

```
1 #!/usr/bin/env python

2 import os
3 from numpy import array, pi, sqrt
4 from geometry import CylindricalSource, SphericalSource,
      EllipticalSpectrometer  # @UnresolvedImport @UnusedImport
5 from geometry import Film, Filter, RectangularAperture, Scene
     # @UnresolvedImport
6 from engine import Display, SaveOutput, ThreadedTracer  #
     @UnresolvedImport @UnusedImport

7 # Change to the script directory so that data
8 #     files can be found.
9 scriptDir = os.path.dirname(os.path.abspath(__file__))
10 os.chdir(scriptDir)

11 # Define unit vectors.
12 origin = array([0., 0., 0.])
13 x = array([1., 0., 0.])
14 y = array([0., 1., 0.])
15 z = array([0., 0., 1.])
```

```
# Define elliptical spectrometer parameters.
#    Note: all length units are in 'mm'.
e = 0.60
f = 2.0 * 25.4
a = f / e
b = a * sqrt(1 - e ** 2)
p = -f * x
axis = x - y

# Mica: 2d = 19.94
# Create the source, elliptical crystal, and detector film.
s = SphericalSource(0.010, spectrum='Ta_250_1e22.spec') #'
    Mg_750_1e21.spec' 'Ta_250_1e22.spec' 'Al_750_1e21.spec'
s.translate(0.5 * z * 25.4)

o = EllipticalSpectrometer(19.94, [2], a, b, p, axis, (0.42,
    0.96), (-2.0 * pi / 180, 2.0 * pi / 180)) #(0.35, 1.1),
    (-3.0 * pi / 180, 3.0 * pi / 180)
o.translate(f * x + 0.5 * 25.4 * z)

# Create the aluminum filter in front of the film.
f1 = Filter(8.0 * 25.4, 1.5 * 25.4, settings=[('Al', 0.008), ('
    Polypropylene', 0.08)])
f1.translate((6.01 * x - 0.65 * y + 1.0 * z) * 25.4)
f1.rotate(origin, z, -1.0 * pi / 4.0)

# Create an aperture at the cassette entrance.
a1 = RectangularAperture(2.0 * 25.4, 2.0 * 25.4, 0.6 * 25.4,
    0.225 * 25.4)
a1.translate((3.85 * x - 0.0 * y + 0.5 * z) * 25.4)

# Create a sagittal aperture.
sa = RectangularAperture(8.0 * 25.4, 2.0 * 25.4, 7.0 * 25.4,
    3.5)
sa.translate((6.0 * x - 0.0 * y + 0.5 * z) * 25.4)
sa.rotate(origin, z, -1.0 * pi / 4.0)

# Meridional focus.
mf = Film(0.2, 6)
mf.translate(4 * 25.4 * x + 0.0 * y + 0.5 * 25.4 * z)

# Sagittal focus.
sf = Film(100, 0.5)
sf.translate((5 * x - 0.0 * y + 0.5 * z) * 25.4)
sf.rotate(origin, z, -1.0 * pi / 4.0)
```

```
# Detector plane.
d = Film(7.125 * 25.4 / 1.1, 1.5 * 25.4 / 1.1)
d.translate((6.5 * x - 2.0 * y + 0.5 * z) * 25.4)
d.rotate(origin, z, -1.0 * pi / 4.0)

scene = Scene(s, o, mf, filters=[], apertures=[])

results = ThreadedTracer(scene, 100000)
Display(scene, results, show2d=True, show3d=True)
```

C.1.4 Spherical Spectrometer

The code used to run the spherical ray tracing calculations in section 5.3 is presented here for completeness.

```
#!/usr/bin/env python

import os
from numpy import array, pi
from geometry import SphericalSource  # @UnresolvedImport
from geometry import Film, Filter, Scene  # @UnresolvedImport
from engine import Display, ThreadedTracer  # @UnresolvedImport
from geometry import SphericalSpectrometer

# Change to the script directory so that data
#    files can be found.
scriptDir = os.path.dirname(os.path.abspath(__file__))
os.chdir(scriptDir)

# Define unit vectors.
origin = array([0., 0., 0.])
x = array([1., 0., 0.])
y = array([0., 1., 0.])
z = array([0., 0., 1.])

# Quartz 1010: 2d = 8.5096
s = SphericalSource(0.010, spectrum='Ta_250_1e22.spec')

o = SphericalSpectrometer(8.5096, [1], 52, 16, 180)
o.translate((28.75 * 25.4 - 180) * x)
#o.rotate(28.75 * 25.4 * x, x, pi / 2.)
```

```
o.rotate(28.75 * 25.4 * x, z, 21 * pi / 180.)

# Detector plane.
d = Film(1.5 * 25.4, 0.5 * 25.4)
d.rotate(origin, z, pi / 2.0)
d.translate(22.2129 * 25.4 * x)
d.rotate(26.25 * 25.4 * x, z, 64. * pi / 180.)

# Model as sample wire as a cold filter.
w = Filter(25.4, 0.250, settings=[('Al', 0.004)])
w.rotate(origin, z, pi / 2.0)
w.translate(1.75 * 25.4 * x)

scene = Scene(s, o, d, filters=[w], apertures=[])

results = ThreadedTracer(scene, 100000)
Display(scene, results, show2d=True, show3d=True)
```

C.2 Abel Inversion

The process of computing an Abel inversion is described in section 7.3. The code to perform that inversion is presented below. The image to be inverted is stored in the 2D array 'imageKEdge'. The coefficients of the Fourier series are computed in 'A'. The array 'F' stores a recreation of the original data as computed from the coefficients in 'A'. Finally, the Abel inverse is computed in 'T'.

```
import numpy as np
from scipy.integrate import simps

# Mirror the image so that it is an even function.  This avoids
#  the necessity of sine functions.
imageTemp = np.vstack((imageKEdge[::-1, :], imageKEdge))
rTemp = np.linspace(0, maxRadius * 2, imageTemp.shape[0])

# Compute the coefficients of the Fourier series.
terms = 5
N = range(0, terms)
rTemp /= rTemp[-1] / 2.
```

```
drTemp = rTemp[1] - rTemp[0]
dr = rTemp[1] - rTemp[0]
A = np.einsum('i,j,k->ijk', 2 * np.pi * rTemp / 2, np.ones(np.
    size(e)), N)
A = np.cos(A)
A *= np.expand_dims(imageTemp, axis=2)
A = simps(A, dx=drTemp, axis=0, even='last')
A *= 2. / 2.
A[:, 0] = np.mean(imageTemp, axis=0)

# Reconstruct the image as a consistency check.
F = np.einsum('i,jk->ijk', np.ones(np.size(r)), A)
Phi = np.einsum('i,j,k->ijk', 2 * np.pi * r / (2 * r[-1]), np.
    ones(np.size(e)), N)
F *= np.cos(Phi)
F = F.sum(axis=2)
F = F[::-1, :]

# Construct the Abel inversion.
T = np.einsum('i,jk->ijk', np.ones(np.size(r)), A)
Phi = np.einsum('i,j,k->ijk', 2 * np.pi * r / (2 * r[-1]), np.
    ones(np.size(e)), N)
T *= j0(Phi)
N[0] = 1
N = np.einsum('i,j,k->ijk', np.ones(np.size(r)), np.ones(np.
    size(e)), N)
T *= np.pi * N
T[:, :, 0] /= np.pi
R = np.einsum('i,j->ij', r, np.ones(np.size(e)))
T[:, :, 0] *= (r[-1] / np.pi) / np.sqrt(r[-1] ** 2 + np.power(R
    , 2))
T = T.sum(axis=2)
```

C.3 Genetic Algorithm

The machinery that forms the building blocks of the genetic algorithm is provided by the Distributed Evolutionary Algorithms in Python (DEAP) package [67]. This package provides algorithms for developing a population of individuals as well as mating and selecting them. Functions to evaluate and mutate individuals are

unique to each problem and must be provided by the user. The DEAP package makes use of the Scalable Concurrent Operations in Python (SCOOP) package [68] to distribute the computational load across multiple CPU threads.

BIBLIOGRAPHY

[1] P. Audebert, P. Renaudin, S. Bastiani-Ceccotti, J. P. Geindre, C. Chenais-Popovics, S. Tzortzakis, V. Nagels-Silvert, R. Shepherd, I. Matsushima, S. Gary, F. Girard, O. Peyrusse, and J. C. Gauthier. Picosecond Time-Resolved X-Ray Absorption Spectroscopy of Ultrafast Aluminum Plasmas. *Physical Review Letters*, 94(2):025004, jan 2005. URL: http://link.aps.org/doi/10.1103/PhysRevLett.94.025004, doi:10.1103/PhysRevLett.94.025004.

[2] P. F. Knapp, S. A. Pikuz, T. A. Shelkovenko, D. A. Hammer, and S. B. Hansen. High resolution absorption spectroscopy of exploding wire plasmas using an x-pinch x-ray source and spherically bent crystal. *The Review of scientific instruments*, 82(6):063501, jun 2011. URL: http://www.ncbi.nlm.nih.gov/pubmed/21721685, doi:10.1063/1.3592582.

[3] J. MacFarlane, J. Bailey, G. Chandler, C. Deeney, M. Douglas, D. Jobe, P. Lake, T. Nash, D. Nielsen, R. Spielman, P. Wang, and P. Woodruff. X-ray absorption spectroscopy measurements of thin foil heating by Z-pinch radiation. *Physical Review E*, 66(4):046416, oct 2002. URL: http://link.aps.org/doi/10.1103/PhysRevE.66.046416, doi:10.1103/PhysRevE.66.046416.

[4] P. F. Knapp, S. A. Pikuz, T. A. Shelkovenko, D A Hammer, and S. B. Hansen. Time and space resolved measurement of the electron temperature, mass density and ionization state in the ablation plasma between two exploding Al wires. *Physics of Plasmas*, 19(5):056302, 2012. URL: http://scitation.aip.org/content/aip/journal/pop/19/5/10.1063/1.3694039, doi:10.1063/1.3694039.

[5] P. A. Gourdain and C. E. Seyler. Impact of the Hall Effect on High-Energy-Density Plasma Jets. *Physical Review Letters*, 110(1):015002, jan 2013. URL: http://link.aps.org/doi/10.1103/PhysRevLett.110.015002, doi:10.1103/PhysRevLett.110.015002.

[6] S. M. Zakharov, G. V. Ivanenkov, A. A. Kolomenskii, S. A. Pikuz, A. I. Samokhin, and I. Ulshmid. Wire X-Pinch in a High Current Diode. *Soviet Technical Physics Letters*, 8(9):456–457, 1982.

[7] D. H. Kalantar. *An Experimental Study of the Dynamics of X-Pinch and Z-Pinch Plasmas*. PhD thesis, 1993.

[8] D. H. Kalantar and D. A. Hammer. The x-pinch as a point source of x rays for backlighting. *Review of Scientific Instruments*, 66(1):779, 1995. URL: http://scitation.aip.org/content/aip/journal/rsi/66/1/10.1063/1.1146219, doi:10.1063/1.1146219.

[9] G. V. Ivanenkov, A. R. Mingaleev, S. A. Pikuz, V. M. Romanova, and T. A. Shelkovenko. Experimental Study of X-Pinch Dynamics. *Plasma Physics Reports*, 22(5):363–378, 1996.

[10] I. H. Mitchell, R. Aliaga-Rossel, R. Saavedra, H. Chuaqui, M. Favre, and E. S. Wyndham. Investigation of the plasma jet formation in X-pinch plasmas using laser interferometry. *Physics of Plasmas*, 7(12):5140, 2000. URL: http://scitation.aip.org/content/aip/journal/pop/7/12/10.1063/1.1321317, doi:10.1063/1.1321317.

[11] T. A. Shelkovenko, S. A. Pikuz, D. B. Sinars, K. M. Chandler, and D. A. Hammer. X pinch : a source of 1 to 10 keV x-rays. In George A. Kyrala and Jean-Claude J. Gauthier, editors, *Applications of X Rays Generated from Lasers and Other Bright Sources II*, volume 4504, pages 180–187, nov 2001. URL: http://proceedings.spiedigitallibrary.org/proceeding.aspx?articleid=894811, doi:10.1117/12.448464.

[12] T. A. Shelkovenko, D. B. Sinars, S. A. Pikuz, and D. A. Hammer. Radiographic and spectroscopic studies of X-pinch plasma implosion dynamics and x-ray burst emission characteristics. *Physics of Plasmas*, 8(4):1305, 2001. URL: http://scitation.aip.org/content/aip/journal/pop/8/4/10.1063/1.1351553, doi:10.1063/1.1351553.

[13] D. B. Sinars, S. A. Pikuz, T. A. Shelkovenko, K. M. Chandler, and D. A. Hammer. Temporal parameters of the X-pinch x-ray source. *Review of Scientific Instruments*, 72(7):2948, 2001. URL: http://scitation.aip.org/content/aip/journal/rsi/72/7/10.1063/1.1379961, doi:10.1063/1.1379961.

[14] T. A. Shelkovenko, S. A. Pikuz, D. B. Sinars, K. M. Chandler, and D. A. Hammer. Time-resolved spectroscopic measurements of 1 keV, dense, subnanosecond X-pinch plasma bright spots. *Physics of Plasmas*, 9(5):2165, 2002. URL: http://scitation.aip.org/content/aip/journal/pop/9/5/10.1063/1.1458587, doi:10.1063/1.1458587.

[15] B. M. Song, S. A. Pikuz, T. A. Shelkovenko, and D. A. Hammer. Determination of the size and structure of an X-pinch x-ray source from the diffraction pattern produced by microfabricated slits. *Applied Optics*, 44(12):2349–58, apr 2005. URL: http://www.ncbi.nlm.nih.gov/pubmed/15861842.

[16] S. A. Pikuz, T. A. Shelkovenko, A. R. Mingaleev, V. M. Romanova, B. M. Song, K. M. Chandler, M. D. Mitchell, and D. A. Hammer. The X pinch as an x-ray source for point-projection radiography. In Sultan B. Dabagov, editor, *International Conference on Charged and Neutral Particles Channeling Phenomena*, volume 5974, pages 59740L–59740L–9, aug 2005. URL: http://proceedings.spiedigitallibrary.org/proceeding.aspx?articleid=878862, doi:10.1117/12.639993.

[17] J. P. Chittenden, A. Ciardi, C. A. Jennings, S. V. Lebedev, D. A. Hammer, S. A. Pikuz, and T. A. Shelkovenko. Structural Evolution and Formation of High-Pressure Plasmas in X Pinches. *Physical Review Letters*, 98(2):025003, jan 2007. URL: http://link.aps.org/doi/10.1103/PhysRevLett.98.025003, doi:10.1103/PhysRevLett.98.025003.

[18] R. K. Appartaim and B. T. Maakuu. X-pinch x-ray sources driven by a 1 μs capacitor discharge. *Physics of Plasmas*, 15(7):072703, 2008. URL: http://scitation.aip.org/content/aip/journal/pop/15/7/10.1063/1.2953800, doi:10.1063/1.2953800.

[19] T. A. Shelkovenko, S. A. Pikuz, R. D. McBride, P. F. Knapp, H. Wilhelm, D. A. Hammer, and D. B. Sinars. Nested multilayered X pinches for generators with mega-ampere current level. *Physics of Plasmas*, 16(5):050702, 2009. URL: http://scitation.aip.org/content/aip/journal/pop/16/5/10.1063/1.3132611, doi:10.1063/1.3132611.

[20] T. A. Shelkovenko, S. A. Pikuz, A. D. Cahill, P. F. Knapp, D. A. Hammer, D. B. Sinars, I. N. Tilikin, and S. N. Mishin. Hybrid X-pinch with conical electrodes. *Physics of Plasmas*, 17(11):112707, 2010. URL: http://scitation.aip.org/content/aip/journal/pop/17/11/10.1063/1.3504226, doi:10.1063/1.3504226.

[21] D. M. Haas, S. C. Bott, J. Kim, D. A. Mariscal, R. E. Madden, Y. Eshaq, U. Ueda, G. Collins IV, K. Gunasekera, F. N. Beg, J. P. Chittenden, N. Niasse, and C. A. Jennings. Supersonic jet formation and propagation in x-pinches. *Astrophysics and Space Science*, 336(1):33–40, jan 2011. URL: http://link.springer.com/10.1007/s10509-011-0599-8, doi:10.1007/s10509-011-0599-8.

[22] R. F. Heeter, J. E. Bailey, M. E. Cuneo, J. Emig, M. E. Foord, P. T. Springer, and R. S. Thoe. Plasma diagnostics for x-ray driven foils at Z. *Review of Scientific Instruments*, 72(1):1224, 2001. URL: http://scitation.aip.org/content/aip/journal/rsi/72/1/10.1063/1.1324749, doi:10.1063/1.1324749.

[23] D. H. Cohen, J. J. MacFarlane, J. E. Bailey, and D. A. Liedahl. X-ray spectral diagnostics of neon photoionization experiments on the Z-machine. *Review of Scientific Instruments*, 74(3):1962, 2003. URL: http://scitation.aip.org/content/aip/journal/rsi/74/3/10.1063/1.1535261, doi:10.1063/1.1535261.

[24] B. Jones, C. Deeney, C. A. Coverdale, P. D. LePell, J. L. McKenney, J.P. Apruzese, J. W. Thornhill, K. G. Whitney, R. W. Clark, A. L. Velikovich, J. Davis, Y. Maron, V. Kantsyrev, A. Safronova, and V. I. Oreshkin. K-shell radiation physics in low- to moderate-atomic-number z-pinch plasmas on the Z accelerator. *Journal of Quantitative Spectroscopy and Radiative Transfer*, 99(1-3):341–348, may 2006. URL: http://linkinghub.elsevier.com/retrieve/pii/S0022407305001585, doi:10.1016/j.jqsrt.2005.05.027.

[25] S. A. Pikuz, T. A. Shelkovenko, K. M. Chandler, M. D. Mitchell, D. A. Hammer, I. Y. Skobelev, A. S. Shlyaptseva, and S. B. Hansen. X-ray spectroscopy for high energy-density X pinch density and temperature measurements (invited). *Review of Scientific Instruments*, 75(10):3666–3671, oct 2004. URL: http://link.aip.org/link/RSINAK/v75/i10/p3666/s1{&}Agg=doihttp://scitation.aip.org/content/aip/journal/rsi/75/10/10.1063/1.1788863, doi:10.1063/1.1788863.

[26] I. H. Mitchell, J. A. Gomez, F. A. Suzuki Vidal, R. Aliaga-Rossel, H. Chuaqui, M. Favre, and E. Wyndham. X-ray emission from 125 μm diameter aluminium wire x-pinches at currents of 400 kA. *Plasma Sources Science and Technology*, 14(3):501–508, aug 2005. URL: http://stacks.iop.org/0963-0252/14/i=3/a=012?key=crossref.e04b5be77011e1405a8e1f6f4eb0560c, doi:10.1088/0963-0252/14/3/012.

[27] R. F. Heeter, J. E. Bailey, M. E. Cuneo, J. Emig, M. E. Foord, P. T. Springer, and R. S. Thoe. X-Ray Spectroscopy of Astrophysically- Relevant Photoionized Iron Plasmas at Z. In *Topical Conference on Atomic Processes in Plasmas*, 2000.

[28] I. M. Hall, T. Durmaz, R. C. Mancini, J. E. Bailey, G. A. Rochau, I. E. Golovkin, and J. J. MacFarlane. Absorption spectroscopy of a laboratory photoionized plasma experiment at Z. *Physics of Plasmas*, 21(3):031203, mar 2014. URL: http://scitation.aip.org/content/aip/journal/pop/21/3/10.1063/1.4865226, doi:10.1063/1.4865226.

[29] D. R. Kania, L. Pan, H. Kornblum, P. Bell, O. N. Landen, and P. Pianetta. Soft x-ray detection with diamond photoconductive detectors. *Review of Scientific Instruments*, 61(10):2765, 1990. URL: http://scitation.

aip.org/content/aip/journal/rsi/61/10/10.1063/1.1141824, doi:10.1063/1.1141824.

[30] R. B. Spielman. Diamond photoconducting detectors as high power z-pinch diagnostics (invited). *Review of Scientific Instruments*, 66(1):867, 1995. URL: http://scitation.aip.org/content/aip/journal/rsi/66/1/10.1063/1.1146188, doi:10.1063/1.1146188.

[31] J. D. Ramboz. Machinable Rogowski coil, design, and calibration. *IEEE Transactions on Instrumentation and Measurement*, 45(2):511–515, apr 1996. URL: http://ieeexplore.ieee.org/lpdocs/epic03/wrapper.htm?arnumber=492777, doi:10.1109/19.492777.

[32] I. Uschmann, E. Förster, K. Gäbel, G. Hölzer, and M. Ensslen. X-ray reflection properties of elastically bent perfect crystals in Bragg geometry. *Journal of Applied Crystallography*, 26(3):405–412, jun 1993. URL: http://scripts.iucr.org/cgi-bin/paper?S0021889892013025, doi:10.1107/S0021889892013025.

[33] L. Antonelli, P. Forestier-Colleoni, G. Folpini, R. Bouillaud, A. Faenov, L. Fedeli, C. Fourment, L. Giuffrida, S. Hulin, S. A. Pikuz, J. J. Santos, L. Volpe, and D. Batani. Measurement of reflectivity of spherically bent crystals using Kα signal from hot electrons produced by laser-matter interaction. *Review of Scientific Instruments*, 86(7):073507, jul 2015. URL: http://scitation.aip.org/content/aip/journal/rsi/86/7/10.1063/1.4926740, doi:10.1063/1.4926740.

[34] D. B. Sinars, Guy R Bennett, David F Wenger, Michael E Cuneo, and John L Porter. Evaluation of Bent-Crystal X-Ray Backlighting and Microscopy Techniques for the Sandia Z Machine. *Applied Optics*, 42(19):4059, 2003. URL: http://www.opticsinfobase.org/abstract.cfm?URI=AO-42-19-4059, doi:10.1364/AO.42.004059.

[35] P. W. Lake, J. E. Bailey, G. A. Rochau, T. C. Moore, D. Petmecky, and P. Gard. Time- and space-resolved elliptical crystal spectrometers for high energy density physics research. *Review of Scientific Instruments*, 75(10):3690, 2004. URL: http://link.aip.org/link/RSINAK/v75/i10/p3690/s1{&}Agg=doi, doi:10.1063/1.1788866.

[36] Alexander P. Shevelko. X-ray spectroscopy of laser-produced plasmas using a von Hamos spectrograph. In Igor I. Sobelman and Vladimir A. Slemzin, editors, *Proc. SPIE 3406, Current Russian Research in Optics and Photonics: New Methods and Instruments for Space- and Earth-based Spectroscopy*

in XUV, UV, IR, and Millimeter Waves, volume 3406, pages 91–108, jun 1998. URL: http://proceedings.spiedigitallibrary.org/proceeding.aspx?articleid=953236, doi:10.1117/12.310986.

[37] G. Hölzer, O. Wehrhan, J. Heinisch, E. Förster, T. A. Pikuz, A. Ya Faenov, S. A. Pikuz, V. M. Romanova, and T. A. Shelkovenko. Flat and Spherically Bent Muscovite (Mica) Crystals for X-ray Spectroscopy. *Physica Scripta*, 57(2):301–309, feb 1998. URL: http://stacks.iop.org/1402-4896/57/i=2/a=029?key=crossref.bb8e9589a3fa802c71bd8279e0d2ee59, doi:10.1088/0031-8949/57/2/029.

[38] A. L. Meadowcroft, C. D. Bentley, and E. N. Stott. Evaluation of the sensitivity and fading characteristics of an image plate system for x-ray diagnostics. *The Review of Scientific Instruments*, 79(11):113102, nov 2008. URL: http://www.ncbi.nlm.nih.gov/pubmed/19045884, doi:10.1063/1.3013123.

[39] PrismSPECT, 2015. URL: http://www.prism-cs.com/.

[40] P. F. Knapp. *Investigation of Conditions in Closely Spaced Parallel Exploding Aluminum Wires Using Point Projection X-Ray Absorption Spectroscopy*. PhD thesis, Cornell University, 2011.

[41] D. B. Sinars, M. Hu, K. M. Chandler, T. A. Shelkovenko, S. A. Pikuz, J. B. Greenly, D. A. Hammer, and B. R. Kusse. Experiments measuring the initial energy deposition, expansion rates and morphology of exploding wires with about 1 kA/wire. *Physics of Plasmas*, 8(1):216, 2001. URL: http://scitation.aip.org/content/aip/journal/pop/8/1/10.1063/1.1323759, doi:10.1063/1.1323759.

[42] K. M. Chandler, D. A. Hammer, D. B. Sinars, S. A. Pikuz, and T. A. Shelkovenko. The relationship between exploding wire expansion rates and wire material properties near the boiling temperature. *IEEE Transactions on Plasma Science*, 30(2):577–587, apr 2002. URL: http://ieeexplore.ieee.org/lpdocs/epic03/wrapper.htm?arnumber=1024292, doi:10.1109/TPS.2002.1024292.

[43] G. S. Sarkisov, S. E. Rosenthal, K. R. Cochrane, K. W. Struve, C. Deeney, and D. H. McDaniel. Nanosecond electrical explosion of thin aluminum wires in a vacuum: Experimental and computational investigations. *Physical Review E*, 71(4):046404, apr 2005. URL: http://link.aps.org/doi/10.1103/PhysRevE.71.046404, doi:10.1103/PhysRevE.71.046404.

[44] J. P. Chittenden, S. V. Lebedev, S. N. Bland, F. N. Beg, and M. G.

Haines. One-, two-, and three-dimensional modeling of the different phases of wire array Z-pinch evolution. *Physics of Plasmas*, 8(5):2305, 2001. URL: http://scitation.aip.org/content/aip/journal/pop/8/5/10.1063/1.1343883, doi:10.1063/1.1343883.

[45] T. A. Haill, K. R. Cochrane, C. J. Garasi, T. A. Mehlhorn, A. C. Robinson, and R. M. Summers. ALEGRA-MHD : Version 4 . 6. Technical Report January, Sandia National Laboratories, 2005. URL: http://prod.sandia.gov/techlib/access-control.cgi/2004/045997.pdf.

[46] S. D. Crockett. Los Alamos National Laboratory Report No. LA-UR-04-6442. Technical report, 2004.

[47] M. P. Desjarlais. Practical Improvements to the Lee-More Conductivity Near the Metal-Insulator Transition. *Contributions to Plasma Physics*, 41:2–3, 2001. URL: http://onlinelibrary.wiley.com/doi/10.1002/1521-3986(200103)41:2/3<267::AID-CTPP267>3.0.CO;2-P/abstract, doi:10.1002/1521-3986(200103)41:2/3<267::AID-CTPP267>3.0.CO;2-P.

[48] M. P. Desjarlais, J. D. Kress, and L. A. Collins. Electrical conductivity for warm, dense aluminum plasmas and liquids. *Physical Review E - Statistical, Nonlinear, and Soft Matter Physics*, 66(2):2–5, 2002. doi:10.1103/PhysRevE.66.025401.

[49] K. Cochrane, M. P. Desjarlais, T. Haill, J. Lawrence, M. Knudson, and G. Dunham. Aluminum Equation of State Validation and Verification for the ALEGRA HEDP Simulation Code. Technical report, 2006.

[50] S. B. Hansen, J. Bauche, C. Bauche-Arnoult, and M. F. Gu. Hybrid atomic models for spectroscopic plasma diagnostics. *High Energy Density Physics*, 3(1-2):109–114, may 2007. URL: http://linkinghub.elsevier.com/retrieve/pii/S1574181807000171, doi:10.1016/j.hedp.2007.02.032.

[51] E. W. Weisstein. Abel Transform, 2015. URL: http://mathworld.wolfram.com/AbelTransform.html.

[52] D. E. Goldberg. *Genetic Algorithms in Search, Optimization, and Machine Learning*. Addison-Wesley Professional, 1st edition, 1989.

[53] W. Schwanda and K. Eidmann. Observation of radiative burnthrough in x-ray heated beryllium by time-resolved spectroscopy. *Physical Review Letters*,

69(24):3507–3510, dec 1992. URL: http://link.aps.org/doi/10.1103/PhysRevLett.69.2013http://link.aps.org/doi/10.1103/PhysRevLett.70.694http://link.aps.org/doi/10.1103/PhysRevLett.69.3507, doi:10.1103/PhysRevLett.69.3507.

[54] S. Tzortzakis, P. Audebert, P. Renaudin, S. Bastiani-Ceccotti, J. P. Geindre, C. Chenais-Popovics, V. Nagels, S. Gary, R. Shepherd, F. Girard, I. Matsushima, O. Peyrusse, and J. C. Gauthier. Time- and space-resolved X-ray absorption spectroscopy of aluminum irradiated by a subpicosecond high-power laser. *Journal of Quantitative Spectroscopy and Radiative Transfer*, 99(1-3):614–626, may 2006. URL: http://linkinghub.elsevier.com/retrieve/pii/S0022407305001809, doi:10.1016/j.jqsrt.2005.05.049.

[55] B. L. Henke, P. Lee, T. J. Tanaka, R. L. Shimabukuro, and B. K. Fujikawa. Low-energy x-ray interaction coefficients: Photoabsorption, scattering, and reflection. *Atomic Data and Nuclear Data Tables*, 27(1):1–144, jan 1982. URL: http://www.sciencedirect.com/science/article/pii/0092640X8290002Xhttp://linkinghub.elsevier.com/retrieve/pii/0092640X8290002X, doi:10.1016/0092-640X(82)90002-X.

[56] B. L. Henke, E. M. Gullikson, and J. C. Davis. X-Ray Interactions: Photoabsorption, Scattering, Transmission, and Reflection at E = 50-30,000 eV, Z = 1-92. *Atomic Data and Nuclear Data Tables*, 54(2):181–342, jul 1993. URL: http://linkinghub.elsevier.com/retrieve/pii/S0092640X83710132, doi:10.1006/adnd.1993.1013.

[57] H. M. Epstein, R. E. Schwerzel, P. J. Mallozzi, and B. E. Campbell. Flash EXAFS for structural analysis of transient species: rapidly melting aluminum. *Journal of the American Chemical Society*, 105(6):1466–1468, mar 1983. URL: http://dx.doi.org/10.1021/ja00344a008http://pubs.acs.org/doi/abs/10.1021/ja00344a008, doi:10.1021/ja00344a008.

[58] E. P. Yu, B. V. Oliver, D. B. Sinars, T. A. Mehlhorn, M. E. Cuneo, P. V. Sasorov, M. G. Haines, and S. V. Lebedev. Steady-state radiation ablation in the wire-array Z pinch. *Physics of Plasmas*, 14(2):022705, 2007. URL: http://link.aip.org/link/?PHP/14/022705/1http://scitation.aip.org/content/aip/journal/pop/14/2/10.1063/1.2435332, doi:10.1063/1.2435332.

[59] T. A. Hall, J. Al-Kuzee, A. Benuzzi, M. Koenig, J. Krishnan, N. Grandjouan, D. Batani, S. Bossi, and S. Nicolella. Experimental observation of the shift and width of the aluminium K absorption edge in

laser shock-compressed plasmas. *Europhysics Letters (EPL)*, 41(5):495–500, 1998. URL: http://iopscience.iop.org/0295-5075/41/5/495/fulltext/, doi:10.1209/epl/i1998-00180-y.

[60] A. Benuzzi-Mounaix, F. Dorchies, V. Recoules, F. Festa, O. Peyrusse, A. Levy, A. Ravasio, T. Hall, M. Koenig, N. Amadou, E. Brambrink, and S. Mazevet. Electronic Structure Investigation of Highly Compressed Aluminum with K Edge Absorption Spectroscopy. *Physical Review Letters*, 107(16):165006, 2011. URL: http://link.aps.org/doi/10.1103/PhysRevLett.107.165006, doi:10.1103/PhysRevLett.107.165006.

[61] A. Mančić, A. Lévy, M. Harmand, M. Nakatsutsumi, P. Antici, P. Audebert, P. Combis, S. Fourmaux, S. Mazevet, O. Peyrusse, V. Recoules, P. Renaudin, J. Robiche, F. Dorchies, and J. Fuchs. Picosecond Short-Range Disordering in Isochorically Heated Aluminum at Solid Density. *Physical Review Letters*, 104(3):035002, 2010. URL: http://link.aps.org/doi/10.1103/PhysRevLett.104.035002, doi:10.1103/PhysRevLett.104.035002.

[62] S. A. Pikuz, T. A. Shelkovenko, D. B. Sinars, J. B. Greenly, Y. S. Dimant, and D. A. Hammer. Multiphase Foamlike Structure of Exploding Wire Cores. *Physical Review Letters*, 83(21):4313–4316, nov 1999. URL: http://link.aps.org/doi/10.1103/PhysRevLett.83.4313, doi:10.1103/PhysRevLett.83.4313.

[63] J. E. Bailey, T. Nagayama, G. P. Loisel, G. A. Rochau, C. Blancard, J. Colgan, P. H. Cosse, G. Faussurier, C. J. Fontes, F. Gilleron, I. Golovkin, S. B. Hansen, C. A. Iglesias, D. P. Kilcrease, J. J. MacFarlane, R. C. Mancini, S. N. Nahar, C. Orban, J. C. Pain, A. K. Pradhan, M. Sherrill, and B. G. Wilson. A higher-than-predicted measurement of iron opacity at solar interior temperatures. *Nature*, 517(7532):56–59, dec 2014. URL: http://dx.doi.org/10.1038/nature14048http://www.nature.com/doifinder/10.1038/nature14048, doi:10.1038/nature14048.

[64] I. H. Hutchinson. *Principles of Plasma Diagnostics*. Cambridge University Press, Cambridge, 2nd edition, 2005.

[65] A. J. Harvey-Thompson, S. V. Lebedev, S. Patankar, S. N. Bland, G. Burdiak, J. P. Chittenden, A. Colaitis, P. De Grouchy, H. W. Doyle, G. N. Hall, E. Khoory, M. Hohenberger, L. Pickworth, F. Suzuki-Vidal, R. a. Smith, J. Skidmore, L. Suttle, and G. F. Swadling. Optical Thomson Scattering Measurements of Cylindrical Wire Array Parameters. *Physical Review Letters*, 108(14):145002, apr 2012. URL: http://link.aps.org/doi/10.1103/PhysRevLett.108.145002, doi:10.1103/PhysRevLett.108.145002.

[66] E. Husain and R. Nema. Analysis of Paschen Curves for air, N2 and SF6 Using the Townsend Breakdown Equation. *IEEE Transactions on Electrical Insulation*, EI-17(4):350–353, aug 1982. URL: http://ieeexplore.ieee.org/lpdocs/epic03/wrapper.htm?arnumber=4080982, doi:10.1109/TEI.1982.298506.

[67] F. Fortin, F. D. Rainville, M. Gardner, M. Parizeau, and C. Gagne. DEAP : Evolutionary Algorithms Made Easy. *Journal of Machine Learning Research*, 13:2171–2175, 2012. URL: http://jmlr.csail.mit.edu/papers/volume13/fortin12a/fortin12a.pdf.

[68] Y. Hold-Geoffroy, O. Gagnon, and M. Parizeau. Once you SCOOP, no need to fork. In *Proceedings of the 2014 Annual Conference on Extreme Science and Engineering Discovery Environment - XSEDE '14*, pages 1–8, New York, New York, USA, 2014. ACM Press. URL: http://dl.acm.org/citation.cfm?doid=2616498.2616565, doi:10.1145/2616498.2616565.